7-19-2019

Analyzing Binary Black hole Spacetimes

Jam Sadiq
jxs1805@rit.edu

Rochester Institute of Technology

Ph.D. Dissertation

Analyzing Binary Black hole Spacetimes

Author:
Jam Sadiq

Advisor:
Dr. Yosef Zlochower

A dissertation submitted in partial fulfilment of the requirements
for the degree of Astrophysical Sciences and Technology

in the

School of Physics and Astronomy

July 19, 2019

Rochester Institute of Technology

Ph.D. Dissertation

Analyzing Binary Black hole Spacetimes

Author:

Jam Sadiq

Advisor:

Dr. Yosef Zlochower

A dissertation submitted in partial fulfilment of the requirements

for the degree of Astrophysical Sciences and Technology

in the

School of Physics and Astronomy

Approved by _____

Prof. Andrew Robinson Date

Director, Astrophysical Sciences and Technology

Certificate of Approval

Astrophysical Sciences and Technologies

R·I·T | *College of* Science

Rochester, NY, USA

The Ph.D. Dissertation of Jam Sadiq has been approved

by the undersigned members of the dissertation committee as satisfactory for the degree of

Doctor of Philosophy in Astrophysical Sciences and Technology.

CHAIR, Dr. David Ross Date

ADVISOR, Dr. Yosef Zlochower Date

COMMITTEE MEMBER, Dr. Richard O'Shaughnessy Date

COMMITTEE MEMBER, Dr. Lawrence Kidder Date

COMMITTEE MEMBER, Dr. Manuela Campanelli Date

ABSTRACT

With the first ever detection of gravitational waves from merging black-hole binaries by LIGO (Laser Interferometer GravitationalWave Observatory), a new era of gravitational wave astronomy was started. With its increased sensitivity, LIGO will see many more black-hole binaries in the future. To detect the gravitational waves and elucidate the properties of their sources, one needs theoretical waveform templates. These, in turn, require solving Einstein field equations, at least approximately. Approximate techniques like post-Newtonian theory and black-hole perturbation theory can produce waveforms that are accurate for certain phases of binaries evolution. Numerical relativity, on the other hand, can in principle produce accurate waveforms models for the full binary evolution. However, such simulations are computationally very expensive for the slow inspiral phase. To overcome this issue, we hybridized numerical relativity obtained by solving the Einstein field equations during the late-inspiral, plunge, and ringdown phase and post-Newtonian waveforms for the early-inspiral phase. Here we focus on hybridizing waveforms for precessing black-hole binaries. In this work we also developed a new tool to test the accuracy limits of approximate a binary black-hole spacetimes constructed using analytical approximate techniques. Our method is based on direct comparison to a numerically generated solution to the Einstein field equations.

CONTENTS

DECLARATION

I, Jam Sadiq ("the Author"), declare that no part of this dissertation is substantially the same as any that has been submitted for a degree or diploma at the Rochester Institute of Technology or any other University. I further declare that the work in Chapters 4 and 5 are entirely mine and collaborators; Chapters 1, 2 and 3 draw heavily from the available scientific work, including textbooks and research articles. Those who have contributed scientific or other collaborative insights are fully credited in this thesis, and all prior work upon which this thesis builds is cited appropriately throughout the text. This thesis was successfully defended in Rochester, NY, USA on the 9th of July, 2019.

Modified portions of this dissertation have previously been published by the Author in a peer-reviewed paper appearing in *Physical Reviews D* (Phys Rev D):

- **Chapter 5:** *Comparing an analytical spacetime metric for a merging binary to a fully non-linear numerical evolution using curvature scalars.*
  Jam Sadiq, Yosef Zlochower, Hiroyuki Nakano
  (Phys.Rev. D97 (2018) no.8, 084007).

LIST OF PUBLISHED WORK

1. *Comparing an analytical spacetime metric for a merging binary to a fully nonlinear numerical evolution using curvature scalars.*
   Jam Sadiq, Yosef Zlochower, Hiroyuki Nakano
   (Phys.Rev. D97 (2018) no.8, 084007).

LIST OF TABLES

LIST OF FIGURES

CHAPTER 1

INTRODUCTION

The contemplation of celestial things will make a man both speak and think more sublimely and magnificently when he descends to human affairs

Cicero

It was 14th of September 2015, when two giant detectors of gravitational waves called the Laser Interferometer gravitational wave observatory (LIGO), in the United States were undergoing final preparation for observations, that an unexpected signal was recorded. It took several months for careful analysis of the recorded data and what come out was one of the greatest observational results of the century. According to the analysis, LIGO observed gravitational waves coming from a far distant place where two black holes, both almost the mass 30 times that of the sun, merged together to form a bigger black hole and released an enormous amount of energy equivalent to 3 times the mass of sun in the form of gravitational waves [2].

Black holes and gravitational waves are both the predictions of Einstein's theory of general relativity. The recorded signals of September 14th, 2015 were very close to the predictions of Einstein's theory. Not only was this an electrifying moment in science, where a theoretical prediction was confirmed, it also started a new era of gravitational wave astronomy. This event is historically

similar to one 400 years ago when Galileo used a telescope and turned it to the sky to see the universe with light. For gravitational wave astronomy, thousands of scientist worked to construct LIGO detectors with about three decades of effort.

The detection of gravitational waves is not only a spectacular confirmation of Einstein's theory, but also the beginning of a new era in astrophysics. Up until now we have created a picture of the universe from the information obtained from amazing telescopes, such as Chandra in the X-rays, Hubble in the optical, Spitzer in the infrared, WMAP in the microwave and Arecibo in the radio frequencies. With current and upcoming LIGO observations, as well as, gravitational wave observations from future detectors including the LISA, Einstein telescope, Pulsar timing arrays etc., we will be exploring the universe in a new way using an entirely new spectrum of gravitational waves. This new type of astrophysics has an immense potential to truly revolutionize science because gravitational waves can provide very clean information about their sources. This will help us explore our universe's most extreme regions which we may not be able to see with electromagnetic waves.

1.1 Black Holes: Taxonomy and properties

Black holes are among the most mysterious astronomical objects in the universe. They are excellent theoretical laboratories that allow us to enhance our understanding of the nature of gravity. A black hole is a region of spacetime toward which matter is drawn and from which escape is impossible. One of the key concept about black hole is their surface called the event horizon. Nothing, not even light, can come out of the event horizon. Mathematically black holes can be completely described by a few parameters. The simplest black hole is the spherically symmetric solution of Einstein field equation known as a Schwarzschild black hole. This solution was first proposed by Karl Schwarzschild soon after Einstein formulated theory of general relativity. The Schwarzschild black hole can be completely described by its mass. The more generic and astrophysically relevant

black holes are the ones which are completely described by their mass and spin. These are called Kerr black holes. A generalization of Kerr black hole that also includes electrical charge is known as a Kerr-Newmann black hole.

There are two general classes of black holes that are believed to exist in the universe. The ones that are observed by LIGO are called stellar-mass black holes. They are believed to be formed by the collapse of massive stars as they run out of fuel. The collapse causes some of the material of star to be blown away as an explosion called a supernova. Depending on how massive the remnant of the supernova is, the remaining matter can form a stable neutron star or completely collapse and form a black hole. Although these black holes are supposed to have mass ranges between three and a few 10s of solar masses. It is supposed that bigger black holes are formed by the merger of smaller mass black holes. It is also plausible that large stellar-mass black holes formed by direct collapse of very massive stars that were present in the early universe. The second kind of black hole is much bigger, with the masses ranging from millions to billions of times the mass of the sun. These are called supermassive black holes. They are believed to exist at the centers of almost every galaxy. Our own galaxy Milky way contains a black hole of mass $\approx 10^6$ times heavier than the sun.

The concept of a black hole was proposed in a speculative way after Newton formulated his theory of universal gravitation. The idea was proposed by John Mitchell [3] and independently by Laplace [4] based on the idea of escape velocity from a gravitational field. Using the then popular idea of light being composed of particles, and using concept of escape velocity, Mitchell speculated about undetectable objects that are small and so massive that the escape velocity from such objects is larger than speed of light. So they might be undetectable by direct radiation but still manifest gravitational effects on material near them. Laplace went on to speculate that such objects may not only exists, but even be as abundant as the visible stars. After the demise of the particle theory of light, speculations of such objects lost popularity.

It was Karl Schwarzschild [5, 6] who solved Einstein's field equations exactly for the first time for a spherically symmetric spacetime. The result was the spacetime describing objects analogous to what Mitchell and Laplace had speculated about. Initially, the Schwarzschild spacetime was regarded as a mathematical curiosity rather than a representation of a real object. The reasons for this was contentious singular terms that obscured the physical interpretation of the spacetime. In addition, no one knew how these objects can form. Decades later in 1939, Oppenheimer and Snyder [7] suggested that the implosion of a dying star might actually create what Schwarzschild had found. They showed this by an analytical calculations of a dust ball undergoing a gravitational collapse which leaves behind the Schwarzschild metric. These calculations describe a crude model for stellar collapse, which was based on very simple idealized assumptions, therefore it was still believed that such collapse could be halted in realistic astrophysical situation. One important point of investigation was the absence of angular momentum in the Schwarzschild spacetime. It was completely unclear how any astrophysical object, which must carry some angular momentum could collapse to form objects described by Schwarzschild spacetime.

In 1963 Roy Kerr [8] discovered a generalization of the Schwarzschild solution with angular momentum, which shows that objects carrying angular momentum can collapsed to form black holes. Moreover, around the same time Hawking and Penrose[9, 10] showed that general relativity predicts the creation of singularities under very generic conditions. The development of astronomical observations and many other theoretical developments have revealed that the black holes actually exists and Laplace was correct in his speculations. Subsequently, interest built up about another predictions of Einstein general relativity, that of gravitational waves. It has been shown that one of the most interesting source of gravitational waves are compact objects like black holes since the gravitational waves emitted by the inspirals and mergers of binary black holes are the most likely sources for gravitational wave detected on Earth.

1.2 Gravitational Waves

Gravitational waves are one of the most exciting predictions of general relativity. Analogous to electromagnetism, where accelerating charges emit electromagnetic waves, the theory of general relativity predicts that accelerating massive bodies can produced ripples in spacetimes called gravitational waves. These waves carry energy and travel at speed of light. However, the intensities of gravitational waves are exceedingly small compared to electromagnetic waves. That is why very sophisticated, sensitive detectors with advanced technologies are required for their detections (e.g., LIGO). Once again, similar to electromagnetic waves which cause electrical charges to oscillate, a passing gravitational wave will induce accelerations of test masses. More precisely, gravitational waves stretch and squeeze the distances between test masses. Similar to electromagnetic waves, gravitational waves have polarization states. However, they cannot be characterized by a single polarization vector, but rather by two perpendicular directions, both also perpendicular to the direction of propagation. The effect of a gravitational wave on a ring of test masses is to alternatively stretch the ring in one of these directions and compress it in the other.

Einstein was the first to solve the equations that describe the rate of energy loss due to emission of gravitational waves from a binary mechanical system [11]. According to his famous quadrupole formula, the gravitational strain due to a gravitational wave is given by,

$$h_{ij} = \frac{2G}{r}\frac{d^2}{dt^2}Q_{ij}(t - r/c), \tag{1.1}$$

where Q_{ij} is the quadrupole tensors of the source. Unlike electromagnetism, there are no gravitational waves due to a changing dipole moment. Just as the strength of the dipole moment governs the efficiency of generation of electromagnetic waves, so to the strength of the quadrupole moment control the output of gravitational waves. Einstein found that gravitational waves from realistic astrophysical sources are so weak as to be undetectable. There was also skepticism on the existence of gravitational waves. But with the advancement of theoretical understanding of massive objects

like black holes and neutron stars, as well as astrophysical observations like binary pulsar system PSR 1913 + 16 [12], it become evident that gravitational waves exist.

Joseph Weber was the pioneer for the detection of gravitational waves. Although his detector, which was based on vibrating bars, was insufficiently sensitive to actually detect astrophysical waves, he created an interest in the field. This, and the indirect evidence of black holes and compact objects like neutron stars and theoretical advancements gave impetus to the field. LIGO was conceived in the 1970s and it took decades of efforts to build the two LIGO detectors in United States. Since then LIGO detected gravitational waves from the mergers of binary compact objects, like binary neutron stars as well as binary black holes. But gravitational waves from other sources like pulsating neutron stars and supernova explosion will hopefully also be detected by LIGO. There is another detectors, similar to LIGO, called Virgo in Italy that is also operational, and in the future other detectors will be built to detect more gravitational waves. Gravitational waves from other sources like supermassive black hole binaries as well as big bang will not be detectable by LIGO but require more advanced detectors, such as planned space-based Laser Interferometer Space Antenna (LISA), the Einstein telescope, A+, LIGO Voyager and Cosmic Explorer.

1.3 Geodesics and Curvature

Newton described gravity as a force that acts at a distance across the empty space between material bodies. The Earth, for example moves in a curved orbit around the Sun because the Sun's gravity forces it away from its natural straight path. Einstein, on the other hand, argued that gravity was better understood not as a force at all, but as a manifestation of spacetime geometry. According to Einstein, the Sun's mass distorts the geometry of spacetime in its vicinity, and the Earth, gliding freely and without experiencing any forces, wanders along the straightest possible path in this curved background (which is to say, it moves on a geodesic of the curved spacetime). Thus, the path of the Earth orbiting the Sun is the projection of a geodesic of the curved 4

dimensional spacetime geometry around the star onto a 3 dimensional space.

Newtonian theory implied that a gravitational field can be detected by the tidal effects it produces. Newton explained the tides generated on the oceans of the Earth were caused by the gravitational field of the Moon. In Einstein's theory tidal forces are particularly important because they are directly related to the curvature of spacetime. This spacetime curvature is expressed in the language of tensors using a mathematical object known as the Riemann tensor. The Riemann tensor contains 20 independent components that encode all the geometrical information about how the spacetime curves in different directions. It can be described by the difference in acceleration due to gravity for two nearby particles in a gravitational field. The tidal acceleration of these particles is proportional to the Riemann tensor and the separation between them. Given the Riemann tensor and gravitational sources that are not too strong, the motion of falling test particles can be computed in a routine way. In most astrophysical situations, the predictions of general relativity and Newtonian gravity agree quite well, but there are small corrections, such as those that account for the perihelion precession of the planet Mercury.

1.4 New Developments in this Thesis

In this work we focused on the dynamics of binary black holes. We studied the binary black hole system using numerical and analytical techniques. In one project, we constructed hybrid waveforms using analytical model waveforms for the early inspiral phase and available numerical relativity waveforms for the late inspiral and merger phases of the binary black hole system. These hybrids are important for LIGO source parameter modeling. We developed a new method for hybridization which can be use to construct hybrid for generic precessing binary black hole system. We then checked the accuracy of our hybrids in the frequency domain using standard mismatch techniques to compared our hybrids with other models describing the same physical system. We studied different errors in the hybrid construction that can affect the accuracy of the hybrids. We also explain how our methods can be further improved.

In another project, we developed tools to compare an analytically constructed spacetime of a binary black hole system with an equivalent numerical spacetime using timelike geodesics. We tested the accuracy of this analytic spacetime by comparing gauge invariant quantities related to geodesic deviation along a set of geodesics. Our method can not only be used to check the accuracy limits of the analytical spacetime, but it can also be used to improve the accuracy of such spacetimes. We also discuss the limitations of our technique.

CHAPTER 2

THE GENERAL THEORY OF RELATIVITY

The general theory of relativity then completed and - in contrast to the special theory - worked out by Einstein alone without simultaneous contributions by other researchers, will forever remain the classic example of a theory of perfect beauty in its mathematical structure.

Wolfang Pauli

2.1 Introduction to General relativity

The general theory of relativity is one of the greatest theoretical achievements of 20th century physics. It is the theory of space, time and gravitation formulated by Einstein in 1915. At the heart of it is the idea that gravity is the geometry of space and time. It describes gravitation in terms of elegant mathematical structure called differential geometry. General relativity describes the macroscopic structure of the universe. It predicts existence of exotic objects like black-holes and neutron stars, and describes the big bang and origin of the universe. It has been verified experimentally and so far it passes all the experimental verification. To understand and use this theory, it is important to understand the language of differential geometry. In this chapter we will explore important mathematical ideas needed to understand general relativity and use them to learn about new areas of current research. This chapter is distilled from [13, 14, 15, 16, 17, 18, 19,

20, 21, 22, 23, 24, 25, 26, 27, 28, 29, 30, 31, 32].

2.1.1 Notation

In this work we express tensors in both the more conventional coordinate basis and in orthonormal bases. Latin indices near the beginning of the alphabet are abstract tensor indices [14], which indicate the type of tensors involved in a calculation, as well as contraction. Latin indices near the end of the alphabet denote coordinate-basis components of spatial tensors, while Greek letters denote 4-dimensional spacetime components in the coordinate basis. Components of tensors in an orthonormal basis (the first element of the orthonormal basis is always timelike) are denoted by a Greek or Latin letter surrounded by square braces. Whether associated with coordinate bases or orthonormal bases, Greek indices range from 0 to 3, while Latin indices near the end of the alphabet range from 1 to 3. We use the geometric unit system, where $G = c = 1$.

2.2 General Relativity Formalism

2.2.1 Space-time Manifold

The mathematical structure of a spacetime is a four-dimensional manifold $\mathcal{M}$. Loosely speaking, a manifold is a continuous space of points that may be curved globally, but locally looks like Euclidean space $\mathbb{R}^n$. Mathematically, a manifold $\mathcal{M}$ of dimension n is defined as a space that can be covered by a collection of charts, that is, one-to one mappings (or coordinates) from $\mathbb{R}^n$ to $\mathcal{M}$. The choice of coordinates is arbitrary. A differentiable manifold is one that is continuous and differentiable. The curved spacetime of general relativity is described in terms of differentiable manifold.

2.2.2 Scalars

Scalar functions are functions that map points in the manifold to real or complex numbers. All points in a spacetime point can be described by multiple coordinate systems. For example a

point may be described by $x^\mu = (t, x, y, z)$ in Cartesian coordinates can also be defined by spherical coordinates $y^\mu = (t, r, \theta, \phi)$. Scalar functions are unaffected by a change of coordinates.

2.2.3 Vectors

In a curved spacetime we define vectors using directional derivatives. Let a curve γ in spacetime be described parametrically by $x^\alpha(\lambda)$, where λ is a parameter. Let a function $f(\lambda) = F(x^\alpha(\lambda))$ be defined on the curve. Then the derivative of $f(\lambda)$ with respect to λ is

$$\frac{df}{d\lambda} = \frac{dx^\mu}{d\lambda}\frac{\partial F}{\partial x^\mu} = u^\mu \frac{\partial F}{\partial x^\mu}, \tag{2.1}$$

where $u^\alpha = \frac{dx^\alpha}{d\lambda}$ are the components of the tangent vector $\mathbf{u} = \frac{d}{d\lambda}$ to the curve γ. That is, a directional derivative of F at a point along the curve γ is associated with a set of components u^α. Clearly the directional derivative of F itself does not depends on the coordinate system on which it is evaluated as $\frac{df}{d\lambda}$ is same for any coordinate choice however, the components of vector are coordinate dependent and given by,

$$\mathbf{u} = u^\mu \frac{\partial}{\partial x^\mu} = u^\mu \frac{\partial x'^\nu}{\partial x^\mu}\frac{\partial}{\partial x'^\nu} \tag{2.2}$$

Thus the components u^α of $\mathbf{u}$ transform as

$$u'^\alpha = \frac{\partial x'^\alpha}{\partial x^\mu} u^\mu$$

under a coordinate transformation from x^μ to x'^μ, and the coordinate basis vectors $\vec{e}_\alpha = \frac{\partial}{\partial x^\alpha}$ transforms as

$$\frac{\partial}{\partial x'^\alpha} = \frac{\partial x^\mu}{\partial x'^\alpha}\frac{\partial}{\partial x^\mu}$$

where the Jacobian matrices are the inverses of each other, i.e., satisfy

$$\frac{\partial x^{\mu}}{\partial x'^{\alpha}}\frac{\partial x'^{\alpha}}{\partial x^{\nu}} = \frac{\partial x'^{\mu}}{\partial x^{\alpha}}\frac{\partial x^{\alpha}}{\partial x'^{\nu}} = \delta^{\mu}_{\nu}$$

and the Kronecker delta (identity matrix)

$$\delta^{\mu}_{\nu} = \begin{cases} 1 & \mu = \nu \\ 0 & \mu \neq \nu \end{cases} \tag{2.3}$$

has same components in every coordinate system.

2.2.4 One-forms or Dual vectors

A dual vector (also called a differential form or one-form) $\boldsymbol{\omega} = \omega_{\mu}\frac{\partial x^{\mu}}{\partial}$ is a linear map which, at each point of spacetime, takes a vector and returns a number. In other words, it takes a vector field and returns a scalar field. The dual basis $\underset{\sim}{e}^{\alpha}$ is defined by its operation on vector basis $\vec{e}_{\alpha}$ via $\underset{\sim}{e}^{\alpha}(\vec{e}_{\beta}) = \delta^{\alpha}_{\beta}$. The components of one-form transform as

$$\omega'_{\mu} = \frac{\partial x^{\nu}}{\partial x'^{\mu}}\omega_{\nu}$$

and the dual basis $\underset{\sim}{e}^{\alpha}$ transforms as

$$\underset{\sim}{e}'^{\mu} = \frac{\partial x'^{\mu}}{\partial x^{\nu}}\underset{\sim}{e}^{\nu}$$

These transformations of the vectors and dual-vectors are the primary building blocks of a more general class of geometric objects called tensors.

2.2.5 Tensors

The Cartesian product of an arbitrary number of dual-vectors and vectors is called a tensor. A tensor $\mathbf{T}$ of rank $\binom{m}{n}$ is expanded in a basis as

$$\mathbf{T} = T^{\alpha_1 \ldots \alpha_m}_{\beta_1 \ldots \beta_n} \vec{e}_{\alpha_1} \otimes \ldots \otimes \vec{e}_{\alpha_m} \otimes \underset{\sim}{e}^{\beta_1} \otimes \ldots \otimes \underset{\sim}{e}^{\beta_n}. \tag{2.4}$$

The tensor product $\otimes$ combines tensors of rank $\binom{m}{n}$ and $\binom{p}{q}$ into a tensor of rank $\binom{m+p}{n+q}$ whose components are the direct product of the input components. Tensors are also defined by their transformation law. The component of a tensor transform as

$$T'^{\alpha_1 \ldots \alpha_m}_{\beta_1 \ldots \beta_n} = \frac{\partial x'^{\alpha_1}}{\partial x^{\gamma_1}} \ldots \frac{\partial x'^{\alpha_m}}{\partial x^{\gamma_m}} \frac{\partial x^{\delta_1}}{\partial x'^{\beta_1}} \ldots \frac{\partial x^{\delta_n}}{\partial x'^{\beta_n}} T^{\gamma_1 \ldots \gamma_m}_{\delta_1 \ldots \delta_n}. \tag{2.5}$$

A scalar function is rank $\binom{0}{0}$ tensor. Vectors and dual vectors are tensors of rank $\binom{1}{0}$ and $\binom{0}{1}$, respectively. It is convenient to introduce notation for totally symmetric and anti symmetric parts of a tensor. Tensor index symmetrization, denoted by parenthesis, is the average over all the permutation of the order of the given indices, for example for a three index tensor

$$T_{(\beta\gamma\delta)} = \frac{1}{3!}(T_{\beta\gamma\delta} + T_{\gamma\delta\beta} + T_{\delta\beta\gamma} + T_{\gamma\beta\delta} + T_{\beta\delta\gamma} + T_{\delta\gamma\beta}) \tag{2.6}$$

Tensor index anti-symmetrization, denoted by square brackets, is the average over all permutation of the order of the indices, with odd permutations carrying a minus sign. For example,

$$T_{[\beta\gamma\delta]} = \frac{1}{3!}(T_{\beta\gamma\delta} + T_{\gamma\delta\beta} + T_{\delta\beta\gamma} - T_{\gamma\beta\delta} - T_{\beta\delta\gamma} - T_{\delta\gamma\beta}) \tag{2.7}$$

2.2.6 The Metric Tensor

One of the most important objects in differential geometry is the rank $\binom{0}{2}$ metric tensor $\boldsymbol{g} = g_{\alpha\beta} \underset{\sim}{e}^{\alpha} \otimes \underset{\sim}{e}^{\beta}$. A metric $\boldsymbol{g}$ is a symmetric tensor and is used to define the scalar product of vectors

$\boldsymbol{u}\cdot\boldsymbol{v} = g_{\mu\nu}u^\mu v^\nu$. The metric acts as bijective map on tangent and cotangent spaces where the vectors and dual-vectors live. The metric is invertible with its inverse given by $g^{\mu\nu}$. The metric is used to lower indices of tensors, while its inverse raises indices. For example it transforms components according to

$$\begin{aligned} \omega^\mu &= g^{\mu\nu}\omega_\nu \\ u_\mu &= g_{\mu\nu}u^\nu \\ T_\lambda{}^{\nu\sigma} &= g_{\mu\lambda}g^{\rho\sigma}T^{\mu\nu}{}_\rho \ . \end{aligned} \tag{2.8}$$

The metric is used to define the invariant line element

$$ds^2 = g_{\alpha\beta}dx^\alpha dx^\beta, \tag{2.9}$$

which is generalization of the Pythagorean theorem, and takes the familiar form when $g_{\alpha\beta} = \delta_{\alpha\beta}$. The line element is an invariant quantity upon which all observer agrees, irrespective of the states of motion of observer and their chosen coordinate system. For a flat spacetime, $g_{\alpha\beta}$ becomes the Minkowski metric $\eta_{\alpha\beta}$. In Cartesian coordinates with $x^\alpha = (t, x, y, z)$ the Minkowski metric components are $\eta_{\alpha\beta} = \mathrm{diag}(-1, 1, 1, 1)$, representing a global inertial frame.

The general theory of relativity is based on the principle that, at any event, one can always find a coordinate system where $g_{\alpha\beta} = \eta_{\alpha\beta}$ at that point. This is a local property of spacetime. In other words the metric $g_{\alpha\beta}$ can be turned into $\eta_{\alpha\beta}$ anywhere, but not everywhere at the same time. This allows us to define the *signature* of a metric: as $g_{\mu\nu}$ locally corresponds to the matrix $\mathrm{diag}(-1, 1, 1, 1)$, we say that its signature is $(-+++)$, which is called a *Lorentzian* signature. A manifold equipped with such a metric is then called a Lorentzian manifold. In contrast, a *Riemannian* manifold would be equipped with a metric with signature $(++++)$.

2.2.7 Covariant Derivative

Differentiation is obviously one of the important topic in general relativity. When studying curved spacetime, we are interested to know how things change in space and time. Differentiation requires comparing two objects at two different points. In a curved geometry, comparing a geometric object at two different points on manifold is not well defined. In addition, the partial derivative of vectors and tensors do not transform like a tensor, and hence are not tensors themselves. We want a derivative operator that does transform like a tensor. There are many different ways to define derivative operator for curved spacetime. One of them is covariant derivative operator. It is a linear and Leibniz map from tensor of rank $\binom{m}{n}$ to rank $\binom{m}{n+1}$. For a scalar f, the covariant derivative reduces to ordinary derivative or partial derivative, i.e., $\nabla_\mu f = \partial_\mu f$.

For tensors the covariant derivative can be seen as a generalization of the partial derivative. It appeared naturally as a way to properly take derivatives of components of vectors or tensors, by taking into account the changes of the coordinate system when one moves from one point to another. The underlying mathematical structure is called a connection.

The covariant derivative of a vector $\vec{v}$ is a tensor $\nabla_\mu \vec{v}$, whose components are

$$\nabla_\mu v^\nu \ = v^\nu{}_{;\mu} = v^\nu{}_{,\mu} + \Gamma^\nu{}_{\rho\mu} v^\rho \ . \tag{2.10}$$

The semicolon ";" and comma "," serves as a short-hand notation for the covariant derivative and partial derivative, respectively and the Christoffel symbols $\Gamma^\nu{}_{\rho\mu}$, also called connection coefficients, are

$$\Gamma^\nu{}_{\rho\mu} = \frac{1}{2}\, g^{\nu\sigma}(g_{\sigma\rho,\mu} + g_{\sigma\mu,\rho} - g_{\mu\rho,\sigma}). \tag{2.11}$$

The Christoffel symbols are symmetric in their last indices: $\Gamma^\nu{}_{\rho\mu} = \Gamma^\nu{}_{\mu\rho}$. The connection is not a tensor, but the difference of two connection is. One can also define the covariant derivative $\nabla_\mu \omega_\nu$

of a dual-vector ω_ν as

$$\nabla_\mu \omega_\nu = \omega_{\nu;\mu} = \partial_\mu \omega_\nu - \Gamma^\rho{}_{\mu\nu}\omega_\rho \ . \tag{2.12}$$

More generally, the covariant derivative of a tensor is a tensor with components

$$\begin{aligned} T^{\mu_1\ldots\mu_n}{}_{\nu_1\ldots\nu_m;\rho} = T^{\mu_1\ldots\mu_n}{}_{\nu_1\ldots\nu_m,\rho} + \Gamma^{\mu_1}{}_{\sigma\rho}T^{\sigma\ldots\mu_n}{}_{\nu_1\ldots\nu_m} + \ldots + \Gamma^{\mu_n}{}_{\sigma\rho}T^{\mu_1\ldots\sigma}{}_{\nu_1\ldots\nu_m} \\ - \Gamma^\sigma{}_{\nu_1\rho}T^{\mu_1\ldots\mu_n}{}_{\sigma\ldots\nu_m} - \ldots - \Gamma^\sigma{}_{\nu_m\rho}T^{\mu_1\ldots\mu_n}{}_{\nu_1\ldots\sigma} \, . \end{aligned} \tag{2.13}$$

The structure is: there is a Christoffel symbol for each index of the tensor, with a plus sign if the index is upstairs (like vectors), and a minus sign if the index is downstairs (like dual-vectors). Just like partial derivatives, covariant derivatives are subject to the Leibniz rule with respect to multiplication, that is

$$\nabla_\mu(T^{\nu\rho}v_\sigma) = (\nabla_\mu T^{\nu\rho})v_\sigma + T^{\nu\rho}(\nabla_\mu v_\sigma) \ . \tag{2.14}$$

Another important property of covariant derivative is that it is compatible with the metric $g_{\mu\nu}$, that is

$$\nabla_\rho g_{\mu\nu} = 0 = \nabla_\rho g^{\mu\nu}. \tag{2.15}$$

This property is called metric-preservation by ∇. Combined with the Leibniz rule, this means that whenever the metric appears in a covariant derivative, it can freely be taken in or out. A particular consequence is that indices can be freely raised and lowered when they are inside a covariant derivative. This property is not true for simple partial derivatives. With the covariant derivatives we can define the parallel propagation of a vector. Parallel propagation restricts the motion of a vector along a curve or path in such a way that it remains as parallel to itself as possible at each step. Mathematically, a tensor T is parallel transported along a curve with a tangent vector u^α if

$u^\mu \nabla_\mu T^{\alpha_1\alpha_2\ldots\alpha_n}_{\beta_1\beta_2\ldots\beta_m} = 0.$

2.2.8 Lie Derivative

The covariant derivative requires a manifold with connection. It is possible to construct derivative for curved spacetime that utilize less structure. The *Lie derivative* is a coordinate invariant map from tensor of rank $\binom{m}{n}$ to rank $\binom{m}{n}$. It measure how a tensor changes as it is moved along the flow defined by a vector field.

Consider a vector field **u** on a manifold, with integral curves $x^\alpha(\lambda)$ defined by

$$\frac{dx^\alpha}{d\lambda} = u^\alpha(x^\beta(\lambda)), \tag{2.16}$$

where λ is parameter along the curves. The curves $x^\alpha(\lambda)$ form a *congruence*. Let T^β_α be a tensor field which changes from $T^\beta_\alpha(x^\gamma)$ to $T'^\beta_\alpha(x'^\gamma)$ by a small displacement along the vector field u^α via active coordinate transformation $x^\alpha \to x'^\alpha = x^\alpha + \epsilon u^\alpha$ then we define the Lie derivative as

$$\mathcal{L}_u T^\beta_\alpha = \lim_{\epsilon\to 0}\left[\frac{T^\beta_\alpha(x'^\gamma) - T'^\beta_\alpha(x'^\gamma)}{\epsilon}\right]. \tag{2.17}$$

By Taylor expanding $T^\beta_\alpha(x'^\gamma)$ about x^γ and taking the limit, we get,

$$\mathcal{L}_u T^\beta_\alpha = u^\gamma \partial_\gamma T^\beta_\alpha + T^\gamma_\alpha \partial_\gamma u^\beta - T^\beta_\gamma \partial_\alpha u^\gamma. \tag{2.18}$$

Using the symmetry of connection coefficients, the Lie derivative can be expressed using covariant derivative as

$$\mathcal{L}_u T^\beta_\alpha = u^\gamma \nabla_\gamma T^\beta_\alpha + T^\gamma_\alpha \nabla_\gamma u^\beta - T^\beta_\gamma \nabla_\alpha u^\gamma. \tag{2.19}$$

To generalize to tensors of arbitrary rank, simply append terms involving the derivative of u^α

for each index of input tensor according to above pattern. For a scalar function f, the Lie derivative reduces to directional derivative

$$\mathcal{L}_u f = u^\alpha \nabla_\alpha f. \tag{2.20}$$

The action of Lie derivative on a vectors is naturally expressed in terms of the *commutator*

$$\mathcal{L}_u v^\alpha = [\boldsymbol{u}, \boldsymbol{v}]^\alpha = u^\beta \nabla_\beta v^\alpha - v^\beta \nabla_\beta u^\alpha \tag{2.21}$$

A tensor T^β_α is said to be *Lie dragged* along u^α if

$$\mathcal{L}_u T^\beta_\alpha = 0. \tag{2.22}$$

An important application of Lie derivative is its action on the metric tensor

$$\mathcal{L}_u g_{\alpha\beta} = u^\gamma \nabla_\gamma g_{\alpha\beta} + g_{\gamma\beta} \nabla_\alpha u^\gamma + g_{\gamma\alpha} \nabla_\beta u^\gamma. \tag{2.23}$$

If ∇_α is metric compatible then

$$\mathcal{L}_u g_{\alpha\beta} = \nabla_\alpha u_\beta + \nabla_\beta u_\alpha. \tag{2.24}$$

A vector ξ^α is called a *Killing vector* if it satisfies

$$\mathcal{L}_{\boldsymbol{\xi}} g_{\alpha\beta} = 0. \tag{2.25}$$

From the above, we see ξ^α is a Killing vector if

$$\nabla_\alpha \xi_\beta + \nabla_\beta \xi_\alpha = 0. \tag{2.26}$$

A Killing vector represents an isometry whereby the metric tensor is unchanged along the direction of vector. If a metric tensor describing a spacetimes is expressed in some coordinates and the components of metric are independent of one or more of these coordinates then there is a Killing vector associated with that coordinate. Spacetime which are constant in time have timelike Killing vectors whereas axisymmetric spacetimes have a space like Killing vector. Since symmetries of a spacetime are related to conserved quantities, the existence of Killing vectors imply the existence of conserved quantities that can be used to find the constants associated with motion along a geodesic. For example, along a geodesic with tangent vector u^α, the quantity $\xi^\alpha u_\alpha$ is unchanged

$$u^\alpha \nabla_\alpha (\xi^\beta u_\beta) = 0. \tag{2.27}$$

2.2.9 Principle of General Covariance

Einstein's theory of general relativity is based on the principle of equivalence which states that, at any point in spacetime, it is always possible to construct a locally inertial coordinate system in which the laws of special relativity are obeyed. The principle of equivalence also implies that any set of coordinate systems are in principle suitable to describe the of laws of general relativity. Therefore, the equations that represent these laws must remain intact with respect to any transformation of coordinates. In other words they must be generally covariant. This led Einstein to describe the principle of general covariance which is a mathematical expression of the generalized principle of the theory of general relativity. The principle of general covariance states that a physical equation holds in general gravitational field, if two conditions are met

- The equation holds in the absence of gravitation; that is, it agrees with the laws of special relativity when the metric tensor $g_{\alpha\beta}$ equals the Minkowski metric $\eta_{\alpha\beta}$ of special relativity

and when connection coefficient $\Gamma^{\alpha}{}_{\beta\gamma}$ vanishes.

- The equation is generally covariant; that is, it preserves its form under general coordinate transformation $(x^{\mu}) \to (y^{\alpha})$

The principle of general covariance can only be applied on a scale that is small compared with spacetime distances typical of gravitational field, for it is only on this small scale that we are assured by principle of equivalence of being able to construct a coordinate system in which the effects of gravitation are absent.

2.2.10 Geodesic Equation

A curve is geodesic if it extremizes the distance between two points on a manifold. It is a generalization of the shortest distance between two points in Euclidean space. There are two equivalent definition of a geodesic in the Lorentzian geometry of general relativity

1. A geodesic is an extremal curve γ. More precisely, for two events A and B in spacetime, the proper length or proper time between A and B along γ must be stationary with respect to infinitesimal variations:

$$\frac{\delta s}{\delta x^{\mu}} = 0, \tag{2.28}$$

with

$$s = \int_A^B ds = \int_A^B \sqrt{|g_{\mu\nu}\frac{dx^{\mu}}{d\lambda}\frac{dx^{\nu}}{d\lambda}|}d\lambda, \tag{2.29}$$

where λ is any parameter on γ. The absolute value in the square-root is here to account for the time-like case. In that case, s is usually denoted τ (and is the proper time between A and B).

2. A geodesic is a *self-parallel* curve, i.e., a curve whose tangent vector $\mathbf{u}$ satisfies $\nabla_{\boldsymbol{u}}\boldsymbol{u} = \kappa\boldsymbol{u}$,

where κ is any scalar function. In terms of components, this reads

$$u^\mu \nabla_\mu u^\nu = \frac{du^\nu}{d\lambda} + \Gamma^\nu{}_{\mu\rho} u^\mu u^\rho = \kappa u^\nu \ . \tag{2.30}$$

Eq. (2.30) is called the *geodesic equation*.

There are three main categories of geodesics denoted by time-like, null, and space-like, where $\boldsymbol{u} \cdot \boldsymbol{u}$ is negative, zero, or positive, respectively. It is easy to show that for a geodesic described by Eq. (2.30), the norm of the tangent vector, $N = \boldsymbol{u} \cdot \boldsymbol{u} = u^\mu u_\mu$, with $u^\mu = \frac{dx^\mu}{d\lambda}$, reads

$$\frac{d}{d\lambda} \ln N = 2\kappa, \tag{2.31}$$

and that there exists a suitable choice for λ, called an *affine parameter*, such that the geodesic equation becomes $u^\mu \nabla_\mu u^\nu = 0$, that is, $\kappa = 0$. In the time-like case, proper time τ is such a parameter while for the spacelike case it is proper distance.

2.2.11 Curvature and Geodesic Deviation

There are various equivalent ways of introducing the curvature of a manifold. One with a particularly attractive geometric interpretation is based on the *geodesic deviation equation*. For any two very close geodesics, affinely parametrised by s, let $\xi^\mu(s) = x_2^\mu(s) - x_1^\mu(s)$ be the separation vector. The separation vector then obeys

$$\frac{D^2 \xi^\mu}{ds^2} = R^\mu{}_{\nu\rho\sigma} u^\nu u^\rho \xi^\sigma \ , \tag{2.32}$$

where $u^\mu = \frac{dx^\mu}{ds}$ is the tangent vector of one of the geodesics, and the four-index quantity $R^\mu{}_{\nu\rho\sigma}$ represents the components of the *Riemann curvature tensor*. The left-hand side of eq. (2.32) can be understood as a relative "acceleration" between the two geodesics, as one moves along them. In a *flat* geometry, geodesics are straight lines, and therefore their relative distance changes at a constant rate, $\xi^\mu \propto s$. This is the case of the Euclidean and Minkowski geometries, for which the

Riemann tensor is zero. In a curved space, or spacetime, things are different as two neighbouring geodesics can, for instance, start diverging and end up converging, like great circles on a sphere.

The Riemann tensor can also be defined by its effect on a vector $\boldsymbol{v}$,

$$(\nabla_\mu \nabla_\nu - \nabla_\nu \nabla_\mu) v^\sigma = R^\sigma{}_{\rho\mu\nu} v^\rho \ , \tag{2.33}$$

from which we can deduce the expression of its components which are

$$R^\sigma{}_{\rho\mu\nu} = \partial_\mu \Gamma^\sigma{}_{\rho\nu} - \partial_\nu \Gamma^\sigma{}_{\rho\mu} + \Gamma^\sigma{}_{\lambda\mu}\Gamma^\lambda{}_{\rho\nu} - \Gamma^\sigma{}_{\lambda\nu}\Gamma^\lambda{}_{\rho\mu} \ . \tag{2.34}$$

Although the Riemann tensor has, in four dimensions, $4^4 = 256$ possible combinations of indices, it enjoys a number of symmetries and identities which make this number fall to 20. These symmetries are

$$R_{\mu\nu\rho\sigma} = -R_{\nu\mu\rho\sigma} \ , \tag{2.35}$$

$$R_{\mu\nu\rho\sigma} = -R_{\mu\nu\sigma\rho} \ , \tag{2.36}$$

$$R_{\mu[\nu\rho\sigma]} = 0 \ . \tag{2.37}$$

Where, $[\nu\rho\sigma]$ represents anti-symmetrization over these indices. Explicitly, we have

$$R_{\mu[\nu\rho\sigma]} = \frac{1}{3!}(R_{\mu\nu\rho\sigma} + R_{\mu\rho\sigma\nu} + R_{\mu\sigma\nu\rho} - R_{\mu\nu\sigma\rho} - R_{\mu\rho\nu\sigma} - R_{\mu\sigma\rho\nu}) \tag{2.38}$$

$$= \frac{1}{3}(R_{\mu\nu\rho\sigma} + R_{\mu\rho\sigma\nu} + R_{\mu\sigma\nu\rho}), \tag{2.39}$$

where the second line is obtained using the anti-symmetry of the last pair of indices. The above relations can also be combined to show that the components of the Riemann tensor are invariant under the exchange of the first pair and second pair of indices,

$$R_{\mu\nu\rho\sigma} = R_{\rho\sigma\mu\nu}. \tag{2.40}$$

Finally, the covariant derivative of the Riemann tensor satisfies the *Bianchi identity*

$$R_{\mu[\nu\rho\sigma;\lambda]} = 0, \tag{2.41}$$

where, again, $[\nu\rho\sigma;\lambda]$ corresponds to a full anti-symmetrization over the indices $(\nu, \rho, \sigma, \lambda)$.

The Ricci tensor $R_{\mu\nu}$ is defined as a trace of the Riemann tensor, in the sense that its components are

$$R_{\mu\nu} = R^{\rho}{}_{\mu\rho\nu} \ , \tag{2.42}$$

where we contracted the first and third indices. Using that the symmetries of the Riemann tensor, it is easy to show that the Ricci tensor is symmetric, i.e. $R_{\mu\nu} = R_{\nu\mu}$. Finally, we refer to the trace of the Ricci tensor as the *Ricci scalar*, which is denoted by $R = R^{\mu}{}_{\mu} = g^{\mu\lambda}R_{\mu\lambda}$.

Another important equation is the second *Bianchi identity*, which is given by

$$\left(R^{\mu}{}_{\nu} - \frac{1}{2}\delta^{\mu}{}_{\nu}R\right)_{;\mu} = 0 \ . \tag{2.43}$$

2.2.12 The Einstein Equations

The Ricci tensor and curvature scalar are combined to form Einstein tensor **G** which is defined as

$$G_{\alpha\beta} = R_{\alpha\beta} - \frac{1}{2}g_{\alpha\beta}R \tag{2.44}$$

The Einstein tensor is also symmetric and due to Eq. (2.41) it satisfies

$$\nabla_{\alpha}G^{\alpha\beta} = 0 \tag{2.45}$$

The Einstein field equations,

$$G_{\alpha\beta} = R_{\alpha\beta} - \frac{1}{2} g_{\alpha\beta} R = 8\pi T_{\alpha\beta} \tag{2.46}$$

relate the spacetime curvature represented by $G_{\alpha\beta}$ to the distribution of matter represented by stress-energy tensor $T_{\alpha\beta}$. Eq. (2.45) implies that the stress-energy tensor must have zero divergence, that is

$$\nabla_\alpha T^{\alpha\beta} = 0 \tag{2.47}$$

A vacuum spacetime is defined by $T_{\alpha\beta} = 0$. Taking the trace of Eq. (2.46) we get $R = 0$ so that the vacuum field equation reduces to

$$R_{\alpha\beta} = 0 \tag{2.48}$$

Einstein's equations are a non-linear system of 10 coupled partial differential equations for 10 functions ($g_{\mu\nu}$) of 4 variables (x^μ). Non-linearity comes from the fact that the Ricci tensor involves the inverse of the metric, which is a non-linear operation, and products of the Christoffel symbols. Einstein's equation tells us that the Ricci curvature of spacetime is locally ruled by the density of energy and momentum of matter. In the words of John Wheeler, "Spacetime tells matter how to move; matter tells spacetime how to curve". Another term can be added to Einstein's equations without changing their essential properties, i.e. the so-called *cosmological constant* Λ. The full Einsteins equations with cosmological constant are

$$R_{\mu\nu} - \frac{1}{2} R g_{\mu\nu} + \Lambda g_{\mu\nu} = 8\pi G\, T_{\mu\nu}. \tag{2.49}$$

2.2.13 Black Holes

A black hole is a region of spacetime that cannot communicate with the outside universe. The boundary of this region is 3-dimensional hypersurfaces in spacetime called the surface of the black hole or event horizon. Nothing can escape from inside of black hole, not even light. An important feature of black hole spacetime is the presence of physical singularities. Singularities are characterized as places where geodesics end in a finite amount of affine parameter. Physically these are locations where tides grow without bound. Einstein's equations continue to describe the outside universe and inside horizon, but they break down at the singularity of the black hole. The most general stationary black hole solution to Einstein's field equations is that analytically known Kerr-Newman [33] metric. This metric is uniquely specified by just three parameters: the mass **M**, angular momentum **J** and the charge **Q** of the black holes. The Kerr metric [8] is special case of Kerr-Newman metric with (**Q** =0) which reduces to Schwarzschild metric [5, 6] with both (**Q** =0 and **J** = 0).

The Schwarzschild Solution

The Schwarzschild metric is static, spherically symmetric vacuum spacetime and describes the field outside a spherically symmetric body. This was the first non-trivial solution of Einstein's field equation found by Schwarzschild [5, 6] in 1916. In Schwarzschild coordinates, the invariant spacetime line element is given by

$$ds^2 = -\left(1 - \frac{2M}{r}\right) + \left(1 + \frac{2M}{r}\right)^{-1} dr^2 + r^2 d\theta^2 + r^2 \sin^2\theta d\phi^2. \tag{2.50}$$

The coordinate r is called the *areal radius*, with the property that two-spheres at constant r have proper area $4\pi r^2$. Birkhoff's theorem [34] states that the Schwarzschild metric represents the unique spherically symmetric solution to the vacuum field equations. The Schwarzschild solution holds in vacuum region of any spherical spacetime, including matter. So the space time can describe the vacuum exterior of a static or collapsing star. The mass of this spacetime, as measured by a distant

static observer in the vacuum exterior, is M. When the vacuum extends down to $r_S = 2M$, the exterior spacetime corresponds a vacuum black hole of mass M. The location $r_S = 2M$, is the event horizon of the black hole and sometimes called the *Schwarzschild radius*. The metric (2.50) is manifestly independent of t, so that we can immediately deduce the existence of a Killing vector $\xi^\alpha = (\partial_t)^\alpha$ which is timelike near infinity. The metric is also independent of ϕ, so that there is another Killing vector $\Psi^\alpha = (\partial_\phi)^\alpha$.

In order to explore the physics of the Schwarzschild geometry, it is useful to determine the trajectories of freely-falling particles, i.e. the geodesics of that spacetime. Suppose that there is a geodesic whose path is $x^\alpha(\lambda)$, where λ is a parameter along the curve. The vector tangent to the geodesic is the four velocity $u^\alpha = \frac{dx^\alpha}{d\lambda}$. Then Eq. (2.27) implies that there is a conserved energy and angular momentum along the geodesic

$$\begin{aligned} E &= -\xi^\alpha u_\alpha = \left(1 - \frac{2M}{r}\right)\frac{dt}{d\lambda} \\ L &= \psi^\alpha u_\alpha = r^2 \frac{d\phi}{d\lambda} \end{aligned} \tag{2.51}$$

By spherical symmetry, we need only consider equatorial motion for which $\theta = \pi/2$ and $\frac{d\theta}{d\lambda} = 0$. Substituting the conserved quantities into the line element result in an equation for radial coordinate

$$\frac{1}{2}\left(\frac{dr}{d\lambda}\right)^2 + V_{\text{eff}}(r) = \frac{E^2}{2}, \tag{2.52}$$

where

$$V_{\text{eff}}(r) = \frac{1}{2}\epsilon - \epsilon\frac{M}{r} + \frac{L^2}{2r^2} - \frac{ML^2}{r^3}, \tag{2.53}$$

plays the role of an effective potential. Circular orbits (r = constant) are possible if $\frac{dV_{\text{eff}}}{dr} = 0$. They are stable if $\frac{d^2V_{\text{eff}}}{d\lambda^2} > 0$. The form of the effective potential is illustrated in Fig. 2.1. For

photons ($\epsilon = 0$), Eq. (2.52) is linear, thus it admits a single solution $r = 3M$. At that distance, the gravitational field of the central massive body is strong enough to allow light to orbit around it. However, this orbit is unstable: $\frac{d^2V}{dr^2}(3M) = -L^2/(3M)^4 < 0$.

For massive particles ($\epsilon = -1$), Eq. (2.52) is quadratic, with discriminant $\Delta = L^2(L^2 - 12M^2) = L^2(L^2 - 3r_S^2)$. There are three possibilities:

1. If $L^2 > 3r_S^2$, eq. (2.52) has two solutions

$$r_\pm = \frac{L}{r_S}(L \pm \sqrt{L^2 - 3r_S^2}), \tag{2.54}$$

   corresponding to one stable (r_+) and one unstable (r_-) orbit. For $L \gg r_S$, the stable orbit $r_+ \approx 2L^2/r_S$ corresponds to the Newtonian limit, while $r_- \approx 3M$ is an unstable relativistic orbit.

2. If $L^2 = 3r_S^2$, the two solutions $r_\pm$ merge at $r_{ISCO} = 6M$, known as the *innermost stable circular orbit* (ISCO).

3. If $L^2 < 3r_S^2$, there is no circular orbit: the particle does not have enough angular momentum to keep away from the central massive object, and spirals towards the center $r = 0$. This is a strictly relativistic prediction; Newtonian gravitation does not have such a feature.

The Schwarzschild metric has two singularities. The singularity in the metric at $r_S = 2M$ is a coordinate singularity and can be eliminated by using different coordinates, while the singularity at $r = 0$ is a physical spacetime singularity. In fact the curvature invariant $K = R^{\mu\nu\rho\sigma}R_{\mu\nu\rho\sigma} = 48M^2/r^6$, also know as *Kretschmann scalar*, clearly blows up at the origin, showing that the tidal gravitational field becomes infinite at the center of the black hole.

The coordinate singularity $r_S = 2M$ of Schwarzschild metric can be eliminated by a choice of coordinates [35, 36, 37, 38, 39, 40, 41]. One of these choices is the *Kruskal-Szekeres* coordinate

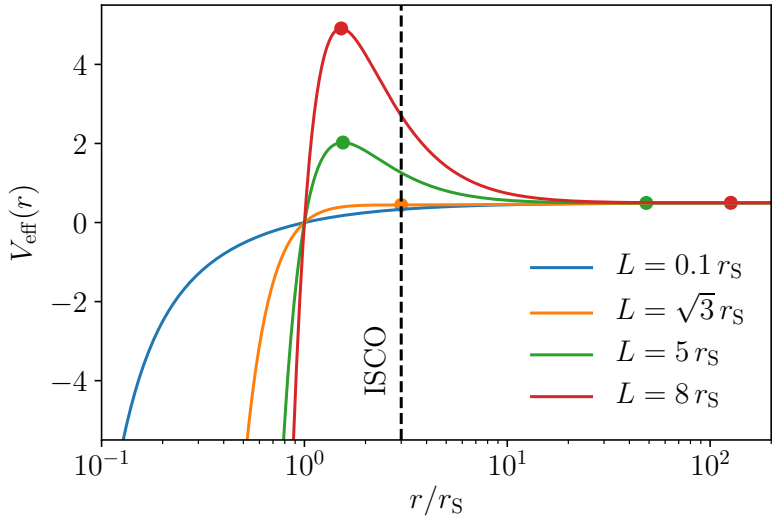

Figure 2.1: Effective potential $V_{\text{eff}}(r)$ for massive particles ($\epsilon = -1$) and different values of L. The positions of circular orbits, when they exist, are indicated with disks. For $L > \sqrt{3} r_S$, there exist one stable and one unstable orbit. They merge into the ISCO for $L = \sqrt{3} r_S$, where $r_S = 2M$ is the Schwarzschild radius.

system in which the detailed structure of the Schwarzschild spacetime can be explored. In these coordinates, the two angular coordinates remain unchanged, but new time and radial coordinates are given by

$$T = \sqrt{\left|\frac{r}{r_S} - 1\right|} \exp\left(\frac{r}{2r_S}\right) \sinh\left(\frac{t}{2r_S}\right), \tag{2.55}$$

$$R = \sqrt{\left|\frac{r}{r_S} - 1\right|} \exp\left(\frac{r}{2r_S}\right) \cosh\left(\frac{t}{2r_S}\right); \tag{2.56}$$

these imply, in particular,

$$\left(\frac{r}{r_S} - 1\right) \exp\left(\frac{r}{r_S}\right) = R^2 - T^2, \tag{2.57}$$

$$\tanh\left(\frac{t}{2r_S}\right) = \frac{T}{R}\,. \tag{2.58}$$

The Schwarzschild metric in Kruskal-Szekeres coordinates reads

$$ds^2 = \frac{4r_S^3}{r}\,\exp\big[-r/r_S\big]\big(-dT^2+dR^2\big)+r^2d\theta^2+r^2\sin^2\theta d\phi^2, \tag{2.59}$$

where it is understood that $r = r(T, R)$ is implicitly defined by eqs. (2.55) and (2.56). This metric is indeed has no singularity at $r = r_S$.

An important feature of Kruskal-Szekeres coordinates is that they trivialise radial null geodesics. Indeed, radial null curves [$ds^2 = 0$ with $d\theta = d\phi = 0$] are simply given by

$$dT = \pm dR\ . \tag{2.60}$$

Thus radial light rays are simply straight lines in the (T, R) plane. The full structure of the Schwarzschild spacetime can then be represented in the *Kruskal diagram* Fig. 2.2, which consists of the plane (T, R). In Kruskal diagram 2.2, region I is the part which is well described by the Schwarzschild coordinates (t, r); it represents the *exterior of the black hole*, $r > r_S$. In this region, a particle can be accelerated in order to maintain $r =$ constant, because the associated hyperbolas are time-like curves. It is not fundamentally different from the exterior of any massive body. A particle following the time-like curve $\mathscr{L}$ upwards moves towards the centre $r = 0$. When the particle crosses the line $T = R$ ($r = r_S$), it enters region II, which is the *interior of the black hole*. From that point, we see that its causal future can only lead to the singularity at $r = 0$. The particle cannot get out of region II, nor send any message to the exterior because that imply faster than light travel. This is why this region is a black hole: nothing can get out of it, not even light. No information can ever propagate from the interior (II) to the exterior (I). The surface $r = r_S$ is called the *event horizon* of the black hole. Note that, in terms of the time coordinate t, the particle never actually reaches the horizon which is not the case from the point of view of the particle itself.
The other two regions of the Schwarzschild space-time (III and IV) could not have been revealed without the Kruskal-Szekeres coordinate system. Region IV is the *interior of a white hole*: contrary

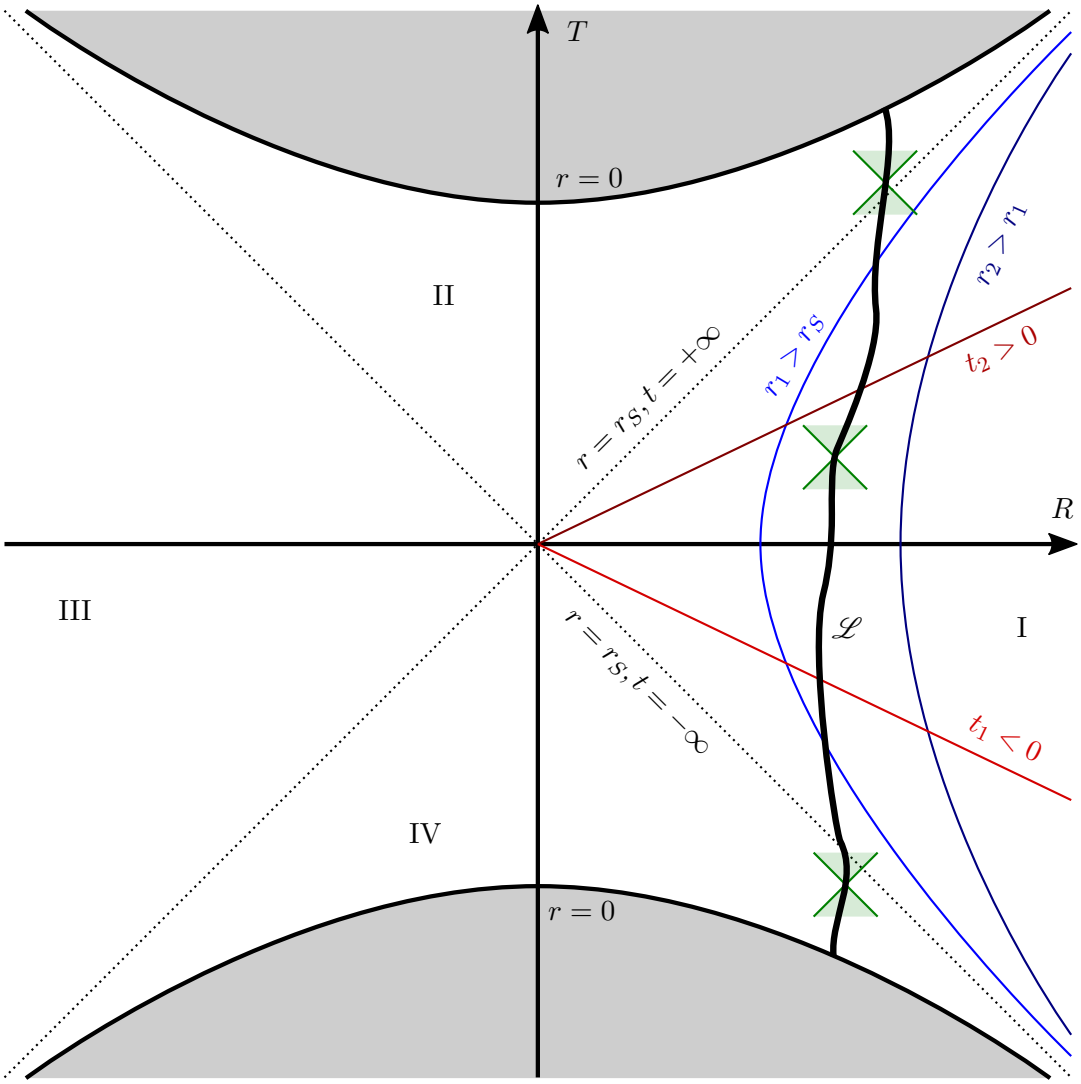

Figure 2.2: Kruskal diagram of the Schwarzschild spacetime. The axes T, R indicate Kruskal-Szekeres coordinates. The two gray regions are excluded, their boundary with bold black contour indicating the central singularity $r = 0$. Dotted lines represent the event horizon of the black hole, and split the diagram into four regions. Region I corresponds to the original $r > r_S$, "our universe". Region II is the black interior where $r < r_S$. Region III and IV represent the "other universe" with region III has parallel exterior with $r > r_S$ and is asymptotically flat, and region IV describe a "white hole" with $r < r_S$. The thick black curve is the world-line of a particle emitted and reabsorbed by the black hole, along which three local light-cones are indicated in green. Blue lines represent $r =$ constant world-lines, while red lines represent $t =$ constant hyper-surfaces.

to the interior of the black hole, the causal future of any particle in that region lies at the exterior ($r > r_S$, region I). Taken as a whole, $\mathscr{L}$ depicts the entire world-line of a particle emitted from the interior of the white hole, which is then re-absorbed by the black hole. Region III is even more intriguing. It represents another exterior for the white/black hole (with $R < 0$) which is causally disconnected from region I. It is sometimes coined as a *parallel Universe*, which people in region I cannot interact with.

The Kerr Solution

The Kerr solution, which describes stationary rotating black holes, ranks among the most important solutions of Einstein's field equations. Originally, it was discovered by Roy Kerr in 1963 [8]. It represents a black hole with mass M and angular momentum $J = aM$, where a is the *spin parameter* and is the angular momentum per unit mass. It is a generalization of Schwarzschild spacetime and it was further generalized to electrically charged black holes by E.T. Newman and coworkers in 1965 [33]. A Kerr metric with mass M and spin a in spherical Boyer-Lindquist coordinates [42] has the invariant spacetime element

$$\begin{aligned} ds^2 &= -\left(1 - \frac{2Mr}{\rho^2}\right)dt^2 - \frac{4aMr\sin^2\theta}{\rho^2}dtd\phi + \frac{\rho^2}{\Delta}dr^2 + \rho^2 d\theta^2 + \\ &\quad \left(r^2 + a^2 + \frac{2a^2Mr\sin^2\theta}{\rho^2}\right)\sin^2\theta d\phi^2 \end{aligned} \tag{2.61}$$

with the definitions,

$$\rho^2 = r^2 + a^2\cos^2\theta, \tag{2.62}$$

$$\Delta = r^2 + a^2 - 2Mr, \tag{2.63}$$

and where the black hole is rotating in the $+\phi$ direction. The Kerr metric with $a = 0$ reduces to Schwarzschild metric (2.50). The spin is restricted to $0 \leq a/M \leq 1$. The Kerr spacetime is stationary and axisymmetric, and hence admits two Killing vector fields: one which is timelike $\xi^\alpha = (\partial_t)^\alpha$, and one which is spacelike with closed circular orbits $\psi^\alpha = (\partial_\phi)^\alpha$. Thus Geodesics with

four velocity u^α have a conserved energy and angular momentum

$$E = -\xi^\alpha u_\alpha = \left(1 - \frac{2Mr}{\rho^2}\right)\frac{dt}{d\lambda} + \frac{2Mar\sin^2\theta}{\rho^2}\frac{d\phi}{d\lambda} \tag{2.64}$$
$$L = \psi^\alpha u_\alpha = -\frac{2Mar\sin^2\theta}{\rho^2}\frac{dt}{d\lambda} + \frac{(r^2+a^2)^2 - \Delta a^2\sin^2\theta}{\rho^2}\sin^2\theta\frac{d\phi}{d\lambda}$$

The Kerr metric also admits a Killing tensor [43]

$$\kappa_{\alpha\beta} = 2\rho^2 l_{(\alpha}n_{\beta)} + r^2 g_{\alpha\beta}, \tag{2.65}$$

where the l^α and n^α are given by

$$l^\alpha = \frac{r^2+a^2}{\Delta}(\partial_t)^\alpha + \frac{a}{\Delta}(\partial_\phi)^\alpha + (\partial_r)^\alpha, \tag{2.66}$$
$$n^\alpha = \frac{r^2+a^2}{2\rho^2}(\partial_t)^\alpha + \frac{a}{2\rho^2}(\partial_\phi)^\alpha - \frac{\Delta}{2\rho^2}(\partial_r)^\alpha.$$

The Killing tensor implies the symmetry of spacetime which is related to constant of motion called *Carter constant* and is given by

$$C = \kappa_{\alpha\beta}u^\alpha u^\beta \tag{2.67}$$

which allows for explicit integration of geodesic equation in generic, non-equatorial trajectories [44]. The geodesic motion in equatorial plane $\theta = \pi/2$ is more complicated than Schwarzschild spacetime due to rotation and was studied in great details in [45, 46]. Using the conserved energy and angular momentum, the geodesic equation for Kerr metric in equatorial plane is given by

$$\frac{1}{2}\left(\frac{dr}{d\lambda}\right)^2 + V(E, L, r) = 0 \tag{2.68}$$

where

$$V(E,L,r) = -\epsilon\frac{M}{r} + \frac{L^2}{2r^2} + \frac{1}{2}(\epsilon - E^2)\left(1 + \frac{a^2}{r^2}\right) - \frac{M}{r^3}(L - aE)^2. \tag{2.69}$$

Photon orbits ($\epsilon = 0$) in the equatorial plane gives insights in which Kerr spacetime differ from non-rotating spacetime. The effective potential can be expressed as

$$W_{\text{eff}}(E,L,r) = \frac{E^2}{2} - \frac{L^2}{2r^2}\left[1 - \frac{a^2E^2}{L^2} - \frac{2M}{r}\left(1 - \sigma\frac{aE}{L}\right)^2\right], \tag{2.70}$$

where $\sigma = \text{sign}(L)$ indicates if the photon is orbiting in the same or opposite direction to the black hole's spin. The radius of a circular photon orbit is given by

$$r_{\text{photon}} = 2M\left\{1 + \cos\left[\frac{2}{3}\arccos\left(\pm\frac{a}{M}\right)\right]\right\}, \tag{2.71}$$

where this orbit is unstable. This reduces to Schwarzschild $r_{\text{photon}} = 3M$ as $a \to 0$, whereas for $a \to M$ the $r_{\text{photon}} = M$ for $L > 0$ and $r_{\text{photon}} = 4M$ for $L < 0$.
For massive particles ($\epsilon = -1$) to follow circular geodesics, $\frac{dr}{d\lambda} = 0$, the conserved energy and angular momentum must obey

$$\begin{aligned} E &= \frac{r^2 - 2Mr \pm a\sqrt{Mr}}{r(r^2 - 3M \pm 2a\sqrt{Mr})^{1/2}}, \\ L &= \pm\frac{\sqrt{Mr}(r^2 \mp 2a\sqrt{Mr} + a^2}{r(r^2 - 3M \pm 2a\sqrt{Mr})^{1/2}}, \end{aligned} \tag{2.72}$$

where the upper sign refers to the co-rotating test particles and the lower sign for counter-rotating ones.

The *inner most stable circular orbit* r_{ISCO}, is given by

$$r_{\text{ms}} = M\left\{3 + Z_2 \mp [(3 - Z_1)(3 + Z_1 + 2Z_2)]^{1/2}\right\}, \tag{2.73}$$

where

$$Z_1 = 1 + (1 - a^2/M^2)^{1/3}[(1 + a/M)^{1/3} + (1 - a/M)^{1/3}], \tag{2.74}$$
$$Z_2 = (3a^2/M^2 + Z_1^2)^{1/2}.$$

The r_{ISCO} for the case of Schwarzschild is obtained by $a = 0$ which yields $r_{\rm ISCO} = 6M$, and for $a \to M$ we have $r_{\rm ISCO} = M$ for co-rotating case and $r_{\rm ISCO} = 9M$ for counter-rotating case.

Of great interest is the binding energy, the difference between energy of particle at rest at infinity and energy of same particle moving in an orbit as measured from infinity, of a marginally stable orbit. This is determined by

$$\frac{a}{M} = \mp \frac{4\sqrt{2}(1 - E^2)^{1/2} - 2E}{3\sqrt{3}(1 - E^2)}. \tag{2.75}$$

From this one finds that E decrease from $\sqrt{8/9}$ for $a = 0$ to $1/\sqrt{3}$ in the extreme limit for co-rotating orbits and $\sqrt{25/27}$ in the extreme limit for counter-rotating orbits. For the co-rotating case, if the particle can inspiral down in an accretion disk from far away to $r_{\rm ISCO}$, the fraction 1 - $\sqrt{3}$ of the rest energy is set free. Thus a rotating black hole allows a gravitational energy conversion upto $\simeq 42.3\%$ [47]. This enormous efficiency is the main reason to suggest the existence of supermassive black holes at the centers of galaxies [48, 49].

The Kerr spacetime has a true singularity at $r = 0$ and is separated into three classes based on the value of dimensionless spin parameter $\chi = a/M$. The case with $\chi > 1$ contains a naked singularity, which is assumed to be prohibited[50, 51, 52]. If $\chi = 1$, then Kerr is said to have extreme spin. When $\chi < 1$, the singularity is hidden behind two horizons at $r = r_{\pm \rm H} = M \pm \sqrt{M^2 + a^2}$. The singularity at the horizons are coordinate singularities and can be removed by an appropriate choice of coordinates [42, 44]. In the region $r_{+\rm H} < r < M + \sqrt{M^2 + a^2 \cos^2\theta}$, the norm of killing field

$\xi^\alpha = (\partial_t)^\alpha$ becomes positive. This part of spacetime is called *ergosphere* and has the property that the time translation Killing field ξ^α becomes spacelike. This implies that an object would require super-luminal velocities in order to not corotate with the black hole. This effect, known as *frame dragging*, extends beyond ergosphere, weakening with distance. This is in complete contrast with the predictions of Newtonian gravity. Newtonian theory implies that a particle starting from the rest in the equatorial plane of a rotating axisymmetric mass falls radially inward along a straight line towards the center of mass. General relativity, on the other hand, implies the deviations from radial infall in the direction of rotation of the mass due to frame dragging effect.

2.2.14 Gravitational Waves on Linearized Minkowski

The existence and properties of gravitational waves can be derived using weak field approximation which is described below. This section closely follows the discussion in [16].
We assume that spacetime is almost flat such that it can be described with Minkowski spacetime $\eta_{\mu\nu}$ with small perturbations $|h_{\mu\nu}| \ll 1$ as

$$g_{\mu\nu} = \eta_{\mu\nu} + h_{\mu\nu}, \tag{2.76}$$

where $h_{\mu\nu}$ represents a linear perturbation and is a symmetric tensor whose components are *small*. Choosing a small *gauge transformation* of type

$$x^{'\mu} = x^\mu + \xi^\mu, \tag{2.77}$$

where ξ^μ are functions of coordinates x^μ. Further demanding that the coordinate transformations are small in the sense $|\partial_\alpha \xi^\alpha| \ll 1$, we find from (2.76) that $h_{\mu\nu}$ transform to linear order in ξ^μ as

$$h_{\mu\nu} \to h_{\mu\nu} - \partial_\mu \xi_\nu - \partial_\nu \xi_\mu. \tag{2.78}$$

To expand Einstein equations (2.46) to linear order in $h_{\mu\nu}$ we note that

$$R_{\mu\nu\rho\sigma} = \frac{1}{2}(\partial_\nu\partial_\rho h_{\mu\sigma} + \partial_\mu\partial_\sigma h_{\nu\rho} - \partial_\mu\partial_\rho h_{\nu\sigma} - \partial_\nu\partial_\sigma h_{\mu\rho}), \tag{2.79}$$

$$R_{\mu\nu} = R^{\lambda}{}_{\mu\lambda\nu} = \frac{1}{2}(\partial_\mu\partial^\lambda h_{\lambda\nu} + \partial_\nu\partial^\lambda h_{\lambda\mu} - \partial^\lambda\partial_\lambda h_{\mu\nu} - \partial_\mu\partial_\nu h), \tag{2.80}$$

$$R = R^{\lambda}{}_{\lambda} = \partial^\nu\partial^\lambda h_{\nu\lambda} - \partial^\lambda\partial_\lambda h, \tag{2.81}$$

where $h = h^{\lambda}{}_{\lambda}$. These expressions can be simplified further by using the *trace reverse* perturbation

$$\bar{h}_{\mu\nu} = h_{\mu\nu} - \frac{1}{2}\eta_{\mu\nu}h \tag{2.82}$$

and imposing $\partial^\lambda\bar{h}_{\lambda\mu} = 0$. This condition is commonly called the *Lorentz gauge*, can always be satisfied by an appropriate coordinate transformation (2.78). With these simplifications, we find that the Einstein's equations, to first order, are given by

$$\Box\bar{h}_{\mu\nu} = \partial^\lambda\partial_\lambda\bar{h}_{\mu\nu} = -16\pi T_{\mu\nu}, \tag{2.83}$$

which is a simple wave equation for $\bar{h}_{\mu\nu}$ on a flat background. For vacuum ($T_{mu\nu} = 0$), the general solution to that wave equation reads

$$\bar{h}_{\mu\nu} = A_{\mu\nu}\exp^{ik_\lambda x^\lambda} \quad \text{with} \quad k^\lambda k_\lambda = 0. \tag{2.84}$$

To satisfy our chosen gauge, we also need $k^\lambda A_{\lambda\mu} = 0$, so the general solution are plane waves that travel at the speed of light.

The coordinate transformation that led to this result is not unique. Any transformation which

satisfy $\Box\xi^\mu = 0$ maintains the Lorentz gauge. This remaining freedom can further be utilized to identify the independent component of $\bar{h}_{\mu\nu}$. In vacuum we can further impose $\bar{h} = 0$, as well as $h_{0i} = h_{00} = 0$ with $(i = 1, 2, 3)$. Setting $\bar{h} = 0$ makes the distinction between $h_{\mu\nu}$ and its trace reverse superfluous. Note that these conditions do not violate the Lorentz gauge. We can further choose the direction of propagation of wave to be along z-axis which implies $h_{\mu 3} = 0$. In the end, there are only two independent components of $h_{\mu\nu}$ that are typically denoted by h_+ and $h_\times$,

$$h_{\mu\nu} = \begin{pmatrix} 0 & 0 & 0 & 0 \\ 0 & h_+ & h_\times & 0 \\ 0 & h_\times & -h_+ & 0 \\ 0 & 0 & 0 & 0 \end{pmatrix}. \tag{2.85}$$

h_+ and $h_\times$ correspond to the two possible polarization states of the gravitational wave.

The set of all gauge conditions used to obtain (2.85) is usually referred to as *transverse traceless* (TT) gauge.

The effect of a gravitational wave on test masses can be seen by the deviation of their geodesics. To show this consider two freely falling particles that are instantaneously with respect to a local inertial frame. Let the deviation vector to the other particle be denoted by ζ^μ. The acceleration of ζ^μ is given by

$$\frac{d^2\zeta^\mu}{dt^2} = R^\mu{}_{00\nu}\zeta^\nu. \tag{2.86}$$

With (2.79) we can express the Riemann tensor in terms of $h_{\mu\nu}$,

$$\frac{d^2\zeta^\mu}{dt^2} = \frac{1}{2}\frac{d^2 h_{\mu\nu}}{dt^2}\zeta^\nu. \tag{2.87}$$

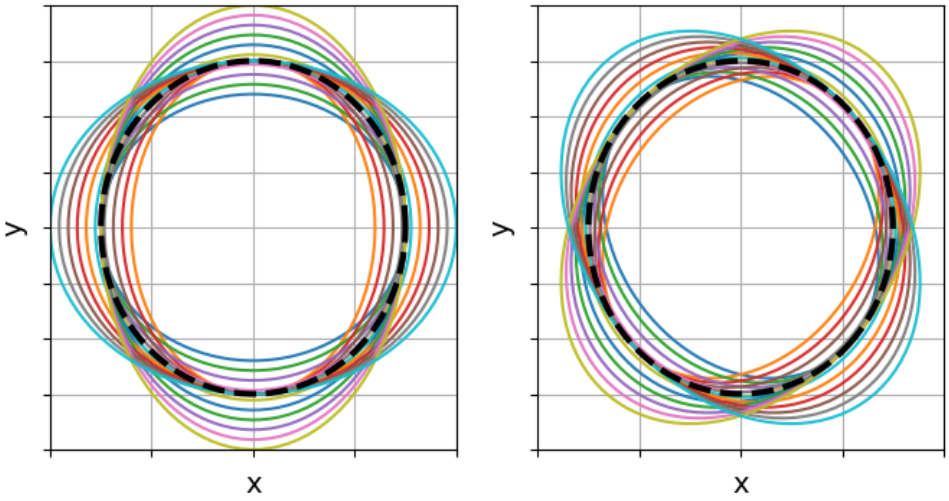

Figure 2.3: Effect of gravitational wave travelling in the z-direction on a ring of test particles. The left panel shows a pure plus polarization, the right panel a cross polarization. The ring initially at rest (bold dashed), is warped periodically (shown with different colors) with the frequency of the gravitational wave.

Solving Eq. (2.87) up to leading order we can get

$$\zeta^{\mu}(t) = \left(\delta^{\mu}_{\nu} + \frac{1}{2}h_{\mu\nu}(t)\right)\zeta^{\nu}(0), \tag{2.88}$$

from which it is easy to deduce a clear picture of the effect of the plus and cross polarization onto freely falling particles.

Imagine a ring of test particles in the $x-y$ plane. Assuming we are in TT gauge and a gravitational wave travels perpendicular to this ring in the z-direction, and we further assume $h_{\times} = 0$, the remaining polarization h_{+} will be an oscillating function that periodically stretches and squeezes the distance between the particles in x-direction and opposite in the y-direction. The cross polarization has a similar effect, but rotated to the plus polarization by 45°. Figure 2.3 shows this periodic changes of the distance between the test particles, which forms the basis of measuring gravitational waves with LIGO detectors.

Sources of Gravitational Waves (quadrupole formula)

To understand the generation of these gravitational waves, we investigate the energy radiated in the form of gravitational waves, by time dependent sources, using the framework of linearized theory. This problem was first studied by Einstein [53, 11] where he worked out his famous quadrupole formula. We will review the basic principles here, following the explanations in [16, 21, 54, 14]. The general solution of Eq. (2.83) can be expressed in terms of retarded integrals

$$h_{\mu\nu}(t,x^i) = 4\int \frac{T_{\mu\nu}(t-|x^i-x'^i|,x'^i)}{|x^i-x'^i|}d^3x' \tag{2.89}$$

We have split the 4-dimensional vectors in their time and spatial part, $x^\mu = (t,x^i)$, and the integral is performed over the past light cone of the event (t,x^i). Assuming that observer is far from the sources and the motion is slow ($v \ll c$), we can replace the denominator of (2.89) by constant distance R as $|x^i - x'^i| = R$, then we have

$$h^{\mu\nu}(t,x^i) = \frac{4}{R}\int T^{\mu\nu}(t-R,x'^i)d^3x' \tag{2.90}$$

The energy momentum tensor satisfies the conservation law $\partial_\mu T^{\mu\nu} = 0$ (in linearized approximation) which after integration by parts can read as the following relation

$$\int T^{ij}d^3x = \frac{1}{2}\frac{\partial^2}{\partial t^2}\int T^{00}x^i x^j d^3x, \tag{2.91}$$

where the surface integral vanished because we assumed a localized source. Using the (2.90) and (2.91) we can get the final result given by

$$h^{jk}(t,x^i) = \frac{2}{R}\frac{\partial^2}{\partial t^2}\int T^{00}(t-R,x'^i)x'^j x'^k d^3x'. \tag{2.92}$$

We have assumed the Lorentz gauge so $h_{\mu\nu}$ can be completely determined by spatial components. The solution (2.92) is instructive in many ways. For near Newtonian sources, the energy density is dominated by the matter density ρ so $T^{00} \simeq \rho$ which implies that gravitational waves are triggered by the second time derivative of mass density distribution. In that case we can write (2.92) as

$$h^{jk}(t, x^i) \simeq \frac{2}{R}\frac{\partial^2}{\partial t^2}\int \rho^{00}(t - R, x'^i)x'^j x'^k d^3x'. \tag{2.93}$$

From (2.92) we can see that the radiation falls off inversely with the distance to the source which means that the gravitational waves triggered by distant astrophysical sources are indeed very weak when they reach the earth. Further (2.93) can be written in terms of the trace free *quadrupole tensor*

$$Q_{ij}(t) = \int (3x^i x^j - r^2\delta_{ij})\rho(t, x^i)d^3x, \tag{2.94}$$

as

$$h^{jk}(t, x^i) \simeq \frac{2}{3R}\left(\frac{\partial^2}{\partial t^2}Q_{jk}(t - R) + \delta_{jk}\frac{\partial^2}{\partial t^2}\int R'^2\rho(t - R, x'^i)d^3x'\right). \tag{2.95}$$

At large distance from the source the wave (2.95) can be considered locally to be a plane wave. The energy flux $\mathcal{L}_{\rm GW}$ to the leading order as given by

$$\mathcal{L}_{\rm GW} = \frac{1}{5c^5}\left\langle \frac{d^3Q_{jk}}{dt^3}\frac{d^3Q^{jk}}{dt^3}\right\rangle, \tag{2.96}$$

where angle brackets denote the average over several characteristic periods of source and we are not using $c = 1$ here to show c^5 corresponds to post-Newtonian order (2.5PN) expansions of Einstein's field equations. This mean the radiation is quadrupolar at the leading order which is in contrast to electrodynamics where the leading order multi-pole for radiation is dipolar one. The total energy radiated by the source due to gravitational wave emission is denote by $E_{\rm GW}$ and is controlled by

the *flux balance* equation

$$\frac{dE_{\rm GW}}{dt} = -\mathcal{L}_{\rm GW}, \tag{2.97}$$

which shows the radiation reaction effect onto the sources. We can express the total $E_{\rm GW}$ radiated by the source in terms of the Fourier transform

$$\hat{Q}_{ij}(\omega) = \frac{1}{2\pi}\int Q_{ij}(t)\exp^{i\omega t}\,dt \tag{2.98}$$

of quadrupole tensor:

$$E_{\rm GW} = \frac{1}{5c^5}\int_{-\infty}^{+\infty} \dddot{Q}_{ij}\dddot{Q}^{ij}dt = \frac{4\pi}{5c^5}\int_0^{\infty} \hat{Q}^*_{ij}(\omega)Q^{ij}(\omega)d\omega, \tag{2.99}$$

where $\dddot{Q}_{ij} = \frac{d^3Q_{ij}i}{dt^3}$. The spectral distribution of the quadrupole radiation is thus

$$\frac{dE_{\rm GW}}{d\omega} = \frac{4\pi}{5c^5}\hat{Q}^*_{ij}(\omega)Q^{ij}(\omega). \tag{2.100}$$

Another important result is that in TT gauge we can get

$$h^{TT}_{ij}(t,x^i) = \frac{2}{3R}\ddot{Q}^{TT}(t-|x^i|). \tag{2.101}$$

In this thesis we focus on dynamics of binary black holes and gravitational waves emitted from their motion. We can use them as an example to illustrate Eq. (2.92). In the context here, we can treat approximately binary black holes orbiting around each other. For circular orbits we find in

the Keplerian case

$$v^2 = \frac{M}{r}, \qquad \omega_{\rm orb} = \sqrt{\frac{M}{r^3}} = \frac{v}{r}, \tag{2.102}$$

with v and r denoting the relative velocity and distance between the two bodies, respectively, $M = m_1 + m_2$ being the total mass and $\omega_{\rm orb}$ is the orbital frequency. We put the two black holes in the $x - y$ plane, with their locations given in the center-of-mass frame by

$$x_1^i = \frac{M\eta r}{m_1}\big(\cos(\omega_{\rm orb}t), \sin(\omega_{\rm orb}t), 0\big), \quad x_2^i = -\frac{m_1}{m_2}x_1^i, \tag{2.103}$$

where $\eta = m_1 m_2/M$ is the symmetric mass ratio. The mass distribution is now constructed from corresponding δ-distributions, and in this particular form, it is easy to solve the integral (2.92) explicitly which results in

$$h_{jk} = \frac{4M\eta r^2\omega_{\rm orb}^2}{R}\begin{pmatrix} -\cos[2\omega_{\rm orb}(t-R)] & -\sin[2\omega_{\rm orb}(t-R)] & 0 \\ -\sin[2\omega_{\rm orb}(t-R)] & \cos[2\omega_{\rm orb}(t-R)] & 0 \\ 0 & 0 & 0 \end{pmatrix}, \tag{2.104}$$

and the *amplitude* can also be written through (2.102) as $M\eta v^2/R$. This is very useful result showing that orbiting compact objects emit gravitational waves at quadrupole order with frequency that is twice of their orbital frequency. To obtain the entire evolution of the binary, we have to include an estimate of the energy and also to study the radiation reaction effect onto the binary's motion. This will be the discussion in the section on Post-Newtonian approximations.

Ambiguities in measuring Gravitational Waves

Einstein predicted the existence of gravitational waves based upon a linearization of his field equations of general relativity, but remained skeptical as to whether or not they were physical. The reason for this skepticism is easy to understand with the following example. Suppose we have the

metric

$$\begin{aligned} g_{\mu\nu}dx^\mu dx^\nu &= (\eta_{\mu\nu}+h_{\mu\nu})dx^\mu dx^\nu = -dt^2+dx^2+dy^2+dz^2 \\ &\quad -\cos(t-x)(2+\cos(t-x))dt^2 \\ &\quad +2\cos(t-x)(1+\cos(t-x))dtdx \\ &\quad -\cos^2(t-x)dx^2, \end{aligned} \tag{2.105}$$

which in some coordinates (t, x, y, z), with t being timelike, has the metric functions depending on $u = t - x$. Looking at a metric in these coordinates, the terms after the Minkowski spacetime are oscillatory, and implies that they are ripples of the perturbation that move at the speed of light along the x-axis. Furthermore if we look at the perturbed metric $h_{\mu\nu}$ coefficient it is easy to verify that they not only satisfy wave equation $\Box h_{\mu\nu} = 0$ as well as Ricci curvature $R = 0$ for $g_{\mu\nu}$. This mean $R_{\mu\nu} = 0$ and metric is solution of fully non-linear Einstein equations in vacuum. But Is this really a real plane gravitational wave? This can be checked via a coordinate transformation. Choosing $T = t + \sin(t + x)$ as a time coordinate transformation, we can get new metric which is Minkowski $\eta_{\mu\nu} = -dT^2 + dx^2 + dy^2 + dz^2$ and have no perturbed parts. There are no gravitational waves in these coordinates. So we can conclude that the metric $g_{\mu\nu}$ in (2.105) is just the flat Minkowski metric, written in nonstandard coordinates.

One must be careful with such gauge waves. They are only the artifacts of choice of the coordinates. Attaching the name of gravitational wave to a spacetime that just satisfies an intuitive condition in some coordinate system is a wrong approach. As we can always introduce a sinusoidal behavior of the metric coefficients and their movement with speed of light by an appropriate change of coordinates as in (2.105). This bothered Einstein in 1937 [55] when he become skeptic after finding such results. We need a mathematically precise definition of even a plane wave solution to describe real gravitational waves. The existence and precise mathematical definition of gravitational waves was worked out by mathematicians and physicists as can be found [56, 57, 58, 59, 60, 61] and gravitational waves were proved to be real in 1960s. These studies define a proper mathematical

definition of a plane wave in full non-linear theory and showed that plane wave solution of full Einstein's field equations do exists and that these gravitational waves carry energy with them. In numerical relativity there are ambiguity is choosing the gauges to solve Einsteins equations numerically and one must also be careful to compute gravitational waves which are independent of coordinate artifacts and describe the real spacetime perturbations. This idea will be more explained in the numerical relativity section.

Gravitational Wave Detector

A gravitational waves changes the proper distance between objects, its effect in principle be measurable by a designed experiment. There have been several attempts to do so. This was pioneered by Joseph Weber's with his resonant bars which he claimed to have detected gravitational waves [62, 63, 64] but was not verified. The reason was the sensitivity of these bars. The gravitational wave signals are too weak with the possible expected gravitational waves from astrophysical sources have amplitudes of $h < 10^{-21}$. So very sensitive advanced technologies are required to detect gravitational waves. One of the promising type of detector with these sensitivity, which have detected gravitational waves recently [65], is a network of large scale laser interferometer first proposed in [66]. The network include two 4km-size detectors called the Laser Interferometer Gravitational wave Observatory (LIGO) [67, 68, 69] which are upgraded to advanced LIGO [70]. The other similar detector in this network is called VIRGO with 3 km arm length [71, 72]. The network also include the GEO600 [73, 74], and TAMA [75, 76] detectors. There are further developments for these detectors [77, 78, 79] as well as upcoming detectors including KAGRA [80] in Japan, which is Large scale Cryogenic gravitational wave detector and LIGO India [81]. In the future, next generation detectors will also join based on similar principles, including the planned Einstein telescope [82] and cosmic explorer [83].

Laser Interferometry is based on Michelson interferometer. Laser light is used to measure the difference between the lengths of two perpendicular arms. Besides many noise sources, such

differences are introduced by the strain of a gravitational wave passing through the instrument. A Michelson interferometer operating between freely suspended test masses or mirrors is ideally suited to measure such differences. A passing gravitational wave will stretch and squeeze the proper distance between the end test masses, and the proper length of the arm, say in x-direction while a gravitational wave is travelling in the z-direction than in TT gauge we can find the length of arm will be

$$L + \Delta L = \int_0^L \sqrt{g_{xx}}dx = \int_0^L \sqrt{1+h_+}dx \approx L\left(1 + \frac{h_+}{2}\right). \tag{2.106}$$

This approximation is only valid in the long wavelength regime, where the wavelength of the gravitational wave λ is larger than the arm length, or $\lambda \gg L$. This condition is always satisfied as LIGO is sensitive to around 100-2000Hz which corresponds to wavelength of gravitational waves which are larger than 3000km. It is important to know that a rigorous derivation of the detector response does not just assume that the light beams measure proper length of arms, their paths and frequencies are affected by the distortions of spacetime themselves. The amplitude of gravitational waves is characterized by two polarization h_+ and $h_\times$, that are transverse to the direction of propagation $\mathbf{n} = n^i$, pointing from the gravitational wave source toward detectors like LIGO. The detector response $h_{\rm resp} = \hat{x}^i\hat{x}^j h_{ij}$, where $\hat{x}^i$ direction of beams, is sensitive to a certain linear combination of these two polarizations which can be expressed in terms of angles (θ, ϕ, ψ) that define the source location with respect to detector frame [84] as

$$\begin{aligned} h_{\rm resp}(t) &= \mathcal{F}_+(\theta,\phi,\psi)\, h_+(t) + \mathcal{F}_\times(\theta,\phi,\psi)\, h_\times(t) \\ \mathcal{F}_+(\theta,\phi,\psi) &= \frac{1}{2}\big(1+\cos^2\theta\big)\cos2\phi\cos2\psi - \cos\theta\sin2\phi\sin2\psi \\ \mathcal{F}_\times(\theta,\phi,\psi) &= \frac{1}{2}\big(1+\cos^2\theta\big)\cos2\phi\sin2\psi - \cos\theta\sin2\phi\cos2\psi. \end{aligned} \tag{2.107}$$

The angles (θ, ϕ) describes the sky location of the source withe θ is the polar angle relative to the

$z-$axis and ϕ is the azimuthal angle from the $x-$axis along the $x-y$ plane. The angle ψ is called the polarization angles as it specifies the plus and cross polarization states. The polarizations are defined as the projection of the waveform along two polarization vectors in plane orthogonal to $\mathbf{n}$. For a compact binary on circular orbits found in (2.104) these polarizations are $h_+ = h_0 \cos\varphi(t)$ and $h_\times = h_0 \sin\varphi(t)$ with $h_0 = \frac{4M\eta r^2\omega_{\rm orb}^2}{R}$, which can be generalized to the case where the orbital plane is inclined to the plane perpendicular to the line of sight. If ι is the inclination angle then

$$h_+ = \frac{h_0}{2}\left(1+\cos^2\iota\right)\cos\varphi(t), \qquad h_\times = h_0\cos\iota\sin\varphi(t). \tag{2.108}$$

The detector response (2.107) then can be reduced to the form

$$h_{\rm resp} = A(\theta,\phi,\psi,\iota)\, h_0 \cos[\varphi(t) + \varphi_0(\theta,\phi,\psi,\iota)], \tag{2.109}$$

where the time dependent geometrical quantities A and φ_0 can be easily deduce from (2.107) and (2.108) as described in detail in [84].

The success of an interferometer ultimately depends on how well noise sources are under control. This is one of the prime technological challenge in this field. Gravitational waves are very weak and many physical effects can cause small vibrations in detectors which could be mistaken as a gravitational wave signal. Noise sources include *seismic noise* caused by natural environment and ground vibrations, *thermal noise* due to vibrations of test masses and their suspensions, *shot noise* due to quantum nature of light, *radiation pressure noise* and *gravity gradient noise* to name a few. External mechanical vibrations must be screened out. A great details of noise sources and other issues is discussed in great details in [85, 86, 84]. All these sources as well as many others contributed to define the sensitivity of the interferometer. The sensitivity of detector can be understood using noise curves $S_n(f)$ as a function of frequency as shown in Fig. 2.4. There is a simple model to the

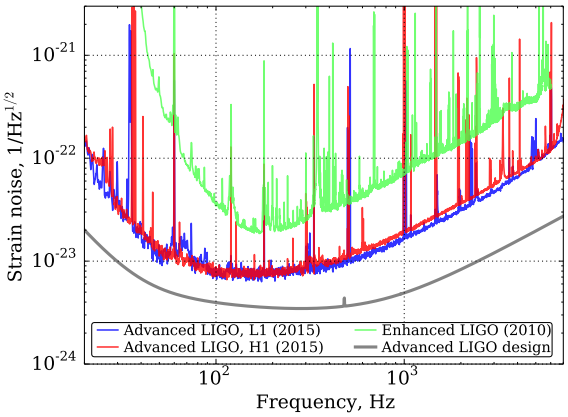

Figure 2.4: Strain Sensitivity: Taken from [1]. The strain sensitivity for the LIGO Livingston detector (L1) and the LIGO Hanford detector (H1) during O1. Also shown is the noise level for the Advanced LIGO design (gray curve) and the sensitivity during the final data collection run (S6) of the initial detectors.

LIGO noise curve given in [84] that reads

$$S_n(f) = 10^{-49}\left(\hat{f}^{-4.14} - \frac{t}{\hat{f}^2} + 111\frac{1-\hat{f}^2+\hat{f}^4/2}{1+\hat{f}^2/2}\right), \tag{2.110}$$

where $\hat{f} = f/215$ Hz. From the figure, we can see that Advanced LIGO will be most sensitive to frequencies from $\sim$ 100Hz to 1000Hz.

CHAPTER 3

BINARY BLACK-HOLE SOLUTION

Truth is much too complicated to allow anything but approximations.

John Von Neumann

Everything we know is only some kind of approximation, because we know that we do not know all the laws yet. Therefore, things must be learned only to be unlearned again or, more likely, to be corrected.

Richard Feynman

As we discussed previously, the amplitude of the emitted gravitational wave is proportional to the second time derivative of the quadrupole moment of its source. It is therefore expected that binary systems of compact objects will be the most promising sources of detectable gravitational waves. The analysis of gravitational waves from these sources required theoretical predictions of waveforms, which required solutions of Einstein's field equations for coalescing black holes. To obtain gravitational waveforms from Einstein's equations, we have to solve a system of nonlinear partial differential equations, which cannot be done exactly. Therefore, we have to make use of the most accurate approximations, either of analytical origin within the post-Newtonian approach [87], or by solving the full equations numerically [88, 89, 90]. Both fields have made great progress over the past years, and each can provide sufficiently accurate description of a different part of

the entire signal. Post-Newtonian methods are based on a series expanded solution of Einstein's equations in terms of a small parameter, such as the ratio of relative velocity of the bodies and the speed of light $\frac{v}{c}$. These approximations are valid as long as the expansion parameter is small. Thus post-Newtonian approximations lose their accuracy when the binary is close to merger and the motion becomes relativistic. This means that the last part of the inspiral, the merger and the ringdown to the final black hole have to be modeled differently. Here, numerical relativity becomes crucial and can provide reliable results. However, performing the simulations in full generality is a time consuming and computationally expensive process. In this chapter we will describe the basics of these two approaches and the generation of waveforms using these methods.

3.1 Post-Newtonian Approximations

The post-Newtonian approximation in general relativity assumes a weak field and slow internal motion. It is characterized by the post-Newtonian parameter $\epsilon \sim \left(\frac{v}{c}\right)^2 \sim \left(\frac{M}{R}\right)$, where M is the total mass of the system, v is the magnitude of relative velocity, c is the speed of light, and R is the distance between two compact bodies. To obtain post-Newtonian waveform templates for a binary system one needs to model both the local conservative dynamics of the system and the generation of gravitational waves.

3.1.1 Energy and Flux

First let us consider the simplest case of a compact binary in a circular orbit. The orbit of this system is calculated in section (2.2.14), where we showed that the gravitational wave signal satisfies

$$h(t) = \frac{4M\eta v^2}{R} e^{-i(2\omega_{\rm orb}t+\phi_0)}, \tag{3.1}$$

where v is the relative velocity, M is total mass of the system, $\eta = \frac{m_1 m_2}{M^2}$, R is the distance between source and observer and $\omega_{\rm orb}$ is the orbital angular frequency. The Newtonian energy of this circular

orbit is given by

$$E = -\frac{M\eta v^2}{2} \tag{3.2}$$

We introduced the gravitational wave as a small perturbation of the Minkowski spacetime to construct an equivalent of the gravitational wave's energy-momentum tensor from second-order terms in $h_{\mu\nu}$ and also use it to define the flux of energy that is radiated away from the source through gravitational waves [16, 21, 14]. Averaging over all directions and extracting at infinite distance from the source, yields [91]

$$\begin{aligned} \frac{dE}{dt} &= -\mathcal{L} \qquad \text{with} \\ \mathcal{L} &= \frac{1}{5}\frac{d^3Q^{jk}}{dt^3}\frac{d^3Q_{jk}}{dt^3}, \\ Q_{jk} &= \int \rho(t, x^i)\left(x_j x_k - \frac{1}{3}\delta_{jk}x^l x_l\right) \end{aligned} \tag{3.3}$$

Here, $\mathcal{L}$ represents the total luminosity, ρ is the mass distribution and δ_{jk} is the Kronecker symbol. Specifying for the two point particles on a circular orbit, we find

$$\mathcal{L} = -\frac{32\eta^2}{5}v^{10}. \tag{3.4}$$

The post-Newtonian approximation can be used to provides further extension of these quantities by expanding the metric and derived quantities in terms of the small parameter $\frac{v}{c}$ [87]. In terms of geometric units ($c = 1$), v itself can be interpreted as the expansion parameter. Currently the post Newtonian expansion for energy computation is determined up to 3PN order, i.e., the expansion is carried out up to v^6 corrections above the leading order. We describe the expression for the energy derived for quasi-circular orbits, and the explicit expressions can be found in [87, 92, 93, 94] and references therein. Leading-order and next-to-leading order spin-orbit effects [95, 96, 97] are included as well as spin-spin effects that appear at relative 2PN order [98, 97, 99, 100].

To write post-Newtonian expressions, we closely follow the presentation of [101]. Specifically we are focusing on black hole binaries with spins aligned to the orbital angular momentum **L**. The expressions for precessing binaries will be described later. Modeling aligned spins is actually an extension of non-spinning models, and it has been shown in the recent studies [102, 103] that the inclusion of this dominant spin effect already allows for the detection of a large fraction of generic systems.

To write post-Newtonian Expressions we first define the following useful quantities for a binary system of the black holes, with masses m_i and the individual spins $\boldsymbol{S}_i$ $(i = 1, 2)$

$$\begin{aligned} M &= m_1 + m_2, & \eta &= \frac{m_1 m_2}{M^2}, \\ \delta &= \frac{m_1 - m_2}{M}, & \chi_i &= \frac{\boldsymbol{S}_i \cdot \boldsymbol{L}}{|\boldsymbol{L}| m_i} \\ \chi_s &= \frac{\chi_1 + \chi_2}{2} & \chi_a &= \frac{\chi_1 - \chi_2}{2} \end{aligned} \tag{3.5}$$

Using these definitions we can write the post-Newtonian orbital energy

$$\begin{aligned} E \;=\; & -\frac{M\eta v^2}{2}\Bigg\{1 - v^2\left(\frac{3}{4} + \frac{\eta}{12}\right) + v^3\left[\frac{8\delta\chi_a}{3} + \left(\frac{8}{3} - \frac{4\eta}{3}\right)\chi_s\right] \\ & + v^4\left[\frac{19\eta}{8} - 2\delta\chi_a\chi_s - \frac{\eta^2}{24} + (4\eta - 1)\chi_a^2 - \chi_s^2 - \frac{27}{8}\right] \\ & + v^5\left[\chi_a\left(8\delta - \frac{31\delta\eta}{9}\right) + \left(\frac{2\eta^2}{9} - \frac{121\eta}{9} + 8\right)\chi_s\right] \\ & - v^6\left[\frac{35\eta^3}{5184} + \frac{155\eta^2}{96} - \left(\frac{34445}{576} - \frac{205\pi^2}{96}\right)\eta + \frac{675}{64}\right]\Bigg\}. \end{aligned} \tag{3.6}$$

The flux is determined up to 3.5PN order, and in addition to the spin effects listed above we add a 2.5PN correction that is due to the energy flow into the black holes, as calculated in [104].

The final result reads

$$\begin{aligned}
\mathcal{L} \;=\; & \frac{32}{5}\eta^2 v^{10}\Bigg\{1 - v^2\left(\frac{1247}{336}+\frac{35}{12}\eta\right) + v^3\left[4\pi - \frac{11\delta\chi_a}{4} + \left(3\eta - \frac{11}{4}\right)\chi_s\right] \\
& + v^4\left[\frac{33\delta\chi_a\chi_s}{8} + \frac{65\eta^2}{18} + \left(\frac{33}{16} - 8\eta\right)\chi_a^2 + \left(\frac{32}{16} - \frac{\eta}{4}\right)\chi_s^2 + \frac{9271\eta}{504} - \frac{44711}{9072}\right] \\
& + v^5\left[\left(\frac{701\delta\eta}{36} - \frac{59\delta}{16}\right)\chi_a + \left(\frac{227\eta}{9} - \frac{157\eta^2}{9} - \frac{59}{16}\right)\chi_s - \frac{583\pi\eta}{24} - \frac{8191\pi}{672}\right. \\
& \left. - \frac{1-3\eta}{4}\chi_s\left(1 + 3\chi_s^2 + 9\chi_a^2\right) - \frac{1-\eta}{4}\delta\chi_a\,\left(1 + 3\chi_s^2 + 9\chi_a^2\right)\right] \\
& + v^6\left[-\frac{1712}{105}\ln(4v) - \frac{1712\gamma}{105} - \frac{775\eta^3}{324} - \frac{94403\eta^2}{3024} + \left(\frac{41\pi^2}{48} - \frac{134543}{7776}\right)\eta\right. \\
& \left. + \frac{16\pi^2}{3} + \frac{6643739519}{69854400}\right] + v^7\left[\frac{193385\pi\eta^2}{3024} + \frac{214745\pi\eta}{1728} - \frac{16285\pi}{504}\right]\Bigg\},
\end{aligned} \tag{3.7}$$

where $\gamma \approx 0.5772$ is the Euler constant. With these expressions for energy and flux, we can construct the inspiral phase of the gravitational wave with the assumption that the energy changes slowly due to outgoing radiation. Several slightly different approximants to obtain the phase evolution are discussed in the next section.

3.1.2 Taylor Waveform Approximations

Using the energy-balance law (3.3) we can solve for the time evolution of the expansion parameter $v(t)$, assuming that the system evolves as a quasi-circular orbits with instantaneous energy (3.6) and (3.7). With the application of the chain rule we have

$$\begin{aligned}
\frac{dE}{dt} &= \frac{dE}{dv}\frac{dv}{dt} = -\mathcal{L}(v) \\
\Rightarrow \frac{dv}{dt} &= -\frac{\mathcal{L}(v)}{dE(v)/dt}
\end{aligned} \tag{3.8}$$

The phase evolution of the binary is given by the integral of the orbital frequency $\omega_{\rm orb}$

$$\phi_{\rm orb} = \int \omega_{\rm orb} dt\,, \qquad\qquad M\omega_{\rm orb} = v^3. \tag{3.9}$$

There are various ways to solve these equations, and each method defines a particular post-Newtonian approximant. The *TaylorT1* approximant, for example, is obtained by numerically integrating (3.8) and (3.9) using (3.7) and the derivative of (3.6). We can also construct the inverse of (3.8) and re-expand $(dE/dv)/\mathcal{L}$ in terms of v to 3.5PN order. This formal re-expansion also yields contributions to higher orders than 3.5PN order. However, since 4PN and higher terms in flux and energy are not fully determined, the expressions one could compute are in principle incomplete. The same applies to spin contributions at relative orders higher than 2.5PN. The advantage of this approach is that we can now analytically integrate $t(v)$, and the resulting *TaylorT2* approximant

can be expressed as

$$
\begin{aligned}
t(v) \;=\; & t_0 - \frac{5M}{256\eta v^8}\Bigg\{1 + v^2\Big[\frac{11\eta}{3} + \frac{743}{252}\Big] + v^3\Big[-\frac{32\pi}{5} + \frac{226\delta\chi_a}{15} + \Big(\frac{226}{15} - \frac{152\eta}{15}\Big)\chi_s\Big] \\
& + v^4\Big[\frac{3058673}{508032} + \frac{5429\eta}{504} + \frac{617\eta^2}{72} - \frac{81}{4}\delta\chi_a\chi_s - \Big(\frac{81}{8} - \frac{\eta}{2}\Big)\chi_s^2 - \Big(\frac{81}{8} - 40\eta\Big)\chi_a^2\Big] \\
& + v^5\Big[-\frac{7729\pi}{252} - \frac{13\pi\eta}{3} + \Big(\frac{147101}{756} - \frac{4906\eta}{27} - \frac{68\eta^2}{3}\Big)\chi_s + \Big(\frac{147101}{756} + \frac{26\eta}{3}\Big)\delta\chi_a \\
& + \big(6 - 6\eta\big)\delta\chi_s^2\chi_a + \big(6 - 18\eta\big)\chi_s\chi_a^2 + \big(2 - 6\eta\big)\chi_s^3 + \big(2 - 2\eta\big)\delta\chi_a^3\Big] \\
& + v^6\Big[\frac{6848\gamma}{105} - \frac{10052469856691}{23471078400} + \frac{128\pi^2}{3} + \Big(\frac{3147553127}{3048192} - \frac{451\pi^2}{12}\Big)\eta - \frac{15211\eta^2}{1728} \\
& + \frac{25565\eta^3}{1296} + \frac{6848\ln(4v)}{105} - \Big(\frac{548\pi}{3} - \frac{448\pi\eta}{3}\Big)\chi_s - \frac{584\pi\delta\chi_a}{3} \\
& + \Big(\frac{6845}{672} - \frac{43427\eta}{168} + \frac{245\eta^2}{3}\Big)\chi_s^2 + \Big(\frac{6845}{672} - \frac{1541\eta}{12} + \frac{964\eta^2}{3}\Big)\chi_a^2 \\
& + \Big(\frac{6845}{336} - \frac{2077\eta}{6}\Big)\delta\chi_s\chi_a\Big] + v^7\Big[-\frac{15419335\pi}{127008} - \frac{75703\pi\eta}{756} + \frac{14809\pi\eta^2}{378} \\
& + \Big(\frac{4074790483}{1524096} + \frac{30187\eta}{112} - \frac{115739\eta^2}{216}\Big)\delta\chi_a \\
& + \Big(\frac{4074790483}{1524096} - \frac{869712071\eta}{381024} - \frac{2237903\eta^2}{1512} + \frac{14341\eta^3}{54}\Big)\delta\chi_s \\
& + \big(228\pi - 16\pi\eta\big)\chi_s^2 + \big(228\pi - 896\pi\eta\big)\chi_a^2 + 456\pi\delta\chi_a\chi_s - \\
& \Big(\frac{3237}{14} - \frac{14929\eta}{84} + \frac{362\eta^2}{3}\Big)\chi_s^3 - \Big(\frac{3237}{14} - \frac{87455\eta}{84} + 34\eta^2\Big)\delta\chi_a^3 \\
& - \Big(\frac{9711}{14} - \frac{39625\eta}{84} + 102\eta^2\Big)\delta\chi_s^2\chi_a - \Big(\frac{9711}{14} - \frac{267527\eta}{84} + \frac{3574\eta^2}{3}\Big)\chi_s\chi_a^2\Big]\Bigg\}.
\end{aligned}
\tag{3.10}
$$

The TaylorT2 approximant is completed by calculating the phase in a similar manner. We use

$$
\frac{d\phi_{\rm orb}}{dv} = \frac{v^3}{M}\frac{dt}{dv} \tag{3.11}
$$

and expand the right-hand side. The analytical integration yields

$$
\begin{aligned}
\phi_{\rm orb}(v) \;=\; & \phi^0_{\rm orb} - \frac{1}{32\eta v^5}\Bigg\{1 + v^2\left[\frac{3715}{1008} + \frac{55\eta}{12}\right] + v^3\left[-10\pi + \frac{565\chi_a}{24} + \left(\frac{565}{24} - \frac{95\eta}{6}\right)\chi_s\right] \\
& + v^4\left[\frac{15293365}{1016064} + \frac{27145\eta}{1008} + \frac{3085\eta^2}{144} - \frac{405}{8}\delta\chi_a\chi_s - \left(\frac{405}{16} - \frac{5\eta}{4}\right)\chi_s^2 - \left(\frac{405}{16} - 100\eta\right)\chi_a^2\right] \\
& + v^5 \ln v\left[\frac{38645\pi}{672} - \frac{65\pi\eta}{8} - \left(\frac{735505}{2016} - \frac{12265\eta}{36} - \frac{85\eta^2}{2}\right)\chi_s - \left(\frac{735505}{2016} + \frac{65\eta}{4}\right)\delta\chi_a \right. \\
& \left. - \left(\frac{45}{4} - \frac{45\eta}{4}\right)\delta\chi_s^2\chi_a - \left(\frac{45}{4} - \frac{135\eta}{4}\right)\chi_a^2\chi_s - \left(\frac{15}{4} - \frac{45\eta}{4}\right)\chi_s^3 - \left(\frac{15}{4} - \frac{15\eta}{4}\right)\delta\chi_a^3\right] \\
& + v^6\left[\frac{12348611926451}{18776862720} - \frac{1712\gamma}{21} - \frac{160\pi^2}{3} - \left(\frac{15737765635}{12192768} - \frac{2255\pi^2}{48}\right)\eta + \frac{76055\eta^2}{6912}\right. \\
& - \frac{127825\eta^3}{5184} - \frac{1712\ln(4v)}{21} + \left(\frac{730\pi}{3} - \frac{560\pi\eta}{3}\right)\chi_s - \left(\frac{34225}{2688} - \frac{217135\eta}{672} + \frac{1225\eta^2}{12}\right)\chi_s^2 \\
& \left. + \frac{730\pi\delta\chi_a}{3} - \left(\frac{34225}{2688} - \frac{7705\eta}{48} + \frac{1205\eta^2}{3}\right)\chi_a^2 - \left(\frac{34225}{1344} - \frac{10385\eta}{24}\right)\delta\chi_s\chi_a\right] \qquad (3.12) \\
& + v^7\left[\frac{77096675\pi}{2032128} + \frac{378515\pi\eta}{12096} - \frac{74045\pi\eta^2}{6048} - \left(\frac{20373952415}{24385536} + \frac{150935\eta}{1792} - \frac{578695\eta^2}{3456}\right)\delta\chi_a \right. \\
& - \left(\frac{20373952415}{24385536} - \frac{4348560355\eta}{6096384} - \frac{11189515\eta^2}{24192} + \frac{71705\eta^3}{864}\right)\chi_s - \left(\frac{285\pi}{4} - 5\pi\eta\right)\chi_s^2 \\
& - \left(\frac{285\pi}{4} - 280\pi\eta\right)\chi_a^2 - \frac{285\pi}{2}\delta\chi_a\chi_s + \left(\frac{16185}{224} - \frac{74645\eta}{1344} + \frac{905\eta^2}{24}\right)\chi_s^3 \\
& + \left(\frac{16185}{224} - \frac{437275\eta}{1344} + \frac{85\eta^2}{8}\right)\delta\chi_a^3 + \left(\frac{48555}{224} - \frac{198125\eta}{1344} + \frac{255\eta^2}{8}\right)\delta\chi_s^2\chi_a \\
& \left. + \left(\frac{48555}{224} - \frac{1337635\eta}{1344} + \frac{8935\eta^2}{24}\right)\chi_s\chi_a^2\right]\Bigg\}.
\end{aligned}
$$

Both $t(v)$ and $\phi_{\rm orb}(v)$ together define $\phi_{\rm orb}(t)$ implicitly. The *TaylorT3* approximant is derived from the TaylorT2 expressions by inverting the Taylor series $t(v)$ analytically and plugging $v(t)$ into (3.12). The final result can be written as an closed-form Taylor expansion $\phi_{\rm orb}(t)$ whose explicit expressions can be found [105, 106].

The *TaylorT4* approximant goes back to the energy-balance law (3.8) and re-expands the right-hand side in terms of v. The resulting differential equation is truncated at the appropriate PN

order (3.5PN), and is given by

$$\begin{aligned}
\frac{dv}{dt} &= \frac{32\eta}{5M}v^9\Bigg\{1+v^2\left[\frac{11\eta}{4}+\frac{743}{336}\right]+v^3\left[4\pi-\frac{113\delta\chi_a}{12}+\left(-\frac{113}{12}+\frac{19\eta}{3}\right)\chi_s\right] \\
&+v^4\left[\frac{81\delta\chi_a\chi_s}{8}+\frac{59\eta^2}{18}+\left(\frac{81}{16}-20\eta\right)\chi_a^2+\left(\frac{81}{16}-\frac{\eta}{4}\right)\chi_s^2+\frac{13661\eta}{2016}+\frac{34103}{18144}\right] \\
&+v^5\left[\left(\frac{3\eta}{4}-\frac{3}{4}\right)\delta\chi_a^3+\left(\frac{9\eta}{4}-\frac{9}{4}\right)\delta\chi_a\chi_s^2+\left(\frac{1165\eta}{24}-\frac{31571}{1008}\right)\delta\chi_a-\frac{189\pi\eta}{8}-\frac{4159\pi}{672}\right. \\
&\left.+\left(\frac{27\eta\chi_a^2}{4}-\frac{9\chi_a^2}{4}-\frac{79\eta^2}{3}+\frac{5791\eta}{63}-\frac{31571}{1008}\right)\chi_s+\left(\frac{9\eta}{4}-\frac{3}{4}\right)\delta\chi_s^3\right] \\
&+v^6\left[\frac{16447322263}{139708800}+\frac{16\pi^2}{3}-\frac{1712\gamma}{105}-\frac{5605\eta^3}{2592}+\frac{541\eta^2}{896}+\left(\frac{451\pi^2}{48}-\frac{56198689}{217728}\right)\eta\right. \\
&-\frac{1712\ln(4v)}{105}+\left(\frac{1517\eta^2}{72}-\frac{23441\eta}{288}+\frac{128495}{2016}\right)\chi_s^2+\left(\frac{565\delta^2}{9}+\frac{89\eta^2}{3}-\frac{2435\eta}{224}+\frac{215}{224}\right)\chi_a^2 \\
&\left.+\left(\frac{128495\delta}{1008}-\frac{12733\delta\eta}{144}\right)\chi_a\chi_s+\left(\frac{40\pi\eta}{3}-\frac{80\pi}{3}\right)\chi_s-\frac{80\pi\delta\chi_a}{3}\right] \\
&+v^7\left[\frac{91495\pi\eta^2}{1512}+\frac{358675\pi\eta}{6048}-\frac{4415\pi}{4032}-\left(\frac{11\eta^2}{24}-\frac{979\eta}{24}+\frac{505}{8}\right)\chi_s^3\right. \\
&+\left(\frac{\delta\eta^2}{8}+\frac{742\eta}{3}-\frac{505\delta}{8}\right)\chi_a^3+\left(\frac{3\eta^2}{8}+\frac{917\eta}{12}-\frac{1515}{8}\right)\delta\chi_a\chi_s^2+12\pi\chi_s^2 \\
&+\left(\frac{7007\eta}{24}-124\delta^2-\frac{3397\eta^2}{24}-\frac{523}{8}\right)\chi_s\chi_a^2+\big(12\pi-48\pi\eta\big)\chi_a^2 \\
&+\left(\frac{2045\eta^3}{216}-\frac{398017\eta^2}{2016}+\frac{10772921\eta}{54432}-\frac{2529407}{27216}\right)\chi_s+24\pi\delta\chi_a\chi_s \\
&\left.+\left(\frac{845827\delta\eta}{6048}-\frac{41551\delta\eta^2}{864}-\frac{2529407\delta}{27216}\right)\chi_a\right]\Bigg\}.
\end{aligned} \tag{3.13}$$

The equations (3.12) and (3.13) are then integrated numerically.

3.1.3 Post Newtonian Waveforms

Using the expressions for $\phi_{\rm orb}(t)$ and $v(t)$ with the above approximants one can express the corresponding quadrupole gravitational wave strain as

$$h(t) = A(t)e^{-2i\phi_{\rm orb}(t)} \tag{3.14}$$

where $A(t)$ is the amplitude, which for lowest order is given by $A(t) = 4M\eta v^2(t)/R$. There exists higher order corrections for (3.14) which can be found in [107, 108]. Since the numerical waveforms are decomposed into *spin-weighted spherical harmonics*, we can use (3.14) to calculate decomposition of strain into spin-weighted spherical harmonics (with spin weight -2)

$$h(t;\theta,\psi) = \sum_{l=2}^{\infty}\sum_{m=-l}^{l} h^{lm}(t)\,{}_{-2}Y^{lm}(\theta,\psi), \tag{3.15}$$

where ${}_{-2}Y^{lm}$ are the basis functions on sphere [109] depending on sky directions (θ,ψ) and are given by

$$-{}_{s}Y^{lm}(\theta,\psi) = (-1)^2\sqrt{\frac{2l\ +\ 1}{4\pi}}\; d^{l}_{ms}(\theta)e^{im\psi} \tag{3.16}$$

where $d^{l}_{ms}(\theta)$ is the *Wigner matrix*. The quantity $h(t,\theta,\psi)$ is similar to the detector response (2.107) and is a combination of real and imaginary polarizations h_+ and $h_\times$. Each successive mode decreases rapidly with ℓ. Not that this may not be case for highly precessing systems where other modes can be significantly dominant. At leading order , we find that

$$h(t;\theta,\psi) = h^{22}(t)\,{}_{-2}Y^{22}(\theta,\psi) + h^{2-2}(t)\,{}_{-2}Y^{2-2}(\theta,\psi) \tag{3.17}$$

with $h^{22} = A^{22}\text{exp}(2i\phi_{\text{orb}})$, $h^{2-2} = (h^{22})^*$ and

$${}_{-2}Y^{22} = \sqrt{\frac{5}{64\pi}}\,(1+\cos\theta)^2\; e^{2i\psi} \qquad\qquad {}_{-2}Y^{2-2} = \sqrt{\frac{5}{64\pi}}\,(1-\cos\theta)^2\; e^{-2i\psi} \tag{3.18}$$

Combining these expressions we can write the strain (3.17) as

$$h(t;\theta,\psi) = A^{22}\sqrt{\frac{5}{4\pi}}\,\frac{(1+\cos\theta)^2}{2}\,\cos(2\phi_{\text{orb}}-2\psi) - iA^{22}\sqrt{\frac{5}{4\pi}}\cos\theta\,\sin(2\phi_{\text{orb}}-2\psi) \tag{3.19}$$

where $A^{22} = \sqrt{\frac{64\pi}{5}}\ \frac{M\eta v^2}{R}$. Incorporating higher order PN terms extends the amplitude A^{22} to a Taylor series in v, but we also find a more complex angular dependency of the full waveform due to non vanishing h^{lm} beyond the leading order contributions. Their general form satisfies

$$h^{lm}(t) = A^{lm} e^{-im\phi_{\rm orb}(t)} \tag{3.20}$$

Explicit expression for A^{lm} can be found [108] up to 3PN order, and spin contributions up to 2PN order are provided in [107]. The dominant A^{22} with the 3PN terms is

$$\begin{aligned} A^{22} \;=\; & \sqrt{\frac{64\pi}{5}}\ \frac{M\eta v^2}{R}\Bigg\{1 - v^2\left[\frac{55}{42}\eta - \frac{107}{42}\right] + v^3\left[2\pi - \frac{4}{3}\chi + \frac{2\eta}{3}(\chi_1+\chi_2)\right] \\ & -v^4\left[\frac{2173}{1512} + \eta\left(\frac{1069}{216} + 2\chi_1\chi_2\right) - \frac{2047}{1512}\eta^2\right] + v^5\left[\frac{107\pi}{21} - \eta\left(\frac{34\pi}{21} - 24i\right)\right] \\ & +v^6\left[\frac{27027409}{646800} - \frac{856\gamma}{105} + \frac{428i\pi}{105} + \frac{2\pi^2}{3} + \eta\left(\frac{41\pi^2}{96} - \frac{278185}{33264}\right) - \frac{20261\eta^2}{2772}\right. \\ & \left. +\frac{114635\eta^3}{99792} - \frac{856}{105}\ln(4v)\right]\Bigg\}, \end{aligned} \tag{3.21}$$

where $\chi = (\chi_1 m_1 + \chi_2 m_2)/M$ [110]

3.1.4 Precession Effects

The post-Newtonian results in the previous section are restricted to non-precessing binary systems. For the general description of arbitrary spin configurations we briefly mention some expressions here for completeness. Such expressions are provided in [102] and further details can also be found in [111, 112, 97, 113, 114, 115, 116, 117, 96]. The spin-dependent contributions to the post Newtonian energy and flux were actually derived in a more general form than was given in (3.6) and (3.7). Specifically there exists expressions involving the scalar products of the 3-dimensional spin vectors $\boldsymbol{S}_i (i = 1, 2)$ and the Newtonian angular momentum $\boldsymbol{L}_N$ to describe the generic spin

configurations. The Newtonian angular momentum is perpendicular to the constantly changing orbital plane, and usually referred as the normalized vector $\hat{\boldsymbol{L}}_N$. With these more general terms, one could simply re-derive all time-domain approximants. The three vectors $\{\boldsymbol{S}_1, \boldsymbol{S}_2, \hat{\boldsymbol{L}}_N\}$ which are constant in the non-precessing case, generally change their directions continuously. Although it is important to note that the spin magnitudes are constants. To incorporate these dynamics an additional set of equations has to be introduced, and the most recent results with including these effects can be found in [96, 118] and are given by

$$\frac{d\boldsymbol{S}_i}{dt} = \boldsymbol{\Omega}_i \times \boldsymbol{S}_i \qquad i = 1, 2, \tag{3.22}$$

where

$$\begin{aligned} \boldsymbol{\Omega}_1 \;=\; & \frac{v^5}{M}\left\{\left(\frac{3}{4}+\frac{\eta}{2}-\frac{3\delta}{4}\right)\hat{\boldsymbol{L}}_N - \frac{v}{2M^2}\left[3\left(\boldsymbol{S}_2+\frac{m_2}{m_1}\boldsymbol{S}_1\right)\hat{\boldsymbol{L}}_N\,\hat{\boldsymbol{L}}_N\cdot\boldsymbol{S}_2\right]\right. \\ & \left. +v^2\left(\frac{9}{16}+\frac{5\eta}{4}-\frac{\eta^2}{24}-\frac{9\delta}{16}+\frac{5\delta\eta}{8}\right)\hat{\boldsymbol{L}}_N\right\}, \end{aligned} \tag{3.23}$$

and $\boldsymbol{\Omega}_2$ is obtained by exchanging the indices $1 \longleftrightarrow 2$ in $\boldsymbol{S}_i$ and $m_1$in (3.23). The set of equations for precessing adiabatic approximations is completed by the evolution of $\hat{\boldsymbol{L}}_N$,

$$\frac{M^2\eta}{v^2}\left[1+\left(\frac{3}{2}+\frac{\eta}{6}\right)v^2\right]\frac{d\hat{\boldsymbol{L}}_N}{dt} = -\frac{d}{dt}(\boldsymbol{S}_1+\boldsymbol{S}_2). \tag{3.24}$$

All equations are required to be solved simultaneously in order to obtain $v(t)$, $\boldsymbol{S}_1(t)$, $\boldsymbol{S}_2(t)$ and $\hat{\boldsymbol{L}}_N(t)$. The solution for the coupled system of differential equations leads to a more complicated gravitational wave signal than for the non-precessing case. The corresponding corrections for arbitrary inclination angles due to precession have been calculated in [107], and one can simply plug the phase evolution and the coordinates of all relevant vectors into those equations. The important fact is that the equivalent of the orbital phase that enters the waveform modes $\sim e^{-im\Phi}$ has an

additional term that originates from the precession of $\boldsymbol{L}_N$ which is given by

$$\Phi(t) = \int \left(\omega_{\rm orb} - \frac{d\boldsymbol{\alpha}}{dt} \cos\boldsymbol{\iota} \right) dt, \tag{3.25}$$

where $\boldsymbol{\alpha}$ and $\boldsymbol{\iota}$ are the spherical coordinates of $\boldsymbol{L}_N$, i.e., the angles measured from the x and z-axis, respectively.

3.1.5 Effective One-Body

The accuracy of the post-Newtonian approximate solutions can be improved by applying resummation techniques. This method is based on rewriting of the perturbative post-Newtonian expansion in a new form (e.g. a Chebyshev decomposition or a Padé series) based on an intuitive guess of some feature that one knows should be present in the exact solution. A particular resummation of the post-Newtonian approximation that has been highly successful at reproducing numerical waveforms is the effective one-body (EOB) approach [119, 120, 121, 122]. The basic idea in this approach is to map a two-body problem into an effective one-body Hamiltonian with appropriate energy levels. By applying various re-expansion and re-summation on various quantities that enter the EOB metric, one obtains improved convergence properties. Recently the post-Newtonian derived EOB description of the inspiral was extended by introducing additional parameters that were determined by comparison with independent numerical simulations of the late inspiral, merger and ringdown [123, 124, 125, 126, 127, 128, 129, 130, 131, 132, 133]. The resulting effective-one-body waveforms are shown to accurately represent the gravitational waves emitted in the inspiral of compact objects, up to the moment when the black holes merge. In addition they become accurate after the merger by adding on information from black hole perturbation theory [134].

3.1.6 Post Newtonian Errors

The post-Newtonian expanded results are expected to yield accurate descriptions of the motion and radiation of binary black holes only during their early inspiralling stage, i.e. as long as the

post Newtonian expansion parameter $\epsilon \sim (v/c)^2 \sim M/R$ stays significantly smaller than $\sim 1/6$ (at larger values the orbital motion is expected to become dynamically unstable). Furthermore, post-Newtonian theory is based on a series expansion and only handful of the terms of the series are known. It is not even guaranteed that the series is a convergent. Thus the post-Newtonian waveforms are prone to certain approximations errors and different post-Newtonian approximants perform better for different systems.

3.2 Basics of Numerical Relativity

General relativity is conceptually a very simple and elegant theory but in practice it is a highly complicated. The Einstein field equations are a system of ten coupled partial differential equations in four dimensions which are highly non-linear. It is very difficult to solve these equations for many important astrophysical systems. Only a handful of exact solution exits characterized by a high degree of symmetry. There exists analytical approximate solutions of Einstein field equations which are limited for weak field and slow velocity regime. Many gravitational wave sources detectable by LIGO involve strong gravitational field and highly relativistic speed. The only way to solve non-linear, dynamical and strong field systems with Einsteins field equations is numerically using powerful supercomputers.

Numerical relativity deals with solving Einstein's field equations on supercomputers. Numerical relativity requires developing efficient and stable numerical algorithms to solve the Einsteins field equations for realistic, highly relativistic, strong field systems. Numerical relativity is crucial to study phenomenon like the late inspiral to merger phases of binary compact objects dynamics, gravitational collapse, supernova, perturbed stars, accretion disks dynamics of binary systems, galaxy interaction and big bang itself. In order to use numerical relativity for solving Einsteins equations on supercomputers, the first step is to rewrite equations in the form that computers can handle. In the standard approach the four dimensional Einstein's field equations are expressed in a way that allows us to give certain initial data, and from there obtain the subsequent evolution of

gravitational field. This means we want to write Einsteins equations as a set of coupled differential equations which satisfies certain constraints and can be evolved as well. This is analogous to solving Maxwell's equations

Constriants	**Evolution**	(3.26)
$\nabla \cdot E = 4\pi\rho$	$\partial_t E = \nabla \times B - 4\pi J$	
$\nabla \cdot B = 0.$	$\partial_t B = -\nabla \times E$	

where constraint equations are conditions that the evolved fields must obey at all times. This system of initial conditions followed by a subsequent evolution is referred to as *Cauchy problem*. Here, it is easy to see that evolution equations are consistent with the constraints

$$\begin{aligned} \partial_t(\nabla \cdot B) &= \nabla \cdot \partial_t B = -\nabla \cdot (\nabla \times E) = 0. \\ \partial_t(\nabla \cdot E - 4\pi\rho) &= \nabla \cdot (\nabla \times B - 4\pi J) - 4\pi\partial_t\rho \qquad (3.27) \\ &= -4\pi(\partial_t\rho + \nabla \cdot J) = 0 \qquad (3.28) \end{aligned}$$

We want to do the same for Einstein's equation and that was done with Hamiltonian formulation of general relativity by the work of Arnowitt, Deser and Misner (ADM) [135, 136, 137, 138, 139, 140, 141, 142, 143, 144]. This section will follow excellent reviews and textbooks by Baumgarte, Shapiro, Alcubierre and Shibata and Gourgoulhon [145, 17, 146, 147].

3.2.1 The 3+1 split and the ADM Equations

3+1 *decomposition* assume four-dimensional spacetime split into a series of three dimensional spatial slices, such that each slice represents one moment along the one dimensional time. This splitting of spacetime is done by foliation. So, for two adjacent hypersurfaces, say Σ_{t_1} and Σ_{t_2}, the geometry of spacetime can be determined from three basic ingredients.

1. The three-dimensional *spatial metric* γ_{ij} which measures proper distances within hyper-

surface itself.

$$d\ell^2 = \gamma_{ij} dx^i dx^j \tag{3.29}$$

2. The *lapse function* α, which describe the lapse of proper time between both hypersurfaces as measured by observer which is moving along the direction normal to the hypersurfaces.

$$d\tau = \alpha(t, x^i) dt \tag{3.30}$$

3. The *shift vector* β^j, which describe the relative velocity between observers and the lines that correspond to the constant spatial coordinates. These observers are called Eulerian observer and are always moving along the direction normal to the hypersurfaces.

$$x^i_{t_2} = x^i_{t_1} - \beta^i(t, x^j) dt. \tag{3.31}$$

With these ingredients of 3+1 decomposition we can write the 4-dimensional metric $g_{\mu\nu}$ in terms of $(\gamma_{ij}, \beta^i, \alpha)$ as

$$ds^2 = -\alpha^2 dt^2 + \gamma_{ij}(dx^i + \beta^i\, dt)\,(dx^j + \beta^j\, dt), \tag{3.32}$$

where $\beta_i = \gamma_{ij}\beta^j$. Another important quantity is the *unit-normal vector*, n^μ, to the spatial hypersurfaces which is the four velocity of Eulerian observer $n^\mu n_\mu = -1$, and whose components are given by

$$n^\mu = (1/\alpha, -\beta^i/\alpha) \qquad\qquad n_\mu = (-\alpha, 0, 0, 0) \tag{3.33}$$

Finally, the quantity that describes the change in normal vectors n^μ as it is parallel-transported from one point in hyper-surface to the other is called *extrinsic curvature tensor* and is denoted by

$K_{\mu\nu}$. Mathematically it is given by

$$K_{\mu\nu} = -(\nabla_\mu n_\nu + n_\mu n^\rho \nabla_\rho n_\nu) \tag{3.34}$$

The extrinsic curvature $K_{\mu\nu}$ is symmetric and purely spatial tensor as $n^\mu K_{\mu\nu} = 0$. Using the definition (3.33) of normal vector, the extrinsic curvature can be expressed in terms of spatial 3 metric

$$K_{ij} = \frac{-1}{2\alpha}\Big[\partial_t \gamma_{ij} + D_i\beta_j + D_j\beta_i\Big], \tag{3.35}$$

where D_i is the three-dimensional covariant derivative related to γ_{ij}. Equation (3.35) can also be written as

$$\partial_t \gamma_{ij} = -2\alpha K ij + D_i\beta_j + D_j\beta_i. \tag{3.36}$$

The above equation shows that extrinsic curvature K_{ij} gives the time rate of change spatial metric γ_{ij}. The extrinsic curvature can be directly written in terms of the Lie derivative of the 3-metric with respect to the normal direction

$$\mathcal{L}_{\vec{n}}\gamma_{ij} = -2Kij, \tag{3.37}$$

which shows that the extrinsic curvature is precisely the change in time of the spatial metric as seen by Eulerian observers.

In addition, one also needs to rewrite the stress energy tensor in terms of 3+1 quantities.

Conventionally, these are

$$\rho = n_\mu n_\nu T^{\mu\nu}, \tag{3.38}$$

$$S_i = -\gamma^\mu{}_i n^\nu T_{\mu\nu}, \tag{3.39}$$

$$S_{ij} = \gamma^\mu{}_i \gamma^\nu{}_j T_{\mu\nu}, \tag{3.40}$$

$$S = \gamma^{ij} S_{ij}. \tag{3.41}$$

With above definitions it is now straightforward for Einstein equations to be decomposed into system of constraints and evolution equations. The constraint equations include the Hamiltonian constraint

$$R + K^2 - K_{ij}\, K^{ij} = 16\pi\, \rho, \tag{3.42}$$

and the momentum constraints

$$D_j(K^{ij} - \gamma^{ij}\, K) = 8\pi\, S^i. \tag{3.43}$$

The evolution equations for the spatial metric and extrinsic curvature are

$$\partial_t \gamma_{ij} = -2\alpha\, K_{ij} + D_i\beta_j + D_j\beta_i, \tag{3.44}$$

and

$$\begin{aligned}\partial_t K_{ij} = \alpha\,(R_{ij} - 2K_{ik}K^k_j K\, K_{ij}) - D_i D_j \alpha + \beta^k \partial_k\, K_{ij} + K_{ik}\partial_j\, \beta^k \\ + K_{kj}\partial_i\, \beta^k - 8\pi\, \alpha(S_{ij} - \frac{1}{2}\gamma_{ij}(S - \rho)).\end{aligned} \tag{3.45}$$

Equations (3.44) and (3.45) form a closed system of evolution equations, and are known as the Arnowitt-Deser-Misner (ADM) equations. These equations allow us to write down Einstein's field equations for general relativity as a Cauchy problem. It is important to note that there

are no evolution equations for the lapse α and shift vector β^i. These quantities represents the coordinate freedom and can be chosen freely. It is also possible to show that, by using the Bianchi identities (2.41), that the evolution equations guarantee that if the constraints (3.42) and (3.43) are satisfied initially, then they will continue to be satisfied during evolution.

3.2.2 The Initial Data Problem

The constraints equations (3.42) and (3.43) form a system of four coupled elliptic partial differential equation. Due to existence of these constraints, it is not possible to arbitrarily choose the 12 dynamical quantities (γ_{ij}, K_{ij}) as initial data. The initial data has to be chosen in such a way that these constraints are satisfied initially. Thus we need to solve the initial data problem to obtain adequate values of (γ_{ij}, K_{ij}) that represent the physical situation we want to study. There exists several methods to write constraints in a form that we can solve numerically. These include *conformal decomposition* of York- Lichnerowicz [148], the *thin sandwich formalism* [149] as well as the *extended thin sandwich decomposition* [150, 151, 152, 153]. A review of different ways to find initial data can be found in [154]. The classic method for finding initial data is the York-Lichnerowicz conformal decomposition [148, 155], which starts by factoring out the spatial metric to give

$$\gamma_{ij} = \Psi^4 \tilde{\gamma}_{ij}, \tag{3.46}$$

where Ψ is the conformal factor, and all object with a tilde are associated with conformally related spatial metric $\tilde{\gamma}_{ij}$. The inverse is $\gamma^{ij} = \Psi^{-4}\tilde{\gamma}^{ij}$, so that the conformally related spatial metric can be used to lower and raise conformal spatial indices. The extrinsic curvature is also decomposed by first separating out its trace K and trace free part A_{ij} such that

$$K_{ij} = A_{ij} + \frac{1}{3}\gamma_{ij}K, \tag{3.47}$$

and further a conformal transformation of A_{ij} gives

$$A_{ij} = \Psi^{-10}\tilde{A}_{ij}. \tag{3.48}$$

Any trace-free symmetric tensor can be split into transverse-traceless part and a longitudinal part in the following way:

$$\tilde{A}_{ij} = \tilde{A}^{*}_{ij} + (\hat{L}W)_{ij}, \tag{3.49}$$

where transverse-traceless part $\tilde{A}^{*}_{ij}$ is divergence-less $\tilde{D}_i\tilde{A}^{*ij} = 0$ and the longitudinal part given by

$$(\hat{L}W)^{ij} = \tilde{D}^iW^j + \tilde{D}^jW^i - \frac{2}{3}\tilde{\gamma}^{ij}\tilde{D}^kW^k. \tag{3.50}$$

Here W^i is a vector potential and $\hat{L}$ is the *longitudinal derivative* and is also known as *vector gradient*. In order to find initial data one assumes that the conformal metric $\tilde{\gamma}_{ij}$, the trace of the extrinsic curvature K and its divergence-less trace-free part $\tilde{A}^{*}_{ij}$ are given, and uses the constraints to solve for conformal factor Ψ and vector potential W^i. The Hamiltonian constraint leads to the following equation for Ψ,

$$8\tilde{D}^2\Psi - \tilde{R}\Psi + \Psi^{-7}\big(\tilde{A}_{ij}\,\tilde{A}^{ij}\big) - \frac{2}{3}\Psi^5K^2 + 16\pi\Psi^{-3}\rho = 0, \tag{3.51}$$

while the momentum constraint leads to the following equations for W^i,

$$\tilde{D}^2W^i - \frac{2}{3}\Psi^6\tilde{D}^iK - 8\pi\Psi^{10}S^i = 0, \tag{3.52}$$

which are three coupled elliptical partial differential equations for W^i. The problem can be considerably simplified if we choose $K = 0$ and also assume that the conformal metric is flat i.e. $\tilde{\gamma}^{ij} = \delta^{ij}$.

The constraints then reduce (in vacuum) to

$$8D^2_{\rm flat}\Psi + \Psi^{-7}(\tilde{A}_{ij}\,\tilde{A}^{ij}) = 0, \tag{3.53}$$

$$D^2_{\rm flat}W^i = 0, \tag{3.54}$$

where $D^2_{\rm flat}$ is the standard flat space Laplacian. The second equation is linear and can be solved analytically in many cases. Using W^i one can reconstruct $\tilde{A}^{ij}$ and then can solve Poisson's equation to get Ψ. It is easy now to construct the vacuum solution corresponding to a conformally flat metric at a moment of time symmetry, that is,$\tilde{\gamma}_{ij} = \delta_{ij}$ and $K_{ij} = 0$. Eq. (3.53) equations then reduce simply to Laplace equation

$$D^2_{\rm flat}\Psi = 0 \tag{3.55}$$

Boundary conditions for an asymptotically flat space imply that far away $\lim_{r\to\infty}\Psi = 1$. The simplest non-trivial solution is then

$$\Psi = 1 + \frac{M}{2r}, \tag{3.56}$$

where $M/2$ is a constant of integration chosen such that we measure the resulting spacetime to have energy M. This fixes the Cauchy initial data for a single black hole. Now, Laplace's equation is linear, so we can superpose solutions to find new solutions. For example, we can take

$$\Psi = 1 + \sum_{i=1}^{N}\frac{M_i}{2|r - r_i|}, \tag{3.57}$$

This represents N black holes momentarily at rest and is known as *Brill-Lindquist data*.

Mass, Momentum and Angular Momentum

The equivalence principle implies that there is no coordinate independent construction of local energy density of gravitational field in general relativity. For asymptotically flat spaces, it is possible to define globally conserved quantities associated with the total energy (mass), momentum, and angular momentum. One useful measure of energy is provided by Arnowitt, Deser, and Misner in [144] and is usually referred as *ADM mass* $M_{\rm ADM}$. The ADM mass is defined as an integral over the two dimensional surface at infinity $\partial\Sigma_\infty$ bounding a spatial slice Σ [156]

$$M_{\rm ADM} = \frac{1}{16\pi} \int_{\partial\Sigma_\infty} \gamma^{ij}\gamma^{kl}(\partial_k\gamma_{jl} - \partial_j\gamma_{kl}\sqrt{\gamma}\, dS_i. \tag{3.58}$$

Here $dS_i = \sigma_i\sqrt{\gamma^{\partial\Sigma_\infty}}d^2z$ is the outward oriented surface element, where z^i are coordinates on $\partial\Sigma_\infty$, and $\gamma_{ij}^{\partial\Sigma_\infty}$ is the induced metric on $\partial\Sigma_\infty$ which means that metric approach Minkowski space sufficiently rapidly $g_{\mu\nu} = \eta_{\mu\nu} + \mathcal{O}(1/r)$. The above definition is not covariant and only valid for asymptotically Cartesian coordinates. If $\Psi = 1 + \mathcal{O}(1/r)$ and we use the conformal metric then the Eq. (3.58) can be expressed as

$$M_{\rm ADM} = \frac{1}{16\pi} \int_{\partial\Sigma_\infty} (\tilde{\gamma}^{jk}\tilde{\Gamma}^i_{jk} - \tilde{\gamma}^{ij}\tilde{\Gamma}^k_{jk})\, d\tilde{S}_i - \frac{1}{2\pi} \int_{\partial\Sigma_\infty} \tilde{D}_i\psi d\tilde{S}^i. \tag{3.59}$$

where $\tilde{\Gamma}^i_{jk}$ are Christoffel symbols related to conformal metric $\tilde{\gamma}_{ij}$. For our black hole initial data Eq. (3.56) $\tilde{\Gamma}^i_{jk} = 0$ in Cartesian coordinates and the ADM mass (3.59) reduces to

$$M_{\rm ADM} = -\frac{1}{2\pi} \int_{\partial\Sigma_\infty} \tilde{D}_i\Psi\tilde{S}^i = M. \tag{3.60}$$

It is important to note that in general M is only a parameter, and does not coincide with the mass of black hole.

In addition to the formula for the ADM mass, one can define the *ADM linear momentum*

$$P^i_{\rm ADM} = \frac{1}{8\pi} \int_{\partial\Sigma_\infty} (K^{ij} - \gamma^{ij} K)\, dS_i. \tag{3.61}$$

and the *ADM angular momentum*

$$J^i_{\rm ADM} = \frac{\epsilon^{ijk}}{8\pi} \int_{\partial\Sigma_\infty} x_j (K_{kl} - \gamma_{kl} K)\, dS^l, \tag{3.62}$$

where x^i is a coordinate vector. For our black hole initial data Eq. (3.56) we can show that $P^i_{\rm ADM} = 0$ and $J^i_{\rm ADM} = 0$.

3.2.3 Gauge Choices and Evolution Equations

The Einsteins equations provide us with evolution equations for the spatial metric γ_{ij} and extrinsic curvature K_{ij}. However, they do not contain evolution equations for the lapse α and shift vector β^i. The lapse and shift are *gauge* functions which represent our freedom in choosing the coordinate system. When one solves the Einstein equations numerically, these gauge functions are chosen carefully to avoid coordinate (and physical) singularities and to cover the interesting regions of spacetime. In addition the lapse and shift must be chosen dynamically as functions of the evolving geometry, that is, one should choose the coordinates as one evolve the system. There are many standard choices for these gauges depending upon the method of solving evolution equations. The simplest choice is *geodesic slicing* where $\alpha = 1$ and $\beta^i = (0, 0, 0)$. Another choice called the *Maximal slicing* assumes $K = 0$ which makes the choice of lapse to be solution of $D^2\alpha = \alpha[K_{ij}K^{ij} + 4\pi(\rho + S)\,]$. One of the most successful gauge choice specifically for the *moving puncture* evolution of binary black hole system are *1+log*

$$(\partial_t - \beta^j \partial_j)\alpha = -2\,\alpha\, K \tag{3.63}$$

choice for the lapse and the *hyperbolic gamma driver* condition

$$\partial_t \beta^i = \frac{3}{4} B^i, \qquad \partial_t B^i = \partial_t \tilde{\Gamma}^i - \eta B^i, \tag{3.64}$$

for the shift vector, where $\tilde{\Gamma}^i = \tilde{\gamma}^{kl}\tilde{\Gamma}^i_{kl}$ and η is a constant of order $1/(2M)$. These gauge conditions can drive the coordinate system to being Cartesian (Minkowski) when spacetime is flat. A detailed analysis for the choices of lapse can be found in [157, 158] and recent attempts for the improvements can be found in [159].

In principle with the ADM evolution equations (3.44) and (3.45) for $\gamma_{ij}$and K_{ij} and choosing appropriate gauge conditions for α and β^i one can solve the equations on a computer. However, this is not the case as it is impossible to do so due to following reasons. First of all there are instabilities in the ADM system that amplifies small errors in the constraints which are numerically always present and secondly, gauge functions can also lead to coordinate singularities. We will discuss appropriate gauge conditions below, however the core issue with the ADM system is that it is only weakly hyperbolic and hence numerically unstable [160]. A lot of efforts have been put to reformulate these ADM equations into a system of strongly hyperbolic evolution equations. One such effort to make ADM equations (3.44) and (3.45) stable is by using a conformal factor $\phi = \frac{1}{12}\ln\gamma$ that fixes the conformal metric $\tilde{\gamma}_{ij} = e^{-4\phi}\gamma_{ij}$ to unit determinant $\tilde{\gamma} = 1$. The trace free extrinsic curvature is transformed in the same way $\tilde{A}_{ij} = e^{-4\phi}A_{ij}$. It is advantageous to evolve with variable $\chi = e^{-4\phi}$ [89]. With the definition $\tilde{\Gamma}^i = -\partial_i\tilde{\gamma}^{ij}$ and

$$\begin{aligned} R_{ij} = &-2\tilde{D}_i\tilde{D}_j\phi - 2\tilde{\gamma}_{ij}\tilde{D}^k\tilde{D}_k\phi + 4\tilde{D}_i\phi\tilde{D}_j\phi - 4\tilde{\gamma}_{ij}\tilde{D}^k\phi\tilde{D}_k\phi - \frac{1}{2}\tilde{\gamma}^{lm}\partial_l\partial_m\tilde{\gamma}_{ij} \\ &+ \tilde{\gamma}_{(i}\partial_{j)}\tilde{\Gamma}^k + \tilde{\Gamma}_k\tilde{\Gamma}^k_{(ij)} + \tilde{\gamma}^{lm}\left(2\tilde{\Gamma}^k_{l(i}\tilde{\Gamma}_{j)km} + \tilde{\Gamma}^k_{im}\tilde{\Gamma}_{klj}\right) \end{aligned} \tag{3.65}$$

We get the Baumgarte-Shapiro-Nakamura-Oohara-Kojima (BSSNOK) evolution formalism [161,

162, 163]

$$\partial_t \tilde{\gamma}_{ij} = -2\alpha + \mathcal{L}_\beta \tilde{\gamma}_{ij}, \tag{3.66}$$

$$\partial_t \chi = \frac{2}{3}\chi(\alpha_K - \partial_i \beta^i) + \beta^i \partial_i \chi, \tag{3.67}$$

$$\partial_t \tilde{A}_{ij} = \chi(-D_i D_j \alpha + \alpha R_{ij})^{\mathrm{TF}} + \alpha(K\tilde{A}_{ij} - 2\tilde{A}_{ik}\tilde{A}^k_j) + \mathcal{L}_\beta \tilde{A}_{ij}, \tag{3.68}$$

$$\partial_t K = -D^i D_i \alpha + \alpha\left(\tilde{A}_{ij}\tilde{A}^{ij} + \frac{1}{3}K^2\right) + \beta^i \partial_i K, \tag{3.69}$$

$$\begin{aligned}\partial_t \tilde{\Gamma}^i = {} & \tilde{\gamma}^{jk}\partial_j\partial_k\beta^i + \frac{1}{3}\tilde{\gamma}^{ij}\partial_j\partial_k\beta^k + \beta^j\partial_j\tilde{\Gamma}^i - \tilde{\Gamma}^j\partial_j\beta^i + \frac{2}{3}\tilde{\Gamma}^i\partial_j\beta^j \\ & -2\tilde{A}^{ij}\partial_j\alpha + 2\alpha\left(\tilde{\Gamma}^i_{jk}\tilde{A}^{jk} + 6\tilde{A}^{ij}\partial_j\phi - \frac{2}{3}\tilde{\gamma}^{ij}\partial_j K\right),\end{aligned} \tag{3.70}$$

where TF represent the trace free part. A related system known as the CCZ4 system [164], modifies the BSSN equations to include constraint damping by adding an additional evolved variable Θ. The

CCZ4 system is given by,

$$\partial_t \tilde{\gamma}_{ij} = -2\alpha \tilde{A}^{TF}_{ij} + 2\tilde{\gamma}_{k(i}\partial_{j)}\ \beta^k - \frac{2}{3}\tilde{\gamma}_{ij}\partial_k\ \beta^k + \beta^k \partial_k \tilde{\gamma}_{ij}\,, \tag{3.71}$$

$$\begin{aligned}\partial_t \tilde{A}_{ij} &= \phi^2 \left[-D_i D_j \alpha + \alpha\left(R_{ij} + D_i Z_j + D_j Z_i\right)\right]^{TF} + \alpha \tilde{A}_{ij}\left(K - 2\Theta\right) \\ &\quad -2\alpha \tilde{A}_{il}\tilde{A}^l_j + 2\tilde{A}_{k(i}\partial_{j)}\ \beta^k - \frac{2}{3}\tilde{A}_{ij}\partial_k\ \beta^k + \beta^k \partial_k \tilde{A}_{ij}\,,\end{aligned} \tag{3.72}$$

$$\partial_t \phi = \frac{1}{3}\alpha\phi K - \frac{1}{3}\phi \partial_k \beta^k + \beta^k \partial_k \phi\,, \tag{3.73}$$

$$\partial_t K = -D^i D_i \alpha + \alpha\left(R + 2D_i Z^i + K^2 - 2\Theta K\right) + \beta^j \partial_j K - 3\alpha\kappa_1\left(1 + \kappa_2\right)\Theta\,, \tag{3.74}$$

$$\begin{aligned}\partial_t \Theta &= \frac{1}{2}\alpha\left(R + 2D_i Z^i - \tilde{A}_{ij}\tilde{A}^{ij} + \frac{2}{3}K^2 - 2\Theta K\right) \\ &\quad -Z^i \partial_i \alpha + \beta^k \partial_k \Theta - \alpha\kappa_1\left(2 + \kappa_2\right)\Theta\,,\end{aligned} \tag{3.75}$$

$$\begin{aligned}\partial_t \hat{\Gamma}^i &= 2\alpha\left(\tilde{\Gamma}^i_{jk}\tilde{A}^{jk} - 3\tilde{A}^{ij}\frac{\partial_j \phi}{\phi} - \frac{2}{3}\tilde{\gamma}^{ij}\partial_j K\right) + 2\tilde{\gamma}^{ki}\left(\alpha\partial_k\Theta - \Theta\partial_k\alpha - \frac{2}{3}\alpha K Z_k\right) - 2\tilde{A}^{ij}\partial_j\alpha \\ &\quad +\tilde{\gamma}^{kl}\partial_k\partial_l\beta^i + \frac{1}{3}\tilde{\gamma}^{ik}\partial_k\partial_l\beta^l + \frac{2}{3}\tilde{\Gamma}^i\partial_k\beta^k - \tilde{\Gamma}^k\partial_k\beta^i + 2\kappa_3\left(\frac{2}{3}\tilde{\gamma}^{ij}Z_j\partial_k\beta^k - \tilde{\gamma}^{jk}Z_j\partial_k\beta^i\right) \\ &\quad +\beta^k\partial_k\hat{\Gamma}^i - 2\alpha\kappa_1\tilde{\gamma}^{ij}Z_j\,,\end{aligned} \tag{3.77}$$

$$\partial_t \alpha = -2\alpha\left(K - 2\Theta\right) + \beta^k \partial_k \alpha\,, \tag{3.78}$$

$$\partial_t \beta^i = fB^i + \beta^k \partial_k \beta^i\,, \tag{3.79}$$

$$\partial_t B^i = \partial_t \hat{\Gamma}^i - \beta^k \partial_k \hat{\Gamma}^i + \beta^k \partial_k B^i - \eta B^i\,, \tag{3.80}$$

where $f = 3/4$, $\tilde{\Gamma}^i = \tilde{\gamma}^{jk}\tilde{\Gamma}^i_{jk}$, $2\tilde{\gamma}^{ij}Z_j = \hat{\Gamma}^i - \tilde{\Gamma}^i$. Θ and $\tilde{\Gamma}^i$ are the new evolution variables. All of the constraint-related modes are damped when $\kappa_1 > 0$ and $\kappa_2 > -1$ [165]. For black hole spacetimes $\kappa_3 = 1/2$ [164]

3.2.4 Numerical Methods

There are various numerical methods that exists to solve the partial differential equations. The most popular ones include *finite differences* [166, 167, 168], *finite elements* [169, 170] , and *spectral methods*[171, 172, 173]. The basic idea of finite difference approximations is to describe the continuous space-time in terms of a discrete set of points. One simplification in this approach is to use evenly spaced points. One then substitutes the differential equations for a system of algebraic

equations using a low-order *Taylor series* expansion to compute approximations to the derivatives using neighboring grid points. This substitutions will then provides one algebraic equation for each differential equation per grid point. For large numbers of grid points, the final number of algebraic equations can be very large, particularly in three dimensions, which is why powerful computers are required for solving such problems.

Finite difference approximations are shown to be excellent methods to solve many computational physics problem but one must check for the consistency, convergence, and stability of the algorithm used. A fundamental result in the theory of finite difference approximations is the *Lax theorem*, which states that for a consistent approximation, stability and convergence are equivalent [166]. There is a simple condition that usually turns out to be necessary, and often also sufficient, for stability. This is known as the *Courant-Feiedrich-Lewy (CFL)* condition, and states that the time interval Δt must be smaller than the spatial interval Δx. This condition requires that the numerical domain of dependence must be larger than the domain of dependence of the differential equation. Without satisfying this condition, the numerical solution will not converge, as no matter whatever the size of the grid is, there would always be information that is left out of the numerical domain of dependence. An approximation is unstable if it is not convergent.

3.2.5 Geodesics in 3+1 form

In this thesis, we will use the dynamics of geodesics to probe the curvature of inspiralling binary black holes. Since we compute the numerical spacetime in a 3+1 framework, it is desirable to have a similar 3+1 split for the geodesic evolution equations. Null geodesics in this formalism have been studied in great details with well defined computational algorithms as in [174, 175]. Recently a more general frame work for both time-like and null geodesics was worked out in [176]. For our purposes, we evolve *time-like geodesics* in a 3+1 formalism that can be used in numerical relativity simulations of binary black holes. Since the metric in 3+1 formalism can be written in terms of spatial metric γ_{ij}, lapse α and the shift vector β^i, we write the geodesics equations $u^\mu \nabla_\mu u^\nu = -1$ for

a particle with 4-velocity u^μ in terms of these quantities. The 4-velocity of geodesic is decomposed into a component tangent to the unit norm n^a and a spatial component V^a. That is,

$$u^\mu = \varpi n^\mu + V^\mu \,, \tag{3.81}$$

where $\varpi = \sqrt{1 + V^i V^j \gamma_{ij}}$ and $V^0 = 0$ (note that $V_i = u_i$ $[i = 1, 2, 3]$). The geodesic equation then gives

$$\begin{aligned} \frac{dx^i}{dt} &= -\beta^i + \frac{\alpha}{\varpi} V^i \,, \\ \frac{d\tau}{dt} &= \frac{\alpha}{\varpi} \,, \\ \frac{dV_i}{dt} &= -\varpi \alpha_{,i} - V_j \beta^j{}_{,i} + \frac{1}{2} V^j V^k \gamma_{jk}{}_{,i} \,. \end{aligned} \tag{3.82}$$

This form of the geodesic equation has the advantage that explicit time derivatives of the 4-metric are not needed for the evolution and the integration variable is t, which is the time coordinate used in the code.

3.2.6 Horizons

Black holes are characterized by the horizons surrounding them. One of most important application of geodesics (null) is to locate and analyze event horizon in numerical evolution of binary black holes. Several different notions of horizons exit in general relativity. *Event and apparent horizons* provide the key diagnostics for the presence and properties of black holes. In addition, the concepts of *isolated and dynamical horizons* serves as useful diagnostics in numerical spacetimes of binary black holes. A complete study of numerical algorithms and codes for horizons in numerical spacetime of binary black holes can be found [145, 177, 178, 179, 174, 180, 181, 182] . Here we are providing definitions for the purpose of completeness.

The *event horizon* of an asymptotically flat spacetime is defined as the boundary between those events from which a future-pointing null geodesic can reach future null infinity, and those events

from which no such geodesic exists. It is a continuous null surface in spacetime. Event horizon describes a global property of the entire spacetime and cannot have any local definition in time. For a numerically computed spacetime the event horizons must be found in a separate post-processing phase *after* (part of) the spacetime has been numerically computed. Three algorithms exists for finding event horizons, based respectively on integrating null geodesics *forwards* in time, integrating null geodesics *backwards* in time, and integrating null *surfaces* backwards in time. The last of these method has been shown to be generally the most efficient and accurate method.

An *apparent horizon*, in contrast to an event horizon, is defined *locally* in time on a spacelike slice. It can be found during the numerical computation of a spacetime. To define apparent horizons one need to first define a marginally trapped outer surface. A marginally trapped outer surface is a smooth closed 2-surface in a spatial slice whose future-pointing outgoing null geodesics have zero expansion Θ. An apparent horizon is defined as a marginally trapped outer surface not contained in any other marginally trapped outer surface. This condition can be expressed as a nonlinear elliptic partial differential equation for the surface shape, the spatial metric γ_{ij}, its spatial derivatives $\partial_k \gamma_{ij}$, and the extrinsic curvature K_{ij} as coefficients. There are a large number of algorithms that are in use to compute the apparent horizons in a numerical relativity simulation.

3.2.7 Handling Black-hole Singularities

Black hole spacetimes are vacuum solutions of Einstein's equations, so the simulation of these systems has the advantage of not having to deal with hydrodynamics. However, black holes have singularities, and dealing with them in a numerical solution is far from trivial. Mathematically, a singularity represents a boundary of the domain where certain field values diverge. Physically, a singularity represents the break down of a theory and it is assumed that general relativity breaks down at singularity.

The traditional techniques to evolve black holes include the use of singularity avoiding gauge conditions, such as maximal slicing. Alternative methods have been proposed and are used for

successful simulations of binary black holes. The most often used methods include excision method [183, 184, 185, 186, 187, 188, 189, 190, 88, 191], puncture [192, 193, 194, 195, 189] and moving puncture techniques [89, 90, 196, 197, 157].

- **Excision** This method uses the idea that as nothing escapes an event horizon, one can cut out the part of the simulation domain inside the event horizon to avoid singularities.
- **Punctures** For this method one handles the divergent part of the evolved fields analytically.
- **Moving Punctures** This is one of the most successful method for the binary black hole evolution in numerical relativity. It based on the idea that as nothing escapes an event horizon, one can *violate* Einstein's equations inside the event horizon. One can either smooth out the solution inside the event horizon (for initial data), or can prevent singularity from forming via dissipation (during the time evolution).

3.3 Extractions of Gravitational Waves in Numerical Relativity

The extraction of numerical waveforms is one of the most important topic in numerical relativity. One of the prime motivation for numerical relativity simulations is to compute accurate gravitational waveforms from promising sources. These waveforms are used to compare with observational data from gravitational wave detector to get information about the sources. This comparison is helpful for the physical interpretation of the observed data, as well as increasing the likelihood of a detection significantly. However, the waveforms are not easy to extract accurately and it is a non-trivial problem. For gravitational wave detectors, asymptotic gravitational waveforms from the sources are required to be located at large distance of the order of 10^{19}M (of the order mega parsec) away from the sources. Numerical relativity codes solve the Einstein equations on a foliation of spatial hypersurfaces that extend to an outer boundary of the computational domain typically $\sim 1000M$ from the black holes. Different techniques are then used to compute gravitational waveform at asymptotic infinity from the data provided by a Cauchy evolution. The details can be

found in a recent review [198].

One of the traditional methods for gravitational waveform extraction is based on *Regge-Wheeler and Zerilli formalism* [199, 200, 201]. This method is based upon the theory of perturbations of a Schwarzschild spacetime and further improved by Moncirief [202], known as the *gauge invariant Moncirief formalism*. The first step is the assumption that far from the sources, the spacetime metric can be described by perturbations of a Schwarzschild metric, $g_{\mu\nu} = g^{\rm Sch}_{\mu\nu} + h_{\mu\nu}$. Then, using the standard linearization procedure(see Sec. 2.2.14) the metric split into a background and perturbative part. The perturbative part of the metric is split into even and odd parity parts and further decomposed in terms of spherical harmonics.

$$h_{\mu\nu} = \sum_{l=2}^{\infty} \sum_{m=-l}^{l} (h^{olm}_{\mu\nu} + h^{elm}_{\mu\nu}) \tag{3.83}$$

The decomposition into spherical harmonics involve scalar, vector and tensor spherical harmonics [203, 204]. For each mode we can form a gauge-invariant *Moncirief function* that satisfies a certain wave equations [199, 200, 201] usually called the *Regge-Wheeler equation* for odd parity and *Zerilli equation* for even parity functions. From these functions one can then extract gravitational radiation. First of all the two gravitational wave polarization is split into even and odd parity parts.

$$h_+(t, r, \theta\phi) = h^{(\rm e)}_+(t, r, \theta\phi) + h^{(\rm o)}_+(t, r, \theta\phi) \tag{3.84}$$

$$h_\times(t, r, \theta\phi) = h^{(\rm e)}_\times(t, r, \theta\phi) + h^{(\rm o)}_\times(t, r, \theta\phi) \tag{3.85}$$

These are then expressed in terms of gauge invariant Moncirief functions at spatial infinity $r \to \infty$.

$$h^{(\rm e)}_+ - \iota\, h^{(\rm e)}_\times = \frac{1}{r} \sum_{l=2}^{\infty} \sum_{m=-l}^{l} \sqrt{\frac{(l+2)!}{(l-2)!}}\, R_{lm}(t, r)\, {}_{-2}Y_{lm}(\theta, \phi), \tag{3.86}$$

$$h_{+}^{(o)} - \iota\, h_{\times}^{(o)} = \frac{-\iota}{r}\sum_{l=2}^{\infty}\sum_{m=-l}^{l}\sqrt{\frac{(l+2)!}{(l-2)!}}\, q_{lm}(t,r)\,{}_{-2}Y_{lm}(\theta,\phi), \tag{3.87}$$

where $q_{lm} = \int_{\infty}^{t} Q_{lm}(\tau, r)d\tau$, and R_{lm} and Q_{lm} are the Monciref functions.

The other method which is widely used is based upon the ψ_4 components of the Weyl tensor. In numerical simulations, ψ_4 can be obtained from 3+1 quantities via

$$\psi_4 = (-R_{ij} - K\, K_{ij} + K_{ik}\, K^{k}_{j} + \iota\epsilon^{kl}_{i}\nabla_k K_{lj})\bar{m}^i\bar{m}^j \tag{3.88}$$

where $\bar{m}^i$ is the spatial projection of the complex vector m^μ, which is one of the vector from a null tetrad. Far from a source, a gravitational wave is locally plane and ψ_4 is directly related to the metric perturbation in the TT gauge by

$$\psi_4 = \partial_t^2(h_{+} - \iota h_{\times}). \tag{3.89}$$

In an asymptotically flat spacetime using appropriate coordinates the peeling theorem [205, 206] shows that ψ_4 falls off as r^{-1}, that is why it is standard practice that gravitational waves are normally described not by ψ_4 but by $r\psi_4$ which should be evaluated in the limit as $r \to \infty$.

The above procedures lead to an estimate $r\psi_4$, but results are rarely reported in this form. Instead, spin-weighted spherical harmonics decomposition of ψ_4

$$\psi_4 = \sum_{l\leq 2, |m|\leq l} \psi_4^{lm}\,{}_{-2}Y^{lm} \qquad\qquad \psi_4^{lm} = \int_{S^2} \psi_4\,{}_{-2}Y^{lm}d\Omega, \tag{3.90}$$

is used and the $r\psi_4^{lm}$ are evaluated and reported. Although, normally, the dominant part of a gravitational wave signal is in the lowest modes with $l = 2$, the other modes are important to gravitational-wave data analysis. The desired output of a computation is a waveform (to be used,

say, in the analysis of LIGO detector data). We can use Eq. (3.89) to obtain gravitational wave polarization components $(h_+, h_\times)$ as

$$h_+^{lm}(t) - \iota\, h_\times^{lm}(t) = \int^t \left(\int^\tau \psi_4^{lm}(\lambda) d\lambda \right) d\tau + A^{lm} t + B^{lm}, \tag{3.91}$$

where the constants of integration A^{lm} and B^{lm} need to be fixed by the imposition of some physical condition, for example that the strain should tend to zero towards the end of the computation. While this procedure is simple and straightforward, in practice it has been observed that the double time integration may lead to a reduction in accuracy, and in particular may introduce nonlinear drifts into the waveform. It was shown in [207] that the presence random noise in ψ_4^{lm} can lead to noticeable drifts after a double integration. The usual procedure to control the effect is via a transform to the Fourier domain and other filtering techniques [208, 209, 110, 210, 207]. Finally another approach which is also useful and shown to give more accurate results is *Cauchy Characteristics Extraction* (CCE) [211, 212, 213] method. Recently a comparison was performed in [214] that shows the advantages of CCE over the other methods.

3.4 CACTUS and the EINSTEIN TOOLKIT

The *Einstein Toolkit* (ET) [215, 216, 217, 218] consists of quite a large number of routines widely used by the numerical relativity community [219, 220, 221, 222], which provides the basic modular infrastructure for numerical simulations. It provides support for a wide range of tools used to investigate black hole and neutron star initial data (TwoPunctures and Lorene), numerical evolution with BSSNOK and CCZ4 formalisms (LaZeV), relativistic magnetohydrodynamics (GRHydro and IllinoisGRMHD), method of lines and Runge-Kutta integration, unigrid and adaptive mesh refinement (the PUGH and Carpet drivers), black hole horizons (AHFinderDirect and EHFinder), parallelized computing (MPI and OpenMP), as well as large number of tools data handling and visualization (HDF5) tools.

The *Cactus* framework is an open source problem solving environment designed for scientists and engineers [223, 224]. Cactus allows us to implement our own thorns, giving us the ability to extend and incorporate modules that are already included. The source code can be written in C, Fortran, or using wrappers, OpenCL and CUDA being supported currently. In Cactus framework programs are split into components (called thorns) with clearly defined dependencies and interactions. Thorns are typically developed independently and should be interchangeable with others with same functionality. Cactus framework flesh which provides the "glue" between different thorns.

3.4.1 Some Important Thorns

Cactus separates physics code from infrastructure code. The CARPET mesh refinement driver provides a "moving boxes" style of adaptive mesh refinement (AMR) [225, 220, 226] which include Berger-Oliger style [227]. In this approach, refined grids of fixed size are arranged about the coordinate centers of both holes in numerical evolution of a binary black hole system. The CARPET code then moves these fine grids about the computational domain by following the trajectories of the two Black holes.

The *Two Puncture* thorn in Cactus framework is a very efficient pseudo-spectral code that computes puncture-type binary black hole initial data [228]. *AHFinderDirect* thorn finds black hole apparent horizons based on given spatial-metric γ_{ij} and extrinsic curvature K_{ij} [229, 230]. AHFinderDirect is very fast and accurate, but requires an initial guess for the apparent horizon position.

CHAPTER 4

HYBRIDIZING PRECESSING WAVEFORMS FOR LIGO DATA ANALYSIS

It is nature of all greatness not to be exact.

Edmund Burke

Gravitational waves will bring us exquisitely accurate maps of black holes- maps of their space-time. Those maps will make it crystal clear whether or not what were dealing with are black holes as described by general relativity.

Kip Thorne

4.1 Introduction

Coalescing black-hole binaries are among the most promising sources for the current and upcoming gravitational wave detectors, such as advanced LIGO, Virgo, KAGRA and LISA [231, 232, 80, 233, 234]. LIGO has already observed gravitational waves from merging compact binaries [65] and it will be observing more as its third observing run continues. There is an expectation that with current capabilities, gravitational wave detectors will observes 10 to 100s of binary black hole

mergers every year [235, 236, 237]; with binaries with a total mass of 100 times the mass of sun being observed at the distances of the order of giga parsecs [235].

The detection of gravitational waves requires theoretical waveform templates to match the observed data at the gravitational wave detector. This technique is called matched filtering, where, a theoretically generated waveform signal appropriate for a given source is cross correlated against the observed signals at the detector. Because the instrumental noise is a random process, a cross correlation will yield positive signature for any signal that matches the template within the detectable band, even if the signal is formally weaker than the noise. Having a bank of theoretically modeled waveforms that depends on the source parameters, such as the two masses, spins, sky location, orbital eccentricities etc., allows for parameter estimation techniques to be used to infer the properties of the systems that produced the waves [238].

To construct the theoretical templates, one needs to solve the Einstein field equations for generic binary black holes. Analytical weak-field approximation methods, such as post-Newtonian theory, can accurately describe the dynamics of such systems in the early inspiral phase prior to merger. Numerical relativity is crucial for the late inspiral to merger phases. Both of these techniques have been developed and shown to be very successful in the past decade [87, 239]. It has been shown that analytical model waveforms have similar accuracies to numerical ones for the early inspiral phase of binary black hole system but lose their accuracy when the binary separation is small. On the other hand, it is practically prohibitive to use numerical relativity for large binary separations, as the simulation time scales roughly as $T \sim D^4$. Because of the computational cost of numerical simulations, most numerical relativity simulations of generic precessing binaries cover relatively few orbits prior to merger. These numerical relativity waveforms can be fused together with analytical model waveforms covering the earlier stage of inspiral. Such fused waveforms are called *hybrid* waveforms.

Hybrid waveforms have many advantages. They combine the best part of two types of waveforms and can play an important role in the construction phenomenological waveforms [240, 241] and surrogate waveforms [242]. However, in order to combine two waveforms, one needs to find an optimal matching region such that the resulting hybrid is sufficiently accurate for parameter estimation and detection of gravitational waves.

The hybridization of post-Newtonian waveforms with numerical relativity waveforms has been performed for non-spinning binaries, as well as binaries where the spins are aligned or anti-aligned with the orbital angular momentum. These hybrid waveforms were then tested for their accuracies and limitations in Refs. [243, 244, 245, 246, 247, 248, 249, 250]. In previous LIGO analyses, non-precessing waveforms were used for extracting signals from data. However, recent studies have indicated that neglecting precession can significantly impact detections and parameter estimations in upcoming runs [251, 252, 253]. Thus having precessing waveforms is now crucial.

Hybridizing precessing waveforms is a complicated process in comparison to the hybridization of non-precessing waveforms. The reason is that the orbital precession strongly affects the gravitational waveforms by modulating both amplitude and phase. This produces a complex waveform that contains rich information about the binary's parameters. In addition, because the orbital plane precesses, one needs to *rotate* the analytical and numerical waveforms in to some standard frame before hybridizing. In addition, there are also a lack of accurate model waveforms for such configurations and work is in progress. On the other hand, the same precessing waveform in a co–precessing frame [254] (one that continually rotates the system so that the orbital plane is always aligned with the xy plane) has a much simpler form. We use the simplicity of the co-precessing waveform to aid in the hybridization procedure.

We construct our hybrids by aligning the analytic and numerical waveforms in a small time interval near the beginning of the numerical waveform by first rotating both waveforms such that the orbital planes are instantaneously aligned with the xy plane at the start if the interval. In doing this, we allow for an arbitrary time and phase shift between the two waveforms. While our

method is designed for precessing binaries, we also reproduce the hybridization results of [243] for non-precessing binaries, as well.

4.2 Techniques

We construct hybrid waveforms using analytical post-Newtonian waveforms for the early inspiral phase and numerical relativity waveforms for late inspiral to merger phases. Our method can be used for hybridization of other analytical model waveforms, too. To check the accuracy of hybrids we use either longer numerical waveforms for the same system, or a longer model waveforms, such as an effective one body waveform.

4.2.1 Waveform Data

We use TaylorT4 and Spin-TaylorT4 post-Newtonian waveforms [102, 111, 112, 97, 113, 114, 115, 116, 117, 96, 118]. These waveforms are obtained from the LALSuite [255] software package. The numerical waveforms are obtained from the SXS and RIT waveform catalogs [256, 257, 258]. In addition we also use effective one body [133] and surrogate waveforms [259] for both the construction of the hybrids and to asses the hybrid errors.

4.2.2 Hybridization Procedure

We hybridize waveform using the following optimization procedure. Starting with an initial guess for the time-offset between the two waveforms, we perform a fixed rotation to align the instantaneous orbital planes of the two waveforms at the beginning of some chosen hybridization interval. The remaining rotational freedom about the z axis is equivalent to a phase shift of the waveform. We then calculate the L^1 norm of the difference between the two waveforms in the hybridization interval. We find the time-shift and additional phase shift that minimizes this norm. Note that each time we chose a new time-offset, we re-align the waveform so that the two orbital planes agree at the beginning of the hybridization interval.

Co-Precessing frame

The dynamics of binary black holes is significantly affected by the spins of individual components. The details of how gravitational radiation is produced also depends on the spin of the two compact objects. The spin of a body thus imprints itself on the gravitational wave signal. When the spins of either one or both compact objects are not aligned with the orbital angular momentum, both the orbital plane itself and the individual spins will precess. This precession can impart interesting modulations on the gravitational-wave signal and the $\ell = 2$, $m = \pm 2$ modes are always dominant, as shown in Figure 4.1

Due to precession, the alignment required for hybridization is more complicated than a simple rotation about the z axis (and hence a simple phase factor). Thus the usual procedure for hybridization, as has been done in [243, 244, 245, 246, 247, 248, 249, 250], cannot work in general. We solve this problem using the above mentioned 3-dimensional rotation. It has been shown that precessing dynamics can be efficiently estimated via two independent procedures. In the first approach, described in [260], an optimization procedure is used to find the 3-dimensional rotation (at each time) that maximizes the magnitude of $\ell = 2$, $m = \pm 2$ modes. This effectively aligns the orbital angular momentum along the z-direction. The maximization is done using two Euler angles. The first Euler angle represents a rotation along the z-direction, the second represents a rotation along the y-direction. These two Euler angles can also be efficiently obtained in another approach, as described in [261], which uses a preferred direction $\hat{\mathrm{V}}$ aligned with the principal axes of a tensor $\left\langle \mathcal{L}_{(ab)} \right\rangle$. This tensor is defined by

$$\left\langle \mathcal{L}_{(ab)} \right\rangle = \frac{\sum\limits_{\ell m m'} h^*_{\ell m'} h_{\ell m} \left\langle \ell m' | \mathcal{L}_{(a} \mathcal{L}_{b)} | \ell m \right\rangle}{\int d\Omega |h|^2}, \tag{4.1}$$

where $\mathcal{L}_a$ is the rotation group generator and in the case of non-precessing binaries, the principle eigenvector of $\left\langle \mathcal{L}_{(ab)} \right\rangle$ is aligned with the orbital angular momentum. A practical formula for this

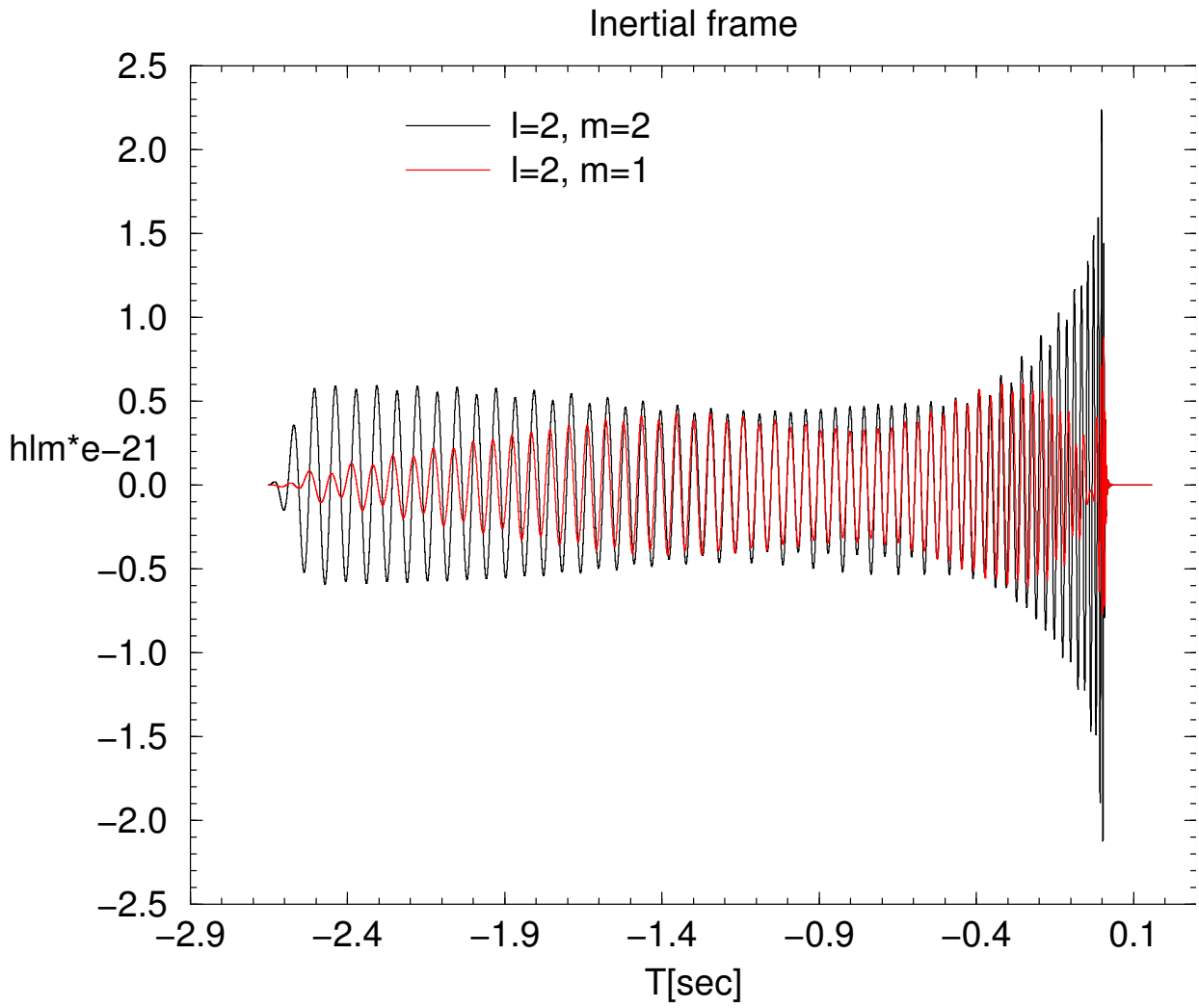

Figure 4.1: The real part of the $\ell = 2$, $m = 2$ and $\ell = 2$, $m = 1$ modes of a precessing binary black hole with $q = 5$, $\chi_1 = (0.5, 0, 0)$, $\chi_2 = (0, 0, 0)$. The $\ell = 2$, $m = 1$ mode contains significant energy and it is important to accurately model this mode for LIGO data analysis.

tensor involving the (ℓ, m) modes of h is given by

$$\left\langle \mathcal{L}_{(ab)} \right\rangle = \frac{1}{\sum_{lm} |h_{lm}|^2} \begin{bmatrix} I_0 + \mathrm{Re}(I_2) & \mathrm{Im}I_2 & \mathrm{Re}I_1 \\ \mathrm{Im}I_2 & I_0 - \mathrm{Re}(I_2) & \mathrm{Im}I_1 \\ \mathrm{Re}I_1 & \mathrm{Im}I_1 & I_{zz} \end{bmatrix} \tag{4.2}$$

where,

$$\begin{aligned} I_2 &\equiv \frac{1}{2} \langle h | L_+ L_+ | h \rangle \\ &= \frac{1}{2} \sum_{lm} c_{lm} c_{l,m+1} h^*_{l,m+2} h_{lm} \\ I_1 &\equiv \langle h | L_+ (L_z + 1/2) | h \rangle \\ &= \sum_{lm} c_{lm} (m + 1/2) h^*_{l,m+1} h_{lm} \\ I_0 &\equiv \frac{1}{2} \langle h | L^2 - L_z^2 | h \rangle \\ I_0 &= \frac{1}{2} \sum_{lm} [l(l+1) - m^2] |h_{lm}|^2 \\ I_{zz} &\equiv \langle h | L_z L_z | h \rangle = \sum_{lm} m^2 |h_{lm}|^2, \end{aligned}$$

with $c_{lm} = \sqrt{l(l+1) - m(m+1)}$.

Two of the Euler angles are related to the principal axes $\hat{V}$ of the orientation-averaged tensor $\left\langle \mathcal{L}_{(ab)} \right\rangle$ by

$$\alpha = \cos^{-1}[\hat{v}_z]$$

$$\beta = \mathrm{Arg}[\hat{v}_x + i\hat{v}_y] - \frac{\pi}{2}$$

The remaining Euler angle can be computed using the techniques of [254], which account for the

gradual buildup of transverse phase due to the orbital motion and is given by

$$\gamma = -\int \dot{\alpha} cos\beta \quad dt$$

Rotating the waveform using these Euler angles causes the $\ell = 2$, $m = \pm 2$ modes to become dominant. The resulting co-precessing modes are given by

$$h^R_{\ell m} = \sum_{m'} D^{\ell}_{mm'}(\alpha, \beta, \gamma) h_{\ell m}, \tag{4.3}$$

where the Wigner rotation matrix $D^{\ell}_{mm'}(\alpha, \beta, \gamma)$ is given by $D^{\ell}_{mm'} = d^{\ell}_{mm'}(\beta) e^{i(m\alpha + m'\gamma)}$ with $d^{\ell}_{mm'}(\beta)$ given by

$$\begin{aligned} d^{l}_{m'm}(\beta) =& \sqrt{(l+m)!(l-m)!(l+m')!(l-m')!} \\ & \times \sum_{k} \frac{(-1)^{k+m'-m}}{k!(l+m-k)!(l-m'-k)!(m'-m+k)!} \\ & \times (\sin\frac{\beta}{2})^{2k+m'-m} (\cos\frac{\beta}{2})^{2l-2k-m'+m}. \end{aligned} \tag{4.4}$$

In this rotating frame, the waveform modes behave very similar to those of a non-precessing binary system, as can be seen in Figure 4.2

The dynamics of the orbital plane in the two frames are shown in Figure 4.3. There, the two eigenvectors of $\langle \mathcal{L}_{(ab)} \rangle$ perpendicular to the principle one are plotted at each time-step. Since these two eigenvectors are orthogonal to the angular momentum direction, the resulting curves trace out the orbital plane.

We use fixed rotations to transform the waveforms into an instantaneously co-precessing frame at the start of the hybridization interval $H^{\rm rot}_{lm}(t) = \sum_{m'=-l}^{l} e^{im'\gamma + im\alpha} d^{l}_{mm'}(\beta) h_{lm}(t)$. Here, (α, β, γ) are angles at the fixed time, such that, at that time, the orbital planes associated with the two waveforms are aligned. It is important to note that the rotation angles are constant in time, thus the waveforms are still in an inertial frame.

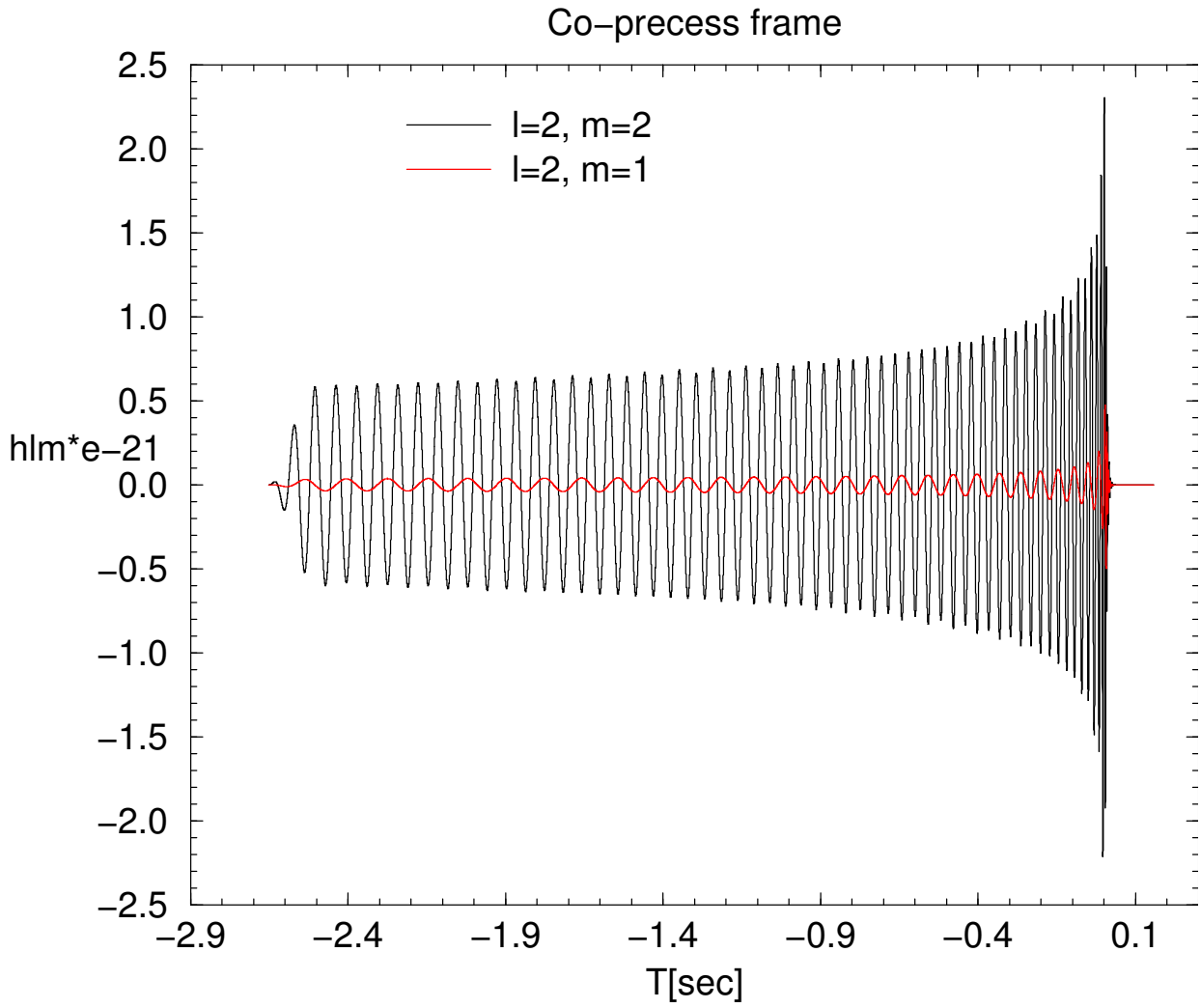

Figure 4.2: Co-precessing frame waveform for the same system shown in Figure 4.1. Here, we show the real part of $\ell = 2$, $m = 2$ and $\ell = 2$, $m = 1$ mode of a precessing binary black hole with $q = 5$, $\chi_1 = (0.5, 0, 0)$, $\chi_2 = (0, 0, 0)$. In the co-precessing frame the precessing binaries behaves like a non precessing binary with $\ell = 2$, $m = 2$ mode being the dominant mode of radiation.

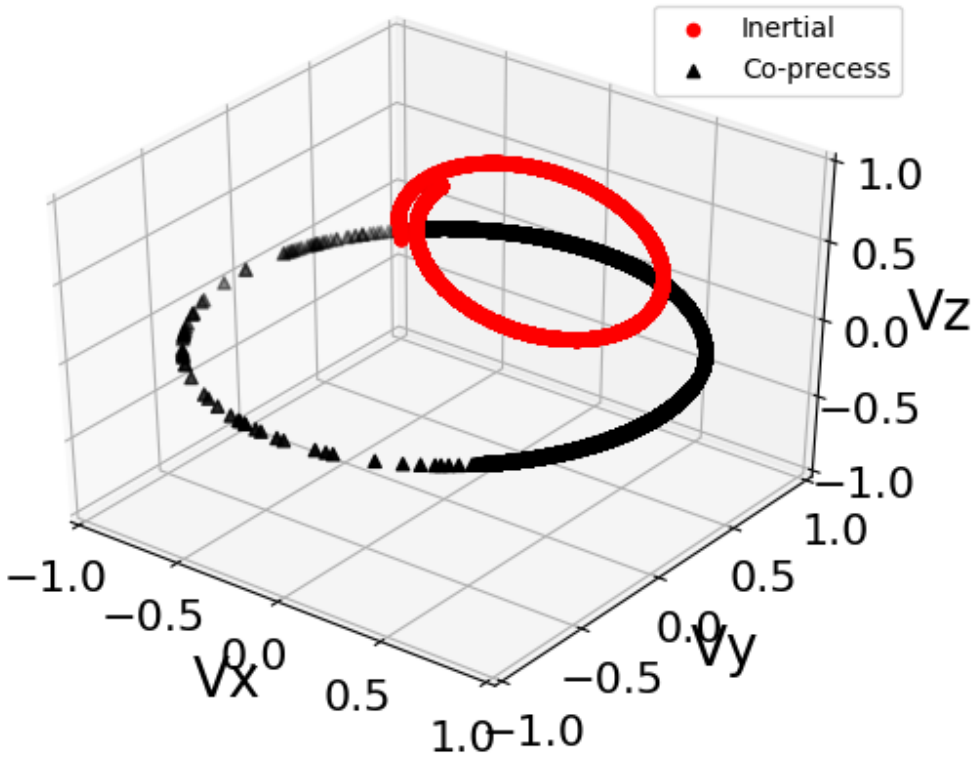

Figure 4.3: Orbital plane for a precessing binary black hole case with $q = 5$, $\chi_1 = (0.5, 0, 0)$, $\chi_2 = (0, 0, 0)$. The orbital plane is not aligned along the z-direction in the inertial frame so the waveform modes behave as shown in Figure 4.1. In the co-precessing frame, the orbital plane is aligned with the z-direction and the quadrupole mode becomes the dominant mode of radiation as shown in Figure 4.2. Here, we plot the two subdominant eigenvectors of $\langle \mathcal{L}_{(ab)} \rangle$ as proxies for the orbital motion.

Aligning the waveforms

The numerical and analytical waveforms are expressed in different gauges. Thus in addition to performing a 3-dimensional rotation to align the waveforms at a fixed time, we have the additional freedom of adding an arbitrary time translation and phase shift to either waveform. The choice of time translation can be chosen by aligning the frequency of two waveforms in an hybrid interval. We align the frequency of two waveforms at a reference frequency. The reference frequency is chosen to be the frequency of the numerical waveform at the start of hybrid interval. We then optimize over time translations and phase shifts using a *Nelder Mead downhill simplex minimization* algorithm, as implemented in Scipy[262]. In order to find the global minimum we optimize using several different initial guesses for the time shift (close to the one obtained from the co-precessing frame) and several choices for phase shifts in $[-\pi, \pi]$. The function we optimize is

$$\Delta = \min_{t_0,\phi_0} \int_{t_1}^{t_2} \sum_{l,m} \left| H_{lm}^{\rm NR}(t) - H_{lm}^{\rm PN}(t-t_0) e^{i(m\phi_0)} \right| {\rm dt}.$$

After optimizing for t_0 and ϕ_0, we taper the time domain waveform using a Planck window [210], and then zero-pad to the nearest power of two. The tapering at the start of the waveform is done to avoid Gibbs phenomena at the start of waveform. The tapering at the end is done right after the merger happen to avoid issues with errors in the numerical waveforms during the latter part of the ringdown phase.

Hybrid Construction

After obtaining the appropriate phase and time shifts, we construct the hybrid waveforms via

$$h_{lm}^{\rm hyb} = \tau(t) H_{lm}^{\rm NR}(t) + \left[1 - \tau(t)\right] H_{lm}^{\rm PN}(t - t_0') e^{i(m\phi_0')}, \tag{4.5}$$

where $\tau(t)$ is function that smoothly goes from 0 to 1 in the hybrid interval and is given by

$$\tau(t) = \begin{cases} 0 & t < t1 \\ \frac{1}{2}(1 + \cos\left(\frac{\pi(t-t1)}{(t2-t1)}\right) & t1 \leq t \leq t2 \\ 1 & t > t2 \end{cases} \tag{4.6}$$

4.2.3 Accuracy of Hybrid Waveforms

To verify the accuracy of our hybrid waveform we use the standard approach of calculating mismatches in the frequency domain. First, we define an inner product

$$\langle h_1|h_2\rangle = 2\int_{-\infty}^{\infty} \frac{h_1^*(f)h_2(f)}{S_n(f)}\mathrm{df} \tag{4.7}$$

where $h(f)$ is the Fourier transform of the complex waveform $h(t)$ and we use the Advanced-LIGO design sensitivity *Zero-Detuned-HighP* noise curve [263] with $f_{\min} = 20$Hz and $f_{\max} = 2000$Hz. This inner product can also be computed with a further maximization over time and phase shifts as described in [264]

$$\langle h_1|h_2\rangle = \underset{t_0,\phi_0}{max}\left[2\left|\int_{-\infty}^{\infty} \frac{h_1^*(f)h_2(f)}{S_n(f)}\mathrm{df}\right|\right] \tag{4.8}$$

The overlap of two waveforms is then given by

$$\mathcal{O} = \frac{\langle h_1|h_2\rangle}{\sqrt{\langle h_1|h_1\rangle \langle h_2|h_2\rangle}} \tag{4.9}$$

and the mismatch is given by

$$\mathcal{M} = 1 - \mathcal{O} \tag{4.10}$$

The mismatch indicates how close the two waveforms h_1 and h_2 are, with a mismatch of 0 indicating the two waveforms are essentially the same. If $\mathcal{M}$ is less than some threshold, we regard the final

hybrid as *accurate enough* for detections. For a maximum loss of 10% of the signals in the detection process, we can accept a mismatch of no more than 1.5 % [250] or even 0.5%, as suggested in [265].

It is important to note that we are computing this mismatch for each mode of hybrid and model waveform separately. Although from these modes one can construct the strain along any direction (ι,φ_0) in the binary's source frame by

$$h(t,\iota,\varphi_0) = \sum_{\ell=2}^{\infty}\sum_{m=-l}^{l} h_{lm}(t)\ {}^{-2}Y_{\ell m}(\iota,\varphi_0), \tag{4.11}$$

where ${}^{-2}Y_{\ell m}$ are the spin$=-2$ weighted spherical harmonics, ι is the inclination angle between the orbital angular momentum of the binary and line-of-sight to the detector, and φ_0 is the initial binary phase. φ_0 can also be thought of as the azimuthal angle between the $x-$axis of the source frame and the line-of-sight to the detector.

4.2.4 Results

We constructed hybrids for a few binary black hole systems with different properties. We show results for three cases. In order to hybridize our waveforms consistently, we perform all hybridizations on waveforms corresponding to binaries with a total mass of $M_{\rm tot} = 70M_{\odot}$. It is only after hybridizing that we rescale to different masses.

The first system we hybridized was a non-spinning binary system with mass ratio $q = 5$. Here we used the BBH0056 waveform from the SXS catalog [267] and the corresponding TaylorT4 approximant with PN terms up to 3.5 PN. We then hybridized a spinning, but non-precessing system, with $q = 3$ and $\chi_1 = (0, 0, 0.5)$ and $\chi_2 = 0$. Here we used the BBH0047 waveform from the SXS catalog [268] and both the SEOBNRv4HM and spin-TaylorT4 waveforms. Finally we hybridized a mildly precessing binary black hole system with $q = 1.513$ and initial spins $\chi_1 = (-0.3955, 0.229, 0.168)$ and $\chi_2 = (0.35401, -0.125, -0.253)$. The numerical waveforms for this system also came from the SXS catalog (BBH1392) [269]. In this case, we used the spin-TaylorT4 approximant with the same parameters. Below we show the numerical and analytical model waveforms before our hybridization

procedure and after it, and then compute the mismatch as function of total mass. The hybridization is done for the system with $M_{\rm tot} = 70M_{\odot}$. We analyze the waveforms and discuss different hybrid errors and issues in analysis section.

Case I: Non-spinning binary hybridization

We test our code on a simple non-spinning binary black hole system. We chose a binary black hole system with mass ratio $q = 5$ from the SXS catalog (BBH0056) and produced the corresponding post-Newtonian waveforms using the TaylorT4 approximant. We constructed hybrids of all modes except the $m = 0$ modes. To compute the mismatch we use the available modes of the same system using EOBNRv4HM modes which has the $\ell = 2\,, m = \pm 2$; $\ell = 2\,, m = \pm 1$; $\ell = 3,\,, m = \pm 3$; $\ell = 4\,, m = \pm 4$ modes. It has been found in previous works on hybridization [245, 242], that the phase of $\ell = 2, m = 2$ mode of EOB waveforms can be used to get improved post-Newtonian modes. We are planning to incorporate this improvement in the future. The resulting hybrid constructed using our method is shown in Figure 4.4, where we show the $\ell = 2$, $m = 2$ mode of waveforms before the alignment and after aligning them. We also plot the hybrid waveforms over the aligned waveforms to show how well the hybrid agrees with both of them. We show the mismatch of this hybrid against the EOB model waveforms with the same parameters in Figure 4.5, where we compute the mismatch with and without tapering the data.

We have hybridized all the available modes except the $m = 0$ modes and report the mode-by-mode mismatches in Table 4.1 (for total mass $M_{\rm tot} = 40M_{\odot}$). The mismatch of the $\ell = 4$, $m = 4$ mode is particularly large. As shown in Figure 4.6, the PN model amplitude for this mode has a large error. A better analytical model for this mode would yield a smaller mismatch.

Case II: Aligned-Spinning binary hybridization

In order to test our code with aligned spin binaries, we chose an SXS waveform (BBH0047) for a $q = 3$ binary with spins $\chi_1 = (0, 0, 0.5)$, $\chi_2 = (0, 0, 0)$. To construct the hybrid, we used the available modes of the SEOBNRv4HM model waveforms. The SEOBNRv4HM approximant

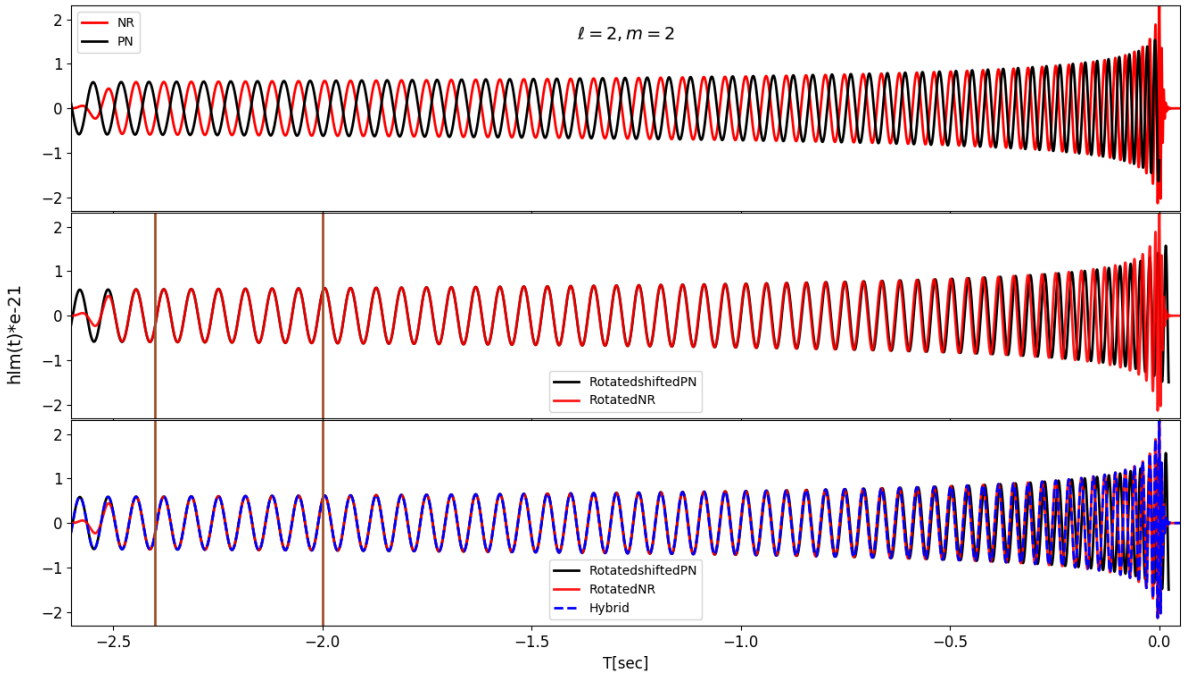

Figure 4.4: Case I: The $\ell = 2, m = 2$ modes of the numerical and PN waveforms. The top panel shows the waveforms before aligning them, the middle panel shows them after alignment, and the bottom panel shows the hybrid plotted over the aligned waveforms. The vertical lines shows the interval of hybridization. Here the total mass is $M_{\rm tot} = 70 M_{\odot}$.

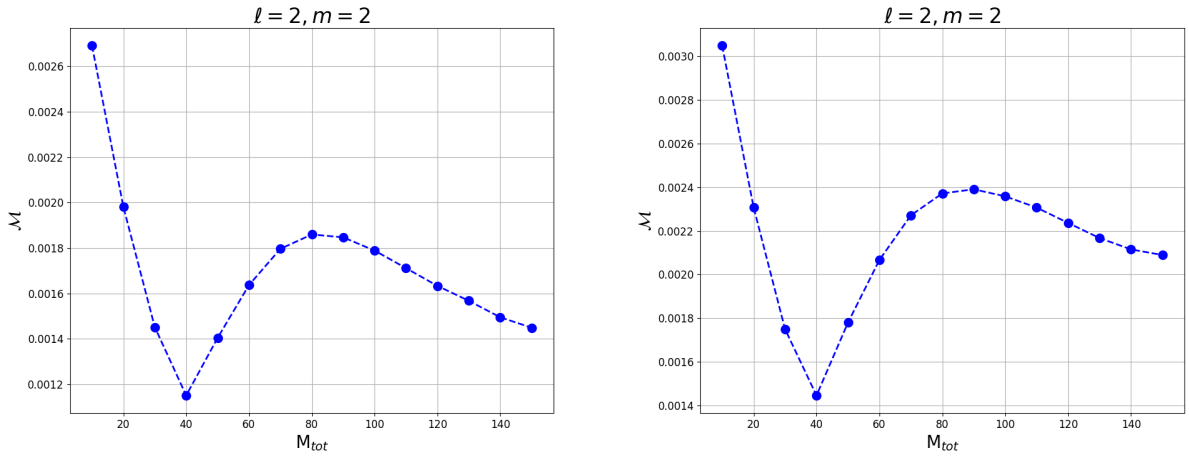

Figure 4.5: Case I: The mismatch for $\ell = 2$, $m = 2$ mode between post-Newtonian-Numerical hybrid and EOB waveforms. The same hybrid waveform (suitably rescaled for different masses) is used for all masses. We align the EOB waveform with the hybrid close to merger. The left panel shows the mismatch between the EOB and hybrid waveforms with tapering and the right panel shown mismatch without any tapering of data. There is very small difference in the mismatch with and without tapering in this case.

only has the $\ell = 2, |m| = 2$; $\ell = 3, |m| = 3$; $\ell = 4, |m| = 4$; and $\ell = 5, m = |5|$ modes. However, we did not use the $\ell = 5, m = \pm 5$ modes for our analysis. As in case I, we first show the $\ell = 2$, $m = 2$ modes before and after the alignment, as well as the hybrid, in Figure 4.7. It is important to note that the SEOBNRv4HM model waveforms match the numerical waveforms even at later times, which was not the case for the PN waveforms used in Case I. For the mismatch, we directly compare the hybrid with the full SEOBNRv4HM modes. Again for the dominant modes, we see that tapering the data has almost no effect on the mismatch, as can be seen in Figure 4.8. We also show the model and numerical modes after alignment in Figure 4.9. Unlike in case I, here the amplitudes of the model waveform agree very well with the numerical waveform. We report the mismatches for all these modes at $M_{\rm tot} = 40 M_{\odot}$ is shown in Table 4.2.

We also hybridized the same numerical waveforms with post-Newtonian waveforms. The post-Newtonian modes given by the spin TaylorT4 approximant. As before, we first show the $\ell = 2$, $m = 2$ modes before and after the alignment, as well as the hybrid in Figure 4.10. It is important

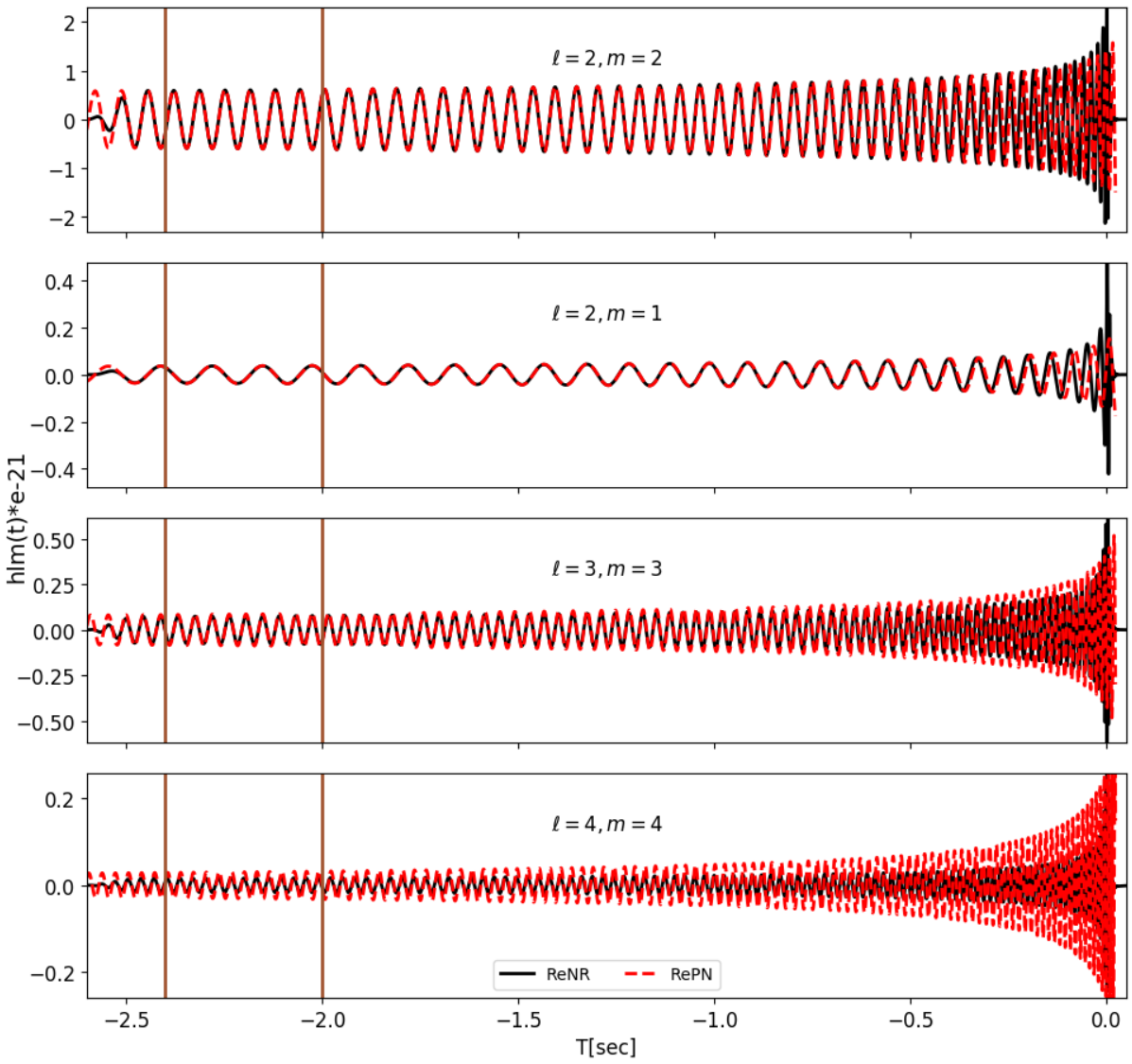

Figure 4.6: The PN and numerical modes for case I. These vertical lines show the hybrid interval where the two waveforms are aligned. The $\ell = 3, m = 3$ and $\ell = 4, m = 4$ post-Newtonian modes show substantial amplitude errors which likely leads to the large mismatch seen in Table 4.1. These waveforms corresponds to a system with $M_{\rm tot} = 70 M_{\odot}$.

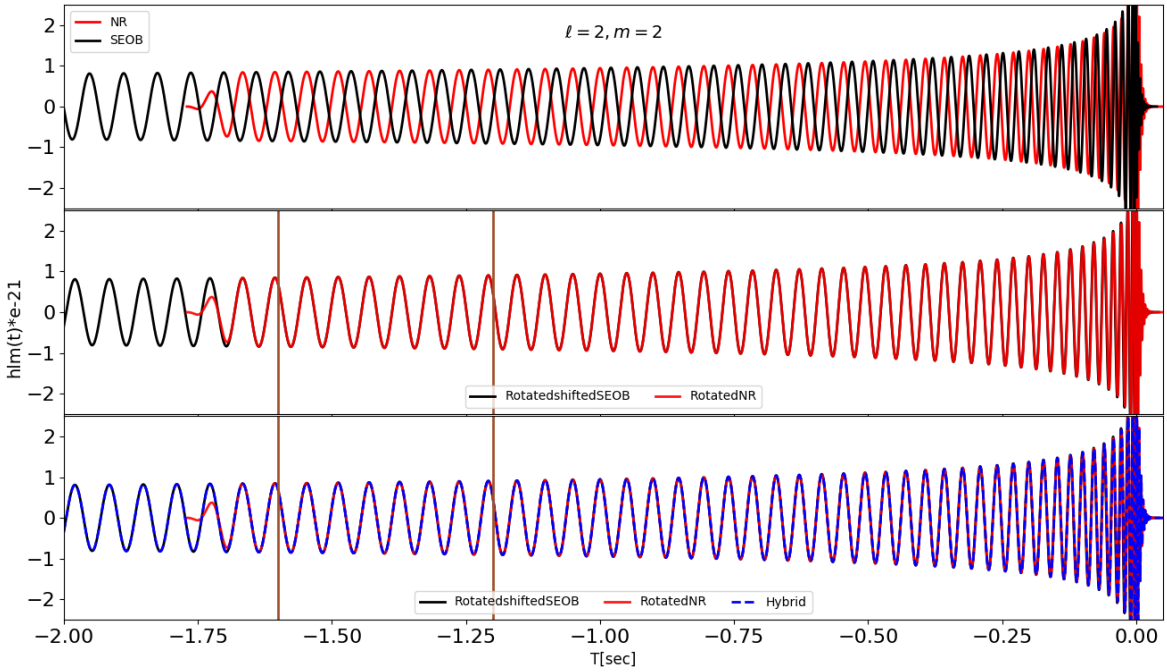

Figure 4.7: Case II: The $\ell = 2, m = 2$ modes of the numerical and SEOBNRv4HM waveforms. The waveforms correspond to $M_{\rm tot} = 70 M_{\odot}$. The top panel shows the waveforms before aligning them, the middle panel show after alignment of two waveforms, and the bottom panel shows the hybrid plotted over the two waveforms.The vertical lines shows the interval of hybridization.

Mismatch for all modes at $M_{\rm tot} = 40M_\odot$			
ℓ	m	$\mathcal{M}$ with taper	$\mathcal{M}$ No taper
2	2	0.001150	0.001445
2	1	0.000614	0.000694
3	3	0.005390	0.005664
4	4	0.042811	0.043508

Table 4.1: Mismatch for all modes at $M_{\rm tot} = 40M_\odot$ for case I. The mismatch for the $\ell = 4\,, m = 4$ is consistent with the large error in the PN waveform for this mode as seen in Fig. 4.6.

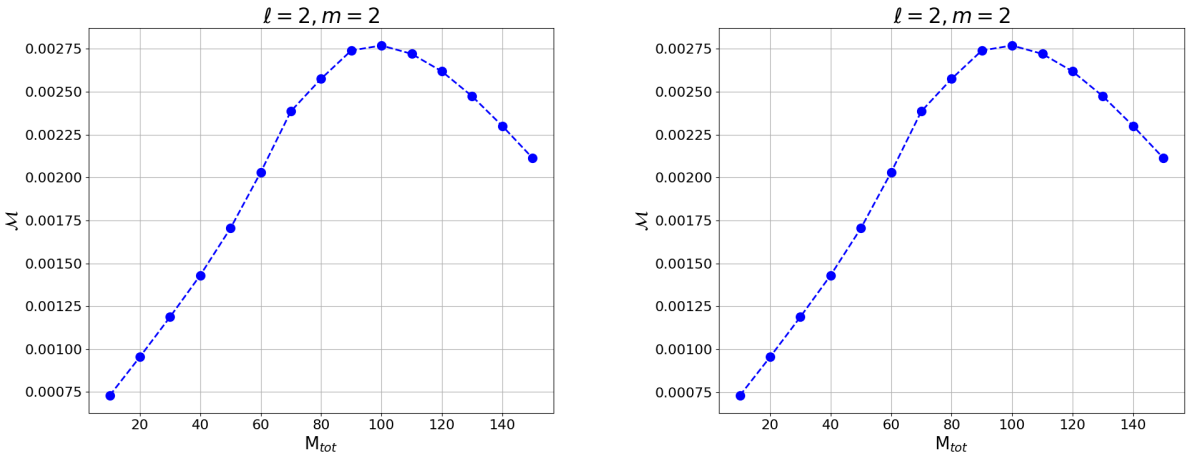

Figure 4.8: Mismatch for $\ell = 2$, $m = 2$ mode between SEOB-Numerical hybrid and SEOB waveforms. The same hybrid waveform (suitably rescaled for different masses) is used for all masses. We align the SEOB mode after the hybrid interval. The left panel shows the mismatch of two waveforms with tapering and the right panel shown mismatch without any tapering of data.

to note that unlike the SEOBNRv4HM model waveforms, which match numerical waveforms even at later times, the PN waveforms do not match as well. For the mismatch, we directly compare the hybrid with the full SEOBNRv4HM waveform. Again, for the dominant modes, we see that tapering of data has almost no effect on the mismatch, as can be seen in Figure 4.11. We also show the model and numerical modes after alignment in Figure 4.12. Unlike with hybrid of SEOB and NR, here the amplitudes of the PN waveform do not agree very well with the numerical waveform. We report the mismatches for all these modes at $M_{\rm tot} = 40M_\odot$ in Table 4.3.

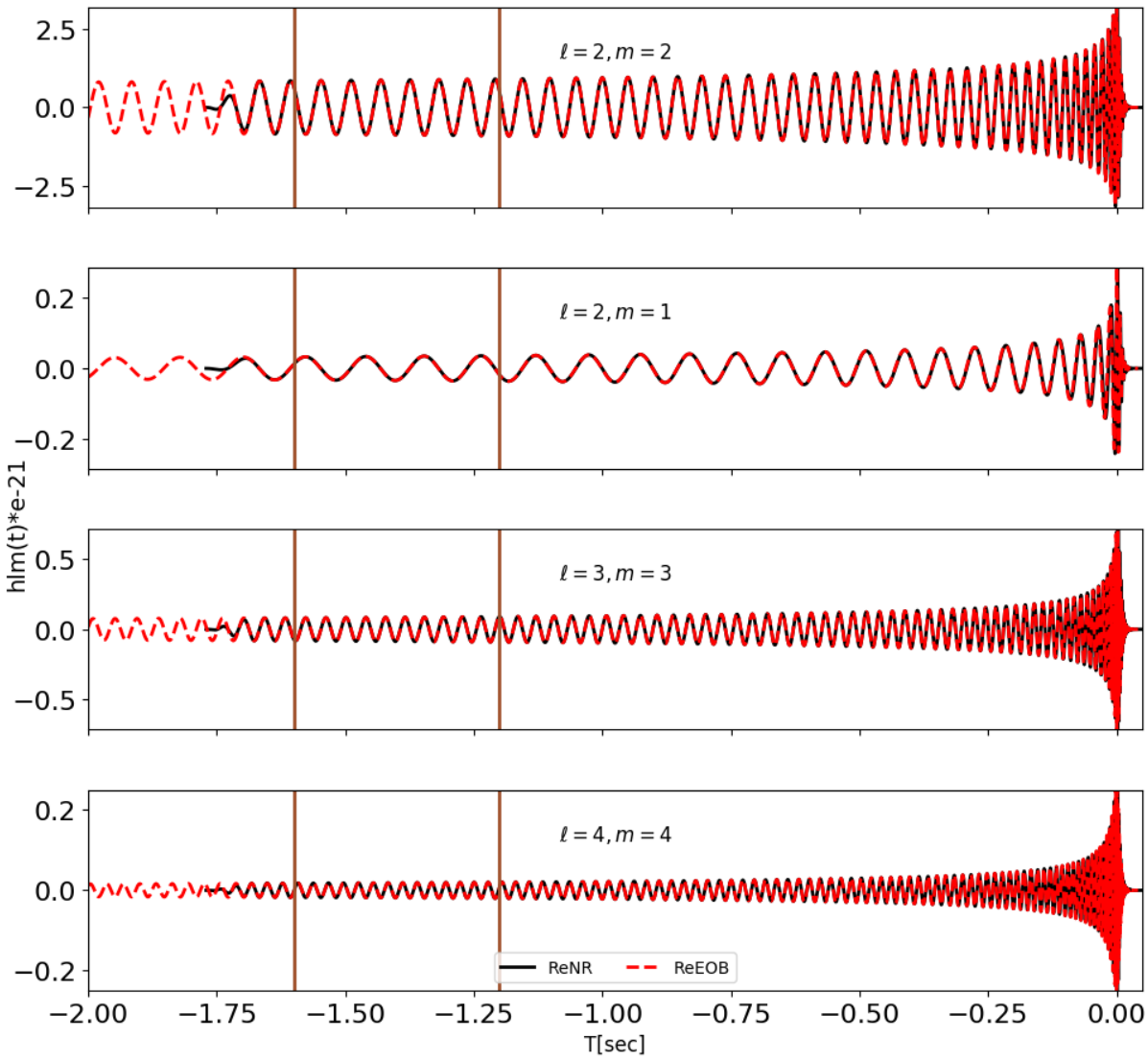

Figure 4.9: Case II: Hybridization of higher-order modes. The vertical lines show the hybrid interval where the two waveforms are aligned. The waveforms corresponds to a system with $M_{\rm tot} = 70 M_{\odot}$. It is important to note that, unlike for the post-Newtonian waveforms, the higher order SEOBNRv4HM waveform modes do match with numerical waveform modes in amplitude.

Mismatch for all modes at $M_{\rm tot} = 40M_{\odot}$			
ℓ	m	$\mathcal{M}$ with taper	$\mathcal{M}$ No taper
2	2	0.001431	0.001431
2	1	0.008181	0.008181
3	3	0.005372	0.005372
4	4	0.015548	0.015595

Table 4.2: Mismatch for all modes at $M_{\rm tot} = 40M_{\odot}$ for case II where the SEOB waveform is hybridized with the numerical one.

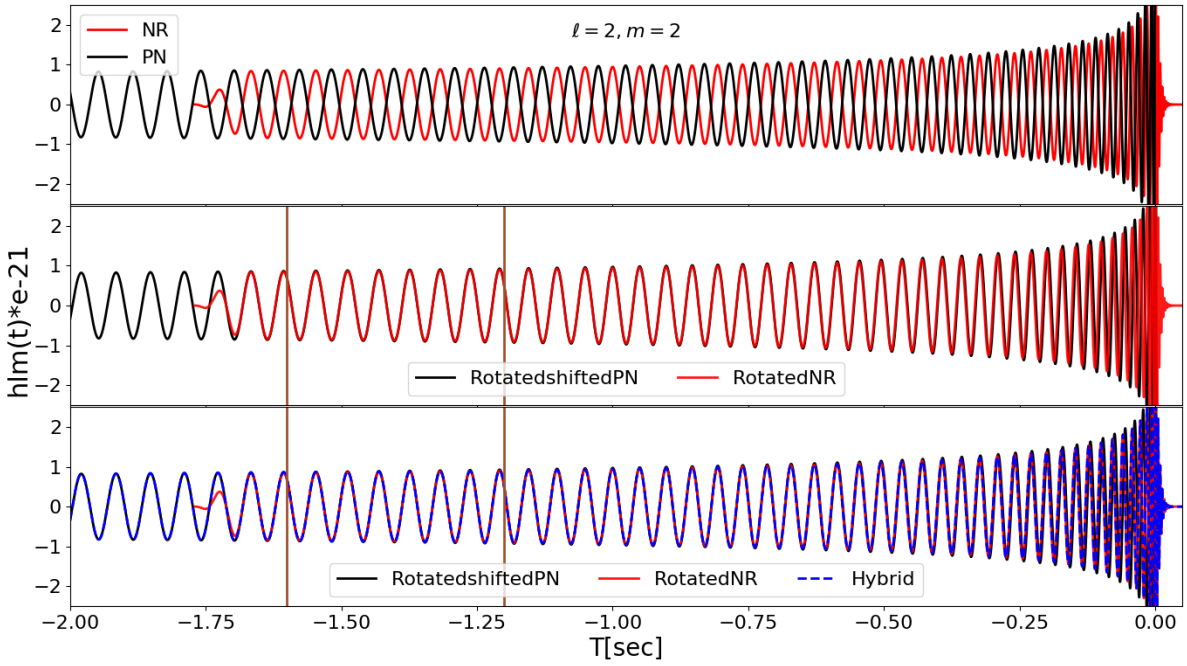

Figure 4.10: Case II: The $\ell = 2, m = 2$ mode constructed by matching the PN model waveform and numerical waveform. The waveforms corresponds to a system with $M_{\rm tot} = 70M_{\odot}$. The top panel shows the waveforms before aligning them, the middle panel show after alignment of two waveforms and the bottom panel shows the hybrid over plotted to the aligned waveforms. The vertical lines shows the interval of hybridization.

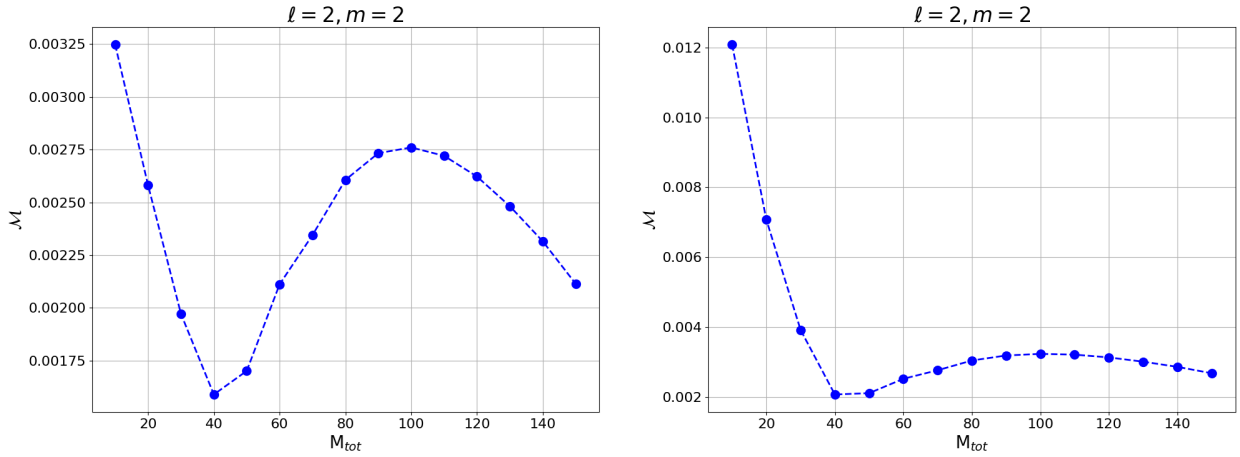

Figure 4.11: Mismatch for $\ell = 2$, $m = 2$ mode between PN-Numerical hybrid and SEOB waveforms. We align the SEOB mode close to merger after the hybrid interval. The hybridization is performed for system with $M_{\rm tot} = 70M_{\odot}$. The same hybrid waveform (suitably rescaled for different masses) is used for all masses. The left panel shows the mismatch of two waveforms with tapering and the right panel shown mismatch without any tapering of data.

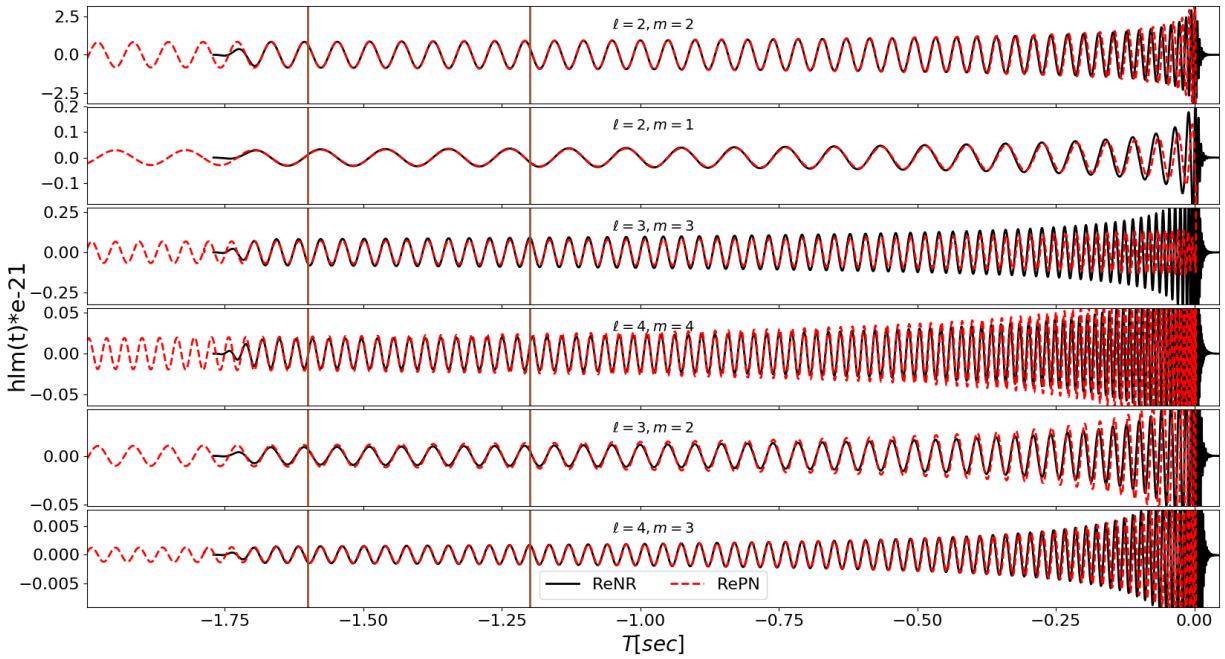

Figure 4.12: Case II: Hybrid waveform modes constructed by matching numerical and PN approximant modes. The vertical lines show the hybrid interval where the two waveforms are aligned. The waveforms corresponds to a system with $M_{\rm tot} = 70M_{\odot}$.

Mismatch for all modes at $M_{\rm tot} = 40M_{\odot}$			
ℓ	m	$\mathcal{M}$ with taper	$\mathcal{M}$ No taper
2	2	0.0015893610191042296	0.0020683631286622095
2	1	0.008080318715053991	0.008274795989216877
3	3	0.007721014519344593	0.008654262953824765
4	4	0.018574182966042074	0.02005533414828664

Table 4.3: Mismatch for all modes at $M_{\rm tot} = 40M_{\odot}$ for case II where the PN waveform is hybridized with the numerical one.

Case III: Precessing binary hybridization

Finally we tested our code with a mildly precessing waveform. Here, we use a very long SXS waveform (BBH1392) with $q = 1.513$, and initial spin parameters $\chi_1 = (-0.3955, 0.229, 0.168)$ and $\chi_2 = (0.35401, -0.125, -0.253)$. We hybridized in the late inspiral phase with the corresponding spin-TaylorT4 approximant. We use the longer numerical waveform to compute mismatch of the hybrid. In this case, the full numerical waveform is known for hundreds of cycles. Thus we can compare our hybrid directly with the full numerical waveform. To see the effects of precession, we show the $\ell = 2$, $m = 1$ mode of the waveform in Fig. 4.13. While there are SEOBNRv3 model waveforms available for precessing binaries, they are limited to the $\ell = 2$, $m = |2|$ modes only (we could hybridized these quadrupole modes with numerical waveforms and that may provide a more accurate hybrid of the quadrupolar modes). One limitations one must deal with is that in the precessing case is that the directions of the spins change with time. Thus one cannot use the values of the spins obtained at the start of the numerical waveform to generate the model waveform at earlier times. Rather, one needs to evolve the configuration backwards in time to obtain the correct spin parameters. This backwards in time integration is easily accomplished with the Taylor waveforms. We compute the mismatch of our post-Newtonian and numerical hybrid against the longer numerical waveform. The mismatch for the $\ell = 2$, $m = 2$ mode with and without tapering the two data sets is shown in Figure 4.14 and for the rest of the modes we show the mismatch in Table 4.14. Finally, we show the PN and numerical modes after alignment in Figure 4.15. Figure 4.15 shows significant amplitude oscillations in the higher-order modes due to precession. Interestingly, the PN modes appear to be quite accurate prior to $t = -1s$.

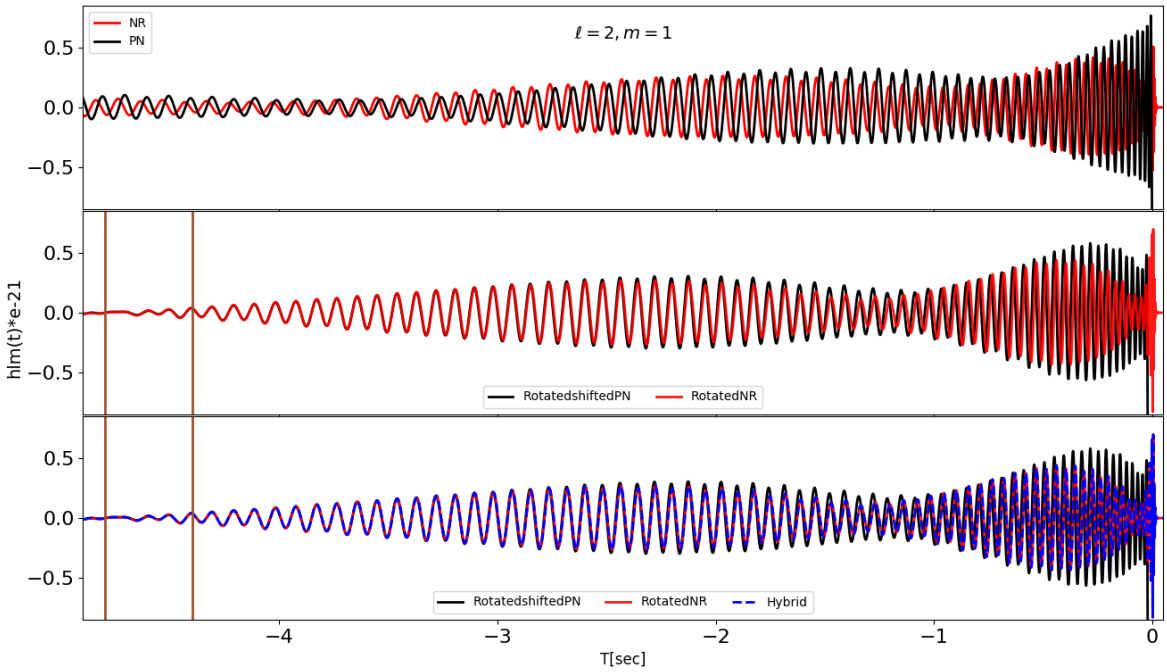

Figure 4.13: Case III: The $\ell = 2, m = 1$ mode constructed by matching spin-TaylorT4 approximant and Numerical waveforms. Both waveforms corresponds to systems with $M_{\rm tot} = 70 M_{\odot}$. The top panel shows the waveforms before aligning them, the middle panel show then after alignment, and the bottom panel shows the hybrid plotted over the two waveforms. The vertical lines shows the interval of hybridization.

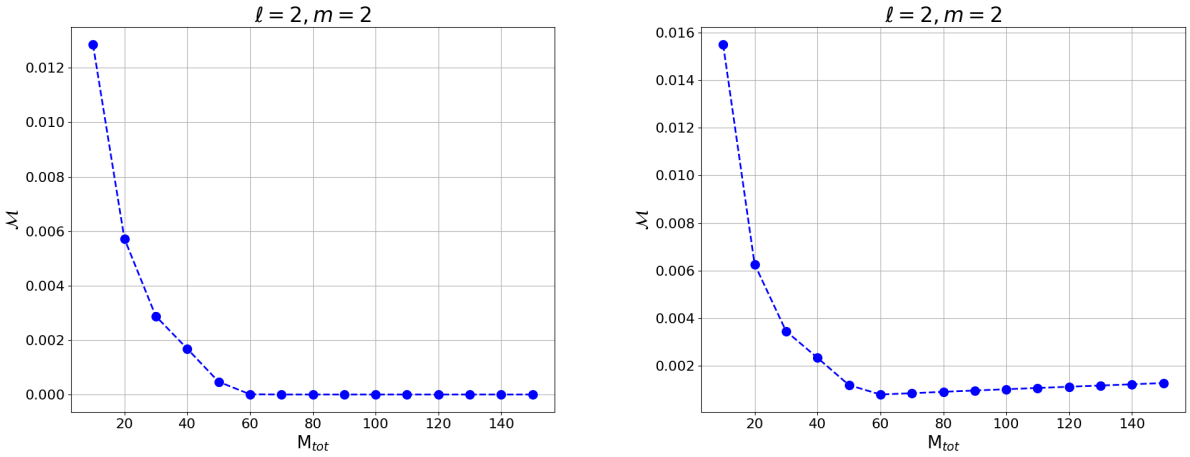

Figure 4.14: Case III: The mismatch for $\ell = 2$, $m = 2$ mode between Post-Newtonian-Numerical hybrid and the longer numerical waveforms. We align the two waveforms at merger. The same hybrid waveform (suitably rescaled for different masses) is used for all masses. The left panel shows the mismatch of two waveforms with tapering and the right panel shows the mismatch without any tapering of data. Here some differences due to tapering are seen for small masses.

Mismatch for all modes at $M_{\rm tot} = 40M_{\odot}$			
ℓ	m	$\mathcal{M}$ with taper	$\mathcal{M}$ No taper
2	2	0.0016834	0.0023262
2	1	0.0073402	0.0075215
3	3	0.0045283	0.0046313
4	4	0.0088217	0.0089692
3	2	0.0046323	0.0047383
4	3	0.0224526	0.0225117

Table 4.4: Mismatch for all modes at $M_{\rm tot} = 40M_{\odot}$ for case III.

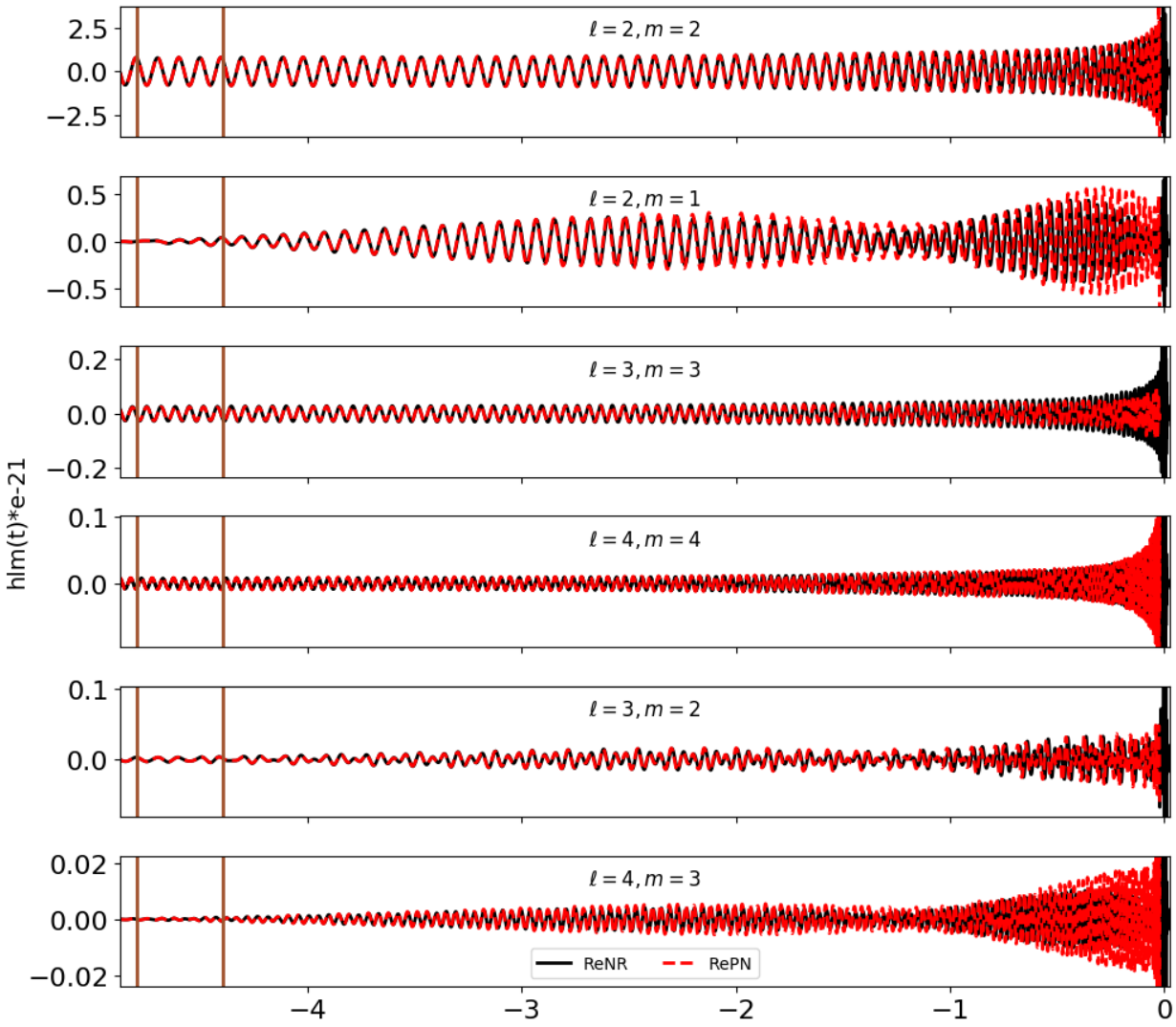

Figure 4.15: Case III: Hybrid waveform modes constructed by matching numerical and post-Newtonian spin-TaylorT4 approximant modes. The vertical lines show the hybridization interval where the two waveforms are aligned. The waveforms corresponds to a system with $M_{\rm tot} = 70 M_{\odot}$.

4.2.5 Analysis

Hybrid waveforms are susceptible to a wide range of errors. First of all, the numerical waveforms that are used can have accuracy issues due to numerical truncation errors. On the other hand post-Newtonian or model waveforms are approximations to solutions of the binary black hole problem in general relativity and thus have their own independent sources of errors based upon their respective approximations.

There are other hybridization errors that can occur due to the particulars of the procedures employed. These include the choices of time translation and phase shift, the start and length of hybrid interval, and the transition function used in the construction of hybrid itself. Thorough studies on hybrids and their errors were performed in [243, 245, 242, 246, 247, 249].

To explore these issues, we performed several diagnostics on our hybridization of the Case III waveform above. First, we computed the mismatch as a function of the length of the numerical waveform used. As the length of numerical waveforms gets smaller, the hybrid loses its accuracy. This is shown in Figure 4.16 below, where we show the mismatch for four different choices of hybridization intervals. It is important to note that these hybrid interval time corresponds to the waveforms with $M_{\rm tot} = 70M_{\odot}$. The resulting hybrid is suitably rescaled for different masses. It is clear that hybrids are more accurate if one uses longer numerical waveforms. Because our hybrid exactly matches the full numerical waveform at merger, and because we are calculating the mismatch of the hybrid with the full numerical waveform, the mismatch tends to zero for high masses (when only the merger phase is in band).

We also study how numerical errors in the waveform data affect the accuracy of the hybrid. We test this by using numerical waveforms for case III with two different numerical resolutions (Level 2 and Level 3). We use the same post-Newtonian waveforms to construct the hybrids. The mismatch is shown in 4.17 and it can be clearly seen that the higher numerical resolution improves the accuracy of hybrid waveform. A better analysis can be done by comparing the two hybrids with longer numerical waveforms at still higher numerical resolutions.

We also test how the precession dynamics can affect the hybridization accuracy. To analyze this,

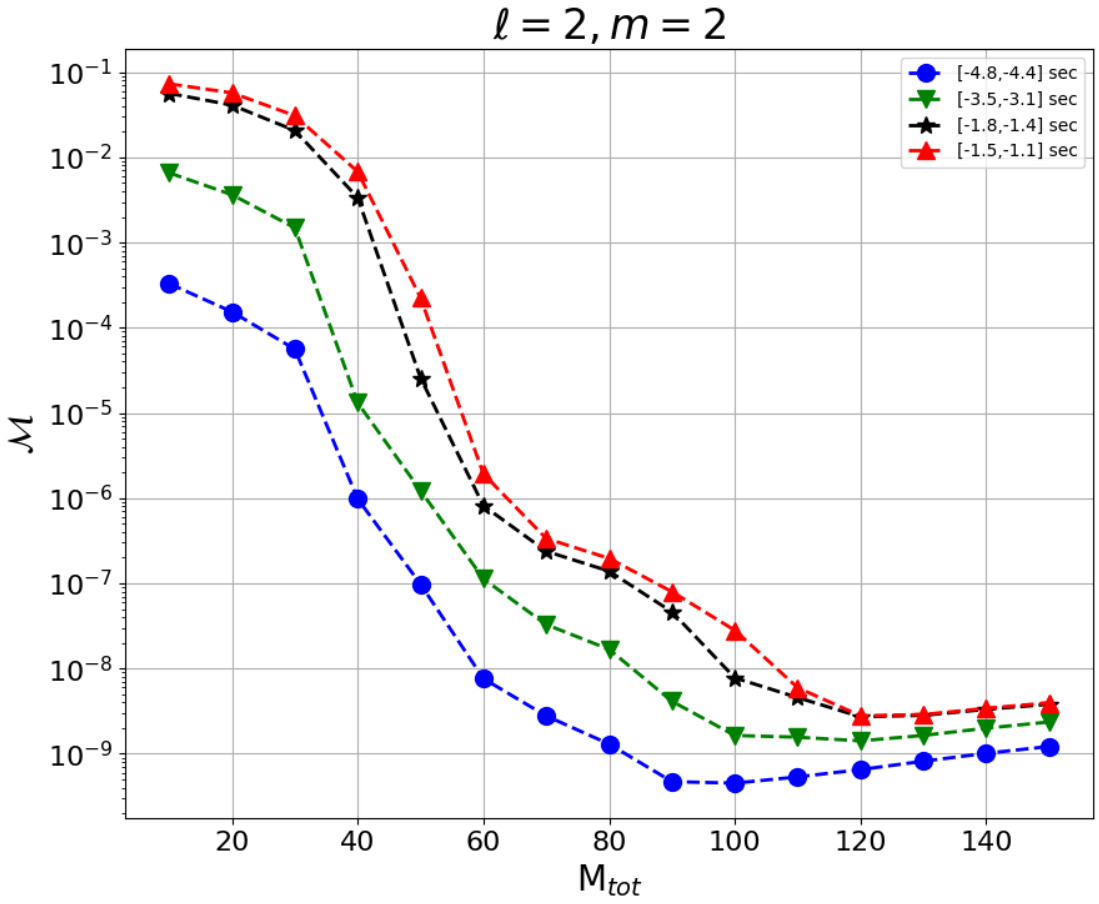

Figure 4.16: The mismatch of $\ell = 2, m = 2$ mode of the Case III hybrid waveform. We choose four different intervals for the hybridization to check the accuracy of hybrid as function of length of numerical waveform used to construct the hybrid. The hybrid interval time corresponds to a system with $M_{\rm tot} = 70M$. It is clear that the longer numerical waveform used, the smaller the mismatch.

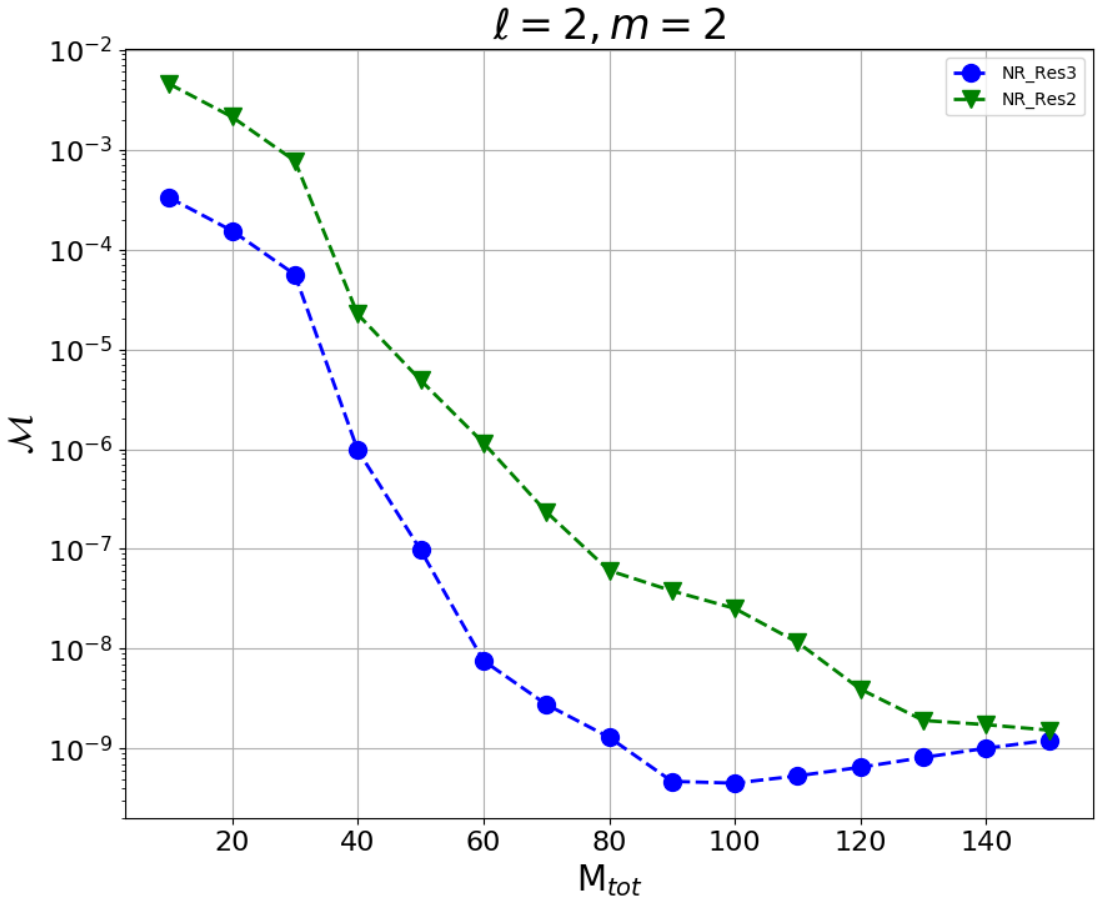

Figure 4.17: The mismatch of $\ell = 2$, $m = 2$ mode using numerical waveforms for case III with two different numerical resolutions. We use the same post-Newtonian waveforms to construct the hybrids. We separately hybridize the low and high resolution numerical runs. The hybridization interval is same in both cases. We see better agreement between the hybrid and numerical waveform for the higher resolution indicating that the numerical error is non-trivial here.

we first choose a hybrid interval in the early part of the waveform that contains a full precession cycle. Here again we chose waveforms corresponding to $M_{\rm tot} = 70M_{\odot}$. Figure 4.18 shows the various modes. With this much longer hybridization interval, we see poorer phase alignment of the $\ell = 2, m = 1$ mode. On the other hand, the remaining modes seem to be well aligned. As a further test, we reduced the hybrid interval to half of a precession cycle and then one fourth of a cycle. We show the results in Figures 4.19 and 4.20. We hybridize the waveforms using a very short, but very early, interval. For this latter test, we choose a hybrid interval of $(-12s, -11.5s)$ (again, for a system with total mass $M_{\rm tot} = 70M_{\odot}$). This hybrid interval contains a few cycles in the early part of precession cycle and is shown in Figure 4.21. We see very good alignment in all cases.

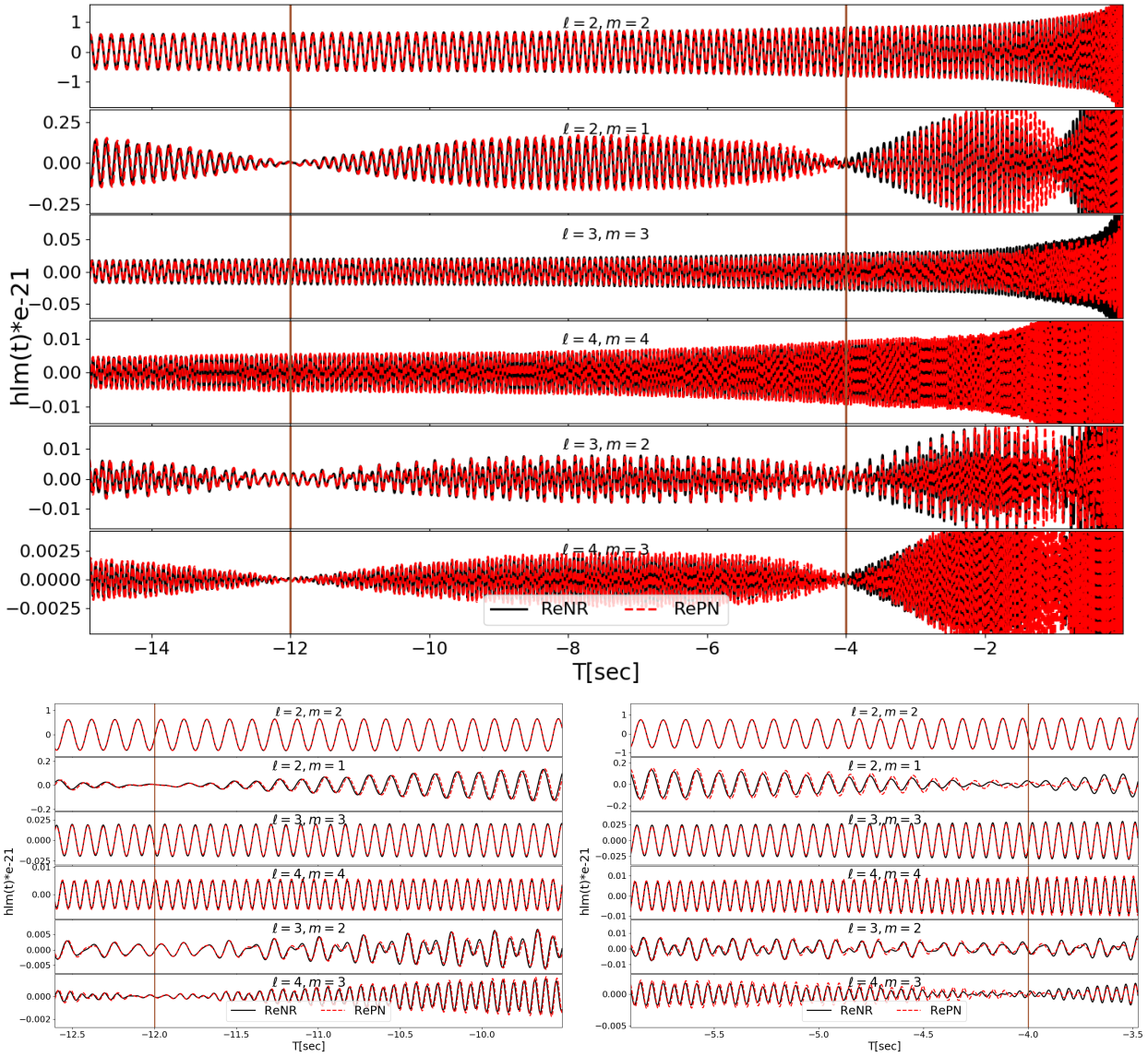

Figure 4.18: All modes of the full precession cycle test for case III. We use a full precession cycle for the length of the hybrid interval. All the modes except the $\ell = 2$, $m = 1$ mode show good alignment and this is more evident in the zoomed in plots on the lower left and right. It is important to note that we are using waveforms with total mass of $M_{\rm tot} = 70 M_{\odot}$.

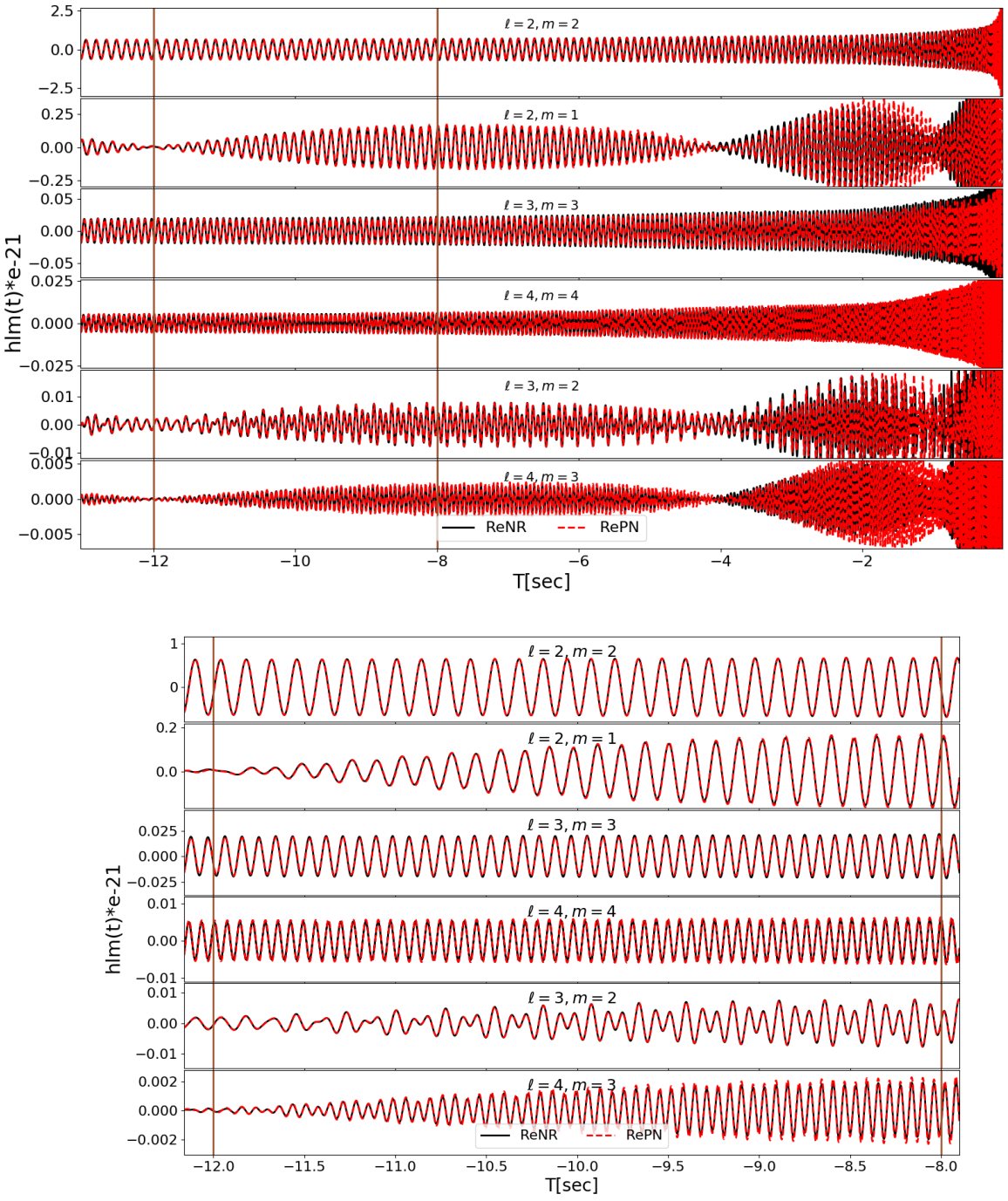

Figure 4.19: All modes of the half precession cycle test for case III. We use a half cycle of precession for the length of the hybrid interval. A zoomed in plot is shown on the bottom. It is important to note that we are using waveforms with total mass of $M_{\rm tot} = 70 M_{\odot}$.

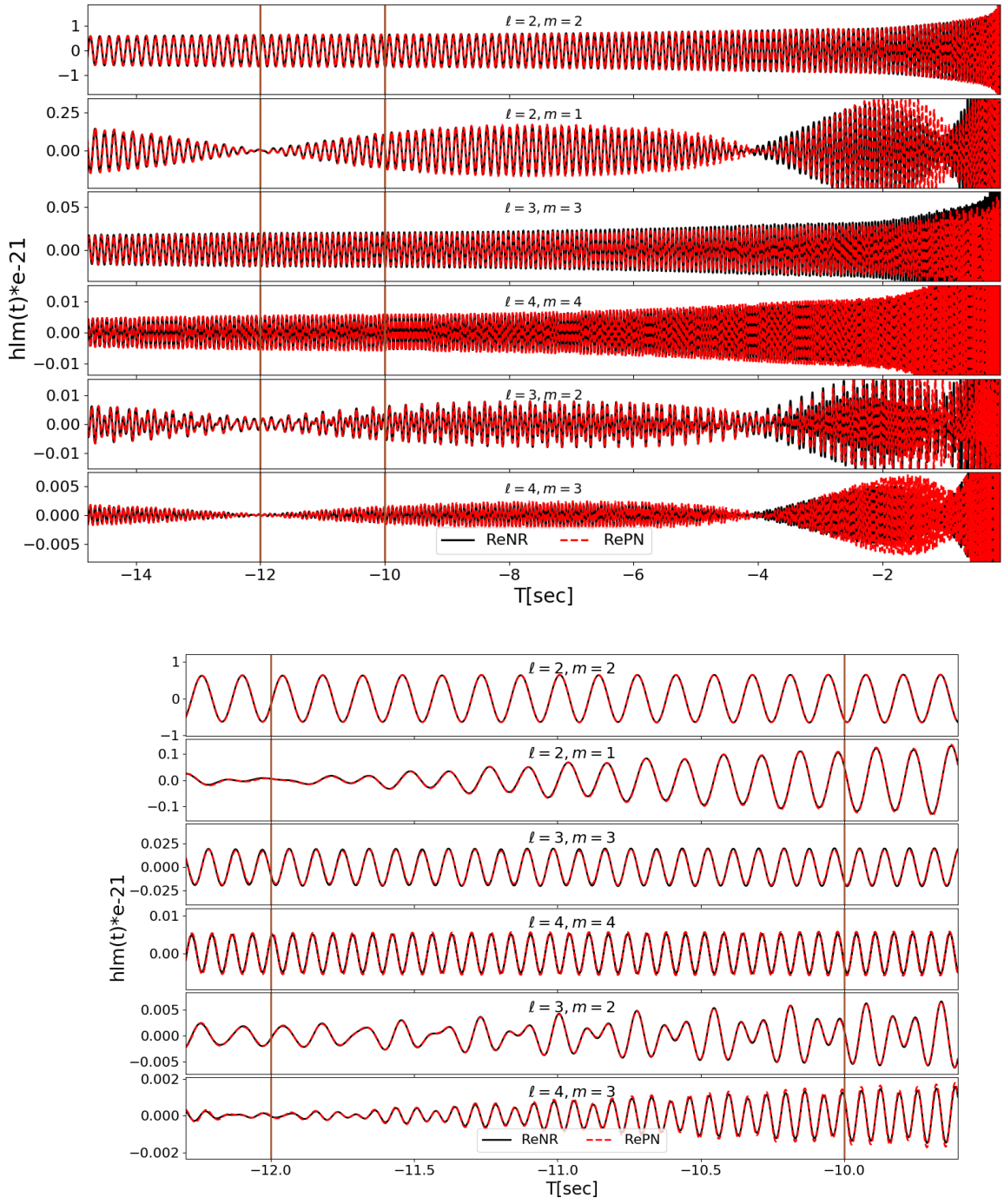

Figure 4.20: All modes of the quarter precession cycle test for case III. We use a quarter precession cycle as a length of hybrid interval. A zoomed in plot is shown on the bottom. It is important to note that we are using waveforms with total mass of $M_{\rm tot} = 70 M_{\odot}$.

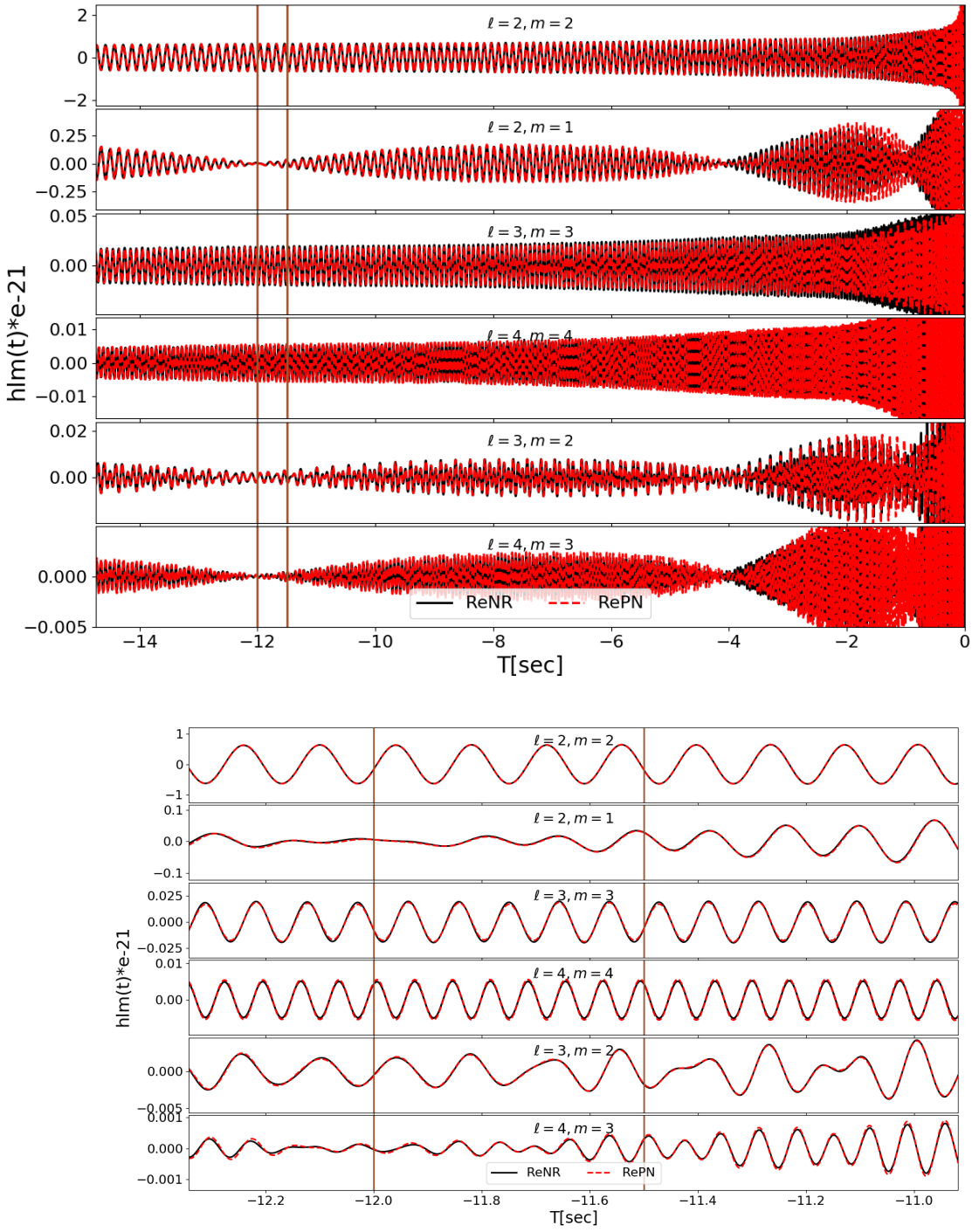

Figure 4.21: All modes of the short early hybridization interval test. We use a short interval, but at 12s (in units where the total mass is $70M_\odot$). A zoomed in plot is below. It is important to note that we are using waveforms with total mass of $M_{\rm tot} = 70M_\odot$.

4.3 Conclusion and Future Directions

We construct hybrid waveforms for binary black holes using analytical model waveforms for the early inspiral and available numerical relativity waveform for late inspiral to merger and post merger phases. Our goal is to hybridize waveforms for more generic precessing binaries and construct longer waveforms that are sufficiently accurate for the parameter estimation techniques for the detection of gravitational waves from upcoming LIGO observations. To hybridize, we align the two waveforms using a standard procedure with an additional rigid rotation to an instantaneous co-precessing frame. First we rotate the two waveforms so that the two orbital planes are aligned at the start of the hybridization interval. We then find appropriate time and phase translations that maximize the overlap of the two waveforms in the hybridization interval. We discuss the accuracy and limitations for such hybrids in the context of LIGO observations.

CHAPTER 5

COMPARING NUMERICAL AND ANALYTICAL SPACETIMES

If only it were not so damnably difficult to find exact solutions!

Einstein to Max Born

The popular mind, in all times and countries, has always tended to go by numbers in estimating the weight of evidence.

Wigmore on Evidence

Understanding the dynamical interactions of binary black holes (BBHs), as predicted by Einstein's theory of general relativity, has been a long-standing unsolved problem in theoretical physics. To obtain an exact solution of this problem one needs to solve Einstein's field equations (EFEqs) that describe the spacetimes from the infinite past of such system, when the black holes (BHs) were stars, to the infinite future when they settle to a single black hole. There is no exact solution for this problem, but different epochs are amenable to different approximations. There are two important parts of binary dynamics that are most relevant for astrophysics.

When the black holes in the binary are well separated and inspiralling and do not have strong gravitational and relativistic interactions, analytical approximate solution of the EFEqs have been

shown to give very accurate description of this system. These approximations include the post-Minkowskian and post-Newtonian approximations. Recent reviews of this important field can be found in [87, 270]. The first indirect evidence of gravitational waves from binary pulsars was tested by comparing the orbital evolution of the binary with these approximate analytical models [271, 272].

As the black holes in the binary get closer, strong gravitational effects kick in, and these approximate techniques lose their accuracy. The most relevant and interesting parts of the binary dynamics is when the BHs in the binary are in their late inspiral phase and then merge. Black hole perturbation theory can be used to understand the post merger dynamics of binaries analytically, and details of these studies are given in [134]. The late inspiral and merger of binary can only be studied accurately using numerical relativity. Numerical relativity is a mature field of study but it took decades of effort to solve BBH problem in numerical relativity. It now provides the most accurate known solution for BBH dynamics.

Ever since the breakthroughs in numerical relativity in the early 2000s [88, 89, 90], it has been possible to simulate BBHs for from the rapid inspiral phase, through the plunge and merger. Modern numerical relativity codes are now capable of simulating inspiralling BBHs for over 100 orbits [273]. These simulations are the most accurate known means of generating the gravitational waveform from such mergers. However, they are also computationally expensive. These numerical solutions can be used to tests the accuracy of analytical approximate solutions of the BBH problem for short evolutions of spacetimes during early inspiral phases of binary.

One astrophysically interesting problem relating to BBHs is the study of accretion physics around super massive BBHs. Understanding interactions of BBHs with the matter in the relativistic regime is important in understanding astrophysically interesting phenomenon, like disk structures and their electromagnetic emissions. Numerical relativity may be too expensive to study such binaries over very many orbits. Newtonian approximations break down as the binary gets closer and relativistic effects become important. But this problem can be studied by including relativistic effects using the analytical approximate solutions of Einstein's field equations that are valid to

describe different regions of spacetimes. Recently, a family of analytic metric representing the inspiral phase of a BBH was proposed and used extensively to study accretion physics [274, 275, 276, 277, 278, 279, 280, 281, 282]. This spacetime has been shown to be very useful for multi-messenger astronomy as in recent detailed study of relativistic prediction of electromagnetic emission from the surrounding gas of a supermassive BBH system approaching merger [283].

Although these spacetimes has been shown to give accurate results and their limitations have been studied, it is interesting to check the accuracy limitations of such spacetimes with a more generic and independent method. In this project, we introduce a new technique to study the accuracy of this family of BBH spacetimes by comparing them to full numerical evolutions starting from a set of fiducial separations. Our method is based on analyzing a set of scalars related to geodesic deviation. We compare the analytical and numerical spacetimes using curvature scalars associated with families of timelike geodesics. Because numerical evolutions are expensive, we evolve the spacetime for a short amount of time, but choose different initial separations and check how the analytical spacetime's accuracy changes with the binary separation. Since the two spacetimes differ also in coordinates, we compare gauge independent scalars that are related to geodesic deviations. These scalars are constructed using contractions of the components of Riemann tensor with a geometrically derived tetrad. The tetrad consists of the four velocity vector tangent to each geodesic and three other orthonormal vectors. Using these geometric scalars avoids any gauge differences of two spacetimes. This study complements previous studies in Ref. [277], where the hydrodynamics and magnetohydrodynamics of accreting gas were compared between versions of the analytical spacetime at different approximation orders.

In Sec. 5.1, we describe the analytical and numerical techniques used in this project. In Sec. 5.2, we present the tests we used to confirm the accuracy of our results. In Sec. 5.3, we describe the results of our study. In Sec. 5.4 we discuss the consequences and limitations of our study.

In this work we express tensors in both the more conventional coordinate basis and in orthonormal bases. Latin indices near the beginning of the alphabet are abstract tensor indices [14], which indicate the type of tensors involved in a calculation, as well as contraction. Latin indices near

the end of the alphabet denote coordinate-basis components of spatial tensors, while Greek letters denote 4-dimensional spacetime components in the coordinate basis. Components of tensors in an orthonormal basis (the first element of the orthonormal basis is always timelike) are denoted by a Greek or Latin letter surrounded by square braces. Whether associated with coordinate bases or orthonormal bases, Greek indices range from 0 to 3, while Latin indices near the end of the alphabet range from 1 to 3. We use the geometric unit system, where $G = c = 1$.

5.1 Techniques

5.1.1 Geodesic Analysis

The primary analysis in this project concerns how the fully nonlinear evolution of initial data based on the analytic metric differs from the analytic metric itself at some later time. In order to do this, we need gauge invariant measurements that can elucidate to what degree two spacetimes are locally similar.

To be precise, on some fiducial spatial slice Σ_0, which corresponds to a surface of constant coordinate time $t = t_0$, the induced metric and extrinsic curvatures of the analytic metric are used as initial data for a CCZ4 (conformal and covariant Z4 system) evolution. The CCZ4 system is advantageous for numerical evolution because it leads to the rapid suppression of the violations of the Hamiltonian and momentum constraints. Critical to our analysis, on Σ_0, the analytic and numerically evolved metrics are identical. Furthermore, if the analytic metric solved the vacuum Einstein equations, up to truncation error, the numerical and analytic metrics would only differ by a gauge transformation at all later times (at least in the domain of dependence on the initial numerical slice, which will be of finite extent).

The fact that gauges are identical on Σ_0 allows us to use geodesic dynamics to explore how the numerical and analytic spacetimes begin to differ with time. In particular, if we take as initial data for a timelike geodesic some given coordinate position and the spatial projection of the 4-velocity, V^a (from which we can reconstruct the full 4-velocity u^a at t_0 via $u^a = \sqrt{1 + \gamma_{ij} V^i V^j} n^a + V^a$,

where $V^0 = 0$ and n^a is the unit norm to Σ_0), and if the analytic metric solved the vacuum Einstein equations, the resulting geodesic, as calculated on the two metrics, would be geometrically identical. By this, we mean that the two geodesics would only differ by a gauge transformation. The question remains though, how do we show that geodesics in two different gauges are identical or not if the gauge transformation is unknown?

To address this question, we consider measuring curvature scalars along each geodesic as a function of proper time. Our construction of these scalars is as follows.

Let $u^a(\tau)$ be the 4-velocity associated with a geodesic (and hence unit norm). At each point along the geodesic construct an orthonormal basis $\{e^a_{[0]}, e^a_{[1]}, e^a_{[2]}, e^a_{[3]}\}$, where $e^a_{[0]} = u^a(\tau)$ and $e^a_{[\mu]} e^b_{[\nu]} g_{ab} = \eta_{[\mu][\nu]}$. The choice of components 1, 2, and 3 of this basis is arbitrary. Given any such basis, we can define a 3×3 symmetric matrix of scalars $\mathbf{M}$, where

$$\mathbf{M} = \begin{pmatrix} M_{[1][1]} & M_{[1][2]} & M_{[1][3]} \\ M_{[2][1]} & M_{[2][2]} & M_{[2][3]} \\ M_{[3][1]} & M_{[3][2]} & M_{[3][3]} \end{pmatrix}, \tag{5.1}$$

and

$$M_{[i][j]} = R_{abcd} u^a e^b_{[i]} u^c e^d_{[j]}, \quad i, j = 1, 2, 3\,. \tag{5.2}$$

Importantly, the eigenvalues of this matrix are independent of how $e^a_{[1]}$, $e^a_{[2]}$, and $e^a_{[3]}$ are constructed. This follows because any two choices $(e^a_{[1]}, e^a_{[2]}, e^a_{[3]})$ only differ by an orthogonal transformation (which preserves eigenvalues). Consequently, if the analytic metric and numerically evolved metric represented the same spacetime, the eigenvalues of $\mathbf{M}$ constructed this way on each metric would be identical. We will refer to these eigenvalues as *curvature eigenvalues* in the sections below.

Of course, the analytic metric, being an approximate solution, violates the vacuum field equations to some degree (see Refs. [276, 277] for a detailed analysis). Thus the analytic metric and its numerical evolution will differ to some level. Our goal here is to demonstrate a local measure of

how the two spacetimes actually differ. To do this, we note that the elements of $M_{[i][j]}$ have the interpretation of being the (negative of the) acceleration of deviation vector $e^a_{[i]}$ along the direction $e^b_{[j]}$. We can thus interpret relative differences in the curvature eigenvalues of $\mathbf{M}$ as proxies for the relative differences in the effective potentials experienced by timelike geodesics traversing these two spacetimes.

Initial Tests

We first compare an exact Schwarzschild spacetime with an approximate Schwarzschild spacetime. The Schwarzschild metric is given by

$$ds^2 = -\left(1-\frac{2M}{r}\right)dt^2 + \left(1-\frac{2M}{r}\right)^{-1} dr^2 + r^2\,d\theta^2 + r^2\,\sin^2\theta\,d\phi^2 \tag{5.3}$$

For an approximate Schwarzschild spacetime we replace the term $\left(1-\frac{2M}{r}\right)^{-1}$ with $1+\sum_{N=1}^{k}\left[\frac{2M}{r}\right]^N$

The agreement of two spacetimes is set by the number of terms, k, in the Taylor series expansion. We compute curvature scalars for the exact and approximate Schwarzschild spacetimes for stable timelike geodesics in circular orbits. These curvature scalars can be constructed analytically. We choose timelike geodesics with a tetrad constructed about u^a, the tangent to a stable circular orbit, and the other three orthonormal vectors are constructed using Gram Schmidt procedure. The resulting curvature scalars for Schwarzschild spacetime are given by

$$\mathbf{M} = \begin{pmatrix} \frac{(3M-2r)M}{(r-3M)r^3} & 0 & 0 \\ 0 & \frac{M}{r^3} & 0 \\ 0 & 0 & \frac{Mr^2}{r-3M} \end{pmatrix}, \tag{5.4}$$

For approximate Schwarzschild spacetimes, using $k = 1$, the curvature scalars are

$$\mathbf{M} = \begin{pmatrix} \frac{(3M-2r)M}{(r-3M)(r^2-4M^2)r} & 0 & 0 \\ 0 & \frac{M}{(r^2-4M^2)r} & 0 \\ 0 & 0 & \frac{Mr^2}{r-3M} \end{pmatrix}, \tag{5.5}$$

The relative difference between two scalars is given by $\frac{4M^2}{r^2-4M^2}$, while the other scalars are identical. We also compute the scalars with different k. We plot the results in Fig. 5.1. As expected, the two spacetimes differ more strongly for smaller values of k and close to the black hole.

We found that the curvature scalars are related to effective potential of two spacetimes. For the Schwarzschild spacetime the effective potential for timelike geodesics is given by

$$V_{\text{eff}} = \frac{1}{2}(E^2 - (1 - \frac{2M}{r})(1 + \frac{L^2}{r^2}))$$

For circular geodesics V_{eff} and its first derivative vanish identically, and $E^2 = \frac{(r-2M)^2}{r(r-3M)}$ and $L^2 = \frac{Mr^2}{r-3M}$ are respectively the energy and angular momentum for circular orbits. The second derivative of the potential is always non-zero. We can similarly compute the potential and its derivatives for the approximate Schwarzschild spacetime. The only difference between approximate and Schwarzschild spacetimes is one of the terms of metric, and this will have no effect on the energy and angular momentum for circular orbits. The effective potential for the approximate spacetime is given by

$$\tilde{V}_{\text{eff}} = V_{\text{eff}} \frac{g_{rr}}{\tilde{g}_{rr}}$$

where $g_{rr} = \frac{1}{1-\frac{2M}{r}} = \frac{r}{r-2M}$ and $\tilde{g}_{rr} = 1 + \sum_{N=1}^{k} \left[\frac{2M}{r}\right]^N$. But this extra factor will give different values for the second derivative of the effective potential. For the $k = 1$ case, we compute the second derivative of potential of two spacetimes. We then calculate the relative difference in the

second derivatives of effective potentials for two spacetimes and found that

$$\frac{\frac{d^2}{dr^2}(V_{\rm eff} - \tilde{V}_{\rm eff})}{\frac{d^2 V_{\rm eff}}{dr^2}} = \frac{4M^2}{r^2 - 4M^2}$$

This is exactly the same as the relative difference of curvature scalars for these two spacetimes. This clearly shows that curvature scalars represent the actual physical difference of two spacetimes. We also found that in general for any k related to the approximate Schwarzschild spacetime, the relative difference of curvature scalars and potential is given is

$$\frac{(2M)^{k+1}}{r^{k+1} - (2M)^{k+1}},$$

as in Fig. 5.1.

Limitation of Technique

One important limitation of our procedure is that because slightly different geodesics can, in principle, follow very different trajectories on secular timescales, our analysis will need to be done when the geodesics are relatively close to Σ_0. Otherwise, a small difference in the two spacetimes may incorrectly be interpreted as a large difference. We ameliorate this problem by only choosing geodesics that are *stable*. By this, we mean that the trajectories are largely insensitive to small perturbations of the initial velocity. As such, we do not include cases where small perturbations lead to the geodesic orbiting a different black hole, or ones where small perturbations lead to geodesics falling into either black hole.

Future Explorations

We also note that our analysis here can be extended in a straightforward manner to include all 20 independent components of the Riemann tensor. To do this, we would need the vectors $e^a_{[i]}$ $(i = 1, 2, 3)$ to obey $u^b \nabla_b e^a_{[i]} = 0$. That is, evolve the entire basis. Under this extended

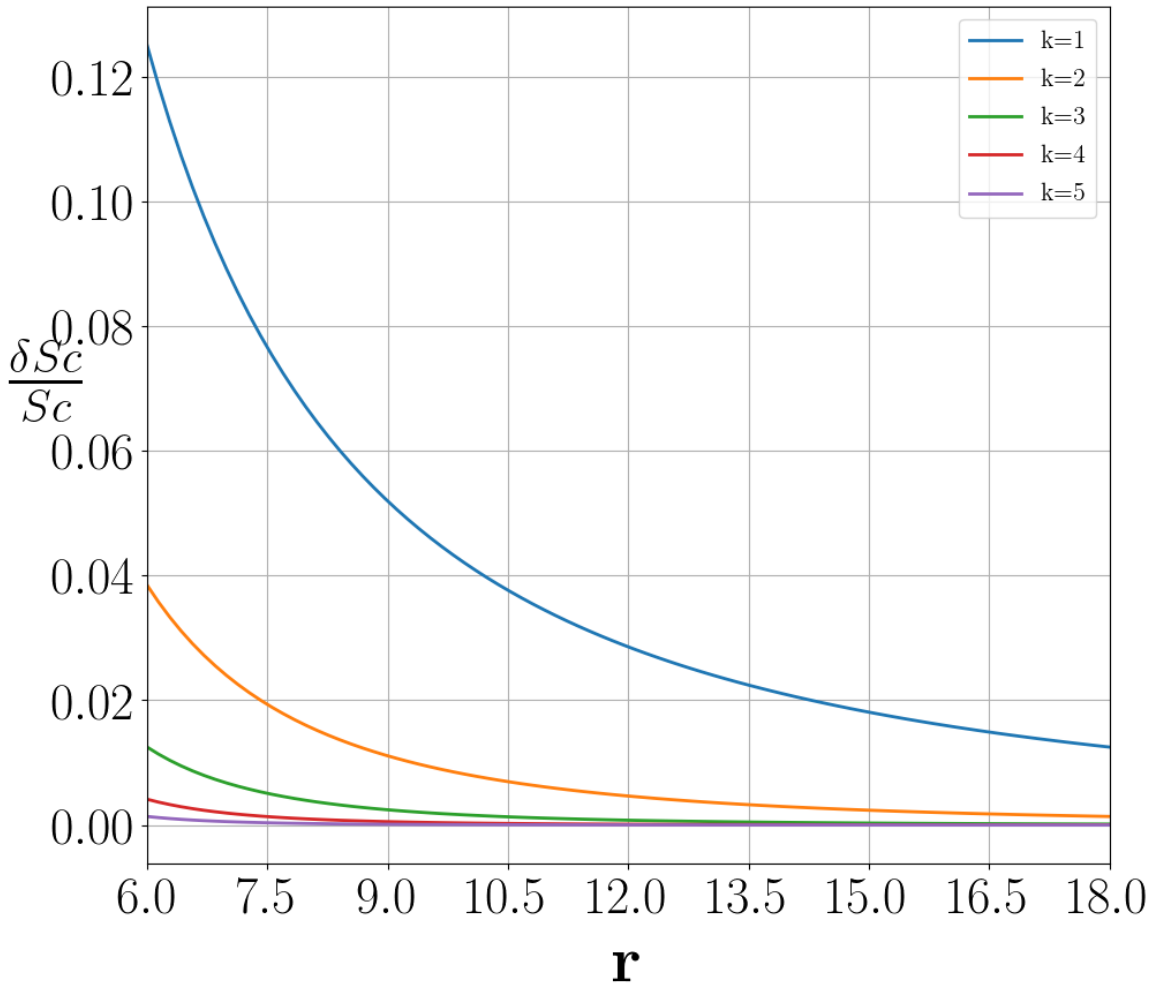

Figure 5.1: Relative difference between invariant scalar for Schwarzschild and approximate Schwarzschild spacetimes. The different number of terms k in Taylor series expansion gives different approximate spacetimes. The larger the k, the better is the agreement of two spacetimes. For fixed k the agreement is better for large $\mathbf{r}$ the coordinate distance from black hole. The curvature scalars are constructed using parameters corresponding to stable circular orbits with a given energy and angular momentum for each spacetime. The relative difference of second derivative of potential also satisfy the same relations.

construction, all components of

$$R_{[\mu][\nu][\rho][\sigma]} = R_{abcd} e^a_{[\mu]} e^b_{[\nu]} e^c_{[\rho]} e^d_{[\sigma]} \tag{5.6}$$

are gauge invariant. We can thus compare each component as constructed on the analytic and numerical spacetimes. We leave this analysis for a later work.

5.1.2 Analytic Black-Hole Binary Spacetime

For our analysis, the analytic metric we consider represents a nonspinning, equal-mass BBH in a quasicircular inspiral. This spacetime was first constructed in Ref. [276] based on earlier work on binary initial data in Refs. [284, 285, 286].

The analytic spacetime is constructed by asymptotically matching metrics in three different zones characterizing three different spacetime regions of validity for different analytic metrics: (i) a far zone (FZ) where the spacetime can be described by a two-body perturbed flat spacetime with outgoing gravitational radiation and where retardation effects are fully accounted for; (ii) a near zone (NZ) which is less than one GW length from the center of mass of the binary [but not too close to each black hole (BH)] that is described by a post-Newtonian metric (this includes retardation effects at a perturbative level and binding interactions between the two BHs); and (iii) inner zones (IZs) that are described by perturbed Schwarzschild (or Kerr) BHs. The full spacetime is then constructed by smoothly transitioning from zone to zone in the so-called buffer zones (BZs). Figure 5.2 shows where these regions are located with respect to the two BHs.

5.1.3 Reconstructing the 4-dimensional Riemann Tensor

As is done by in many numerical relativity codes, our numerical evolutions uses the standard 3+1 Arnowitt-Deser-Misner [144] split of the Einstein equations. In this work, we will need to reconstruct the full 4-dimensional Riemann tensor from the three dimensional quantities evolved by our code. In this section, we provide the details of how this is accomplished. In order to avoid

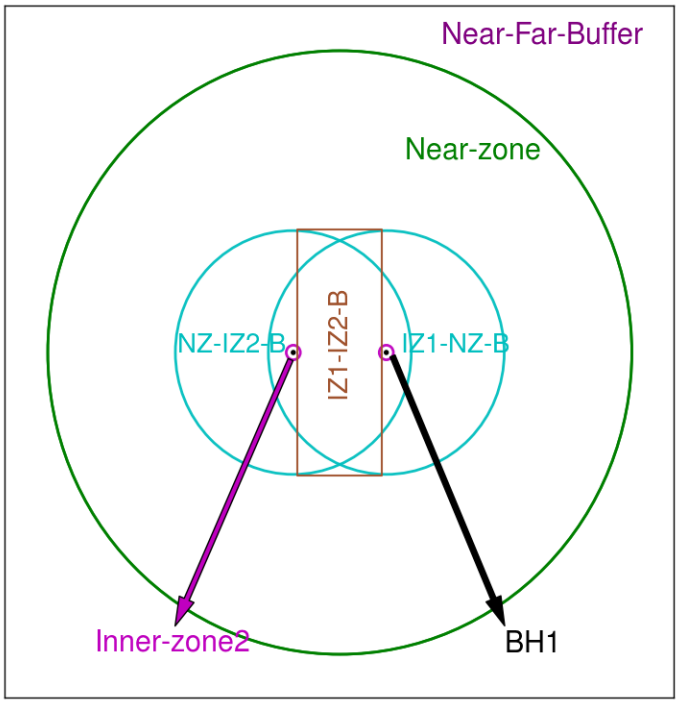

Figure 5.2: The zones for the analytic metric. The large (green) circle is the outer boundary of the near zone. Immediately inside this circle the metric is exclusively the post-Newtonian near-zone metric, while outside, it is a superposition of the near and far zone metrics. All points in the figure outside this circle are in the near-far buffer zone (the other boundary of this zone is not show). The smaller (cyan) circles denote the inner boundary of the near zone. Inside the envelope of these circles is the near-inner buffer zones. The box (orange) denotes the region inside the near-inner buffer zone where the metric is a superposition of both BH1 and BH2 inner zones, as well as the near zone. Outside the box, the metric is a superposition of the near zone metric and either one of the inner zone metrics. Finally inside the very small (magenta) circles are the two inner zones, where the metric is purely the inner zone perturbed Schwarzschild metric.

confusion, we will use the notation (2.7) and (2.8) to indicate a three or four dimensional tensors, respectively.

In the standard 3+1 split, the metric on a spatial slice (given by $t = \text{const}$) is obtained from the full 4-dimensional metric via

$$\gamma_{\mu\nu} = g_{\mu\nu} + n_\mu n_\nu \,, \tag{5.7}$$

where n^μ is the unit norm to the spatial hypersurface and the spatial components of this tensor (i.e., indices 1 through 3) form the 3-dimensional metric tensor. Note that while $\gamma_{ij} = g_{ij}$, $\gamma^{ij} \neq g^{ij}$. The full 4-dimensional tensor $\gamma_{\mu\nu}$ also serves as a projection operator which takes four-dimensional tensors to three-dimensional ones. To avoid confusion, we will use $P_{\mu\nu} = \gamma_{\mu\nu}$ to denote the projection tensor.

In order to reconstruct the 4-dimensional Riemann tensor, ${}^{(4)}R_{\mu\nu\epsilon\delta}$, we follow Ref. [145] and write it as

$$\begin{aligned}
{}^{(4)}R_{\mu\nu\epsilon\delta} \;=\; & P_\mu{}^\zeta P_\nu{}^\tau P_\epsilon{}^\kappa P_\delta{}^\sigma \; {}^{(4)}R_{\zeta\tau\kappa\sigma} \\
& -2P_\mu{}^\zeta P_\nu{}^\tau P_{[\epsilon}{}^\kappa n_{\delta]} n^\sigma \; {}^{(4)}R_{\zeta\tau\kappa\sigma} \\
& -2P_\epsilon{}^\zeta P_\delta{}^\tau P_{[\mu}{}^\kappa n_{\nu]} n^\sigma \; {}^{(4)}R_{\zeta\tau\kappa\sigma} \\
& +2P_\mu{}^\zeta P_{[\epsilon}{}^\kappa n_{\delta]} n_\nu n^\tau n^\sigma \; {}^{(4)}R_{\zeta\tau\kappa\sigma} \\
& -2P_\nu{}^\zeta P_{[\epsilon}{}^\kappa n_{\delta]} n_\mu n^\tau n^\sigma \; {}^{(4)}R_{\zeta\tau\kappa\sigma} \,,
\end{aligned} \tag{5.8}$$

where

$$\begin{aligned}
P^\zeta{}_\mu P^\eta{}_\nu P^\kappa{}_\epsilon P^\sigma{}_\delta \; {}^{(4)}R_{\zeta\eta\kappa\sigma} \;=\; & {}^{(3)}R_{\mu\nu\epsilon\delta} \\
& + K_{\mu\epsilon}K_{\nu\delta} - K_{\mu\delta}K_{\epsilon\nu} \,,
\end{aligned} \tag{5.9}$$

$$P^\sigma{}_\mu P^\eta{}_\nu P^\kappa{}_\delta n^\zeta R_{\sigma\eta\kappa\zeta} \;=\; D_\nu K_{\mu\delta} - D_\mu K_{\nu\delta} \,, \tag{5.10}$$

$$\begin{aligned}
P^\zeta{}_\mu P^\kappa{}_\nu n^\delta n^\epsilon R_{\delta\kappa\epsilon\zeta} \;=\; & \mathcal{L}_n K_{\mu\nu} + \frac{1}{\alpha} D_\mu D_\nu \alpha \\
& + K^\epsilon{}_\nu K_{\mu\epsilon} \,,
\end{aligned} \tag{5.11}$$

and D_i is the covariant derivative associated with γ_{ij}, α is the lapse, and K_{ij} is the extrinsic curvature.

Note that the left-hand sides of Eqs. (5.9)–(5.11) are all naturally defined in terms of 3-dimensional tensors. To construct a 4-dimension tensor from a 3-dimension tensor $T^{i_1 i_2 \cdots}_{j_1 j_2 \cdots}$, we use the following operator,

$$T^{\mu_1 \mu_2 \cdots}_{\nu_1 \nu_2 \cdots} = \Lambda^{\mu_1}{}_{i_1} \Lambda^{\mu_2}{}_{i_2} \cdots \Lambda_{\nu_1}{}^{j_1} \Lambda_{\nu_2}{}^{j_2} \cdots T^{i_1 i_2 \cdots}_{j_1 j_2 \cdots} , \tag{5.12}$$

where

$$\Lambda_\mu{}^i = \begin{pmatrix} \beta^1 & \beta^2 & \beta^3 \\ 1 & 0 & 0 \\ 0 & 1 & 0 \\ 0 & 0 & 1 \end{pmatrix} , \tag{5.13}$$

where β^i is the shift, and

$$\Lambda^\mu{}_i = \begin{pmatrix} 0 & 0 & 0 \\ 1 & 0 & 0 \\ 0 & 1 & 0 \\ 0 & 0 & 1 \end{pmatrix} . \tag{5.14}$$

Finally, the left-hand side of Eq. (5.11) is evaluated by assuming the standard ADM vacuum evolution equations are obeyed. That is,

$$\begin{aligned} \mathcal{L}_n K_{\mu\nu} &= \frac{1}{\alpha}(\mathcal{L}_t K_{\mu\nu} - \mathcal{L}_\beta K_{\mu\nu}) , \\ \mathcal{L}_t K_{\mu\nu} &= -D_\mu D_\nu \alpha + \alpha({}^{(3)}R_{\mu\nu} - 2K^\kappa{}_\nu K_{\mu\kappa} + K K_{\mu\nu}) \\ &\quad -8\pi\alpha(S_{\mu\nu} - \frac{1}{2}\gamma_{\mu\nu}(S-\rho)) + \mathcal{L}_\beta K_{\mu\nu} , \end{aligned} \tag{5.15}$$

where $S_{\mu\nu} = \gamma_\mu{}^\kappa \gamma_\nu{}^\sigma T_{\kappa\sigma}$, $S = S^\mu{}_\mu$, and $\rho = n^\mu n^\nu T_{\mu\nu}$ are all assumed to be zero.

Since we actually evolve the metric using the CCZ4 system [164], the actual form of the evolution equation for the extrinsic curvature is

$$\begin{aligned}\mathcal{L}_t K_{\mu\nu} &= -D_\mu D_\nu \alpha + \alpha({}^{(3)}R_{\mu\nu} - 2K^\kappa{}_\nu K_{\mu\kappa} + K K_{\mu\nu}) \\ &\quad +\alpha(D_\mu Z_\nu + D_\nu Z_\mu) \\ &\quad -\left(2\alpha K_{\mu\nu} + \alpha\gamma_{\mu\nu}\frac{1}{\phi^2}\kappa_1(1+\kappa_2)\right)\Theta \\ &\quad +\mathcal{L}_\beta K_{\mu\nu}\,, \end{aligned} \tag{5.16}$$

where Θ and Z_i denote deviations from the Einstein equations, and constants κ_i are free parameters. Thus using Eq. (5.15) is equivalent to assuming Θ and Z_i are zero. At $t = 0$ this is the case, and both variables remain small due to the constraint damping of the CCZ4 system. In order to make our code more general, we assume Eq. (5.15), which means that it can be used equally well with a BSSN, CCZ4, or other 3+1 evolution system.

To reconstruct ${}^{(4)}R_{\mu\nu\kappa\sigma}$, we interpolate γ_{ij}, $\partial_k\gamma_{ij}$, the 3-dimensional Ricci tensor ${}^{(3)}R_{ij}$, K_{ij}, $\partial_k K_{ij}$, α, β^i, and $\partial_j\beta^i$ along each geodesic. Note that we do not need second derivatives of the lapse because the $D_\mu D_\nu\alpha$ terms cancel out. From these quantities, we can reconstruct all terms in Eqs. (5.9)–(5.11). Note that the 3-dimensional Riemann tensor can be reconstructed directly from the 3-dimensional Ricci tensor.

To compute the Riemann tensor for the analytic spacetime, we use an eighth-order finite differencing algorithm and directly differentiate the 4-dimensional metric.

5.1.4 Numerical Evolutions

We first explored evolving the analytic metric using the fully nonlinear numerical relativity codes in Ref. [278]. We use an identical procedure here, which we summarize below.

We evolved the BBH initial data using the LazEv [287] implementation of the moving puncture approach [89, 90] with the conformal function $W = \sqrt{\chi} = \exp(-2\phi)$ suggested by Ref. [288] and the Z4 [289, 290, 164] and BSSN [291, 292, 293] evolution systems. Here, we use the conformal covariant Z4 (CCZ4) implementation of Ref. [164]. Note that the same technique has been recently applied to

the evolution of binary neutron stars [294, 295]. For the CCZ4 system, we again used the conformal factor W. We used centered eighth-order finite differencing for all spatial derivatives, a fourth-order Runge-Kutta time integrator, and both fifth- and seventh-order Kreiss-Oliger dissipation [296].

Our code uses the EinsteinToolkit [215, 216, 217] / Cactus [223] / Carpet [297, 225] infrastructure. The Carpet mesh refinement driver provides a "moving boxes" style of adaptive mesh refinement (AMR). In this approach, refined grids of fixed size are arranged about the coordinate centers of both holes. The Carpet code then moves these fine grids about the computational domain by following the trajectories of the two BHs. To obtain initial data, we use eighth-order finite differencing of the analytic global metric to obtain the 4-metric and all its first derivatives at every point on our simulation grid. The finite differencing of the global metric is constructed so that the truncation error is negligible compared to the subsequent truncation errors in the full numerical simulation (here we used finite difference step size of 10^{-4}, which is 90 times smaller than our smallest grid size in any of the numerical simulations discussed below). We then reconstruct the spatial 3-metric γ_{ij} and extrinsic curvature K_{ij} from the global metric data. Note that with the exception of the calculation of the extrinsic curvature, we do not use the global metric's lapse and shift. In order to evolve these data, we need to remove the singularity at the two BH centers. Unlike in the puncture formalism [298], the singularities here are true curvature singularities. We *stuff* [299, 300, 301] the BH interiors in order to remove the singularity. Our procedure is to replace the singular metric well inside the horizons with nonsingular (but constraint violating) data through the transformations,

$$\begin{aligned}
&\gamma_{ij} \to f(r)\ \gamma_{ij}\,, \quad i \neq j\,,\\
&\gamma_{ii} \to f(r)\ \gamma_{ii} + (1 - f(r))\Xi\,,\\
&K_{ij} \to f(r)\ K_{ij}\,,
\end{aligned} \tag{5.17}$$

where

$$f(r) = \begin{cases} 0\,, & r < r_{\rm min} \\ 1\,, & r > r_{\rm max} \\ P(r)\,, & r_{\rm min} \leq r \leq r_{\rm max} \end{cases} . \tag{5.18}$$

Here, r is the distance to a BH center, and $P(r)$ is a fifth-order polynomial that obeys $P(r_{\rm min}) = P'(r_{\rm min}) = P''(r_{\rm min}) = 0$, $P(r_{\rm max}) = 1$, $P'(r_{\rm max}) = P''(r_{\rm max}) = 0$, and Ξ is a large number. The resulting data are therefore C^2 globally. The parameters $r_{\rm min}$, $r_{\rm max}$, and Ξ are chosen such that both transitions occur inside the BHs and so that W varies smoothly with negligible shoulders in the transition region and is small at the centers.

The grid structure for the runs below consisted of a course grid extending to $(x, y, z) = \pm(3200, 3200, 3200)M$ (we exploited both the z-reflection and π-rotational symmetry of the data in order to reduce the computational volume by a factor of 4). We used 12 levels of mesh refinement. In the sections below, we indicate the global resolution of each simulation by indicating the number of points on the coarsest grid from the origin to each outer face. That is, a resolution of $N = 100$ indicated that the coarsest grid spacing is $3200M/100 = 32M$. The resolution was always set to be the same in each direction.

To evolve timelike geodesics in the numerical spacetime, we use the following algorithm. The 4-velocity of each geodesic is decomposed into a component tangent to the unit norm n^a and a spatial component V^a. That is,

$$u^\mu = \varpi n^\mu + V^\mu\,, \tag{5.19}$$

where $\varpi = \sqrt{1 + V^i V^j \gamma_{ij}}$ and $V^0 = 0$ [174] (note that $V_i = u_i$ $[i = 1, 2, 3]$). The geodesic equation

then gives

$$\begin{aligned}
\frac{dx^i}{dt} &= -\beta^i + \frac{\alpha}{\varpi} V^i \,, \\
\frac{d\tau}{dt} &= \frac{\alpha}{\varpi} \,, \\
\frac{dV_i}{dt} &= -\varpi \alpha_{,i} - V_j \beta^j{}_{,i} + \frac{1}{2} V^j V^k \gamma_{jk\,,i} \,.
\end{aligned} \tag{5.20}$$

This form of the geodesic equation has the advantage that explicit time derivatives of the 4-metric are not needed for the evolution and the integration variable is t, which is the time coordinate used in the code. We evolve the geodesics using the same RK4 time integrator used to evolve the metric itself.

Since we evolve these geodesics with an adaptive-mesh code, there are complication associated with geodesics crossing refinement level boundaries. Our algorithm is as follows. The AMR grid is distributed such that on a given refinement level, a single CPU will only *own* a single Cartesian box. We then search for the finest resolution box that contains that geodesic and assign the evolution of the geodesics (at that time step) to that processor. For our purposes, a geodesic is only contained in a given box if all points used by the interpolation stencil are in that box (excluding buffer zones, but including ghost zones). If a geodesic is too close to buffer zones, then it will be evolved using the next coarsest level.

A geodesic that crosses from a coarse refinement level to a finer one may actually be ahead, in time, of the rest of the fields on that refinement level. In such a case, the evolution of the geodesic is stalled until the time associated with that refinement level catches up. On the other hand, when a geodesic moves from a finer level to a coarser one, it is generally behind. In that case, we use a second-order accurate algorithm to evolve the geodesic forward in time until it is *caught up* with the rest of the fields on that refinement level.

On the other hand, for the analytic metric, we use the more conventional formulation of the

geodesic equation,

$$\begin{aligned} \frac{dx^\mu}{d\tau} &= u^\mu \,, \\ \frac{du^\mu}{d\tau} &= -\Gamma^\mu{}_{\rho\sigma} u^\rho u^\sigma \,, \end{aligned} \tag{5.21}$$

where $\Gamma^\mu{}_{\rho\sigma}$ is the 4-dimensional Christoffel symbols. Here, we evolve the geodesics using an adaptive RK45 algorithm.

5.2 Code Verification

Our code suite consists of three parts. A stand-alone code written in C++ that integrates geodesics and calculates the Riemann tensor given a function that can provide $g_{\mu\nu}$ at arbitrary coordinate positions. A Cactus Thorn that evolves geodesics alongside the metric within the Einstein Toolkit, as well as interpolates the metric (and derivatives) along these geodesics. Finally, our toolkit contains a set of Python scripts that calculates the curvature eigenvalues of Eq. (5.5) given the data provided by the previous two programs.

We performed several verification tests of the this code suite, which we will describe here. Our first test consisted of using the stand-alone C++ code to evolve identical geodesics on Schwarzschild backgrounds, but in very different gauges.

To do this, we started with the standard Schwarzschild metric,

$$\begin{aligned} ds^2 &= -\left(1-\frac{2M}{R}\right) dT^2 + \left(1-\frac{2M}{R}\right)^{-1} dR^2 \\ &\quad + R^2\, d\Theta^2 + R^2\, \sin^2\Theta\, d\Phi^2 \,, \end{aligned} \tag{5.22}$$

and used the simple coordinate transformation,

$$\begin{aligned} T &= t + A\, \sin(\omega t)\, \sin(\omega t)\, \cos(r) \,, \\ R &= r + A\, \sin(\omega t)\, \sin(\omega t) \,, \\ \Theta &= \theta \,, \end{aligned}$$

$$\Phi = \phi\,, \tag{5.23}$$

where A is a constant. As is readily apparent in Fig. 5.3, the coordinate trajectory of the geodesic is quite different in the two coordinate systems. However, the calculated curvature eigenvalues (only one shown) are identical. There are three curvature eigenvalues, two are positive with very similar magnitudes and one has a negative value, but is roughly a factor of two larger in absolution value than the other two. When plotting the eigenvalues, we make the fiducial choice of plotting the intermediate eigenvalue, which we denote by **Sc** in the figures below.

Next, we repeated the same calculation using our EinsteinToolkit-based geodesic thorn. Here we set the metric analytically, but evolved the geodesics, and calculated the Riemann tensor (see Sec. 5.1) numerically. Here, three grid resolutions were used to test the numerical convergence. As shown in Fig. 5.4, the relative differences between the analytical and numerical evolution of the curvature eigenvalues shows the expected fourth-order convergence.

To test for convergence of our geodesic thorn in the context of a fully nonlinear numerical spacetime, we evolve the Schwarzschild metric in trumpet coordinates [302] (with the trumpet parameter $R_0 = M$). For reference, the metric has the form,

$$\begin{aligned} ds^2 = &-\left(\frac{R-M}{R+M}\right) dT^2 + \frac{2M}{R} dT dR \\ &+ \left(1+\frac{M}{R}\right)^2 \left(dR^2 + R^2\, d\Theta^2 + R^2\, \sin^2\Theta\, d\Phi^2\right)\,. \end{aligned} \tag{5.24}$$

Following Ref. [303], we use the lapse condition $\partial_t \alpha = \mathcal{L}_\beta \alpha - \alpha(1-\alpha)K$, for which all the metric functions are constants (up to truncation error) as functions of time.

A convergence plot of the curvature eigenvalues from a fiducial geodesic is shown in Fig. 5.5. Here, too, we find fourth-order convergence.

One aspect of numerical evolutions of a binary spacetime on AMR grids that we will encounter is stochastic noise in the curvature [304] due to unresolved gauge waves [159]. In order to test our code with a time dependent metric, we evolved the same trumpet data, but with a modified lapse condition $\partial_t \alpha = \mathcal{L}_\beta \alpha - 1.001\alpha(1-\alpha)K$. This introduces a small time dependence to the metric

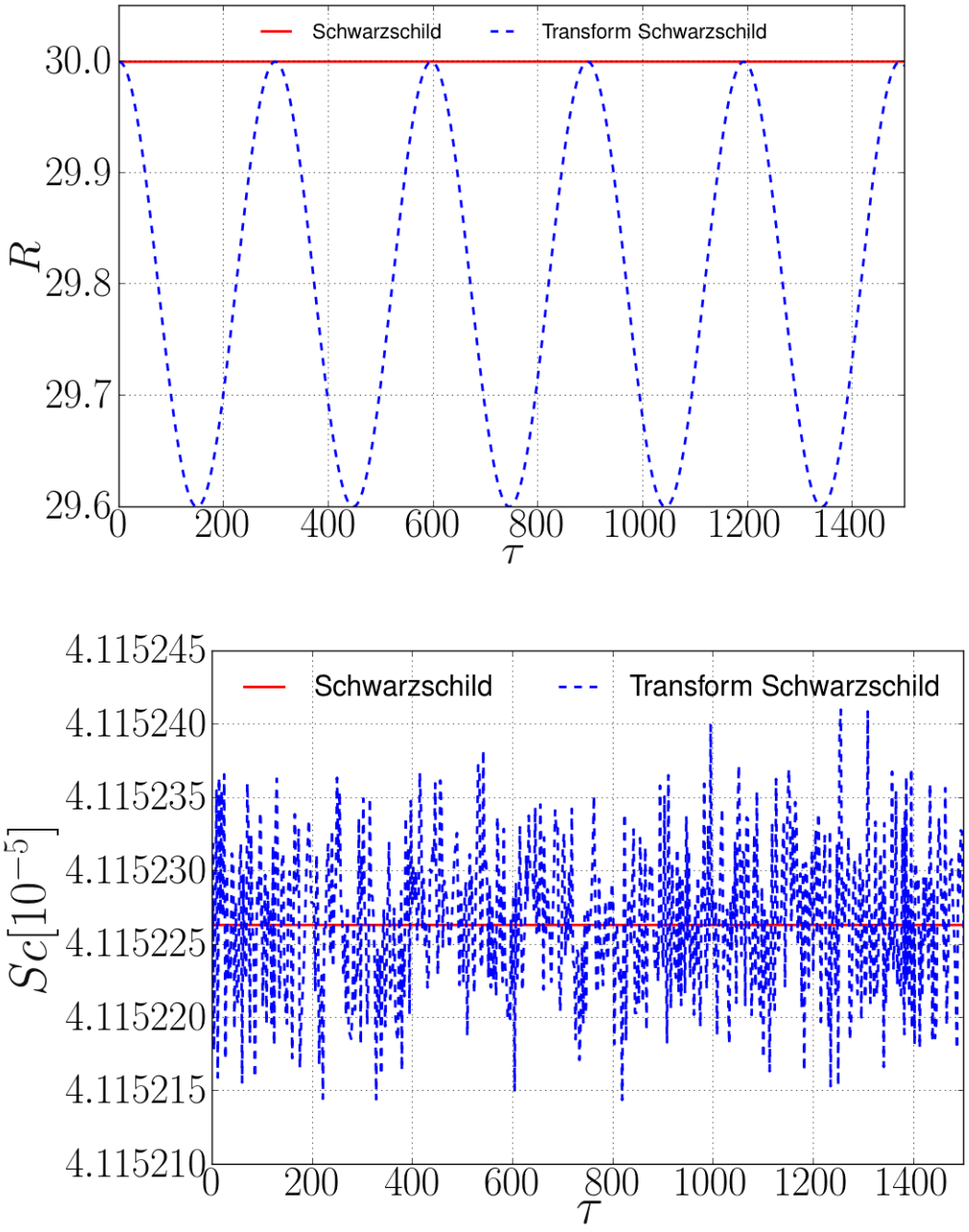

Figure 5.3: Circular geodesics in standard Schwarzschild and transformed Schwarzschild coordinates. While the trajectory is gauge dependent (top), the associated curvature eigenvalues (only one shown) are not (bottom). The differences between the eigenvalues (**Sc**) calculated in to the two gauges are consistent with roundoff errors.

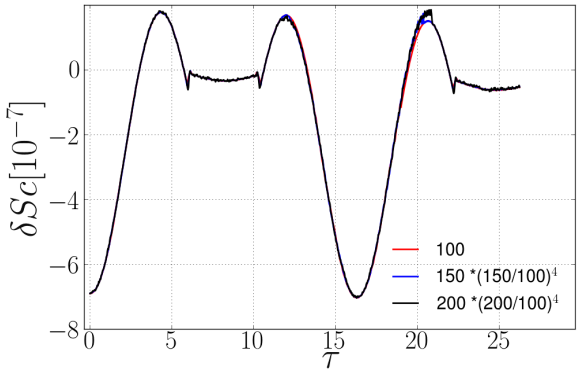

Figure 5.4: The differences between one of curvature eigenvalues(**Sc**) versus time from our new geodesic thorn and the exact values (as determined by a stand-alone code). Here, we denote the resolution of a given simulation by the number of gridpoint, per dimension, from the origin to the outer boundary, and rescale the differences by the ratio of the grid resolution to the fourth power.

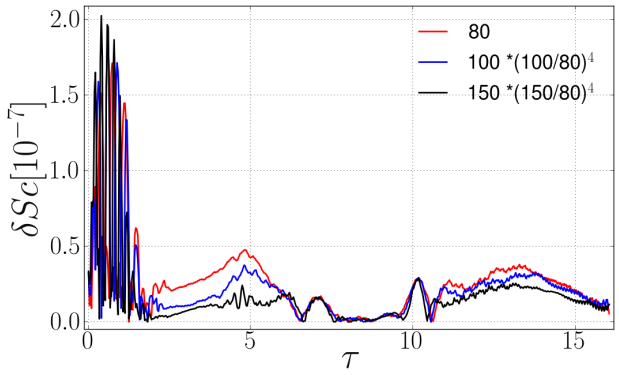

Figure 5.5: The difference between one of the gauge independent curvature eigenvalue (**Sc**) as calculated using a fully nonlinear numerical evolution of time independent trumpet Schwarzschild data using the EinsteinToolkit, and as calculated using the exact trumpet Schwarzschild metric with the trumpet parameter $R_0 = M$. Here, we rescale the differences by the ratio of the grid resolution to the fourth power.

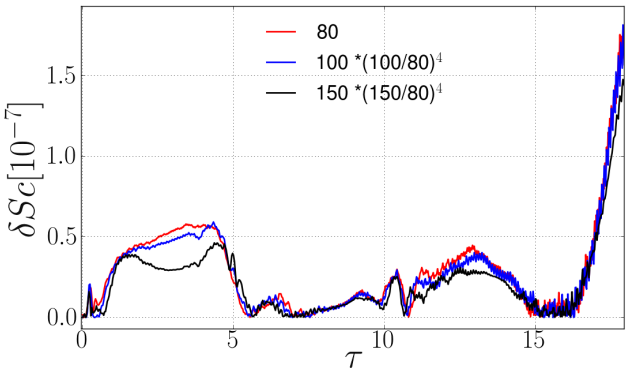

Figure 5.6: The convergence of the one of the gauge independent curvature eigenvalues (**Sc**) for a slowly time-dependent Schwarzschild trumpet. The convergence order is still fourth-order.

without simultaneously introducing an unresolved gauge wave. As seen in Fig. 5.6, the convergence is still fourth-order. However, when using a more standard puncture-based initial data and $1+\log$ lapse, the convergence order reduced to second-order, which is consistent with the second-order time prolongation we use. The reason for this drop in convergence rate is likely the very rapid evolution of the gauge during the first few M of evolution. These rapid changes can lead to the second order (in time) prolongation error dominating the error budget.

Finally, we evolved a set of geodesics in Kerr spacetime in quasi-isotropic coordinates [305] and fully nonlinear numerical evolutions of a Kerr BH starting with quasi-isotropic initial data. Here the two codes evolve the geodesics in gauges that rapidly deviate from each other. The effects of the unresolved gauge wave are apparent in the noise and lower-order convergence seen in Fig. 5.7. We see a similar lower order convergence when using Schwarzschild isotropic data.

5.3 Results

The main analysis of this project concerns the dynamics of geodesics on spacetimes obtained by numerically evolving (using CCZ4) initial data obtained from the analytic metric at various starting separations. In particular, we compare those geodesics with the ones obtained by solving

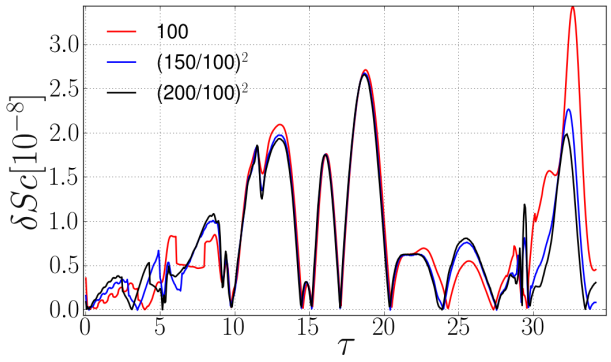

Figure 5.7: Second-order convergence of the gauge independent curvature eigenvalues (**Sc**) as calculated using a fully nonlinear numerical evolution of Kerr data using the EinsteinToolkit, and as calculated using the exact Kerr metric in quasi-isotropic coordinates.

the geodesic equation on the analytic spacetime. The differences between the numerically evolved metric and the analytic one arise from the differences in the Ricci tensor of the two. The CCZ4 algorithm drives the constraint violation toward small values, at which point the evolved metric is consistent with $T_{\mu\nu} = 0$. The analytic metric, on the other hand, has $T_{\mu\nu} \neq 0$. Differences in $T_{\mu\nu}$ exist even at $t = 0$, which means that the Riemann tensor on the initial slice is not the same between the numerical and analytic metrics.

We use the EinsteinToolkit to evolve geodesics on spacetimes obtained by using the analytic metric, with $m_1 = m_2 = M/2$, as initial data with separations of $D = 50M$, $25M$, $20M$, $15M$, and $10M$. We simultaneously evolve these geodesics using our stand-alone C++ code with the purely analytic metric.

In Fig. 5.8, we show how the constraint violations decay with time using the CCZ4 evolution code (we see a decrease of over three orders of magnitude).

The results from a wide variety of geodesics are shown in Figs. 5.9, 5.10, and 5.11. The figures show one of the curvature eigenvalues (**Sc**) versus proper time, τ, for various starting configurations. The coordinate trajectories of the geodesics *in a corotating frame* are also shown. The boundaries of the inner, near, far, and buffer zones are denoted by vertical lines and ellipses.

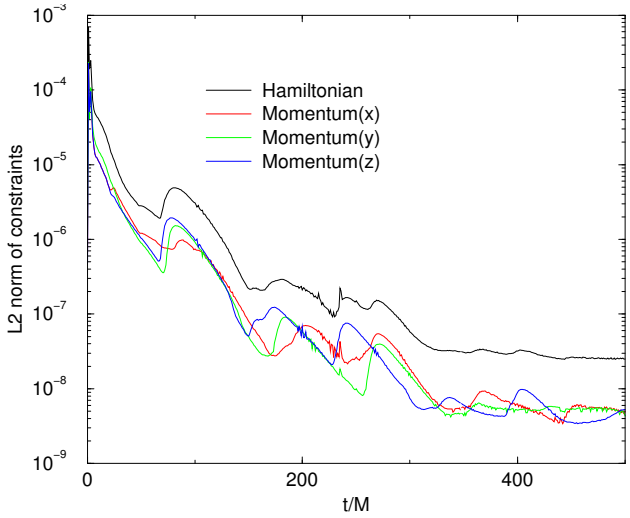

Figure 5.8: The L2 norm of the constraints for the $D = 25M$ configuration. Here the constraints are calculated within the volume outside the two horizons and inside the coordinate sphere $r = 30M$.

The noise apparent in the curvature eigenvalues for the geodesics far from the BHs is due reflections of spurious waves off of the AMR boundaries (this is the same error associated with high-frequency oscillations in the waveform seen in numerical evolutions of BBHs using AMR-based codes). At far distances, this noise is larger in magnitude than the curvature eigenvalues. See, for example, the $r_0 \gtrsim 100M$ curves for the $D = 50M$ configuration in Fig. 5.9.

At a separation of $D = 50M$ in Fig. 5.9, one would expect very good agreement between the analytic metric and the numerical one. Quantitatively, there is remarkably good agreement when the geodesics are about $20M \lesssim r_0 \lesssim 100M$ from the BHs. Closer than this, there are small, but noticeable differences, and farther than this, there is some evidence significant differences, but in those cases the noise is significantly larger than the curvature eigenvalues themselves.

We find that initial conditions that lead to nearly circular geodesics for one metric do lead to nearly circular geodesics for the other. The best agreement here are for geodesics in the outer regions of the inner-to-near-zone buffer regions and the near zone.

At a binary separation of $D = 25M$ (see Fig. 5.10), the disagreement between the analytical and numerical results when the geodesics are close are exacerbated. Good agreement between the

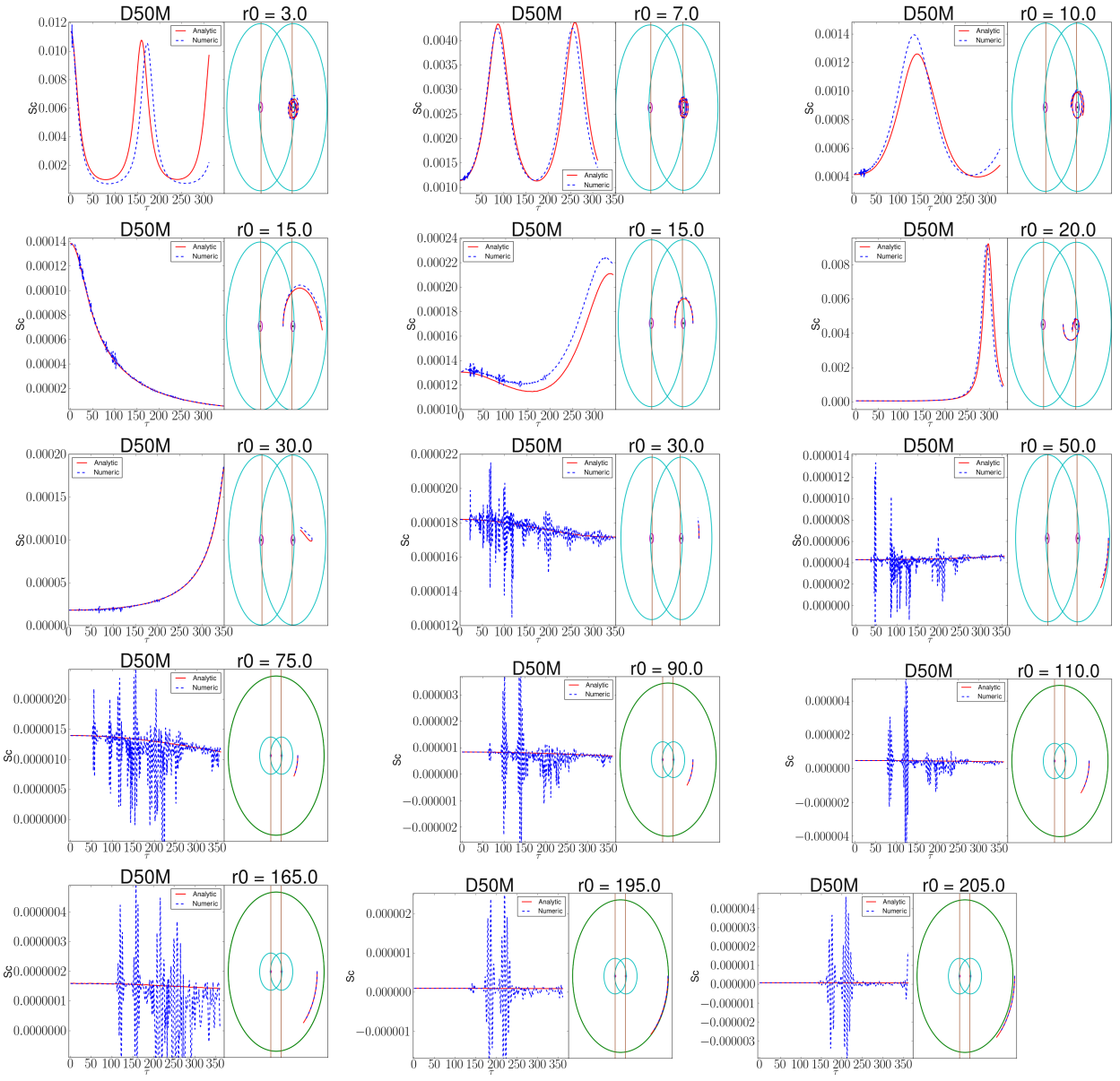

Figure 5.9: Separation $D = 50M$ results. Here we plot the value of the largest (in magnitude) curvature eigenvalue (**Sc**) versus time (as evolved using the numerical and analytic metric), as well as plot the coordinate position of the geodesics *in a corotating frame* (i.e., one where the BH positions are nearly fixed) on the right side of each panel. The vertical lines and circles in these trajectory plots show the location of the various zones described in Sec. 5.1.2. The number r_0 (normalized by M) is the initial coordinate distance of the geodesic from the nearest BH. For the geodesics close to the BHs, the noise in the numerically evolved spacetime is low compared to the magnitude of the curvature eigenvalues, the opposite is true for the farthest ones.

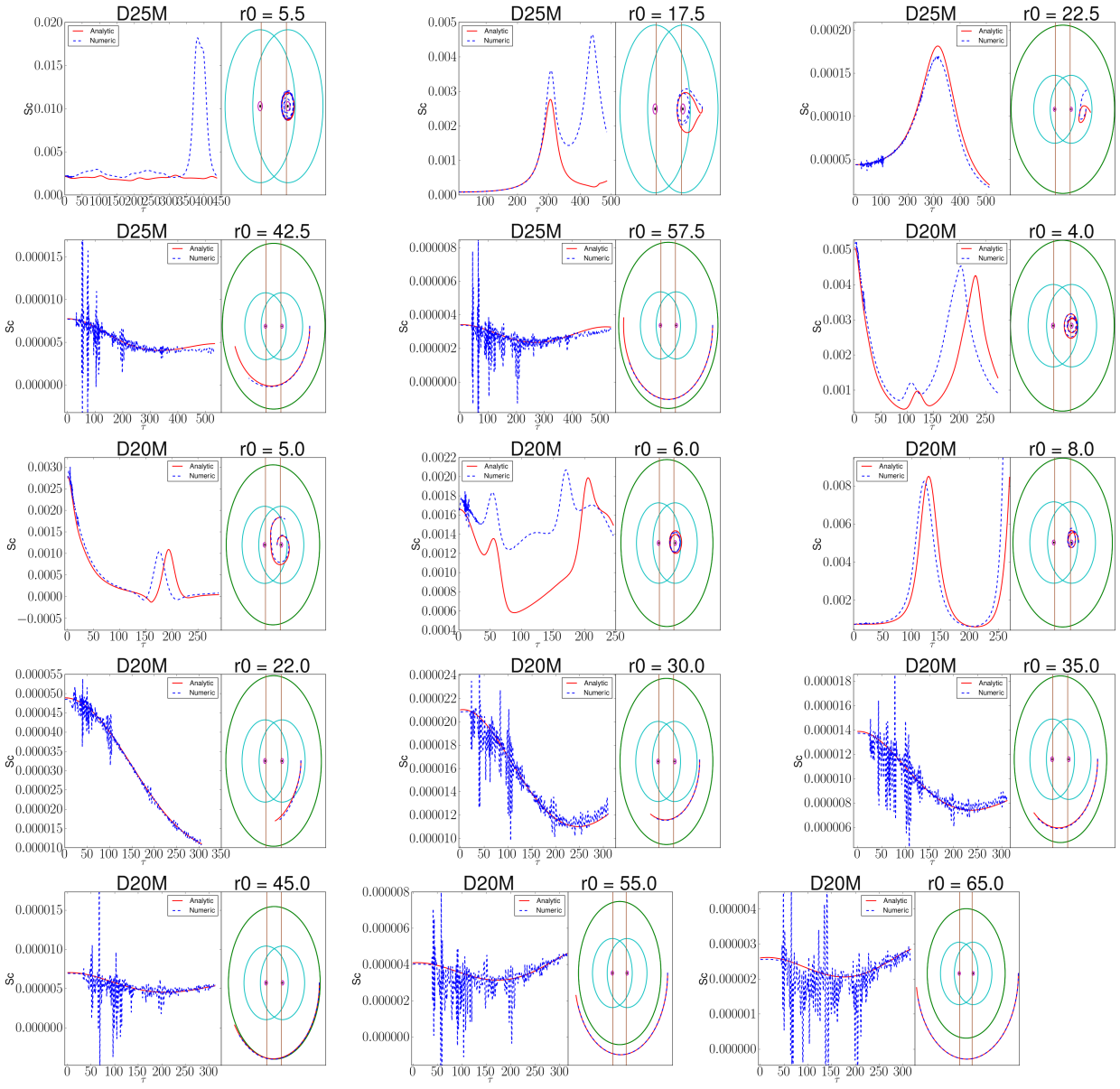

Figure 5.10: Separation $D = 25M$ and $D = 20M$ results. Here we plot the value of the largest (in magnitude) curvature eigenvalue (**Sc**) versus time (as evolved using the numerical and analytic metric), as well as plot the coordinate position of the geodesics *in a corotating frame* (i.e., one where the BH positions are nearly fixed) on the right side of each panel. The vertical lines and circles in these trajectory plots show the location of the various zones described in Sec. 5.1.2. The number r_0 (normalized by M) is the initial coordinate distance of the geodesic from the nearest BH. For the geodesics close to the BHs, the noise in the numerically evolved spacetime is low compared to the magnitude of the curvature eigenvalues, the opposite is true for the farthest ones.

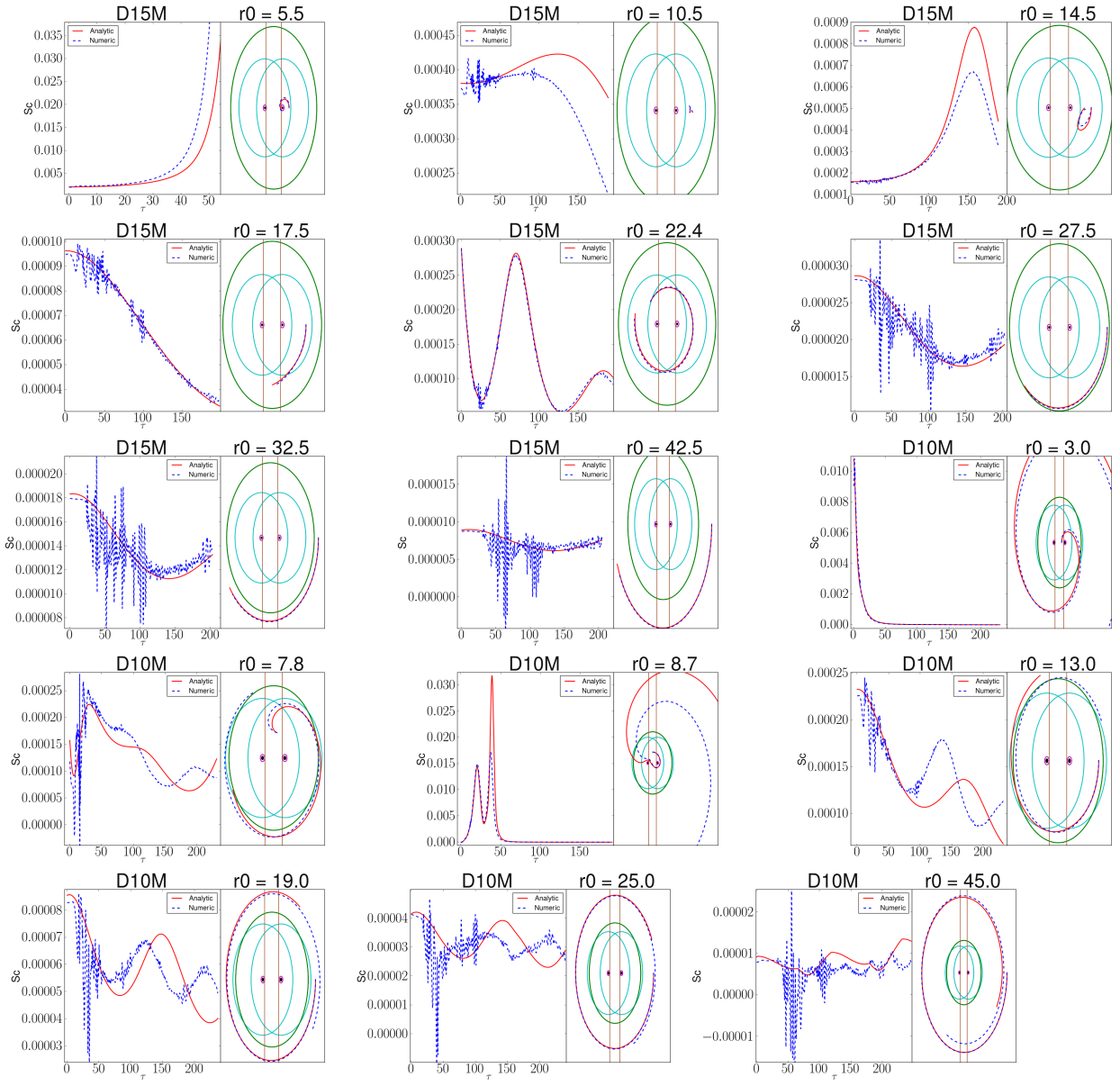

Figure 5.11: Separation $D = 15M$ and $D = 10M$ results. Here we plot the value of the largest (in magnitude) curvature eigenvalue (**Sc**) versus time (as evolved using the numerical and analytic metric), as well as plot the coordinate position of the geodesics *in a corotating frame* (i.e., one where the BH positions are nearly fixed) on the right side of each panel. The vertical lines and circles in these trajectory plots show the location of the various zones described in Sec. 5.1.2. The number r_0 (normalized by M) is the initial coordinate distance of the geodesic from the nearest BH. For the geodesics close to the BHs, the noise in the numerically evolved spacetime is low compared to the magnitude of the curvature eigenvalues, the opposite is true for the farthest ones.

curvature eigenvalues is still apparent in the outer part of the inner-to-near zone buffer region and the near zone, although at late times these geodesics show deviations as shown for the $r_0 > 40M$ cases. At a binary separation of $D = 10M$ (see Fig. 5.11), there are noticeable differences in the curvature eigenvalues for almost all geodesics. However, examining the $D = 15M$ geodesics (see Fig. 5.11) shows something perhaps surprising. The geodesics in the outer part of the inner-to-near zone buffer region and the near zone are remarkably good. Here, the deviations for far geodesics also start to deviate at later times. It seems these deviations are dependent on the binary separation. One may have expected these geodesics to be substantially worse than the $D = 25M$ and $D = 20M$ analogs, but we do not see this.

In Fig. 5.12, we show the relative difference between the curvature eigenvalues calculated using the numerical and analytic metrics. Here, we use a running average to smooth out the noise. Note that the color scale changes from blue to red at a 10% relative difference. From these plots, we can see that the buffer zone between the inner and near zones, as well as the near zone itself shows the smallest relative errors. The near-to-far zone buffer region (no plot shows the far zone) is generally worse, as least in terms of relative errors, than the near zone. The large relative differences seen for the $D = 50M$ case may be due to noise, but as seen in Fig. 5.12, there are hints of systematic differences between the analytic and numerical spacetimes. Note that in Fig. 5.12, we plot the geodesics *in a non-corotating frame*. The reason for this is, that while plotting in a corotating frame allows us to see which zones the geodesics pass through, it also gives a false sense of how far in (quasi) inertial coordinates the geodesics actually traveled. By comparing the plots in Fig. 5.12 with Figs. 5.9–5.11, one can get a more accurate of the actual motion of each geodesic.

5.3.1 Comparing First and Second-order Matched Spacetime

There are two versions of the analytic metric presented above. The standard one, known as the second-order metric, uses higher-order PN terms in the near zone, and matches the $\ell = 2$ and $\ell = 3$ multipoles in the inner zone. The first-order metric, which we will explore below, uses lower-order PN terms and only matches the $\ell = 2$ multipoles in the inner zone.

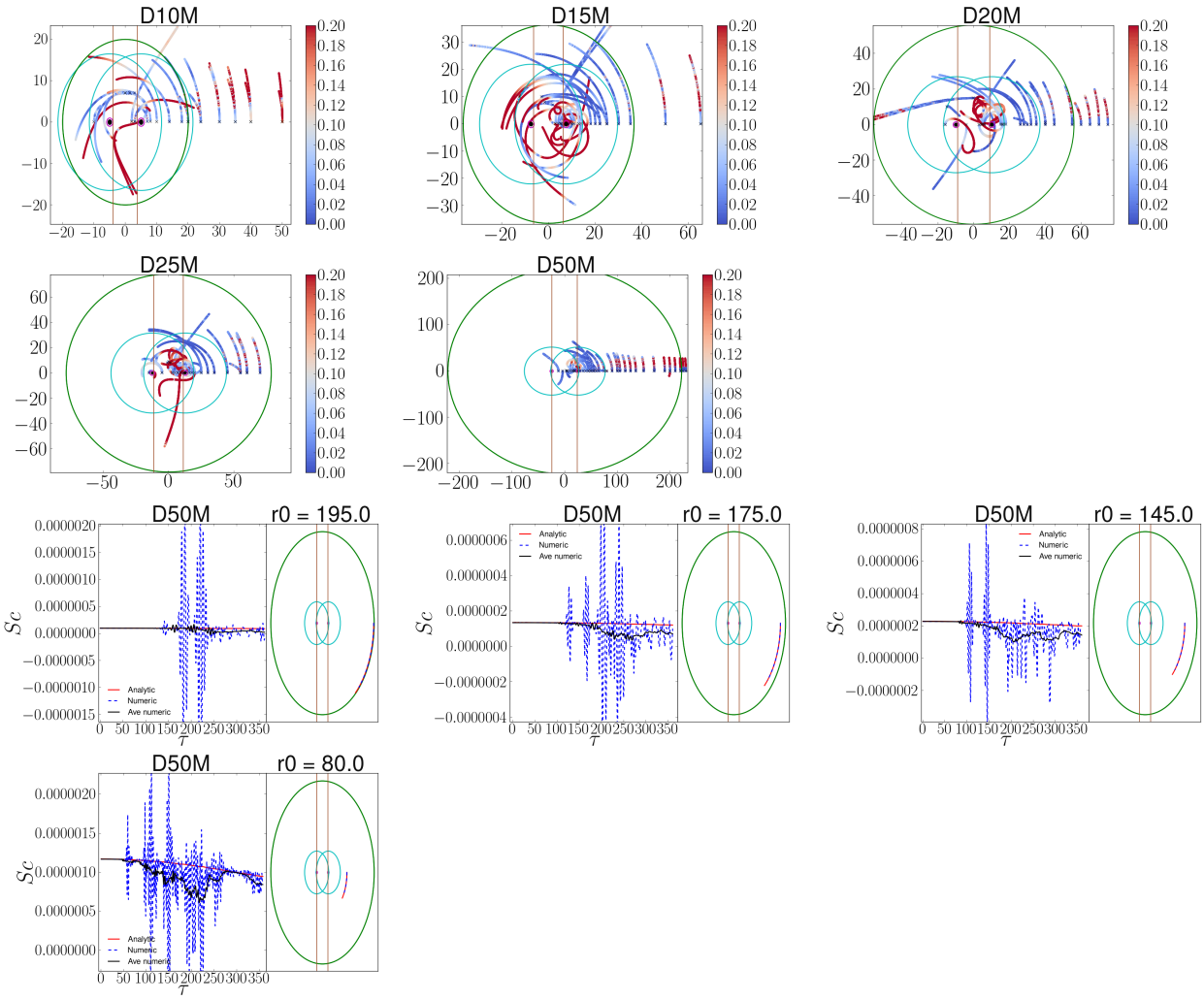

Figure 5.12: (Top two rows) A summary of the results. The plots show the trajectories of the geodesics *in a non-corotating frame*. The color scale gives the relative differences between the curvature eigenvalues (**Sc**) as calculated using the numerical (and smoothed by a running average) and analytic metrics. Note that the color changes from blues to reds at 10% relative difference. (Bottom two rows) Plots showing curvature eigenvalues as calculated using the analytical and numerical metrics, as well as a running average of the latter. There are hints here of systematic differences between the analytical and numerical results. However, as can be seen, the noise is much larger than these differences.

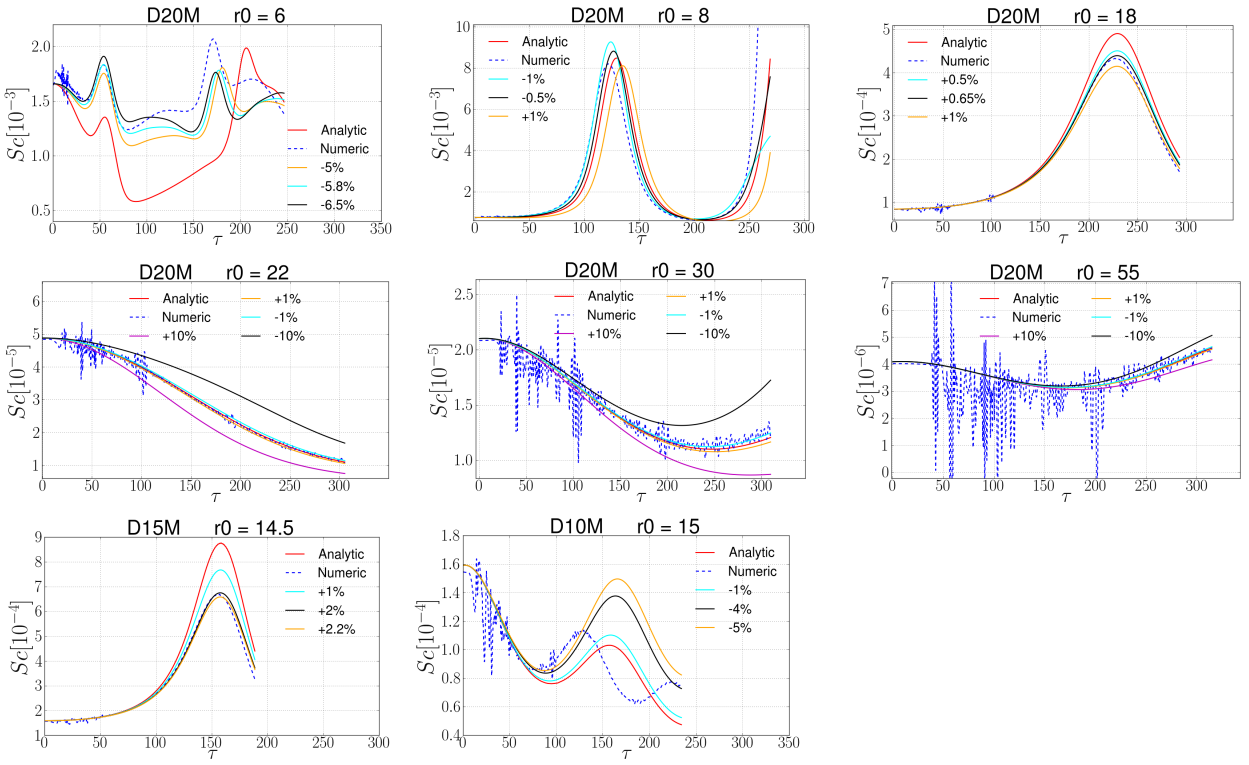

Figure 5.13: Curvature eigenvalues (**Sc**) for numerical and analytical spacetimes. For the analytical spacetime, we perturb the initial velocity of geodesics by the factors shown in the graphs. The dotted blue curve is the numerical result with velocity associated with the unperturbed analytic geodesic. As can be seen, the larger the value of the eigenvalues (i.e., geodesic deviation) the larger the effect of a $\pm 10\%$ perturbation. On the other hand, with small perturbations, we were able to find geodesics in the analytical spacetime that closely matched the dynamics (time dependence the eigenvalue) of the numerical one for geodesics farther than $r_0 \sim 10M$ from the BHs.

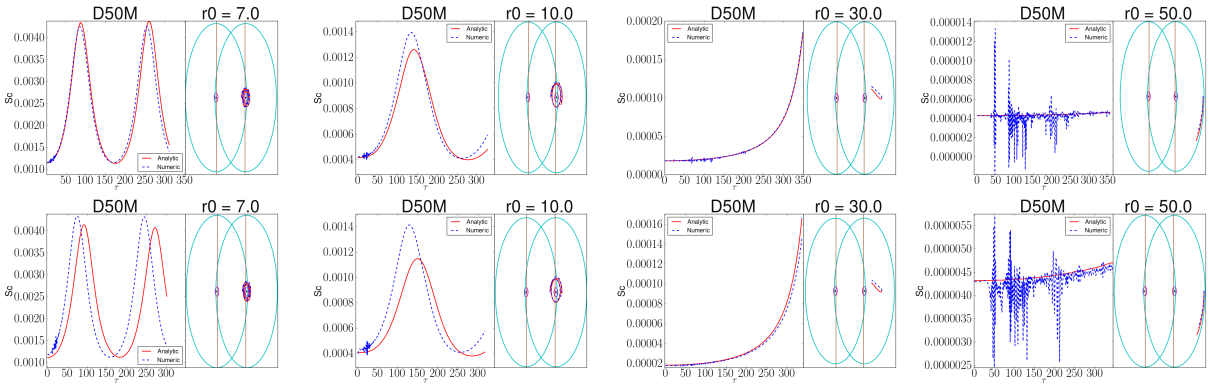

Figure 5.14: A comparison of how well the curvature eigenvalues of the second-order metric and first-order metric agree with the eigenvalues of the associated numerical metrics for the $D = 50M$ case. The top row shows the second-order results (which were previously shown in Fig. 5.9). The bottom row shows the first-order results. Note that at larger distances from the black holes the two results are comparable, while at closer distances the second-order results are qualitatively better.

Thus, we expect the second-order metric to be superior to the first-order one. In this section, we repeat our calculations comparing analytic metric to numerically evolved ones, but this time using the first-order analytic metric. Again, we plot results for $D = 50M$, $D = 20M$, $D = 15M$, and $D = 10M$ in Figs. 5.14, 5.15, 5.16, and 5.17. As in the sections above, we compare the curvature eigenvalues for from the analytic metric with the eigenvalues obtained by numerically evolving the analytic metric using the CCZ4 system. Thus we compare the second-order analytic eigenvalues with those obtained by numerically evolving the second-order metric and compare the first-order analytic eigenvalues with those obtained by numerically evolving the first-order metric. As expected, for $D \geq 15M$, the second-order curvature eigenvalues more closely match the associated numerical ones than the first-order eigenvalues do. For both metrics, the general trend for $D \geq 15M$ is that the first and second order results both become better at larger distances from the black holes and larger black-hole separations. The $D = 10M$ results appear to be equally inaccurate for the first and second-order metrics. Our method is thus able to distinguish between a lower-accuracy and a higher-accuracy metric. Thus, we expect it will be a useful testing ground for developing still higher-accuracy analytic metrics.

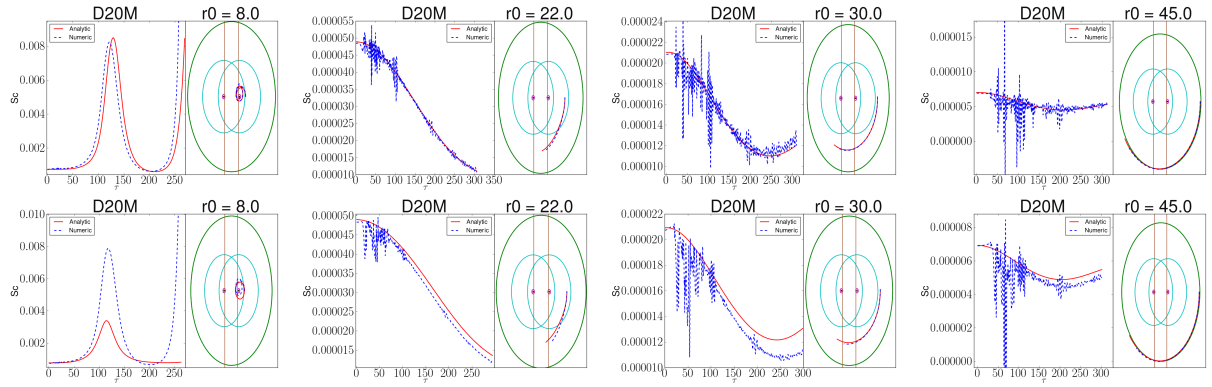

Figure 5.15: A comparison of how well the curvature eigenvalues of the second-order metric and first-order metric agree with the eigenvalues of the associated numerical metrics for the $D = 20M$ case. The top row shows the second-order results (which were previously shown in Fig. 5.10). The bottom row shows the first-order results. Unlike for the $D = 50M$ case, there are significant differences between the analytical and numerical scalars for the first-order metric even at larger distances from the black holes.

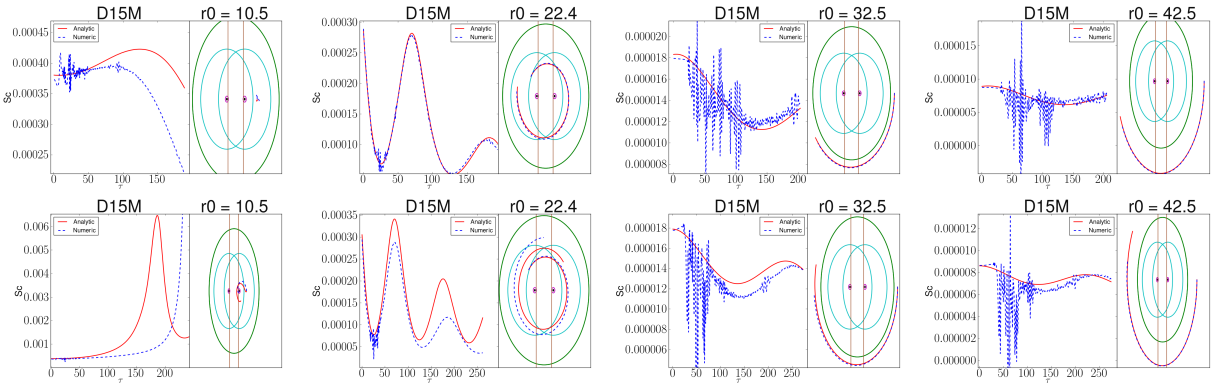

Figure 5.16: A comparison of how well the curvature eigenvalues of the second-order metric and first-order metric agree with the eigenvalues of the associated numerical metrics for the $D = 15M$ case. The top row shows the second-order results (which were previously shown in Fig. 5.11). The bottom row shows the first-order results. As with the $D = 20M$ case, there are significant differences between the analytical and numerical scalars for the first-order metric even at larger distances from the black holes.

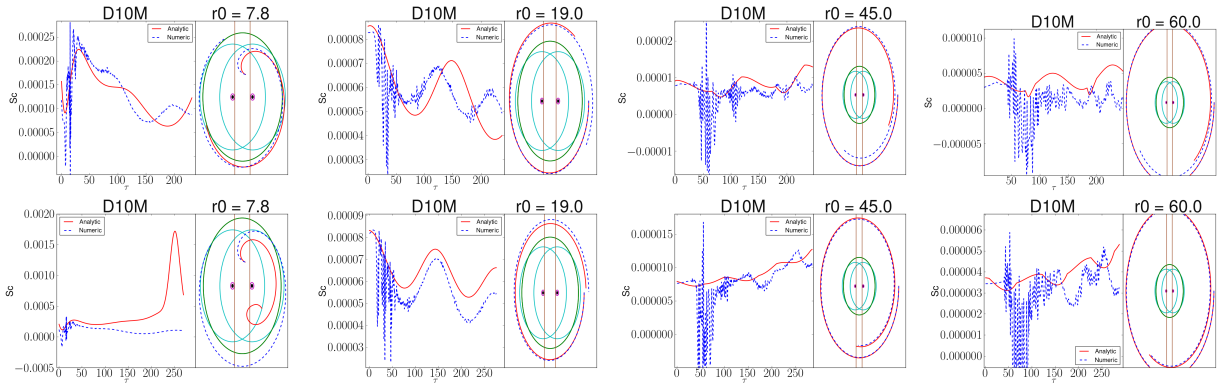

Figure 5.17: A comparison of how well the curvature eigenvalues of the second-order metric and first-order metric agree with the eigenvalues of the associated numerical metrics for the $D = 10M$ case. The top row shows the second-order results (which were previously shown in Fig. 5.11). The bottom row shows the first-order results. Here, we do not see a significant improvement of the second-order metric over the first-order one.

5.4 Discussion

In order to conclude if there are important systematic differences between the numerical and analytic metrics, we need to consider the possibility that the analytical metric is better approximated by an exact solution that does not agree exactly with the analytic metric on Σ_0. In such a case, one would expect that the appropriate initial conditions for the geodesics in the exact spacetime are not identical to those for the analytic one. But since small perturbations in the initial conditions of a geodesic can lead to significant differences on secular timescales (e.g., fall into one BH or the other, bounded versus unbounded, etc.), we considered here only geodesics that did not fall into the BHs or escape to large radii.

To see how small differences in the initial affect the geodesics we presented above (i.e., the stability of the above geodesics), we perturbed the initial velocities of a set of included geodesics by up to 10%. The results several geodesics are shown in Fig. 5.13 for the $D = 20M$ case. We find that the effect of a $\sim 10\%$ perturbation is smaller for the farther out geodesics. We also find that a perturbation of $\lesssim 1\%$ seems to be sufficient to get reasonable agreement between the geodesics in the numerical and analytic spacetimes for geodesics farther than $r_0 \sim 10M$ from the BHs. However,

for the closer geodesic, the agreement is much poorer than for further out ones, which matches the general trend seen in Fig. 5.10. Indeed, for the $r_0 = 6M$ case, no perturbation is able to reproduce the behavior of the numerical geodesic past $\tau \sim 75M$. To further support the argument that small differences in the scalars can be removed by small changes on the initial conditions of the geodesics but large differences cannot be removed, we examined geodesics a distance of $\sim 15M$ from the black holes for the $D = 15M$ and $D = 10M$ case. Here we see that no perturbation of the $D = 10M$ geodesic's initial conditions will lead to qualitative agreement between the analytical and numerical eigenvalues. On the other hand, for the $D = 15M$ very good agreement is achieved.

The fact that reasonable agreement between the analytical and numerical eigenvalues can be achieved by perturbing the analytical geodesics indicates a limitation of our basic method in that it may overemphasize the differences between to similar spacetimes. Large differences in the eigenvalues, like the ones seen in the $D = 20M$ case near the BHs (and $D = 10M$ everywhere) seem to be indicative of significant differences between the two spacetimes. On the other hand, where the differences are small, a given geodesic in one spacetime may behave nearly identically to one in the other, just with slightly different initial conditions. Consequently, one may expect that small differences in the eigenvalues will have little effect on, among others, gas dynamics.

One final note concerns the potential usefulness of our analysis at late times. The issue is that small differences in the trajectories generally grow on secular timescales. Thus the numerical and analytical eigenvalues represent curvature terms at increasingly different points of the spacetimes. For example, in the $D = 25M$ case (see Fig. 5.10) for the farthest geodesics, we see differences between the numerical and analytic eigenvalues after about $\tau = 400M$. From this point on, the geodesics will start taking different paths, and the scalars will disagree more and more, even though the two spacetimes are quite close, as is evident by the early time agreement of the scalars and the fact that the geodesics do not get significantly closer to either black hole. At close separations, these effects are larger and happen earlier. For example the $r_0 = 17.5M$ case shows significant deviations after $\tau = 250M$, and the $r_0 = 9.5M$ shows significant differences after $\tau = 75M$. The net effect is, the closer the two spacetimes are to each other (in the vicinity of the geodesic), the

longer in time the analysis is valid.

5.5 Conclusion

We introduced a new method for comparing the geodesic dynamics of two spacetimes. We used this method to compare the dynamics of recently developed analytical metrics that approximate the metric from an inspiralling black hole binary with fully nonlinear numerical evolutions of the Einstein equations. We find that the agreement in the dynamics between the two spacetimes is generally better for more separated binaries. Close to the black holes, as one might expect, we see the largest differences. Interestingly, we see that these differences scale in a highly nonlinear way with separation, with the $D = 10M$ spacetime showing much larger differences than the $D = 15M$ one. On the other hand, even for the $D = 50M$ case, there are measurable differences in the geodesic deviation scalars between the analytical and numerical spacetimes for geodesics farther than $r_0 \sim 100M$ from the black holes.

CHAPTER 6

DISCUSSION

Now this is not the end. It is not even the beginning of the end. But it is, perhaps, the end of the beginning.

Winston Churchill

The best time to take action toward a dream is yesterday; the worst is tomorrow; the best compromise is today.

Alvah Simon

6.1 Summary

General relativity is one of the cornerstones of 21st century physics. It revolutionized our understanding of the universe and black holes are one of the most fantastic predictions of general relativity. The detections of gravitational waves from binary black hole mergers opened up a new window on the universe because, by using gravitational waves, we can explore gravity in the strong field regime and see objects that may not be observable through other means. To learn from these observed gravitational waves, one needs to solve Einstein field equations to make theoretical predictions that then can be used to compare with observed data. In this thesis we have explored binary

black hole dynamics using both analytical approximate solutions of the Einstein field equations and numerical relativity.

In our first project we hybridized numerical relativity waveforms with analytical waveforms. In our analysis, we used the LIGO LaLSuite library to obtain the analytical waveforms. We use post-Newtonian waveforms based on the Taylor T4 approximant, the effective one body EOB model, and the available numerical waveforms using the SXS collaboration and RIT waveforms. Our method of hybridization is valid for generic precessing binaries. We first rotate the two waveforms using fixed Euler angles at a chosen time, such that, at that time, the instantaneous orbital plane is aligned with the xy plane. We then align the two waveform in an interval by choosing the appropriate time and phase shifts. The hybrids are then constructed by smoothly combining the resulting waveforms. We determined the accuracy of our hybrids using the mismatch of our hybrid with other available waveforms.

We successfully applied our method to both precessing and non-precessing systems. We also studied different errors in the hybrid construction that can affect the accuracy of hybrid. These include a study of the hybridization errors as a function of the length of numerical waveforms used to construct hybrids, the effects of tapering the waveform on the waveform error, and the mismatch of as a function of waveform mode.

In another project we developed a new technique to study the accuracy limits of a binary of black hole spacetime constructed via analytical solutions to the Einstein field equations. This spacetime was recently used to study binary supermassive black hole dynamics and their effects gas dynamics and electromagnetic signatures associated with the disk structures around these binaries. The accuracy of this spacetime has been studied before, but we developed a novel independent method. In this project we used numerical relativity to compare the dynamics of the analytic spacetime to a numerically evolved one by analyzing the geodesics of both spacetimes. We studied the differences in geodesics between the two spacetimes for different initial separations of the binary. Since the

two spacetimes are expressed in different gauges, we use the geometrically invariant scalars that represent geodesic deviations to probe the difference in the two evolutions. We showed that our method can be use to check the accuracy limitations of such analytical spacetimes in a generic way with less computational resources than, say, a full GRMHD evolution would entail. Our methods can also be used to improve accuracy of analytical spacetimes. We discussed the limitations of our method as well.

6.2 Future Work

We have developed a method to hybridize numerically generated waveforms with analytical model waveforms for generic precessing binaries. This method can be improved in many ways.

6.2.1 Future Analysis on Hybrid Error Estimation

Currently we have studied the accuracy limitation of the waveforms used in constructing the hybrids through the effects of time and phase shifts, the choice of hybrid interval, and the length of the numerical waveforms used to construct the hybrid. In the future we will extend this to do more detailed analysis. We are aiming to do following:

- We can improve the hybrid accuracy by constructing the hybrid in the co-precessing frame. This mean we will rotate the two waveforms completely into the co-precessing frame, hybridized them and then rotate back into inertial frame using appropriate reverse transformations which include the effects of time and phase shifting.

- Currently we are rigidly rotating waveform at fix time which is chosen to be the starting point of the hybrid interval. We have not yet tested how the different choices may affect the accuracy.

- By using different numerical resolutions of the numerical waveforms one can estimate how the numerical truncation errors effect the accuracy of the hybrids. Of course, the highest

numerical resolution gives the most accurate hybrid, but one can check how the accuracy of the hybrids improved with using different waveforms based on different numerical resolution.

- We are also aiming to do thorough analysis on how the width of hybrid interval affects the global waveform accuracy.

- We also want to do an analysis of using different models for the early inspiral and see which one can give the most accurate hybrids. The post-Newtonian waveforms can be constructed using different approximants which are based on different methods. We have currently used the Taylor T4 approximant, but in the future we want to use the Taylor T5 (which may improve accuracy of hybrids). In addition, improved SEOB model waveforms (which now only contains $\ell = 2$ modes) are under development. Using them to construct hybrids and to check the effects of non-quadrupole modes will be the aim of future investigations.

- We are also planing to use these hybrids to help in improving the accuracy of models waveforms such as the various phenomenological waveforms and surrogate models. In addition we can use these hybrids for testing general relativity for upcoming LIGO observations.

It is important to note that we currently checking the accuracy of hybrids mode by mode. A measure of the mismatch as function of orientation angles may also yield interesting results.

6.3 Acknowledgements

I would like to thank my dissertation advisor Dr. Yosef Zlochower for his great inspiration, guidance, and patience. I thank Dr. Richard O'Shaughnessy, Dr. Joshua Faber, Dr. Manuela Campanelli, Dr. Hiroyuki Nakano and Jacob Lange for many helpful discussions. I also gratefully acknowledge the support from the Fulbright PhD Program and the National Science Foundation (NSF) for financial support from Grants No. PHY-1607520, No. PHY-1707946, No. ACI1550436, No. AST-1516150, No. ACI-1516125, No. PHY1726215. In this work we used the Extreme Science and Engineering Discovery Environment (XSEDE) [allocation TGPHY060027N], which is

supported by NSF grant No. ACI-1548562. Computational resources were also provided by the NewHorizons and BlueSky Clusters at the Rochester Institute of Technology, which were supported by NSF grants No. PHY-0722703, No. DMS-0820923, No. AST-1028087, and No. PHY-1229173.

I am eternally grateful towards my family and friends in Pakistan as well as people in USA including the faculty, postdoctoral, and graduate student members of the Center for Computational Relativity and Gravitation research group and the Astrophysical Sciences and Technology program for their instruction and support in what has been one of the best ever opportunities of my life. I will strive to continue their example of excellence wherever I may go.

BIBLIOGRAPHY

[1] Benjamin P. Abbott et al. Sensitivity of the Advanced LIGO detectors at the beginning of gravitational wave astronomy. *Phys. Rev.*, D93(11):112004, 2016. [Addendum: Phys. Rev.D97,no.5,059901(2018)].

[2] Steven S. Gubser and Frans Pretorius. *The Little Book of Black Holes*. Princeton University Press, Princeton, NJ, USA, 2018.

[3] John Mitchell. Phil.Trans.Roy.Soc.Lond.,141,1232. 1796.

[4] P.S Laplace. Exposition du systeme du monde, L'imprimerie du Cercle-social, Paris, l'an IV de la République Françise. (Otherwise known as 1795).

[5] Karl Schwarzschild. On the gravitational field of a mass point according to Einstein's theory. *Sitzungsber. Preuss. Akad. Wiss. Berlin (Math. Phys.)*, 1916:189–196, 1916.

[6] Karl Schwarzschild. On the gravitational field of a sphere of incompressible fluid according to Einstein's theory. *Sitzungsber. Preuss. Akad. Wiss. Berlin (Math. Phys.)*, 1916:424–434, 1916.

[7] J. R. Oppenheimer and H. Snyder. On Continued gravitational contraction. *Phys. Rev.*, 56:455–459, 1939.

[8] Roy P. Kerr. Gravitational field of a spinning mass as an example of algebraically special metrics. *Phys. Rev. Lett.*, 11:237–238, 1963.

[9] R. Penrose. Gravitational Collapse and Space-Time Singularities. *Physical Review Letters*, 14:57–59, January 1965.

[10] S. W. Hawking and G. F. R. Ellis. *The Large Scale Structure of Space-Time*. Cambridge Monographs on Mathematical Physics. Cambridge University Press, 2011.

[11] Albert Einstein. Über Gravitationswellen. *Sitzungsber. Preuss. Akad. Wiss. Berlin (Math. Phys.)*, 1918:154–167, 1918.

[12] J. H. Taylor. Binary pulsars and relativistic gravity. In *100 years of gravity and accelerated frames: The deepest insights of Einstein and Yang-Mills*, pages 494–502, 1993. [,494(1993)].

[13] Steven Weinberg. *Gravitation and Cosmology*. John Wiley and Sons, New York, 1972.

[14] Robert M. Wald. *General Relativity*. Chicago Univ. Pr., Chicago, USA, 1984.

[15] Charles W. Misner, K. S. Thorne, and J. A. Wheeler. *Gravitation*. W. H. Freeman, San Francisco, 1973.

[16] Schutz Bernard. *A First Course in General Relativity*. Cambridge University Press, Cambridge, UK, 2009.

[17] AlcubierreBernard Miguel. *Introduction to 3+1 Numerical Relativity*. Oxford University Press, New York, Oxford.

[18] Jolien D. E. Creighton and Warren G. Anderson. *Gravitational-wave physics and astronomy: An introduction to theory, experiment and data analysis*. 2011.

[19] H. Ohanian and R. Ruffini. *Gravitation and space-time*. 1995.

[20] J. B. Hartle. *An introduction to Einstein's general relativity*. 2003.

[21] Sean M. Carroll. *Spacetime and geometry: An introduction to general relativity*. 2004.

[22] Hughston L. P. and Tod. K. P. *An Introduction to General Relativity*. 1991.

[23] Eric Poisson. *A Relativist's Toolkit: The Mathematics of Black-Hole Mechanics*. Cambridge University Press, 2009.

[24] Norbert Straumann. *General Relativity*. Graduate Texts in Physics. Springer, Dordrecht, 2013.

[25] P. C. W. Davies. *The Search for Gravity Waves*. 1989.

[26] Hans Stephani, D. Kramer, Malcolm A. H. MacCallum, Cornelius Hoenselaers, and Eduard Herlt. *Exact solutions of Einstein's field equations*. Cambridge Monographs on Mathematical Physics. Cambridge Univ. Press, Cambridge, 2003.

[27] E. Grant. *The Foundations of Modern Science in the Middle Ages*. Cambridge Univ. Pr., Cambridge, UK, 1996.

[28] P. G. Bergmann. *The Riddle of Gravitation*. 1987.

[29] Kip S. Thorne. *Black holes and time warps: Einstein's outrageous legacy*. 1994.

[30] Jürgen Renn, Matthias Schemmel, Christopher Smeenk, Christopher Martin, and Lindy Divarci, editors. *The Genesis of General Relativity*, volume 250 of *Boston Studies in the Philosophy and History of Science*. Springer, 2007.

[31] Subrahmanyan Chandrasekhar. The mathematical theory of black holes. In *Oxford, UK: Clarendon (1992) 646 p., OXFORD, UK: CLARENDON (1985) 646 P.*, 1985.

[32] Pierre Fleury. Gravitation: from Newton to Einstein. 2019.

[33] E T. Newman, R. Couch, K. Chinnapared, A. Exton, A. Prakash, and R. Torrence. Metric of a Rotating, Charged Mass. *J. Math. Phys.*, 6:918–919, 1965.

[34] G. D. Birkhoff and R. E. Langer. *Relativity and modern physics*. Relativity (Physics). Harvard University Press, Cambridge, Mass., USA, 1923. 2.1.9.1.

[35] A. S. Eddington. A comparison of Whitehead's and Einstein's formulas. *Nature*, 113:192, 1924. 2.1.9.1.

[36] David Finkelstein. Past-Future Asymmetry of the Gravitational Field of a Point Particle. *Phys. Rev.*, 110:965–967, 1958.

[37] P. Painleve. Le Mecanique Classique et la Theorie de la Relativite. *L'Astronomie*, 36:6–9, 1922.

[38] Allvar Gullstrand. *Allgemeine Lošung des statischen Einkoŕperproblems in der Einsteinschen Gravitationstheorie*, volume 16. 16,8 of *Arkiv foŕ matematik, astronomi och fysik*. Almqvist and Wiksell, Stockholm, 1922.

[39] G. Lemaitre. The expanding universe. *Gen. Rel. Grav.*, 29:641–680, 1997. [Annales Soc. Sci. Bruxelles A53,51(1933)].

[40] M. D. Kruskal. Maximal extension of Schwarzschild metric. *Phys. Rev.*, 119:1743–1745, 1960.

[41] G. Szekeres. On the singularities of a Riemannian manifold. *Publ. Math. Debrecen*, 7:285–301, 1960.

[42] Robert H. Boyer and Richard W. Lindquist. Maximal analytic extension of the Kerr metric. *J. Math. Phys.*, 8:265, 1967.

[43] M. Walker and R. Penrose. On quadratic first integrals of the geodesic equations for type [22] spacetimes. *Commun. Math. Phys.*, 18:265–274, 1970.

[44] Brandon Carter. Global structure of the Kerr family of gravitational fields. *Phys. Rev.*, 174:1559–1571, 1968.

[45] James M. Bardeen, William H. Press, and Saul A Teukolsky. Rotating black holes: Locally nonrotating frames, energy extraction, and scalar synchrotron radiation. *Astrophys. J.*, 178:347, 1972.

[46] S. L. Shapiro and S. A. Teukolsky. *Black holes, white dwarfs, and neutron stars: The physics of compact objects*. 1983.

[47] R. Penrose. Gravitational collapse: The role of general relativity. *Riv. Nuovo Cim.*, 1:252–276, 1969. [Gen. Rel. Grav.34,1141(2002)].

[48] Kip S. Thorne, R. H. Price, and D. A. Macdonald, editors. *BLACK HOLES: THE MEMBRANE PARADIGM*. 1986.

[49] R. Genzel, R. Schodel, Thomas Ott, A. Eckart, T. Alexander, F. Lacombe, D. Rouan, and B. Aschenbach. Near-infrared flares from accreting gas around the supermassive black hole at the galactic centre. *Nature*, 425:934–937, 2003.

[50] R. Penrose. Naked singularities. *Annals N. Y. Acad. Sci.*, 224:125–134, 1973.

[51] R. Penrose. Singularities and Time Asymmetry. In *General Relativity: An Einstein Centenary Survey*, pages 581–638. 1980.

[52] Robert P. Geroch and G. T. Horowitz. Global structure of spacetimes. In *General Relativity: An Einstein Centenary Survey*, pages 212–293. 1979.

[53] Albert Einstein. Approximative Integration of the Field Equations of Gravitation. *Sitzungsber. Preuss. Akad. Wiss. Berlin (Math. Phys.)*, 1916:688–696, 1916.

[54] Sean M. Carroll. Lecture notes on general relativity. 1997.

[55] Albert Einstein and N. Rosen. On Gravitational waves. *J. Franklin Inst.*, 223:43–54, 1937.

[56] Hermann Bondi. Plane gravitational waves in general relativity. *Nature*, 179:1072–1073, 1957.

[57] F. A. E. Pirani. Invariant formulation of gravitational radiation theory. *Phys. Rev.*, 105:1089–1099, 1957.

[58] H. Bondi, F. A. E. Pirani, and I. Robinson. Gravitational waves in general relativity. 3. Exact plane waves. *Proc. Roy. Soc. Lond.*, A251:519–533, 1959.

[59] Ivor Robinson and A. Trautman. Spherical Gravitational Waves. *Phys. Rev. Lett.*, 4:431–432, 1960.

[60] Andrzej Trautman. Boundary Conditions at Infinity for Physical Theories. *Bull. Acad. Pol. Sci. Ser. Sci. Math. Astron. Phys.*, 6(6):403–406, 1958.

[61] Andrzej Trautman. Radiation and Boundary Conditions in the Theory of Gravitation. *Bull. Acad. Pol. Sci. Ser. Sci. Math. Astron. Phys.*, 6(6):407–412, 1958.

[62] J. Weber. Observation of the Thermal Fluctuations of a Gravitational-Wave Detector. *Phys. Rev. Lett.*, 17:1228–1230, 1966.

[63] J. Weber. Evidence for discovery of gravitational radiation. *Phys. Rev. Lett.*, 22:1320–1324, 1969.

[64] J. Weber. Anisotropy and polarization in the gravitational-radiation experiments. *Phys. Rev. Lett.*, 25:180–184, 1970.

[65] GWTC-1: A Gravitational-Wave Transient Catalog of Compact Binary Mergers Observed by LIGO and Virgo during the First and Second Observing Runs. 2018.

[66] Rainer Weiss. Electromagnetically coupled broadband gravitational antenna. *Quarterly Progress Report, Research Lab. of Electronics, M.I.T., 105, 54Phys*, 1972.

[67] B. P. Abbott et al. LIGO: The Laser interferometer gravitational-wave observatory. *Rept. Prog. Phys.*, 72:076901, 2009.

[68] Daniel Sigg. Status of the LIGO detectors. *Class. Quant. Grav.*, 25:114041, 2008.

[69] J. R. Smith. The Path to the enhanced and advanced LIGO gravitational-wave detectors. *Class. Quant. Grav.*, 26:114013, 2009.

[70] J. Aasi et al. Advanced LIGO. *Class. Quant. Grav.*, 32:074001, 2015.

[71] T. Accadia et al. Status and perspectives of the Virgo gravitational wave detector. *J. Phys. Conf. Ser.*, 203:012074, 2010.

[72] F. Acernese et al. Advanced Virgo: a second-generation interferometric gravitational wave detector. *Class. Quant. Grav.*, 32(2):024001, 2015.

[73] B. Willke et al. The GEO 600 gravitational wave detector. *Class. Quant. Grav.*, 19:1377–1387, 2002.

[74] Harald Luck et al. The upgrade of GEO600. *J. Phys. Conf. Ser.*, 228:012012, 2010.

[75] M. Ando et al. Analysis methods for burst gravitational waves with TAMA data. *Class. Quant. Grav.*, 21:S1679–S1684, 2004.

[76] M. Ando. Current status of the TAMA300 gravitational-wave detector. *Class. Quant. Grav.*, 22:S881–S889, 2005.

[77] John Miller, Lisa Barsotti, Salvatore Vitale, Peter Fritschel, Matthew Evans, and Daniel Sigg. Prospects for doubling the range of Advanced LIGO. *Phys. Rev.*, D91:062005, 2015.

[78] F. Acernese et al. Status of Advanced Virgo. *EPJ Web Conf.*, 182:02003, 2018.

[79] B. P. Abbott et al. Prospects for Observing and Localizing Gravitational-Wave Transients with Advanced LIGO, Advanced Virgo and KAGRA. *Living Rev. Rel.*, 21(1):3, 2018.

[80] T. Akutsu et al. KAGRA: 2.5 Generation Interferometric Gravitational Wave Detector. *Nat. Astron.*, 3(1):35–40, 2019.

[81] David Shoemaker. Gravitational wave astronomy with LIGO and similar detectors in the next decade. 2019.

[82] M. Punturo et al. The Einstein Telescope: A third-generation gravitational wave observatory. *Class. Quant. Grav.*, 27:194002, 2010.

[83] Benjamin P Abbott et al. Exploring the Sensitivity of Next Generation Gravitational Wave Detectors. *Class. Quant. Grav.*, 34(4):044001, 2017.

[84] B. S. Sathyaprakash and Bernard F. Schutz. Physics, astrophysics and cosmology with gravitational waves. *Living Reviews in Relativity*, 12(1):2, Mar 2009.

[85] Sheila Rowan and Jim Hough. Gravitational wave detection by interferometry (ground and space). *Living Rev. Rel.*, 3:3, 2000.

[86] Scott A. Hughes, Szabolcs Marka, Peter L. Bender, and Craig J. Hogan. New physics and astronomy with the new gravitational wave observatories. *eConf*, C010630:P402, 2001.

[87] Luc Blanchet. Gravitational Radiation from Post-Newtonian Sources and Inspiralling Compact Binaries. *Living Rev. Rel.*, 17:2, 2014.

[88] Frans Pretorius. Evolution of binary black hole spacetimes. *Phys. Rev. Lett.*, 95:121101, 2005.

[89] Manuela Campanelli, C. O. Lousto, P. Marronetti, and Y. Zlochower. Accurate evolutions of orbiting black-hole binaries without excision. *Phys. Rev. Lett.*, 96:111101, 2006.

[90] John G. Baker, Joan Centrella, Dae-Il Choi, Michael Koppitz, and James van Meter. Gravitational wave extraction from an inspiraling configuration of merging black holes. *Phys. Rev. Lett.*, 96:111102, 2006.

[91] P. C. Peters and J. Mathews. Gravitational radiation from point masses in a Keplerian orbit. *Phys. Rev.*, 131:435–439, 1963.

[92] Luc Blanchet, Thibault Damour, Gilles Esposito-Farese, and Bala R. Iyer. Gravitational radiation from inspiralling compact binaries completed at the third post-Newtonian order. *Phys. Rev. Lett.*, 93:091101, 2004.

[93] Alessandra Buonanno, Yanbei Chen, and Thibault Damour. Transition from inspiral to plunge in precessing binaries of spinning black holes. *Phys. Rev.*, D74:104005, 2006.

[94] Thibault Damour, Piotr Jaranowski, and Gerhard Schaefer. Dimensional regularization of the gravitational interaction of point masses. *Phys. Lett.*, B513:147–155, 2001.

[95] Theocharis A. Apostolatos, Curt Cutler, Gerald J. Sussman, and Kip S. Thorne. Spin induced orbital precession and its modulation of the gravitational wave forms from merging binaries. *Phys. Rev.*, D49:6274–6297, 1994.

[96] Luc Blanchet, Alessandra Buonanno, and Guillaume Faye. Higher-order spin effects in the dynamics of compact binaries. II. Radiation field. *Phys. Rev.*, D74:104034, 2006. [Erratum: Phys. Rev.D81,089901(2010)].

[97] Lawrence E. Kidder. Coalescing binary systems of compact objects to postNewtonian 5/2 order. 5. Spin effects. *Phys. Rev.*, D52:821–847, 1995.

[98] Thibault Damour. Coalescence of two spinning black holes: an effective one-body approach. *Phys. Rev.*, D64:124013, 2001.

[99] Balazs Mikoczi, Matyas Vasuth, and Laszlo A. Gergely. Self-interaction spin effects in inspiralling compact binaries. *Phys. Rev.*, D71:124043, 2005.

[100] Eric Poisson. Gravitational waves from inspiraling compact binaries: The Quadrupole moment term. *Phys. Rev.*, D57:5287–5290, 1998.

[101] D. Brown, S. Fairhurst, B. Krishnan, R. A. Mercer, R. K. Kopparapu, L. Santamaria, and J. T. Whelan. Data formats for numerical relativity waves. 2007.

[102] P. Ajith. Addressing the spin question in gravitational-wave searches: Waveform templates for inspiralling compact binaries with nonprecessing spins. *Phys. Rev.*, D84:084037, 2011.

[103] P. Ajith et al. Inspiral-merger-ringdown waveforms for black-hole binaries with non-precessing spins. *Phys. Rev. Lett.*, 106:241101, 2011.

[104] Kashif Alvi. Energy and angular momentum flow into a black hole in a binary. *Phys. Rev.*, D64:104020, 2001.

[105] Michael Boyle, Duncan A. Brown, Lawrence E. Kidder, Abdul H. Mroue, Harald P. Pfeiffer, Mark A. Scheel, Gregory B. Cook, and Saul A. Teukolsky. High-accuracy comparison of numerical relativity simulations with post-Newtonian expansions. *Phys. Rev.*, D76:124038, 2007.

[106] Alessandra Buonanno, Bala Iyer, Evan Ochsner, Yi Pan, and B. S. Sathyaprakash. Comparison of post-Newtonian templates for compact binary inspiral signals in gravitational-wave detectors. *Phys. Rev.*, D80:084043, 2009.

[107] K. G. Arun, Alessandra Buonanno, Guillaume Faye, and Evan Ochsner. Higher-order spin effects in the amplitude and phase of gravitational waveforms emitted by inspiraling compact binaries: Ready-to-use gravitational waveforms. *Phys. Rev.*, D79:104023, 2009. [Erratum: Phys. Rev.D84,049901(2011)].

[108] Luc Blanchet, Guillaume Faye, Bala R. Iyer, and Siddhartha Sinha. The Third post-Newtonian gravitational wave polarisations and associated spherical harmonic modes for inspiralling compact binaries in quasi-circular orbits. *Class. Quant. Grav.*, 25:165003, 2008. [Erratum: Class. Quant. Grav.29,239501(2012)].

[109] J. N. Goldberg, A. J. MacFarlane, E. T. Newman, F. Rohrlich, and E. C. G. Sudarshan. Spin s spherical harmonics and edth. *J. Math. Phys.*, 8:2155, 1967.

[110] L. Santamaria et al. Matching post-Newtonian and numerical relativity waveforms: systematic errors and a new phenomenological model for non-precessing black hole binaries. *Phys. Rev.*, D82:064016, 2010.

[111] Michael Boyle, Lawrence E. Kidder, Serguei Ossokine, and Harald P. Pfeiffer. Gravitational-wave modes from precessing black-hole binaries. 2014.

[112] B. M. Barker and R. F. O'Connell. Gravitational Two-Body Problem with Arbitrary Masses, Spins, and Quadrupole Moments. *Phys. Rev.*, D12:329–335, 1975.

[113] Sylvain Marsat, Alejandro Bohé, Luc Blanchet, and Alessandra Buonanno. Next-to-leading tail-induced spin–orbit effects in the gravitational radiation flux of compact binaries. *Class. Quant. Grav.*, 31:025023, 2014.

[114] Alejandro Bohé, Guillaume Faye, Sylvain Marsat, and Edward K. Porter. Quadratic-in-spin effects in the orbital dynamics and gravitational-wave energy flux of compact binaries at the 3PN order. *Class. Quant. Grav.*, 32(19):195010, 2015.

[115] Alejandro Bohe, Sylvain Marsat, Guillaume Faye, and Luc Blanchet. Next-to-next-to-leading order spin-orbit effects in the near-zone metric and precession equations of compact binaries. *Class. Quant. Grav.*, 30:075017, 2013.

[116] Sylvain Marsat. Cubic order spin effects in the dynamics and gravitational wave energy flux of compact object binaries. *Class. Quant. Grav.*, 32(8):085008, 2015.

[117] Michele Levi and Jan Steinhoff. Leading order finite size effects with spins for inspiralling compact binaries. *JHEP*, 06:059, 2015.

[118] Alessandra Buonanno, Yan-bei Chen, and Michele Vallisneri. Detecting gravitational waves from precessing binaries of spinning compact objects: Adiabatic limit. *Phys. Rev.*, D67:104025, 2003. [Erratum: Phys. Rev.D74,029904(2006)].

[119] A. Buonanno and T. Damour. Effective one-body approach to general relativistic two-body dynamics. *Phys. Rev.*, D59:084006, 1999.

[120] Alessandra Buonanno and Thibault Damour. Transition from inspiral to plunge in binary black hole coalescences. *Phys. Rev.*, D62:064015, 2000.

[121] Thibault Damour, Bala R. Iyer, and B. S. Sathyaprakash. Improved filters for gravitational waves from inspiralling compact binaries. *Phys. Rev.*, D57:885–907, 1998.

[122] Thibault Damour, Piotr Jaranowski, and Gerhard Schaefer. On the determination of the last stable orbit for circular general relativistic binaries at the third postNewtonian approximation. *Phys. Rev.*, D62:084011, 2000.

[123] Alessandra Buonanno, Yi Pan, John G. Baker, Joan Centrella, Bernard J. Kelly, Sean T. McWilliams, and James R. van Meter. Toward faithful templates for non-spinning binary black holes using the effective-one-body approach. *Phys. Rev.*, D76:104049, 2007.

[124] Alessandra Buonanno, Yi Pan, Harald P. Pfeiffer, Mark A. Scheel, Luisa T. Buchman, and Lawrence E. Kidder. Effective-one-body waveforms calibrated to numerical relativity simulations: Coalescence of non-spinning, equal-mass black holes. *Phys. Rev.*, D79:124028, 2009.

[125] Thibault Damour and Alessandro Nagar. An Improved analytical description of inspiralling and coalescing black-hole binaries. *Phys. Rev.*, D79:081503, 2009.

[126] Thibault Damour, Alessandro Nagar, Ernst Nils Dorband, Denis Pollney, and Luciano Rezzolla. Faithful Effective-One-Body waveforms of equal-mass coalescing black-hole binaries. *Phys. Rev.*, D77:084017, 2008.

[127] Thibault Damour, Alessandro Nagar, Mark Hannam, Sascha Husa, and Bernd Bruegmann. Accurate Effective-One-Body waveforms of inspiralling and coalescing black-hole binaries. *Phys. Rev.*, D78:044039, 2008.

[128] Yi Pan, Alessandra Buonanno, Michael Boyle, Luisa T. Buchman, Lawrence E. Kidder, Harald P. Pfeiffer, and Mark A. Scheel. Inspiral-merger-ringdown multipolar waveforms of non-spinning black-hole binaries using the effective-one-body formalism. *Phys. Rev.*, D84:124052, 2011.

[129] Yi Pan, Alessandra Buonanno, Luisa T. Buchman, Tony Chu, Lawrence E. Kidder, Harald P. Pfeiffer, and Mark A. Scheel. Effective-one-body waveforms calibrated to numerical relativity simulations: coalescence of non-precessing, spinning, equal-mass black holes. *Phys. Rev.*, D81:084041, 2010.

[130] Andrea Taracchini, Yi Pan, Alessandra Buonanno, Enrico Barausse, Michael Boyle, Tony Chu, Geoffrey Lovelace, Harald P. Pfeiffer, and Mark A. Scheel. Prototype effective-one-body model for nonprecessing spinning inspiral-merger-ringdown waveforms. *Phys. Rev.*, D86:024011, 2012.

[131] Nicolas Yunes, Alessandra Buonanno, Scott A. Hughes, M. Coleman Miller, and Yi Pan. Modeling Extreme Mass Ratio Inspirals within the Effective-One-Body Approach. *Phys. Rev. Lett.*, 104:091102, 2010.

[132] Andrea Taracchini et al. Effective-one-body model for black-hole binaries with generic mass ratios and spins. *Phys. Rev.*, D89(6):061502, 2014.

[133] Yi Pan, Alessandra Buonanno, Andrea Taracchini, Lawrence E. Kidder, Abdul H. Mroué, Harald P. Pfeiffer, Mark A. Scheel, and Béla Szilágyi. Inspiral-merger-ringdown waveforms of spinning, precessing black-hole binaries in the effective-one-body formalism. *Phys. Rev.*, D89(8):084006, 2014.

[134] Paolo Pani. Advanced Methods in Black-Hole Perturbation Theory. *Int. J. Mod. Phys.*, A28:1340018, 2013.

[135] R. Arnowitt and S. Deser. Quantum Theory of Gravitation: General Formulation and Linearized Theory. *Phys. Rev.*, 113:745–750, 1959.

[136] Richard L. Arnowitt, Stanley Deser, and Charles W. Misner. Dynamical Structure and Definition of Energy in General Relativity. *Phys. Rev.*, 116:1322–1330, 1959.

[137] Richard L. Arnowitt, Stanley Deser, and Charles W. Misner. Canonical variables for general relativity. *Phys. Rev.*, 117:1595–1602, 1960.

[138] R. Arnowitt, S. Deser, and C. W. Misner. Finite Self-Energy of Classical Point Particles. *Phys. Rev. Lett.*, 4:375–377, 1960.

[139] R. Arnowitt, S. Deser, and C. W. Misner. Energy and the Criteria for Radiation in General Relativity. *Phys. Rev.*, 118:1100–1104, 1960.

[140] Richard L. Arnowitt, Stanley Deser, and Charles W. Misner. Gravitational-electromagnetic coupling and the classical self-energy problem. *Phys. Rev.*, 120:313–320, 1960.

[141] R. Arnowitt, S. Deser, and C. W. Misner. Interior Schwarzschild solutions and interpretation of source terms. *Phys. Rev.*, 120:321, 1960.

[142] Richard L. Arnowitt, Stanley Deser, and Charles W. Misner. Wave zone in general relativity. *Phys. Rev.*, 121:1556, 1961.

[143] Richard L. Arnowitt, Stanley Deser, and Charles W. Misner. Coordinate invariance and energy expressions in general relativity. *Phys. Rev.*, 122:997, 1961.

[144] Richard L. Arnowitt, Stanley Deser, and Charles W. Misner. The Dynamics of general relativity. *Gen. Rel. Grav.*, 40:1997–2027, 2008.

[145] Thomas W. Baumgarte and Stuart L. Shapiro. *Numerical Relativity: Solving Einstein's Equations on the Computer*. Cambridge University Press, 2010.

[146] Masaru Shibata. *Numerical Relativity*. World Scientific Publishing Co., Inc., River Edge, NJ, USA, 2015.

[147] Eric Gourgoulhon. 3+1 formalism and bases of numerical relativity. 2007.

[148] A. A. Lichnerowicz. *L'intégration des équations de la gravitation relativiste et le problème des n corps. J. Math. Pures Appl.* ***23***, 37, 1944.

[149] James W. York, Jr. Conformal 'thin sandwich' data for the initial-value problem. *Phys. Rev. Lett.*, 82:1350–1353, 1999.

[150] Harald P. Pfeiffer and James W. York, Jr. Extrinsic curvature and the Einstein constraints. *Phys. Rev.*, D67:044022, 2003.

[151] Harald P. Pfeiffer and James W. York, Jr. Uniqueness and non-uniqueness in the Einstein constraints. *Phys. Rev. Lett.*, 95:091101, 2005.

[152] Thomas W. Baumgarte, Niall O Murchadha, and Harald P. Pfeiffer. The Einstein constraints: Uniqueness and non-uniqueness in the conformal thin sandwich approach. *Phys. Rev.*, D75:044009, 2007.

[153] Darragh M. Walsh. Non-uniqueness in conformal formulations of the Einstein constraints. *Class. Quant. Grav.*, 24:1911–1926, 2007.

[154] Gregory B. Cook. Initial data for numerical relativity. *Living Rev. Rel.*, 3:5, 2000.

[155] James W. York, Jr. Kinematics and Dynamics of General Relativity. In *Proceedings, Sources of Gravitational Radiation: Seattle, WA, USA, July 24 - August 4, 1978*, pages 83–126.

[156] Niall O Murchadha and James W. York. Gravitational energy. *Phys. Rev.*, D10:2345–2357, 1974.

[157] James R. van Meter, John G. Baker, Michael Koppitz, and Dae-Il Choi. How to move a black hole without excision: Gauge conditions for the numerical evolution of a moving puncture. *Phys. Rev.*, D73:124011, 2006.

[158] Carsten Gundlach and Jose M. Martin-Garcia. Well-posedness of formulations of the Einstein equations with dynamical lapse and shift conditions. *Phys. Rev.*, D74:024016, 2006.

[159] Zachariah B. Etienne, John G. Baker, Vasileios Paschalidis, Bernard J. Kelly, and Stuart L. Shapiro. Improved Moving Puncture Gauge Conditions for Compact Binary Evolutions. *Phys. Rev.*, D90(6):064032, 2014.

[160] H. Kreiss and J. Lorenz. *Initial-Boundary Value Problems and the Navier-Stokes Equations.* Society for Industrial and Applied Mathematics, 2004.

[161] T. Nakamura, K. Oohara, and Y. Kojima. General Relativistic Collapse to Black Holes and Gravitational Waves from Black Holes. *Prog. Theor. Phys. Suppl.*, 90:1–218, 1987.

[162] Masaru Shibata and Takashi Nakamura. Evolution of three-dimensional gravitational waves: Harmonic slicing case. *Phys. Rev.*, D52:5428–5444, 1995.

[163] Thomas W. Baumgarte and Stuart L. Shapiro. On the numerical integration of Einstein's field equations. *Phys. Rev.*, D59:024007, 1999.

[164] Daniela Alic, Carles Bona-Casas, Carles Bona, Luciano Rezzolla, and Carlos Palenzuela. Conformal and covariant formulation of the Z4 system with constraint-violation damping. *Phys. Rev.*, D85:064040, 2012.

[165] Carsten Gundlach, Jose M. Martin-Garcia, Gioel Calabrese, and Ian Hinder. Constraint damping in the Z4 formulation and harmonic gauge. *Class. Quant. Grav.*, 22:3767–3774, 2005.

[166] R. D. Richtmyer and K. W. Morton. *Difference methods for initial-value problems.* 1967.

[167] L. Smarr. Basic concepts in finite differencing of partial differential equations. In *Proceedings, Sources of Gravitational Radiation: Seattle, WA, USA, July 24 - August 4, 1978*, pages 139–159, 1979.

[168] William H. Press, Saul A. Teukolsky, William T. Vetterling, and Brian P. Flannery. Numerical Recipes: The Art of Scientific Computing, Third edition. *Cambridge University Press, Cambridge*, 2007.

[169] A. R. Mitchell and R. Wait. *The Finite Element Method in Partial Differential Equations.* 1977.

[170] C. R. Evan, L. S. Finn, and D. W. Hobill. *Frontiers in Numerical Relativity.* 1989.

[171] S. Bonazzola and J.-A. Marck. *Pseudo-spectral methods applied to gravitational collapse.*, pages 239–253. 1989.

[172] Lawrence E. Kidder and Lee Samuel Finn. Spectral methods for numerical relativity: The Initial data problem. *Phys. Rev.*, D62:084026, 2000.

[173] Lawrence E. Kidder, Mark A. Scheel, Saul A. Teukolsky, Eric D. Carlson, and Gregory B. Cook. Black hole evolution by spectral methods. *Phys. Rev.*, D62:084032, 2000.

[174] Scott A. Hughes, Charles R. Keeton, Paul Walker, Kevin T. Walsh, Stuart L. Shapiro, and Saul A. Teukolsky. Finding black holes in numerical space-times. *Phys. Rev.*, D49:4004–4015, 1994.

[175] F. H. Vincent, T. Paumard, E. Gourgoulhon, and G. Perrin. GYOTO: a new general relativistic ray-tracing code. *Class. Quant. Grav.*, 28:225011, 2011.

[176] Frederic H. Vincent, Eric Gourgoulhon, and Jerome Novak. 3+1 geodesic equation and images in numerical spacetimes. *Class. Quant. Grav.*, 29:245005, 2012.

[177] Jonathan Thornburg. Event and apparent horizon finders for 3+1 numerical relativity. *Living Rev. Rel.*, 10:3, 2007.

[178] Peter Anninos, David Bernstein, Steven Brandt, Joseph Libson, Joan Masso, Edward Seidel, Larry Smarr, Wai-Mo Suen, and Paul Walker. Dynamics of apparent and event horizons. *Phys. Rev. Lett.*, 74:630–633, 1995.

[179] Joseph Libson, Joan Masso, Edward Seidel, Wai-Mo Suen, and Paul Walker. Event horizons in numerical relativity. 1: Methods and tests. *Phys. Rev.*, D53:4335–4350, 1996.

[180] Erik Schnetter, Badri Krishnan, and Florian Beyer. Introduction to dynamical horizons in numerical relativity. *Phys. Rev.*, D74:024028, 2006.

[181] Olaf Dreyer, Badri Krishnan, Deirdre Shoemaker, and Erik Schnetter. Introduction to isolated horizons in numerical relativity. *Phys. Rev.*, D67:024018, 2003.

[182] Abhay Ashtekar and Badri Krishnan. Isolated and dynamical horizons and their applications. *Living Rev. Rel.*, 7:10, 2004.

[183] J. Thornburg. , Numerical Relativity in Black Hole Spacetimes, Ph.D. thesis. *University of British Columbia, Vancouver, British Columbia*, 1993.

[184] J Thornburg. Coordinates and boundary conditions for the general relativistic initial data problem. *Classical and Quantum Gravity*, 4(5):1119–1131, sep 1987.

[185] Edward Seidel and Wai-Mo Suen. Towards a singularity proof scheme in numerical relativity. *Phys. Rev. Lett.*, 69:1845–1848, 1992.

[186] Mark A. Scheel, Stuart L. Shapiro, and Saul A. Teukolsky. Collapse to black holes in Brans-Dicke theory. 1. Horizon boundary conditions for dynamical space-times. *Phys. Rev.*, D51:4208–4235, 1995.

[187] Miguel Alcubierre and Bernd Bruegmann. Simple excision of a black hole in (3+1)-numerical relativity. *Phys. Rev.*, D63:104006, 2001.

[188] Hwei-Jang Yo, Thomas W. Baumgarte, and Stuart L. Shapiro. Improved numerical stability of stationary black hole evolution calculations. *Phys. Rev.*, D66:084026, 2002.

[189] Bernd Bruegmann, Wolfgang Tichy, and Nina Jansen. Numerical simulation of orbiting black holes. *Phys. Rev. Lett.*, 92:211101, 2004.

[190] Miguel Alcubierre et al. Dynamical evolution of quasi-circular binary black hole data. *Phys. Rev.*, D72:044004, 2005.

[191] Frans Pretorius. Numerical relativity using a generalized harmonic decomposition. *Class. Quant. Grav.*, 22:425–452, 2005.

[192] Bernd Bruegmann. Binary black hole mergers in 3-d numerical relativity. *Int. J. Mod. Phys.*, D8:85, 1999.

[193] Mark D. Hannam, Charles R. Evans, Gregory B. Cook, and Thomas W. Baumgarte. Can a combination of the conformal thin sandwich and puncture methods yield binary black hole solutions in quasiequilibrium? *Phys. Rev.*, D68:064003, 2003.

[194] Bernd Reimann and Bernd Bruegmann. Maximal slicing for puncture evolutions of Schwarzschild and Reissner-Nordstrom black holes. *Phys. Rev.*, D69:044006, 2004.

[195] Miguel Alcubierre, Werner Benger, Bernd Bruegmann, Gerd Lanfermann, Lars Nerger, Edward Seidel, and Ryoji Takahashi. The 3-D grazing collision of two black holes. *Phys. Rev. Lett.*, 87:271103, 2001.

[196] Bernd Bruegmann, Jose A. Gonzalez, Mark Hannam, Sascha Husa, Ulrich Sperhake, and Wolfgang Tichy. Calibration of Moving Puncture Simulations. *Phys. Rev.*, D77:024027, 2008.

[197] Mark Hannam, Sascha Husa, Frank Ohme, Bernd Bruegmann, and Niall O'Murchadha. Wormholes and trumpets: The Schwarzschild spacetime for the moving-puncture generation. *Phys. Rev.*, D78:064020, 2008.

[198] Nigel T. Bishop and Luciano Rezzolla. Extraction of Gravitational Waves in Numerical Relativity. *Living Rev. Rel.*, 19:2, 2016.

[199] Tullio Regge and John A. Wheeler. Stability of a Schwarzschild singularity. *Phys. Rev.*, 108:1063–1069, 1957.

[200] Frank J. Zerilli. Effective potential for even parity Regge-Wheeler gravitational perturbation equations. *Phys. Rev. Lett.*, 24:737–738, 1970.

[201] F. J. Zerilli. Gravitational field of a particle falling in a schwarzschild geometry analyzed in tensor harmonics. *Phys. Rev.*, D2:2141–2160, 1970.

[202] V. Moncrief. Gravitational perturbations of spherically symmetric systems. I. The exterior problem. *Annals Phys.*, 88:323–342, 1974.

[203] K. S. Thorne. Multipole Expansions of Gravitational Radiation. *Rev. Mod. Phys.*, 52:299–339, 1980.

[204] Alessandro Nagar and Luciano Rezzolla. Gauge-invariant non-spherical metric perturbations of Schwarzschild black-hole spacetimes. *Class. Quant. Grav.*, 22:R167, 2005. [Erratum: Class. Quant. Grav.23,4297(2006)].

[205] Roger Penrose. Gravitational collapse and space-time singularities. *Phys. Rev. Lett.*, 14:57–59, 1965.

[206] Ian Hinder, Barry Wardell, and Eloisa Bentivegna. Falloff of the Weyl scalars in binary black hole spacetimes. *Phys. Rev.*, D84:024036, 2011.

[207] Christian Reisswig and Denis Pollney. Notes on the integration of numerical relativity waveforms. *Class. Quant. Grav.*, 28:195015, 2011.

[208] Manuela Campanelli, Carlos O. Lousto, Hiroyuki Nakano, and Yosef Zlochower. Comparison of Numerical and Post-Newtonian Waveforms for Generic Precessing Black-Hole Binaries. *Phys. Rev.*, D79:084010, 2009.

[209] Benjamin Aylott et al. Testing gravitational-wave searches with numerical relativity waveforms: Results from the first Numerical INJection Analysis (NINJA) project. *Class. Quant. Grav.*, 26:165008, 2009.

[210] D. J. A. McKechan, C. Robinson, and B. S. Sathyaprakash. A tapering window for time-domain templates and simulated signals in the detection of gravitational waves from coalescing compact binaries. *Class. Quant. Grav.*, 27:084020, 2010.

[211] Jeffrey Winicour. Characteristic evolution and matching. *Living Rev. Rel.*, 4:3, 2001.

[212] Nigel T. Bishop, Roberto Gomez, Luis Lehner, and Jeffrey Winicour. Cauchy-characteristic extraction in numerical relativity. *Phys. Rev.*, D54:6153–6165, 1996.

[213] M. C. Babiuc, B. Szilagyi, J. Winicour, and Y. Zlochower. A Characteristic Extraction Tool for Gravitational Waveforms. *Phys. Rev.*, D84:044057, 2011.

[214] Tony Chu, Heather Fong, Prayush Kumar, Harald P. Pfeiffer, Michael Boyle, Daniel A. Hemberger, Lawrence E. Kidder, Mark A. Scheel, and Bela Szilagyi. On the accuracy and precision of numerical waveforms: Effect of waveform extraction methodology. *Class. Quant. Grav.*, 33(16):165001, 2016.

[215] Frank Löffler, Joshua Faber, Eloisa Bentivegna, Tanja Bode, Peter Diener, Roland Haas, Ian Hinder, Bruno C Mundim, Christian D Ott, Erik Schnetter, Gabrielle Allen, Manuela Campanelli, and Pablo Laguna. The Einstein Toolkit: A Community Computational Infrastructure for Relativistic Astrophysics. *Class. Quant. Grav.*, 29:115001, 2012.

[216] Philipp Mösta, Bruno C. Mundim, Joshua A. Faber, Roland Haas, Scott C. Noble, Tanja Bode, Frank Löffler, Christian D. Ott, Christian Reisswig, and Erik Schnetter. GRHydro: A new open source general-relativistic magnetohydrodynamics code for the Einstein Toolkit. *Class. Quant. Grav.*, 31:015005, 2014.

[217] Einstein Toolkit home page: `http://einsteintoolkit.org`.

[218] Miguel Zilhão and Frank Löffler. An Introduction to the Einstein Toolkit. *Int. J. Mod. Phys.*, A28:1340014, 2013.

[219] G. Allen, T. Goodale, and E. Seidel. The cactus computational collaboratory: enabling technologies for relativistic astrophysics, and a toolkit for solving pde's by communities in science and engineering. In *Proceedings. Frontiers '99. Seventh Symposium on the Frontiers of Massively Parallel Computation*, pages 36–41, Feb 1999.

[220] Erik Schnetter, Scott H. Hawley, and Ian Hawke. Evolutions in 3-D numerical relativity using fixed mesh refinement. *Class. Quant. Grav.*, 21:1465–1488, 2004.

[221] Erik Schnetter, Christian D. Ott, Gabrielle Allen, Peter Diener, Tom Goodale, Thomas Radke, Edward Seidel, and John Shalf. Cactus Framework: Black Holes to Gamma Ray Bursts. 2007.

[222] Gabrielle Allen, Tom Goodale, Frank Löffler, David Rideout, Erik Schnetter, and Eric Seidel. Component specification in the cactus framework: The cactus configuration language. *Computing Research Repository - CORR*, 09 2010.

[223] Cactus Computational Toolkit home page: `http://cactuscode.org`.

[224] Tom Goodale, Gabrielle Allen, Gerd Lanfermann, Joan Massó, Thomas Radke, Edward Seidel, and John Shalf. The cactus framework and toolkit: Design and applications. In *Proceedings of the 5th International Conference on High Performance Computing for Computational Science*, VECPAR'02, pages 197–227, Berlin, Heidelberg, 2003. Springer-Verlag.

[225] carpet - adaptive mesh refinement for the cactus framework: `https://carpetcode.org`.

[226] Erik Schnetter, Peter Diener, Ernst Nils Dorband, and Manuel Tiglio. A Multi-block infrastructure for three-dimensional time-dependent numerical relativity. *Class. Quant. Grav.*, 23:S553–S578, 2006.

[227] Marsha Berger and Joseph Oliger. Adaptive mesh refinement for hyperbolic partial differential equations. *Journal of Computational Physics*, 53(3):484–512, 1984.

[228] Marcus Ansorg, Bernd Bruegmann, and Wolfgang Tichy. A Single-domain spectral method for black hole puncture data. *Phys. Rev.*, D70:064011, 2004.

[229] Jonathan Thornburg. A Fast apparent horizon finder for three-dimensional Cartesian grids in numerical relativity. *Class. Quant. Grav.*, 21:743–766, 2004.

[230] Jonathan Thornburg. Finding apparent horizons in numerical relativity. *Phys. Rev.*, D54:4899–4918, 1996.

[231] S. Dwyer. Advanced LIGO status. *J. Phys. Conf. Ser.*, 610(1):012013, 2015.

[232] Henrich Heitmann. Status of the advanced Virgo gravitational wave detector. *Proc. SPIE Int. Soc. Opt. Eng.*, 10700:1070017, 2018.

[233] A. Sesana et al. Space-based detectors. *Gen. Rel. Grav.*, 46(12):1793, 2014.

[234] P. McNamara et al. The LISA Pathfinder Mission. *ASP Conf. Ser.*, 467:5–16, 2013.

[235] B. P. Abbott et al. The Rate of Binary Black Hole Mergers Inferred from Advanced LIGO Observations Surrounding GW150914. *Astrophys. J.*, 833(1):L1, 2016.

[236] B. P. Abbott et al. Binary Black Hole Population Properties Inferred from the First and Second Observing Runs of Advanced LIGO and Advanced Virgo. 2018.

[237] Davide Gerosa, Sizheng Ma, Kaze W. K. Wong, Emanuele Berti, Richard O'Shaughnessy, Yanbei Chen, and Krzysztof Belczynski. Multiband gravitational-wave event rates and stellar physics. *Phys. Rev.*, D99(10):103004, 2019.

[238] Curt Cutler et al. The Last three minutes: issues in gravitational wave measurements of coalescing compact binaries. *Phys. Rev. Lett.*, 70:2984–2987, 1993.

[239] Joan Centrella, John G. Baker, Bernard J. Kelly, and James R. van Meter. Black-hole binaries, gravitational waves, and numerical relativity. *Rev. Mod. Phys.*, 82:3069, 2010.

[240] R. Sturani, S. Fischetti, L. Cadonati, G. M. Guidi, J. Healy, D. Shoemaker, and A. Vicere. Complete phenomenological gravitational waveforms from spinning coalescing binaries. *J. Phys. Conf. Ser.*, 243:012007, 2010.

[241] Sebastian Khan, Katerina Chatziioannou, Mark Hannam, and Frank Ohme. Phenomenological model for the gravitational-wave signal from precessing binary black holes with two-spin effects. 2018.

[242] Vijay Varma, Scott E. Field, Mark A. Scheel, Jonathan Blackman, Lawrence E. Kidder, and Harald P. Pfeiffer. Surrogate model of hybridized numerical relativity binary black hole waveforms. *Phys. Rev.*, D99(6):064045, 2019.

[243] Ilana MacDonald, Abdul H. Mroue, Harald P. Pfeiffer, Michael Boyle, Lawrence E. Kidder, Mark A. Scheel, Bela Szilagyi, and Nicholas W. Taylor. Suitability of hybrid gravitational waveforms for unequal-mass binaries. *Phys. Rev.*, D87(2):024009, 2013.

[244] Vijay Varma, Parameswaran Ajith, Sascha Husa, Juan Calderon Bustillo, Mark Hannam, and Michael Pürrer. Gravitational-wave observations of binary black holes: Effect of non-quadrupole modes. *Phys. Rev. D*, 90:124004, Dec 2014.

[245] Vijay Varma and Parameswaran Ajith. Effects of nonquadrupole modes in the detection and parameter estimation of black hole binaries with nonprecessing spins. *Phys. Rev.*, D96(12):124024, 2017.

[246] Juan Calderón Bustillo, Sascha Husa, Alicia M. Sintes, and Michael Pürrer. Impact of gravitational radiation higher order modes on single aligned-spin gravitational wave searches for binary black holes. *Phys. Rev. D*, 93:084019, Apr 2016.

[247] Ilana MacDonald, Samaya Nissanke, Harald P. Pfeiffer, and Harald P. Pfeiffer. Suitability of post-Newtonian/numerical-relativity hybrid waveforms for gravitational wave detectors. *Class. Quant. Grav.*, 28:134002, 2011.

[248] Mark Hannam, Sascha Husa, Ulrich Sperhake, Bernd Bruegmann, and Jose A. Gonzalez. Where post-Newtonian and numerical-relativity waveforms meet. *Phys. Rev.*, D77:044020, 2008.

[249] P. Ajith. Gravitational-wave data analysis using binary black-hole waveforms. *Class. Quant. Grav.*, 25:114033, 2008.

[250] Mark Hannam, Sascha Husa, Frank Ohme, and P. Ajith. Length requirements for numerical-relativity waveforms. *Phys. Rev.*, D82:124052, 2010.

[251] Ian W. Harry, Alexander H. Nitz, Duncan A. Brown, Andrew P. Lundgren, Evan Ochsner, and Drew Keppel. Investigating the effect of precession on searches for neutron-star-black-hole binaries with Advanced LIGO. *Phys. Rev.*, D89(2):024010, 2014.

[252] Katerina Chatziioannou, Neil Cornish, Antoine Klein, and Nicolás Yunes. Detection and

Parameter Estimation of Gravitational Waves from Compact Binary Inspirals with Analytical Double-Precessing Templates. *Phys. Rev.*, D89(10):104023, 2014.

[253] Tito Dal Canton, Andrew P. Lundgren, and Alex B. Nielsen. Impact of precession on aligned-spin searches for neutron star black-hole binaries. *Phys. Rev.*, D91(6):062010, 2015.

[254] Michael Boyle, Robert Owen, and Harald P. Pfeiffer. A geometric approach to the precession of compact binaries. *Phys. Rev.*, D84:124011, 2011.

[255] LIGO Scientific Collaboration. LIGO Algorithm Library - LALSuite. free software (GPL), 2018.

[256] http://www.black-holes.org/waveforms.

[257] Abdul H. Mroue et al. Catalog of 174 Binary Black Hole Simulations for Gravitational Wave Astronomy. *Phys. Rev. Lett.*, 111(24):241104, 2013.

[258] http://ccrgpages.rit.edu/~RITCatalog/.

[259] Scott E. Field, Chad R. Galley, Jan S. Hesthaven, Jason Kaye, Manuel Tiglio, Jonathan Blackman, Béla Szilágyi, Mark A. Scheel, Daniel A. Hemberger, Patricia Schmidt, Rory Smith, Christian D. Ott, Michael Boyle, Lawrence E. Kidder, Harald P. Pfeiffer, and Vijay Varma. Binary black-hole surrogate waveform catalog, May 2019.

[260] Patricia Schmidt, Mark Hannam, Sascha Husa, and P. Ajith. Tracking the precession of compact binaries from their gravitational-wave signal. *Phys. Rev. D*, 84:024046, Jul 2011.

[261] R. O'Shaughnessy, B. Vaishnav, J. Healy, Z. Meeks, and D. Shoemaker. Efficient asymptotic frame selection for binary black hole spacetimes using asymptotic radiation. *Phys. Rev.*, D84:124002, 2011.

[262] Eric Jones, Travis Oliphant, Pearu Peterson, et al. SciPy: Open source scientific tools for Python, 2001–. [Online; accessed ¡today¿].

[263] LIGO Scientific Collaboration. Advanced ligo anticipated sensitivity curves, 2011.

[264] Frank Ohme, Mark Hannam, and Sascha Husa. Reliability of complete gravitational waveform models for compact binary coalescences. *Phys. Rev.*, D84:064029, 2011.

[265] Lee Lindblom, Benjamin J. Owen, and Duncan A. Brown. Model Waveform Accuracy Standards for Gravitational Wave Data Analysis. *Phys. Rev.*, D78:124020, 2008.

[266] Jonathan Blackman, Scott E. Field, Mark A. Scheel, Chad R. Galley, Daniel A. Hemberger, Patricia Schmidt, and Rory Smith. A Surrogate Model of Gravitational Waveforms from Numerical Relativity Simulations of Precessing Binary Black Hole Mergers. *Phys. Rev.*, D95(10):104023, 2017.

[267] Abdul Mroue, Michael Boyle, Geoffrey Lovelace, Bela Szilagyi, Harald Pfeiffer, Anil Zenginoglu, Larry Kidder, Nicholas Taylor, Dan Hemberger, and Mark Scheel. Binary black-hole simulation sxs:bbh:0056, July 2019.

[268] Abdul Mroue, Michael Boyle, Geoffrey Lovelace, Bela Szilagyi, Harald Pfeiffer, Anil Zenginoglu, Larry Kidder, Nicholas Taylor, Dan Hemberger, and Mark Scheel. Binary black-hole simulation sxs:bbh:0047, July 2019.

[269] SXS Collaboration. Binary black-hole simulation sxs:bbh:1392, July 2019.

[270] Clifford M. Will Eric Poisson. *Gravity: Newtonian, Post-Newtonian, Relativistic.* 2014.

[271] J. M. Weisberg, D. J. Nice, and J. H. Taylor. Timing Measurements of the Relativistic Binary Pulsar PSR B1913+16. *Astrophys. J.*, 722:1030–1034, 2010.

[272] Joel M. Weisberg and Yuping Huang. Relativistic Measurements from Timing the Binary Pulsar PSR B1913+16. *Astrophys. J.*, 829(1):55, 2016.

[273] Bela Szilagyi, Jonathan Blackman, Alessandra Buonanno, Andrea Taracchini, Harald P. Pfeiffer, Mark A. Scheel, Tony Chu, Lawrence E. Kidder, and Yi Pan. Approaching the

Post-Newtonian Regime with Numerical Relativity: A Compact-Object Binary Simulation Spanning 350 Gravitational-Wave Cycles. *Phys. Rev. Lett.*, 115(3):031102, 2015.

[274] Scott C. Noble, Bruno C. Mundim, Hiroyuki Nakano, Julian H. Krolik, Manuela Campanelli, Yosef Zlochower, and Nicolas Yunes. Circumbinary MHD Accretion into Inspiraling Binary Black Holes. *Astrophys. J.*, 755:51, 2012.

[275] Louis Gallouin, Hiroyuki Nakano, Nicolas Yunes, and Manuela Campanelli. Asymptotically Matched Spacetime Metric for Non-Precessing, Spinning Black Hole Binaries. *Class. Quant. Grav.*, 29:235013, 2012.

[276] Bruno C. Mundim, Hiroyuki Nakano, Nicolas Yunes, Manuela Campanelli, Scott C. Noble, and Yosef Zlochower. Approximate black hole binary spacetime via asymptotic matching. *Phys. Rev.*, D89(8):084008, 2014.

[277] Miguel Zilhao, Scott C. Noble, Manuela Campanelli, and Yosef Zlochower. Resolving the relative influence of strong field spacetime dynamics and MHD on circumbinary disk physics. *Phys. Rev.*, D91(2):024034, 2015.

[278] Yosef Zlochower, Hiroyuki Nakano, Bruno C. Mundim, Manuela Campanelli, Scott Noble, and Miguel Zilhao. Inspiraling black-hole binary spacetimes: Challenges in transitioning from analytical to numerical techniques. *Phys. Rev.*, D93(12):124072, 2016.

[279] Brennan Ireland, Bruno C. Mundim, Hiroyuki Nakano, and Manuela Campanelli. Inspiralling, nonprecessing, spinning black hole binary spacetime via asymptotic matching. *Phys. Rev.*, D93(10):104057, 2016.

[280] Hiroyuki Nakano, Brennan Ireland, Manuela Campanelli, and Eric J. West. Spinning, Precessing, Black Hole Binary Spacetime via Asymptotic Matching. *Class. Quant. Grav.*, 33(24):247001, 2016.

[281] Dennis B. Bowen, Manuela Campanelli, Julian H. Krolik, Vassilios Mewes, and Scott C. Noble. Relativistic Dynamics and Mass Exchange in Binary Black Hole Mini-Disks. *Astrophys. J.*, 838(1):42, 2017.

[282] Dennis B. Bowen, Vassilios Mewes, Manuela Campanelli, Scott C. Noble, Julian H. Krolik, and Miguel Zilhao. Quasi-Periodic Behavior of Mini-Disks in Binary Black Holes Approaching Merger. *Astrophys. J.*, 853(1):L17, 2018.

[283] Stéphane D'Ascoli, Scott C. Noble, Dennis B. Bowen, Manuela Campanelli, Julian H. Krolik, and Vassilios Mewes. Electromagnetic Emission from Supermassive Binary Black Holes Approaching Merger. *Astrophys. J.*, 865(2):140, 2018.

[284] Nicolas Yunes, Wolfgang Tichy, Benjamin J. Owen, and Bernd Bruegmann. Binary black hole initial data from matched asymptotic expansions. *Phys. Rev.*, D74:104011, 2006.

[285] Nicolas Yunes and Wolfgang Tichy. Improved initial data for black hole binaries by asymptotic matching of post-Newtonian and perturbed black hole solutions. *Phys. Rev.*, D74:064013, 2006.

[286] Nathan K. Johnson-McDaniel, Nicolas Yunes, Wolfgang Tichy, and Benjamin J. Owen. Conformally curved binary black hole initial data including tidal deformations and outgoing radiation. *Phys. Rev.*, D80:124039, 2009.

[287] Y. Zlochower, J. G. Baker, Manuela Campanelli, and C. O. Lousto. Accurate black hole evolutions by fourth-order numerical relativity. *Phys. Rev.*, D72:024021, 2005.

[288] Pedro Marronetti, Wolfgang Tichy, Bernd Brügmann, Jose Gonzalez, and Ulrich Sperhake. High-spin binary black hole mergers. *Phys. Rev.*, D77:064010, 2008.

[289] C. Bona, T. Ledvinka, C. Palenzuela, and M. Zacek. General-covariant evolution formalism for Numerical Relativity. *Phys. Rev.*, D67:104005, 2003.

[290] Sebastiano Bernuzzi and David Hilditch. Constraint violation in free evolution schemes: Comparing BSSNOK with a conformal decomposition of Z4. *Phys. Rev.*, D81:084003, 2010.

[291] Takashi Nakamura, Ken-ichi Oohara, and Y. Kojima. General relativistic collapse to black holes and gravitational waves from black holes. *Prog. Theor. Phys. Suppl.*, 90:1–218, 1987.

[292] M. Shibata and Takashi Nakamura. Evolution of three-dimensional gravitational waves: Harmonic slicing case. *Phys. Rev.*, D52:5428, 1995.

[293] T. W. Baumgarte and S. L. Shapiro. Numerical integration of Einstein's field equations. *Phys. Rev.*, D59:024007, 1998.

[294] Wolfgang Kastaun, Filippo Galeazzi, Daniela Alic, Luciano Rezzolla, and José A. Font. Black hole from merging binary neutron stars: How fast can it spin? *Phys. Rev.*, D88(2):021501, 2013.

[295] Daniela Alic, Wolfgang Kastaun, and Luciano Rezzolla. Constraint damping of the conformal and covariant formulation of the Z4 system in simulations of binary neutron stars. *Phys. Rev.*, D88(6):064049, 2013.

[296] Heinz-Otto Kreiss and Joseph Oliger. Methods for the approximate solution of time dependent problems. *Global atmospheric research programme publications series*, 10, 1973.

[297] Erik Schnetter, Scott H. Hawley, and Ian Hawke. Evolutions in 3D numerical relativity using fixed mesh refinement. *Class. Quant. Grav.*, 21(6):1465–1488, 21 March 2004.

[298] S. Brandt and B. Brügmann. A simple construction of initial data for multiple black holes. *Phys. Rev. Lett.*, 78(19):3606–3609, 1997.

[299] Zachariah B. Etienne, Joshua A. Faber, Yuk Tung Liu, Stuart L. Shapiro, and Thomas W. Baumgarte. Filling the holes: Evolving excised binary black hole initial data with puncture techniques. *Phys. Rev.*, D76:101503, 2007.

[300] David Brown, Olivier Sarbach, Erik Schnetter, Manuel Tiglio, Peter Diener, et al. Excision without excision: The Relativistic turducken. *Phys. Rev.*, D76:081503, 2007.

[301] David Brown, Peter Diener, Olivier Sarbach, Erik Schnetter, and Manuel Tiglio. Turducken-ing black holes: An Analytical and computational study. *Phys. Rev.*, D79:044023, 2009.

[302] Kenneth A. Dennison, Thomas W. Baumgarte, and Pedro J. Montero. Trumpet Slices in Kerr Spacetimes. *Phys. Rev. Lett.*, 113(26):261101, 2014.

[303] Kenneth A. Dennison and Thomas W. Baumgarte. A Simple Family of Analytical Trumpet Slices of the Schwarzschild Spacetime. *Class. Quant. Grav.*, 31:117001, 2014.

[304] Yosef Zlochower, Marcelo Ponce, and Carlos O. Lousto. Accuracy Issues for Numerical Waveforms. *Phys. Rev.*, D86:104056, 2012.

[305] Steven R. Brandt and Edward Seidel. The Evolution of distorted rotating black holes. 3: Initial data. *Phys. Rev.*, D54:1403–1416, 1996.